Performance Analysis of Multicarrier and Multiple Access Schemes Compatible with IM/DD Systems for VLC

Submitted in partial fulfilment of the requirements
for the award of the degree of

Doctor of Philosophy

by

Suseela Vappangi
(Roll No: 716143)

Under the supervision of

Dr. V. Venkata Mani

Associate Professor

Department of Electronics & Communication Engineering

National Institute of Technology Warangal

Telangana, India - 506004

2019

Dedicated

To

The Almighty Lord,

My Parents, Family Members,

Teachers, Well-wishers, & Friends

Approval Sheet

This thesis entitled **Performance Analysis of Multicarrier and Multiple Access Schemes Compatible with IM/DD systems for VLC** by **Suseela Vappangi** is approved for the degree of **Doctor of Philosophy**.

Examiners

Research Supervisor

Dr. V. Venkata Mani
Associate Professor
Department of ECE
NIT Warangal, India-506004

Chairman & Head

Prof. N. Bheema Rao
Department of ECE
NIT Warangal, India-506004

Place:
Date:

Declaration

This is to certify that the work presented in this thesis entitled **Performance Analysis of Multicarrier and Multiple Access Schemes Compatible with IM/DD Systems for VLC** is a bonafied work done by me under the supervision of **Dr. V. Venkata Mani** and was not submitted elsewhere for the award of any degree.

I declare that this written submission represents my own ideas and even considered others ideas which are adequately cited and further referenced the original sources. I understand that any violation of the above will cause disciplinary action by the institute and can also evoke panel action from the sources or from whom proper permission has not been taken when needed. I also declare that I have adhered to all principles of academic honesty and integrity and have not misrepresented or fabricated or falsified any idea or data or fact or source in my submission.

Suseela Vappangi
Research Scholar
Roll No.: 716143

Place:
Date:

NATIONAL INSTITUTE OF TECHNOLOGY
WARANGAL, INDIA-506004
Department of Electronics & Communication Engineering

CERTIFICATE

This is to certify that the thesis work entitled **Performance Analysis of Multicarrier and Multiple Access Schemes Compatible with IM/DD Systems for VLC** is a bonafide record of work carried out by **Suseela Vappangi**, **716143**, submitted to the faculty of **Electronics & Communication Engineering** department, in partial fulfilment of the requirements for the award of the degree of **Doctor of Philosophy** in **Electronics and Communication Engineering, National Institute of Technology Warangal, India-506004**. The contributions embodied in this thesis have not been submitted to any other university or institute for the award of any degree.

Dr. V. Venkata Mani
Research Supervisor
Associate Professor
Department of ECE
NIT Warangal, India-506 004.

Place:
Date:

Acknowledgements

First and foremost, I wholeheartedly thank God Almighty for showering his blessings on me and giving me the strength, knowledge, ability and opportunity to undertake this research study and to persevere and complete it satisfactorily. Without his abundant mercy and grace, this achievement would not have been possible. I would like to express my immesurable appreciation and deepest gratitude to the following persons who in one way or the other played a major role for enabling this study possible.

I would like to express my deep and sincere gratitude to my research supervisor Dr. V. V. Mani for giving me an oppurtunity to work under her esteemed guidance and for providing invaluable guidance, encouragement and continuous support throughout this entire tenure of my research. Her vision, sincerity and motivation have deeply inspired me. It's my immense pleasure to work with her, especially a person who is having immense knowledge, enthusiasm, energy, passion and strong potential in the areas of wireless communications, detection and estimation theory which helped me to develop some basic concepts pertaining to my research area. She gave me valuable insights to carry out the research work and to present the work as clearly as possible. She is the one whom I admire the most, her love, care and trust towards me, helped me to reach the position in what I am holding. I could not have imagined having a better advisor and mentor for my Ph.D study.

I express my sincere thanks to chairman of the Doctoral Scrutiny Committee (DSC) and Head of the department Prof. N. Bheema Rao for his invaluable advices, motivation and insightful comments at various stages of this work. I would also like to thank the DSC members, Prof. D. Srinivasacharya (Department of Mathematics) and Prof. L. Anjaneyulu (Department of Electronics and Communication Engineering) for their insightful comments, encouragement, constructive suggestions, fruitful discussions and thought provoking words incented me to widen my research from various perspectives. I also thank Prof. T. Kishore Kumar for his valuable suggestions throughout this entire tenure of my research. I extend my thanks to all the faculty members of the Department of E.C.E and non-teaching staff for their support, friendly nature and timely help.

I would also like to thank my seniors Dr. D. Santhosh Kumar, Dr. Sai Krishna Kondoju and Dr. Shravan Kumar Bandari for their timely help and technical debates. Furthermore, I also thank my fellow labmates Mr. Siva Prasad Valluri, Mr. Kishore Vejandla and Mr. Ganesh Miriyala for creating a friendly atmosphere in the wireless communication research laboratory. From my fellow labmates, I have learnt innumerable aspects like leading an independent life at all times which helped me to become strong and to gain sufficient amount of courage to handle any tough situations in my further life ahead. From the depth of my heart, I once again thank them and wish them a great success in all their future endeavours.

I am extremely grateful to my parents V. Chalapathi Rao and V. Rama Devi for their intensive love, prayers, caring and sacrifices for educating and preparing me for my future. Without their love, trust and encouragement, it would be difficult for me to accomplish this study. I am very much thankful to my family members for their prayers and continuing support to complete this research work. Also, I express my thanks to my dearest and loved friend Ms. Radhika Kala Sridhar for being with me, caring me, expressing her love, encouraging me and lifting me up during my tough times. She always holds a special position in my heart. I wish her good luck for her future endeavours.

Last but not the least, I express my sincere gratitude to my school teachers, family friends, well wishers and cousins Y. Likhitha and Y. Bharathi for their continuous prayers, encouragement, support and their soothing words helped me to accomplish this study peacefully.

Suseela Vappangi

Abstract

During the last decade, the rapid proliferation of mobile devices created an ever-increasing need for high speed data access. This unintermittedly manifested the present radio frequency (RF) based wireless communication systems to suffer from spectrum congestion, limited data rates, huge increase in latency, decrease in reliability of services and interference. Concurrently, indoor illumination has been revolutionized by solid-state lighting, where light emitting diodes (LEDs) have been emanating as potential technology to replace current incandescent and fluorescent lamps due to their distinguished advantages such as long lighting hours, high efficiency, small size and low power consumption. Persuaded by this striking augmentation of LED technologies and in order to alleviate the RF spectrum scarcity problem, visible light communication (VLC) is arousing invariably tremendous momentum in both academia and industry. The noteworthy features offered by VLC like its worldwide usage, huge, license-free bandwidth and enhanced security facilitated VLC to evolve as a promising candidate to complement the conventional RF counterpart. The stupendous notability of VLC to facilitate illumination and communication contemporaneously by exploiting illuminating devices like LEDs will definitely enable VLC to emerge as an intriguing alternative to traditional RF-based wireless communication.

Foreseeing the future demands of several applications, this dissertation focuses on several aspects of VLC which are vital to be addressed to render high data rate communication. In spite of significant amount of prevalence, the low modulation bandwidth of white phosphorescent LEDs hinders the high data rate communication. Therefore, to boost the data rates, VLC adopts the robust multicarrier modulation technique like orthogonal frequency division multiplexing (OFDM) due to its inherent advantages like combating inter symbol interference, being resilient to frequency selective fading channel effects, simple single tap-equalization techniques, etc. The non-coherent emission characteristics of LEDs make intensity modulation (IM) and direct detection (DD) as the most viable modulation scheme for VLC. This is obvious because the data is transmitted by modulating the intensity of light. However, the traditional OFDM as used in RF cannot be directly employed in VLC due to the constraint that the transmitted signal has to be both real and positive-valued i.e., unipolar. It is apparent that inverse fast Fourier transform (IFFT) and fast Fourier transform (FFT) play a vital role for enabling modulation and demodulation in OFDM. When the incoming stream of data is mapped by employing complex constellation techniques like quadrature amplitude modulation (QAM), the output of the IFFT will be a complex and bipolar signal. Since, light intensity cannot be negative and complex, the input to the IFFT is constrained to satisfy Hermitian Symmetry criteria for yielding a real valued signal while dealing with optical OFDM. However, in doing so, only half of the subcarriers are utilized for the transmission of the data because the rest half are flipped complex conjugate versions of the previous ones. Therefore, this leads to a decrease in throughput and moreover incurs additional digital signal processing for the computation of Hermitian Symmetry.

Consequently, this entails to exploit real transformation techniques like discrete cosine transform (DCT), discrete sine transform (DST), and discrete Hartley transform (DHT), etc for obtaining a real-valued signal. In order to yield a positive-valued signal, DC-biased optical OFDM (DCO-OFDM), asymmetrically clipped optical OFDM (ACO-OFDM) are considered in this work. In general DCO-OFDM consists of adding a DC bias to the time-domain signal in order to attain a positive valued signal. In specific, this addition of DC bias has made DCO-OFDM as a power inefficient scheme. ACO-OFDM overcomes this drawback by avoiding the addition of DC bias but, this is at the expense of reduced throughput. Due to real and positive nature of the transmitted time-domain signal, firstly we derive the mathematical expressions for the time-domain signal formats in accordant with IM/DD systems for VLC. Taking into consideration the dispersive VLC channel environment in an indoor room environment, sensing and estimation of the channel is necessary. This work analyses the performance of comb-type pilot arrangement aided channel estimation for different multicarrier transmission systems like DCO-OFDM, ACO-OFDM, DHT-based ACO-OFDM and Fast-Walsh Hadamard Coded Modulation (HCM), DCT-based DCO-OFDM over dispersive VLC channel. In addition, for the first time this work proposes a DST-based DCO-OFDM and ACO-OFDM system and evaluates the bit error rate (BER) performance of the developed system over both additive white Gaussian noise (AWGN) channel and diffused optical channel environment. Various channel estimation techniques like least square (LS), minimum mean square error (MMSE), different interpolation techniques like linear, spline and low-pass interpolation schemes are evaluated and compared for the aforementioned multicarrier systems. In addition, Cramer Rao Lower Bound (CRLB) is derived for the channel estimation error.

Furthermore, this thesis addresses a vital aspect like peak to average power ratio (PAPR) which arises due to the superimposition of huge number of subcarriers in optical OFDM. This aspect is fuelled with the limited dynamic range of LEDs, where it leads to clipping of the time-domain optical OFDM signal which doesn't fit within the linear range of LEDs. Hence, investigations are carried to reduce the amount of PAPR by imposing several PAPR reduction techniques like Spreading technique, Partial Transmit Sequence (PTS), clipping and filtering. Exploiting the advantages of real trigonometric transform like DCT and DST, this work proposes DCT-spread and DST-spread technique to reduce the amount of PAPR in DCT/DST-based DCO-OFDM system. Upon comparison with other PAPR reduction schemes, the spreading technique significantly reduces the amount of PAPR. Additionally, in order to reduce the amount of PAPR in a multicarrier based system, this thesis expedites single carrier frequency division multiple access (SC-FDMA) and derives the mathematical expressions for different mapping strategies like optical localized frequency division multiple access (OLFDMA), optical interleaved FDMA (OIFDMA) and compares the PAPR performance with optical orthogonal frequency division multiple access (OOFDMA) for both DCT and DST based multiple access systems. The simulated results emphasize that among the multiple access schemes, PAPR reduction in OIFDMA is superior than OLFDMA and outperforms OOFDMA in both DCT/DST based systems.

Finally, this work addresses the performance of the developed multicarrier and multiple access systems in the presence of frequency offset (FO) and symbol time offset (STO) and furthermore, derives the mathematical analysis for different sorts of interferences like inter carrier interference (ICI), multi user interference (MUI) emanating in the uplink scenario in DFT-based and DCT-based DCO-OFDMA systems. This is a vital issue which needs to be addressed because, the presence of these offsets hinders the detection capability of the desired subscriber signal in the presence of multiple users. From the simulated results it can be evidenced that the BER performance of the proposed system deteriorates as the sensitivity of the offsets increases. Hence, in order to effectively estimate these offsets, this thesis imposes synchronization algorithms like Classen, Moose, Training symbol-assisted, Maximum correlation and Minimum difference algorithms. Additionally, CRLB is derived for the estimation of FO and STO and is verified through simulation results. From the simulation results, it can be evidenced that CRLB attains the minimum mean square error (MSE) upon comparison with other algorithms.

The major focus of this thesis is to derive the analytical expressions for different time-domain signals for both multicarrier and multiple access schemes which are fulfilling the requirements of cost-effective IM/DD systems for VLC. For the provision of reducing the computational complexity, this work analyses the performance of DCO-OFDM and ACO-OFDM system based on real signal transformation techniques like DCT, DST and DHT in terms of BER, MSE and PAPR and compares with the traditional HS imposed FFT-based optical OFDM. Even though several variants of OFDM have been proposed in the literature, the main motive behind employing DCO and ACO-OFDM is that majority of the variants are a combination of DCO and ACO-OFDM. Moreover, the other variants involve a complexity in the design of receiver. The proposed system models and the mathematical analysis carried in this work will enable VLC to be envisaged as a potential complementary to RF-based wireless communication.

Contents

List of Figures

List of Tables

List of Abbreviations

ACO-OFDM asymmetrically clipped optical-OFDM

ACE active constellation extension

ADO-OFDM asymmetrically clipped DC-biased optical-OFDM

ADSL asymmetric digital subscriber line

ANN artificial neural network

AWGN Additive White Gaussian Noise

AS-BMMSE-CE adaptive stastical Bayesian minimum mean square error channel estimation

ASICs Application Specific Integrated Circuits

BBM branch and bound method

BE bandwidth efficiency

BER Bit Error Rate

bps bits per second

CAN Controller area network

CIR Channel Impulse Response

CSI Channel State Information

CDMA Code Division Multiple Access

CCDF Complementary Cumulative Distribution Function

CM cubic metric

CP Cyclic Prefix

CSK color shift keying

DAB Digital Audio Broadcasting

DCO-OFDM DC-biased optical-OFDM

DCT discrete cosine transform

DFDMA distributed frequency division multiple access

DMT discrete multitone modulation

DPPM Differential PPM

DOPPM Differential Overlapping PPM

DSP Digital Signal Processing

DST discrete sine transform

DVB Digital Video Broadcasting

DVB-T DVB-Terrestrial

DFT Discrete Fourier Transform

DFE decision feedback equalizer

DHT discrete Hartley transform

DSL Digital Subscriber Line

DSRC dedicated short range communications

E/O electrical-to-optical

EPPM Expurgated PPM

eU-OFDM enhanced unipolar optical OFDM

EVM error vector magnitude

FD-DFE frequency-domain decision feedback equalizer

FDM Frequency Division Multiplexing

FDMA Frequency Division Multiple Access

FFT Fast Fourier Transform

FIR finite impulse response

FO frequency offset

FOV Field of View

FSO Free Space Optical Wireless Communication

Gbps Giga bps

GHz Giga Hertz

GLRT generalized likelihood ratio test

HACO-OFDM hybrid ACO-OFDM

ICI Inter Carrier Interference

ICSA Infrared Communication Systems Association

ICT information and communication technology

IDFT Inverse Discrete Fourier Transform

IDWT Inverse Discrete Wavelet Transform

IEEE Institute of Electrical and Electronics Engineers

IFDMA interleaved frequency division multiple access

i.i.d independent and identically distributed

ISFA intra-symbol frequency-domain averaging

IoT Internet of Things

IP Internet Protocol

ISI Inter Symbol Interference

IFFT Inverse Fast Fourier Transform

IrDA Infrared Data Association

ITS intelligent transportation system

JEITA Japan Electronics and Information Technology Industries Association

Kbps Kilo bits per second

KHz Kilo Hertz

km kilo meters

LED Light Emitting Diode

LFDMA localized frequency division multiple access

LFFE linear feed forward equalization

LOS Line of Sight

LS Least Squares

LSA least squares approximation

LTE Long term Evolution

MAC medium access control

MEPPM Multi-level EPPM

MFTP maximum flickering time period

MIMO multiple input multiple output

MLSD maximum likelihood sequence detection

MMSE	Minimum Mean Square Error
MUI	multi user interference
MPPM	multipulse PPM
MSE	mean square error
NLOS	Non Line of Sight
NRZ	non-return-to-zero
OAP	Optical access point
OCI	optical communication image sensor
OEOSC	optimized even and odd sequence combination
OFDM	Orthogonal Frequency Division Multiplexing
OFDMA	Orthogonal Frequency Division Multiple Access
OLEDs	organic LEDs
O-OFDM-IDMA	optical OFDM interleave division multiple access
OOK	on-off keying
OPPM	Overlapping PPM
OWC	optical wireless communication
PAPR	Peak-to-Average-Power Ratio
PAM-DMT	pulse amplitude modulated discrete multitone modulation
PD	Photodiode
PDF	probability density function
PLC	power line communication
PTS	Partial Transmit Sequence

PSK Phase Shift Keying

PWM pulse width modulation

PPM pulse position modulation

PRIC pseudo-random interferometry code

QAM Quadrature Amplitude Modulation

QPSK Quadrature Phase Shift Keying

QoS Quality of Service

RF Radio Frequency

RGB red, green and blue

RLL run length limited

RPO-OFDM reverse polarity optical OFDM

RSU Road Side Unit

SC-FDMA Single Carrier-Frequency Division Multiple Access

SCR signal-to-clipping noise ratio

SNR signal to noise ratio

SLM selected mapping

SSL solid state lighting

STO Symbol Time Offset

TDMA Time Division Multiple Access

THz terahertz

TIA Transimpedance Amplifier

TI Texas Instrument

TKM-TR time-domain kernel matrix

TLED TriLED

TOV turn on voltage

VANET Vehicle Ad-hoc Network

VLC Visible Light Communication

VLCA Visible Light Communication Association

VLCC Visible Light Communication Consortium

VoIP voice over internet protocol

VPPM variable pulse position modulation

VRPPM variable rate multi PPM

VSCC vehicle safety communications consortium

V2V vehicle to vehicle

V2I vehicle to infrastructure

WHT Walsh Hadamard Transform

WIFA weighted inter-frame averaging

Chapter 1

Brief Overview

1.1 Introduction and Literature Survey

The sophisticated advancements of technology sparked a significant amount of attraction in the modern society to rely on wireless communication technologies for achieving an economical and ubiquitous data transmission aid. This is further escalated with the expeditious augmentation of mobile devices which includes laptops, tablets, palmtops, smart phones and diverse number of devices which are on the internet of things (IoT) have lead to a drastic increase in the insistence for data access over the wireless networks. In the recent times, several studies in the literature reveal that mobile data traffic is increasing explosively [1]. Consequently, this exponential increase of mobile data traffic saturates the existing radio frequency (RF) spectrum thereby enabling it to emerge as an inadequate resource in the near future. This unprecedented increase in the demand for data manifests to curtail the reliability of services which leads to a huge increase in latency and decrease in network throughput. This is referred to as ‘spectrum crunch’. To alleviate this congested RF spectrum problem, definitely alternative technologies are necessitated to fill in the existing gap [2], [3].

This progressively garnered a tremendous interest towards the visible light portion of the electromagnetic spectrum and has given rise to a novel communication based technology called visible light communication (VLC). The distinctive nature of VLC is that it exploits simple, solid-state, cost-effective, energy-efficient and sustainable opto-electronic devices like light emitting diodes (LEDs) to facilitate ‘illumination’ and ‘communication’ contemporaneously. VLC has gained a significant momentum in the recent years due to its distinguishing characteristic features of offering a prodigious, unregulated and licensed-free bandwidth in the range of several terahertz (THz) frequency range i.e., corresponding to a frequency of 430 THz to 790 THz. Thus, the abundance of unlicensed and re-usable visible light band bestows as the most feasible solution to support and complement the RF-based wireless communications. Additionally, the energy consumption at a global level laid the platform to instigate economically and ecologically amicable solutions. This is further intensified with the reformation of indoor illumination where the incandescent and fluorescent lamps have been replaced by a more compact lighting sources like LEDs.

This evolves to be a simple and cost-effective solution to reduce the emission of green house gases and to effectively increase the energy-utilization efficiency. Furthermore, the rapid deployment of LEDs has accelerated their interface in many illumination appliances, smart phones, televisions, road side units (RSU) like traffic signals, vehicular based infrastructure namely head and tail lights of cars, advertising panels, street lights, dashboards and several other applications [4]. A myriad variety of applications are becoming LED-based because of their remarkable benefits which includes compactness, sustainability, low power consumption, high tolerance to humidity, longer operational life time, easier and smoother operation, no electromagnetic interference, high energy efficiency, etc. The prominent virtue of LED is that it can be switched at a rapid speed to modulate the data signal without the change being perceived by the human eye. Thus, it facilitates simultaneous communication and illumination which is aesthetically pleasing to the human eye.

Accordingly, the several distinguished traits of LEDs exhibit clear advantages over the incandescent and fluorescent lamps and unambiguously they are foreseen to emerge as potential candidates for future illumination equipments. Moreover, the fast switching speeds of LEDs, i.e., their fast response time allows for the realization of efficient high speed wireless links, where each LED can act as an optical access point (OAPs). In particular, an indoor optical wireless link can be effectively realized by utilizing simple, cost-effective, power-efficient and reliable opto-electronic devices like LEDs and photodiodes (PDs). Moreover, the omnipresence of LEDs provides the flexibility of creation of a small scale communication network where each installed LED lighting fixture acts as a base station or as an OAP rendering service to multitude of subscribers which are within the vicinity of the LEDs. If the indoor base stations are merged with LED-based illumination devices and amalgamated with other communication networks in a manner to facilitate the intelligence combination of ‘illumination’ and ‘communication’ then, a power and spectrally efficient indoor communication can be accomplished.

This emanating technology imparts several illustrious benefits among of which are the following:

- VLC does not exhibit any interference with RF based electronic circuitry thus, allowing for its easy interface in planes, hospitals, public places like museums, auditoriums, etc.
- It is referred to as a safer technology because it assures no health hazards as long as skin and eye safety regulations are fulfilled.
- Moreover, its energy-efficient nature enabled it to be referred to as a green communication technology as there is significant reduction in the levels of emission of carbon-dioxide.
- Additionally, it guarantees a secure and reliable communication because the light signals do not penetrate through walls and opaque objects therefore, certainly the amount of inter-cell interference can be effectively reduced thus assuring protection of data against eavesdropping.
- The rapid deployment of LEDs enables their easy interface with almost every unit present in the city which includes, RSU like street lightings, traffic signals, dashboards, advertisements panels and sign-boards thus, imbibing the city to emerge as a smart city.
- The abundance amount of unlicensed bandwidth will definitely guarantee a high data rate communication. Thus, this technology can be claimed to be an intriguing revolutionary to traditional RF-based wireless communication counterparts because it copes up with the future demand of indoor access to many real-time bandwidth intensive applications like streaming audio, video, high definition television, voice over internet protocol (VoIP), etc.

Going into the details about the origin of VLC: The tremendous efforts by the researchers at Keio University in Japan has resulted in the development of a home based access network by exploiting white LEDs [5]. Later on, progressed by the rapid research in Japan, with the motive of enabling VLC support for hand-held devices and vehicles paved the way for the formation of Visible Light Communications Consortium (VLCC), in Japan in the year November 2003 [6]. This consortium contributes to research, augmentation and professed two standards namely Visible Light Communication System standard and Visible Light ID System for VLC. Later on, these aforesaid standards were disseminated by Japan Electronics and Information Technology Industries Association (JEITA) in the year June 2007 as JEITA CP-1221 and JEITA CP-1222 [7]. Subsequently in October 2008, VLCC started cooperation with the Infrared Data Association (IrDA) and the Infrared Communication Systems Association (ICSA) [8]. VLCC specification standard adopting and expanding the IrDA physical layer was announced in the year 2009.

Concurrently, much relevant work was strived in OMEGA Project (home Gigabit Access) in [9] which was supported by the European Community. This work emphasizes that optical wireless communication (OWC) will unambiguously furnish the desired high data rate communication [10]. With the motive of further enhancing the standardization of VLC, it can be claimed that Visible Light Communications Association (VLCA) is descendant of VLCC [11]. In the year 2011, an IEEE standard for VLC was formulated, named as IEEE 802.15.7 which gives all the information pertaining to the link and physical layers. Furthermore, IEEE 802.15.7 formed a Task Group to revise the current IEEE 802.15.7-2011 standard and announced for the development of IEEE 802.15.7 r1 [12]. The technical specification of IEEE 802.15.7 r1 standard provides the optical camera communication (OCC) i.e., VLC exploiting a camera and LED-identification system. Even till to-date, the research efforts are striving forward to revise this IEEE 802.15.7 standard. The IEEE 802.15.7-2018 which is said to be a revised version of IEEE 802.15.7-2011, elucidates physical and medium access control (MAC) sublayer for short range OWC in optically transparent media which is exploiting light wavelengths ranging from 10000 nm to 190 nm [13]. Moreover, this standard exhibits its potential to impart data rates that are sufficient enough to reinforce both audio and video multimedia services and broadens the scope to include more OWC technologies. This standard takes into consideration several aspects like: the mobility of the optical link, checks for the compatibility with several other illumination infrastructures, the impairments due to noise as well as the interference arising from other sources of ambient light and artificial light sources. It even defines a MAC sublayer that furnishes the exclusive needs of the visible links as well as other targeted light wavelengths. The most vital aspect of this standard is that it complies to eye safety regulations.

Additionally, the applicability of OWC in optical wireless personal area networks (OWPANS) is also outlined in this standard and furthermore, addresses several topics like the usage of OWC in network topologies, addressing, collision avoidance, acknowledgment, performance quality indication, visibility and dimming support, etc. A comprehensive current state-of-the art aspects pertaining to VLC which includes the brief overview of the VLC technology, from its physical aspects and communication architecture to its main applications and research challenges can be found in the latest survey as stated in [14].

1.2 A Basic VLC System Model

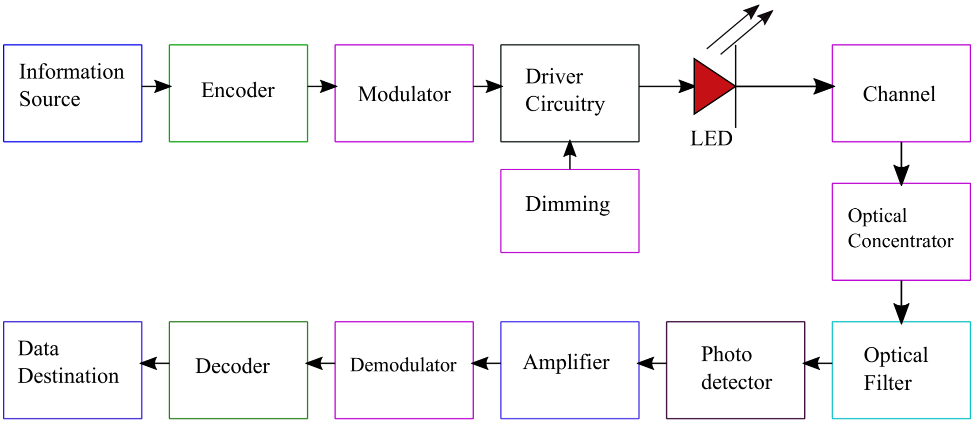

Figure 1.1: VLC System Model

A schematic representation of a typical VLC system model is delineated in Fig. 1.1. This block diagram illustrates that a typical VLC link can be realized by exploiting opto-electronic devices like LEDs at the transmitting end and a PD at the receiving end. As evident from the figure, since light is used as a medium of transmission, the incoming stream of data is modulated by varying the intensity of LED. Furthermore, the key prerequisite of driver circuitry is to control the amount of current passing through the LED i.e., it is responsible for adjusting the luminosity (brightness) levels of LEDs. In the perspective of energy saving this is of paramount important. When the LED is meant to be used for communication, the role of the driver circuitry is to combine the input data and the dimming control signal (DC power level), and to superimpose them to drive the LED [15]. In particular, as per the requirements of the data application, the LED driver circuitry is modified in a manner where the data is modulated by using emitted light. Further, this optical signal is passed through an optical amplifier lens or a collimator or a diffuser to broaden the beam. Thereupon, after propagation through the optical wireless channel, this emitted light message gets intercepted by the PD based VLC receiver.

Since, the signal invades the receiver after undergoing several reflections due to the presence of obstacles so, both Line of Sight (LOS) and Non Line of Sight (NLOS) components arrive at the receiving side. Therefore, in order to chose the desired signal of interest, an optical filter plays a vital role at the receiving end. Moreover, it can greatly reduce the effect of ambient light sources like sunlight as well as artificial light sources. The PD converts light intensity into electrical signal, which is then amplified by means of a transimpedance amplifier (TIA) and then processed to obtain the final output. Hence, while dealing with the transmitter LED and the receiver PD in the optical domain, it is of major prerequisite to consider the primary characteristics like radiation and detection pattern of LED/PD, output power emanating from LED, Field of View (FOV) of the PD, electrical modulation bandwidth, etc.

Generally, white light is the most prevalent source of light for both indoor and outdoor scenarios. There are two approaches for generating white light: (*i*) conjoining three underlying colours such as red, green and blue emitters. (*ii*) Secondly, a blue LED with yellow phosphor coating generates white light. However, the later is more desired for illumination due to its low production cost. But, from the communication point of view, the speed at which the LED switches is limited by the phosphor coating. Consequently, this hinders the assurance of high data rate communication. To overcome the limited modulation bandwidth of such kind of LEDs, extensive research has been carried. Few such are:

- Employing blue-filters for filtering the yellowish-phosphor component [16].
- Exploiting pre-equalization techniques at the transmitting LED driver module [17].
- Using post-equalization at the receiving end [18].

- By combining the above three approaches.
- Additionally, utilizing sophisticated multicarrier modulation schemes like orthogonal frequency division multiplexing (OFDM) and multiple input multiple output (MIMO) schemes proved to be an effective solution for rendering high data rate transmission.

1.3 Modulation Schemes in accordant with IM/DD systems for VLC

1.3.1 Factors affecting the design of modulation formats pertaining to IM/DD systems for VLC

While designing the modulation formats reconciling with the IM/DD systems, it is vital to take into consideration two prime factors like

- Flickering
- Dimming

The rapid fluctuations in the brightness of light is referred to as flicker. In generality, for the purpose of enabling communication, the light sources are modulated resulting in a significant amount of flicker. In order to avoid flicker, the changes in the brightness of light should fall within the maximum flickering time period (MFTP). The MFTP is defined as the maximum time period over which the light intensity can change without the human eye perceiving it. However, there is no widely accepted optimal flicker mitigation frequency, a frequency greater than 200 Hz (MFTP $< 5\ ms$) is generally considered safe. The IEEE 802.15.7 standard [19] is particular in mitigating the problem of flickering. It proposed the usage of run length limited (RLL) codes such as $Manchester$, $4B6B$ or $8B10$ to overcome the aforementioned drawback since, these codes have an equal number of $1s$ and $0s$. However, the authors in [20] demonstrated that, the $Manchester$ code consumes huge amount of bandwidth, whereas $4B6B$ or $8B10B$ codes are less efficient in terms of throughput.

Flickering does not impose severe hazardous effects in vehicular applications. Besides the usage of *RLL* codes, vehicular applications even employ different codes to assure high performances. Thus, the significance and suitability of Miller codes for future MIMO applications was given in [20], [21]. The importance of spread spectrum codes and their robustness to noise was briefed in [22], [23]. For the purpose of power saving and energy efficiency, dimming support is another important prerequisite for VLC. In this regard, it is vital to enforce sophisticated modulation formats to ensure that both communication and energy saving phenomenon are implemented concurrently. Earlier OOK and VPPM was propounded by IEEE 802.15.7 standard, where a certain desired amount of dimming is attained but at the expense of reduction in data rates. However, reverse polarity optical OFDM (RPO-OFDM), a variant of optical OFDM in [24] emphasizes that both dimming and high data rate communication can be imparted.

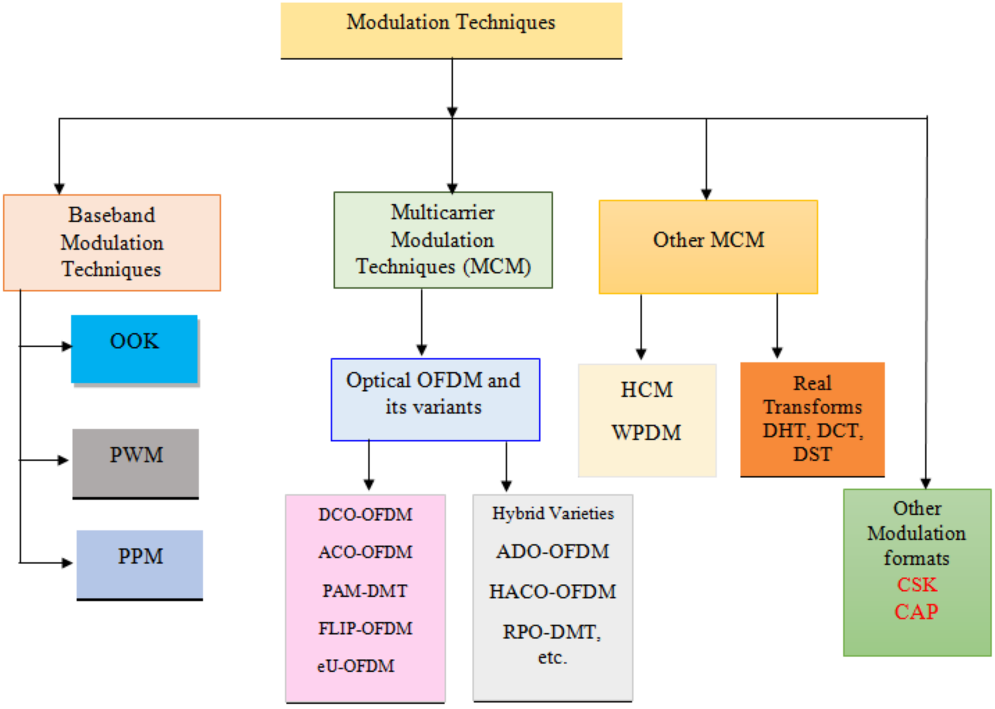

Figure 1.2: Modulation Schemes in accordant with IM/DD systems

1.3.2 Baseband Modulation Schemes

Baseband modulation schemes provide the flexibility in terms of their ease of implementation in IM/DD based VLC systems. Predominantly, the modulation techniques like on-off keying (OOK), pulse width modulation (PWM) and pulse position modulation (PPM) are much appropriate when low to moderate data rates are desired. Upon increasing the spectral efficiency under highly dispersive optical channel environment, these techniques eventually lead to deterioration of the system performance due to prevalence of ISI. Consequently, for attaining a better and improved system performance it obliges these schemes to rely on complex equalization techniques like maximum likelihood sequence detection (MLSD), decision feedback equalization (DFE), linear feed forward equalization (LFFE), etc.

In particular, the huge sets of incoming bit stream is modulated by turning the LEDs ‘ON’ and ‘OFF’. Prior works in the literature illustrate that OOK modulation is implemented for a VLC system exploiting phosphorescent white LED. The slow relaxation time of phosphor hinders the high transmission speeds [25]. Therefore, to overcome the limited modulation bandwidth, various techniques were proposed which resulted into several publications, few such are [26], [27], [28], etc. Among these published works, [26] proposes for the first time non-return-to-zero (NRZ) OOK modulation for the VLC system, where the VLC link utilizes a white LED and delivered a data rate of 10 Mbps. The later published works depicts the improvement in data rates varying in the range from 40, 100 and 125 Mbps by adopting blue filter for eliminating the phosphorescent light, as well as employing equalization techniques along with blue filtering at the receiver side. Furthermore, the work in [29] reports that the VLC system achieves a data rate of 230 Mbps by employing an avalanche PD at the receiver end and NRZ OOK modulation.

White light can also be generated by employing the red, green and blue (RGB) frequencies, therefore, RGB LED is advantageous over white phosphorescent LED because it avoids the slow-responding yellow phosphor component. However, this is at the expense of involving three different driver circuits for the different RGB components. Consequently, it can be evidenced from [30], where the authors overcomes this drawback by using only red light for data modulation while the green and blue components were provided with constant current in order to be used for illumination purpose. This kind of VLC system which exploits RGB LED delivers a data rate of 470 Mbps by employing simple NRZ-OOK modulation. Extensive research has been carried out to extend the bandwidth of VLC system that utilizes white phosphorescent LEDs. The authors in [31] presented a post-equalization circuit which consists of two passive equalizers and one active equalizer.

The experimental results evidences that a bandwidth of 151 MHz has been achieved by employing blue-filtering and post-equalization circuit. Moreover, this system allows for a data transmission up to 340 Mbps. The work in [32] demonstrates a real-time VLC system imparting data rate of 550 Mbps. This VLC link is based on NRZ-OOK modulation and utilizes a phosphorescent white LED. This work reports that by employing the pre-emphasis and post-equalization circuits, the 3 dB bandwidth is improved from 3 to 233 MHz. In [33], the authors used duobinary technique to achieve a transmission speed of 614 Mbps for a VLC link which uses OOK modulation and a single commercially available visible LED by adopting pre-emphasis and post-equalizing circuits. Experimental demonstrations of an OOK based VLC system delivering data rate of 170 Mbps by utilizing an artificial neural network (ANN) based equalizer was depicted in [34]. In this work, the authors have evaluated the performance of linear, DFE and ANN equalizers in real time environment by exploiting Texas Instrument (TI)-TMS320C6713 digital signal processing board. Additionally, the performance of these aforesaid equalizers are also verified in MATLAB environment.

Besides imparting high data rate communication, illumination is also the foremost task which can be controlled by properly varying the light intensities between the ‘ON’ and ‘OFF’ states. For the purpose of enabling efficient illumination control, the IEEE 802.15.7 standard provides compensation symbols. In general, the dimming levels of the LED are adjusted based on the requirement of the application, consequently this lowers the data rates when using OOK. Therefore, this paved the platform for the emergence of alternative pulsed modulation schemes like PWM and PPM. The interesting aspect with PWM is that it fulfills both modulation and dimming support simultaneously. This is accomplished by conveying the modulated signal with the help of pulses and varying the width of the pulse in accordant with the desired level of dimming pertaining to the need of the application. The authors in [35] proposed dimming techniques by employing PWM or by varying the depth of modulation in the physical layer for rendering simultaneous brightness control and wireless transfer of information. However, the major constraint was, data rates of 4.8 kbps was only achieved. Therefore, in order to overcome this, the authors in [36] for the first time exploited the combination of PWM and discrete multitone modulation (DMT) to attain both dimming and high data rate communication.

The other pulse modulation technique which can be employed in VLC is PPM. The concept behind PPM, is that the symbol duration is divided into t slots of equal duration, and a pulse is transmitted in one of the t slots. The position of the pulse identifies the transmitted symbol. Its ease of implementation enabled it to be adapted by OWC system in the early days [37], [38]. However, due to its lower spectral efficiency and data rate, other variants of pulse position-based modulation have been emerged out. Few such are tabulated in Table. 1.1. In order to ensure adequate dimming control mechanisms, several modulation methods have been exploited. One such scheme which is proposed by the IEEE 802.15.7 VLC standard is variable pulse position modulation (VPPM) [39]. However, this scheme is limited to be employed for high data rate applications. In this regard, the authors in [40], employed M-ary VPPM to facilitate high data rate communication and at the same time dimmable illumination is also assured.

Table 1.1: Different Variants of PPM

S No	**Variant of PPM**
1	*Overlapping PPM (OPPM)* [41]
2	*Multipulse PPM (MPPM)* [42], [38]
3	*Overlapping MPPM (OMPPM)* [43], [44], [45], [46], [47]
4	*Differential PPM (DPPM)* [48]
5	*Differential Overlapping PPM (DOPPM)* [49]
6	*Expurgated PPM (EPPM)* [50]
7	*MEPPM (Multi-level EPPM)* [51]
8	*Variable PPM (VPPM)* [19]

Multiple PPM (MPPM) was proposed in [52] to offer both functionalities simultaneously like modulating the data stream as well as carefully adjusting the brightness levels. This technique exhibits higher potential in terms of spectral efficiency when compared with VPPM. Under such similar purposes, for attaining joint brightness control as well as to accomplish data transmission, variable rate multi PPM (VRPPM) was proposed in [53]. Much recent work in [54] signifies that spectral efficiency along with dimming support is accomplished by employing the combination of MPPM along with RPO-OFDM, a variant of optical OFDM.

1.3.3 Multicarrier modulation formats for VLC

In the recent times, optical OFDM has been considered as a prominent high dimensional multicarrier modulation format for facilitating high data rate transmission and has gained an appreciable propulsion in both academic and industrial sectors. It has been extensively included in broadband communications and many industrial standards due to its inherent advantages which include high spectral-efficiency, simple, single-tap frequency-domain equalization, resilient to frequency-selective fading channel and robustness against narrow-band interference. However, the conventional RF-based OFDM cannot be exploited in a straightforward manner in VLC due to the constraint of real and positive-valued signal transmission. In precise, unlike RF, where the baseband OFDM signal modulates the amplitude and phase information, the scenario pertaining with IM/DD systems is quite different, where the optical OFDM signal modulates the intensity of the carrier signal rather than the amplitude and phase information. This implicitly confirms that the signal transmission has to be assured of its real and positive nature.

It is apparent that inverse fast Fourier transform (IFFT) and fast Fourier transform (FFT) modules play a vital role in enabling OFDM modulation and demodulation. When the input data to the IFFT module is mapped by utilizing complex mapping schemes like M-ary quadrature amplitude modulation (M-QAM), the output of the IFFT module will be definitely a complex valued and bipolar signal. Therefore, in order to comply with the pre-requisites of IM/DD systems, the input to the IFFT module is constrained to satisfy Hermitian Symmetry criteria for the purpose of yielding a real-valued signal. However, this is at the expense of reduced spectral efficiency as all of the subcarriers are not exploited for data transmission. Accordingly, a real-valued signal transmission can be accomplished but the obtained signal cannot be assured of its positivity. Consequently, to address this issue, several other variants of optical OFDM have been proposed in the literature.

To list a few: DC-biased optical orthogonal frequency division multiplexing (DCO-OFDM), asymmetrically clipped optical orthogonal frequency division multiplexing (ACO-OFDM), flip OFDM, pulse amplitude modulated discrete multitone modulation (PAM-DMT), enhanced unipolar optical OFDM (eU-OFDM), layered ACO-OFDM (LACO-OFDM), several other hybrid varieties which includes reverse polarity optical OFDM

(RPO-OFDM), asymmetrically clipped DC biased optical OFDM (ADO-OFDM), hybrid ACO-OFDM (HACO-OFDM), etc. In particular, these diverse variants were proposed by taking into consideration several factors like spectral-efficiency, power-efficiency, etc. However, the major pre-requisite is to accomplish a unipolar signal transmission. Even though, several variants of optical OFDM have been proposed in the literature, most of them are a combination of the earliest variants like DCO-OFDM and ACO-OFDM. Moreover, in the hybrid varieties, the design of receiver circuitry becomes complex when compared with these earliest variants.

DCO-OFDM is a straightforward approach of converting the bipolar signal into unipolar and this methodology consists of addition of a certain amount of DC bias to the bipolar signal in order to yield a positive signal [55]. In specific, the amount of DC bias which is to be added is equal to the absolute value of the maximum negative amplitude of the bipolar signal. In general, the amount of DC bias which is to be added has got a relation with the order of the constellation. As the order of constellation increases, the amount of added DC bias also increases. However, this leads to clipping of the peaks which doesn't fit within the linear range of LEDs. Therefore, this induces clipping distortion. However, the addition of DC bias leads to power inefficiency. But, in the literature, it is revealed that such high powers are essential for the purpose of illumination. Subsequently, in order to overcome the increased power-efficiency of DCO-OFDM, ACO-OFDM methodology was proposed. Without the requirement of DC bias, a real-valued signal is attained by carefully selecting the subcarriers. In this scenario, only odd subcarriers are modulated and the even subcarriers are set to zero. This is done to ensure that the clipping noise falls on even subcarriers.

However, in doing so, there is a decrement in spectral-efficiency when compared with DCO-OFDM system because, if there are N number of subcarriers, only $^{N}/_{2}$ are utilized due to odd subcarrier modulation and out of the remaining $^{N}/_{2}$ subcarriers, only $^{N}/_{4}$ are meant of data transmission. Thus, this incurs a huge decrement in spectral efficiency when compared with DCO-OFDM methodology. However, by applying some modification to the conventional optical OFDM system, a real and positive signal is obtained. In our work we have employed the basic variants like DCO-OFDM and ACO-OFDM methodologies because in rest all other varieties, the design of receiver circuitry is complex because it requires to deploy additional digital signal processing hardware.

1.3.4 Color Shift Keying (CSK)

This type of modulation format has gained significant interest in the field of research in the recent days. As discussed earlier, the fast switching capability of the LED is reduced in the process of generating white light by employing blue LED with yellow phosphor coating. As a result, this drawback imparts a difficulty to render high data rate communication. So, as an alternative methodology, white light can be generated by utilizing three separate LEDs of red, green and blue color. This combined source of RGB LEDs is often referred as $TriLED$ ($TLED$). CSK modulates the signal using the intensity of the three colors in the TLED source.

1.3.5 Carrierless Amplitude and Phase Modulation (CAP)

To tackle the limited modulation bandwidth of white illuminating LEDs in VLC, CAP have been proposed as one the spectrally efficient modulation schemes to assure high data rate transfer of information. Original studies in the literature reveal that, CAP was employed for enabling signal transmission over the telephone cables for asymmetric digital subscriber line connections (ADSL) [56]. In particular, CAP employs a set of finite impulse response digital filters (FIR) to transmit different streams of data. In precise, similar to QAM, the data is transmitted by exploiting two orthogonal FIR digital filters to represent the in-phase and quadrature components. However, CAP doesn't employ a local oscillator, but relies on pulse shaping filters like square-root raised cosine function (SRRF) for obtaining the two signals. Furthermore, the time-domain orthogonality is assured by designing the transmit filters as a Hilbert transform pair i.e., their impulse responses are maintained orthogonal in time (i.e., 90^0 phase shift). At the receiving end, the in-phase and quadrature components are separated by utilizing two FIR matched filters and for the purpose of combating the effects of ISI, channel equalization is performed.

Being a single carrier modulation format, CAP assures for low PAPR which emerges as the most important advantage in comparison the other multicarrier modulation formats, where PAPR stems out as the major issue [57]. As discussed in the former subsections, several modifications have been applied to the input and output OFDM frame structure to guarantee for the real and positive signal transmission. The CAP signal is real-valued and therefore, avoids the need of complex signal processing for attaining a real-valued signal. A list of publications depicts that CAP was proposed as an alternative to OFDM over polymer optical fibre systems, few such are [58], [59], [60], [61]. Much relevant work pertaining to CAP-based VLC system can be found in [62], [63], [64], [65]. The work in [62] manifests through experimental validations, data rates of 1.1 Gbps in a VLC based CAP system which is utilizing a commercially available phosphorescent white LED. To attain better frequency response, optical blue filtering and DFE were incorporated.

In [63], experimental demonstrations were carried out to significantly illustrate that CAP attains a better performance when compared with optical OFDM in a high capacity wavelength division multiplexing (WDM)-VLC system based on a commercially accessible RGB-type white LED reporting the maximum aggregate data rates of 1.32 (CAP) and 1.08 Gbps (optical OFDM) respectively. The authors in [64] experimentally evaluated the performance of PAM, CAP and DMT modulation techniques over a white LED transmission link. The work in [65] signifies that, the performance of a CAP based VLC system employing frequency domain equalization (FDE) exhibits a better performance in terms of reduced PAPR when compared with optical OFDM. The aforementioned works in the literature focuses on designing suitable equalization techniques to improve the achievable data rate of CAP resulting in the significant increase in the overall complexity of the system design. However, the research work as portrayed in [66] proposes spatial modulation-based CAP (S-CAP) for the purpose of improving the spectral efficiency of CAP while still assuring for low complexity.

Despite offering several remarkable characteristic features, CAP-based VLC is not devoid of its challenges. The usage of orthogonal filters for pulse-shaping and matched filtering operations in the design of CAP-based VLC transceiver consequently increases its sensitivity to timing jitter [67]. However, CAP-based VLC system is out of scope of this thesis. Exploitation of CAP for VLC and handling its challenges will be towards the future scope of our work.

1.4 Channel Estimation in optical OFDM

Besides, having seen the different modulation formats which are associated with VLC, it is also imperative to have a clear understanding about the channel modeling in optical domain. Substantially, for the purpose of designing a communication system, it is of major prerequisite to characterize the channel environment. Subsequently, this section exemplifies the literature survey emphasizing the significance of channel estimation in VLC. The exceptional characteristics of VLC is that it not only assures 'illumination' which is aesthetically pleasing to the human eye but also guarantees 'communication' and indoor positioning [68], [69]. Additionally, the accuracy of the positioning systems depends on how accurately the channel state information from multiple transmitters are estimated. In particular, the channel state information is also vital to ameliorate the data transmission rates [70], [71]. Consequently, it is essential to design robust channel estimation schemes for precisely estimating the channel state information. Additionally, even for the purpose of ensuring perfect reception of the transmitted data, sensing and tracking of the channel is essential.

Upon comparison with traditional RF based wireless communication systems, VLC systems possess distinct unique properties which imposes a challenge to enable the design of robust channel estimation schemes. Firstly, since IM/DD systems are quite commonly used for VLC, the transmitted signal must be both non-negative and real-valued signal. Secondly, the channel estimation gains are also non-negative and the design of VLC channel modeling is quite different than that of RF-based wireless channel estimation. Notably, for the purpose of estimating the channel, pilot tones can be inserted into the OFDM symbols. Accordingly, there are two types of pilot arrangements namely: block type and comb type. Pertaining to block type pilot arrangement, the pilot tones are inserted into all of the subcarriers of the OFDM symbols based on a specific period. While, the latter type consists of inserting pilot tones into each of the OFDM symbol [72]. The same type of pilot arrangement schemes can also be applied for VLC systems by taking into consideration the necessary pre-requisites for signal transmission.

Wireless channel estimation can be performed by exploiting channel estimation algorithms like least square (LS), minimum mean square error (MMSE). Once, the channel state information at the pilots is obtained, then the channel response at the data can be interpolated by utilizing interpolation based channel estimation algorithms like linear, spline, and low-pass. Since, the indoor optical wireless channel differs from the conventional RF-based wireless channel, there has been limited considerations on the channel estimation for VLC domain. Much significant literature in relevant to VLC channel modeling can be found in: the authors in [73], evaluated the performance of block-type and comb-type pilot arrangement based channel estimation in DCO-OFDM system. The performance of the system is analysed in terms of bit error rate (BER) and signal to noise ratio (SNR). In this work, the result analysis emphasizes that high amount of SNRs are required to attain a reduced probability of error.

The work in [74] depicts that comb-type pilot arrangement based channel estimation has been proposed in ACO-OFDM system and the performance of different interpolation based techniques are analyzed. However, the result analysis infers that, a reduced error floor is attained at higher SNRs which is not desirable if ACO-OFDM is employed. An adaptive statistical Bayesian minimum mean square error channel estimation (AS-BMMSE-CE) for DCO-OFDM system has been proposed in [75], [76]. This sort of channel estimation technique exploits the historical information in an adaptive and efficient way and gives superior performance in terms of both mean square error (MSE) and BER but at the cost of modest complexity under practical scenarios. A LS-based channel estimation algorithm for optical OFDM-based multi-user multiple input single output VLC system has been proposed in [77]. In this work, the pilot tones are optimized in order to derive the MMSE of the channel estimation and the channel is estimated independently by each user where these channel estimates are sent back to the transmitters and accordingly, zero-forcing precoding is applied at the transmitter end to achieve the spatial multiplexing gain.

Taking into considerations the robust nature of high intensity of LEDs which allowed for the replacement of incandescent-based lights, unfolds the realization of a VLC based system in an outdoor environment. Few such examples where VLC can be implemented is traffic lighting system and public illumination system [78]. The channel conditions of outdoor scenarios is different than that of indoor channel modeling. For outdoor environment, several factors like effects of ambient light sources like sunlight, artificial light sources, inhomogeneities in the temperature and pressure need to be taken into account. The work in [79] portrays that in order to improve the error performance as well as to reduce the detection complexity a fast blind detection algorithm which is based on generalized likelihood ratio test (GLRT) principle was developed for an optical communication system which employs OOK modulation over atmospheric turbulence induced slow fading channel.

The authors in [80] present efficient frequency-domain channel estimation methods which are based on intra-symbol frequency-domain averaging (ISFA), MMSE and weighted inter-frame averaging (WIFA) schemes for OFDM-VLC system. This work experimentally investigates the performance of 16 and 64-QAM-based OFDM-VLC system. Additionally, the result analysis infers that upon comparison with conventional LS-based channel estimation algorithm, ISFA, MMSE and WIFA offers best performance in terms of error vector magnitude but this is at the cost of high complexity.

1.5 PAPR Analysis in multicarrier and multiple access schemes for VLC

Despite being superior in terms of high data rate transmission as well as possessing several attractions, the certainty of the individual subcarrier signals to add up coherently result in high peaks in the time-domain signal of optical OFDM, which in turn leads to high peak to average power ratio (PAPR) and stems out to be the most vital aspect which needs to be addressed especially for VLC. The emergence of high peaks indicate that the optical source will have to operate outside its linear region for the sake of accommodation of the entire amplitude swings of the corresponding time-domain signal. If this scenario prevails, this is very unappealing as the levels of distortion present in the time-domain transmitted signal increases significantly and ultimately, the overall performance of the system deteriorates.

1.5.1 Non-linearity in Optical Sources:

Principally, an optical communication system is build with an optical source, in the scenario of IM/DD systems, the key optical source is LED. In particular, this optical source is used for generating an optical power which is a function of modulated input electrical signal where the information is converted into optical beam. Generally, the optical sources which are used in OWC systems have a peak-power limit which enforces that the optical time-domain signals should have limited peak amplitudes. Therefore, this peak power constraint results in distortion on the optical OFDM signal. LED is the foremost source of non-linearity in VLC. As delineated in Fig. 1.3, LED has a turn on voltage (TOV) as minimum threshold value which is the onset of current flow and emission of light. For voltages below TOV, the LED is considered to be in cut-off region i.e., it doesn't conduct any current. However, above TOV, the LED conducts and the amount of current flows and the light output increases exponentially with voltage. It is to be noted that LED outputs light power that is linear with the drive current [81]. Thermal aspects which causes a drop in the electrical-to-optical (E/O) conversion efficiency in precise, light output of the LED decreases and then approaches a steady-state value hence, it is vital to consider such aspects. Therefore, in order to prevent the degradation in output light or in the worst case, the total failure of the LED chip, it necessitates to adjust the dc and ac/pulsed currents accordingly.

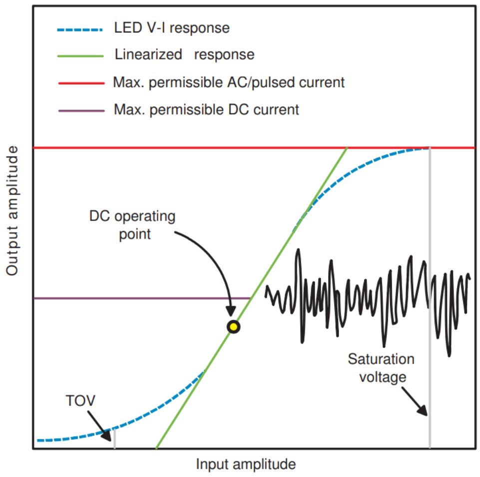

Figure 1.3: Depiction of Non-linear and Linearized transfer function of LED

The transfer function of the LED distorts the signal amplitude which forces the signal peaks which are below the TOV of the LED to be clipped as well as the upper peaks are clipped purposefully before modulating the LED for the sake of avoiding chip overheating. Hence, the transmitted time-domain signal of optical OFDM should be constrained to a limited range due to the non-linear characteristics of LEDs. As a result, the high PAPR of optical OFDM signals gives rise to a large dynamic power excursion which harms the energy-efficiency at both the transmitting and receiving ends. Thus, the optical OFDM signal with high PAPR is subsequently clipped by the LED transmitter originating the serious clipping distortion.

To circumvent this major drawback, there are certain solutions proposed in the literature: In general, because of the structure of the LEDs, the output optical power and the forward current are related by a non-linear function. Therefore, the non-linearities of LEDs can be overcome by linearizing the non-linear region of LED and the second approach is to adopt PAPR reduction techniques. One such technique is predistortion which is proposed in [82] to linearize the relationship between the output optical power and the forward current. However, this technique requires an accurate model for the design of predistortion and linearization over the dynamic range of optical source. It can be reported in [83], a polynomial model is employed for the purpose of describing the non-linear transfer function of the optical sources from which a predistortion function can be designed to linearize the non-linear region. The problem encountered while employing the predistortion technique is that the non-linear transfer function of the optical sources can change due to many reasons one of which is the temperature of the transmitter. It is apparent that the optical sources dissipates a portion of the input energy as heat and this leads to the increase of the temperature of the device which consecutively changes the non-linear relation between the output power and forward current. Hence, the predistortion function is not sufficient enough to maintain the linearity of the device and subsequently, this scenario compels the necessity of dynamic feedback for modifying the instantaneous non-linear transfer function of the optical sources [84].

1.5.2 PAPR reduction techniques for IM/DD systems

This section highlights the research efforts done by several researchers to reduce the detrimental aspect like PAPR in optical OFDM. Among the variants of optical OFDM, DCO-OFDM system suffers from high PAPR due to the superimposition of huge number of subcarriers as well as for assuring a positive-valued signal, a certain amount of DC bias is added. Therefore, there is a necessity to reduce the amount of PAPR in such system. Hence, it is vital to rely on few such PAPR reduction techniques which include clipping with filtering [85], selected mapping (SLM) [86], [87], [88] partial transmit sequence

(PTS) [89], discrete Fourier transform (DFT)-Spread [90] and signal companding [91], [92]. However, the traditional PAPR reduction schemes cannot be directly implemented in case of optical domain because of the real and positive signal transmission.

The aforementioned methods result in certain correlation between the subcarrier symbols of the OFDM blocks and such methods can be classified into deterministic and probabilistic approaches. Firstly, clipping with filtering falls into the category of deterministic approach i.e., signal distortion technique and in general it is referred to as a non-linear process which causes serious in-band and out-of band distortion because it limits the overshooting signal amplitude to a predefined level. The second category of PAPR reduction techniques like SLM, PTS, signal companding and DFT-Spread comes under multiple signalling and probabilistic approaches which tend to reduce the probability of high PAPR. SLM and PTS are most widely employed PAPR reduction techniques, but the major drawback associated with them is that they require the side information which significantly reduce the bandwidth-efficiency of the system. Companding is a non-linear transformation technique which tends to destroy the orthogonality among the OFDM subcarriers. While, DFT-Spread technique is a type of precoding method which exploits the DFT operation before the IFFT transformation module to negate the levels of high PAPR.

While dealing with the optical domain, several techniques have been proposed to reduce the peaks of the time-domain optical OFDM signal. Among of which are the following:

In [93], the authors addresses the performance-limiting factor like high PAPR in DCO-OFDM system by applying semi-definite relaxation approach to tone-injection scheme. From the simulated results it can be evidenced that there is a significant reduction in PAPR by approximately 5 dB when compared to traditional DCO-OFDM system. The work in [94] employs branch-and-bound method (BBM)-based tone injection scheme for the purpose of reducing the amount of PAPR in DCO-OFDM system. Tone injection is an effective way for reducing the amount of PAPR when compared to PTS and SLM techniques because it doesn’t transmit any side-information. The simulated results emphasizes that the proposed BBM-based tone injection method is superior than the existing methods in terms of PAPR reduction. However, the aforementioned techniques as used in [93] and [94] results in the increase of power in order to achieve a distinct improvement in BER performance in the presence of LED non-linearities. Additionally, the amount of computational complexity incurred is also high.

In [95], in order to resolve the problem of high PAPR, the authors proposed to apply a modified active constellation extension (ACE) method or tone reservation as a power derating reduction technique in DCO-OFDM VLC systems. In this work, the authors takes into account cubic metric (CM) because, CM focuses on the cubic non-linearities which generally emanates due to several types of distortions including both in-band and out-of-band distortion. The research in [96] signifies that for the purpose of reducing the PAPR effectively with faster convergence and lower complexity, a tone reservation scheme which is based on the combination of signal-to-clipping noise ratio (SCR) procedure and the least squares approximation (LSA) approach. In [97], a tone reservation technique which is based on the time-domain kernel matrix (TKM-TR) scheme is utilized for reducing the PAPR in DCO-OFDM system. The computational complexity of these aforesaid methods is extremely high since they need to search over all possible combinations of the expanded constellation i.e., peak cancelling signals.

An iterative clipping method as proposed in [98] reduces the upper and lower PAPR of the oversampled VLC-OFDM signals without introducing in-band distortions. The work in [99] proposes an exponential non-linear companding method to reduce the PAPR in VLC-OFDM systems and this method exploits the advantages of exponential companding function to compress large signals and to expand small signals at the same time. One major drawback associated with iterative-clipping and exponential companding is that the property of the transmitted signal is destroyed. Pilot-aided PAPR reduction schemes were proposed in [100], [101] and [102] where the reduction in PAPR depends upon the density of pilot sequences. But, these methods leads to data rate loss and there is a degradation in bandwidth efficiency due to the introduction of pilot sequences.

One of the popular technique for reducing the PAPR in RF-based OFDM system is SLM. For exploiting the SLM concept in DCO-OFDM VLC systems, several studies have been conducted and few such can be reported in [103], [104], [105]. The work in [103] combines chaos with SLM technique so that the generation of phase factors can be controlled with the help of chaotic sequences. The result analysis emphasizes that chaotic SLM (CSLM) technique attains better BER performance than traditional SLM technique in OFDM IM/DD system. Specifically, the performance of SLM technique was investigated in [104] which employs five different families of phase sequences namely, chaotic, Shapiro-Rudin, pseudo-random interferometry code (PRIC), Walsh-Hadamard and random sequences. These different phase sequences result in different levels of PAPR reduction. It is to be noted that by exploiting SLM technique, it is obligatory to utilize the side information for indicating the transmitted candidate signal and this subsequently reduces the bandwidth efficiency. The work in [105], employs a special set of symmetric vectors as phase sequences in SLM technique for the purpose of reducing PAPR in DCO-OFDM based VLC system. In this approach, the magnitude difference between the received signal and the pre-defined phase sequences in the frequency domain was used to detect the side information blindly. Nevertheless, these aforesaid methods have extremely high computational complexity as they need multiple IFFT operations for candidate generation.

The deleterious aspect like PAPR is addressed even in the recent times, where the research in [106] proposes a novel PAPR reduction scheme using optimized even and odd sequence combination (OEOSC) technique for DCO-OFDM VLC systems to avoid side information transmission and high computational complexity while preserving the PAPR reduction capability.

1.5.3 PAPR analysis in multiple access schemes for VLC

It is apparent that, OFDM by itself cannot be utilized as a multiple access scheme, in order for it to be employed as a multiple access scheme it needs to be interfaced with several other existing multiple access schemes like frequency division multiple access (FDMA), time division multiple access (TDMA), and code division multiple access (CDMA). The well known combination of OFDM and FDMA is orthogonal frequency division multiple access (OFDMA), which is most widely used multiple access scheme in cellular mobile communication. The same can be incorporated in optical domain complying with real and positive signal transmission and this type of multiple access scheme employed in IM/DD systems is called as optical OFDMA (OOFDMA). However, since the envelope in OFDMA undergoes random fluctuations giving rise to high peaks, it necessitated to rely on single carrier frequency division multiple access (SC-FDMA). The amount of PAPR reduction depends upon the way the number of subcarriers are allocated to the users/subscribers. Accordingly, there are three different ways namely, distributed frequency division multiple access (DFDMA), localized frequency division multiple access (LFDMA), interleaved frequency division multiple access (IFDMA).

In general, DFT spreading is employed to effectively reduce the amount of PAPR of a multicarrier system to the level of a single carrier system. Therefore, M point DFT is employed for spreading and N point IDFT is employed for fetching a time-domain signal. In case of DFDMA, the M DFT outputs are distributed over the entire band of N subcarriers with zeros filled in the unused $(N-M)$ subcarriers. While, if DFDMA distributes the M DFT outputs with equidistant as $\frac{N}{M}=Q$, where Q is the spreading factor, then it is referred to as IFDMA. Whereas, LFDMA distributes the DFT outputs to M consecutive subcarriers out of the N subcarriers. Relevant works pertaining to the exploitation of the aforesaid multiple access schemes to IM/DD systems can be reported in [107], [108], [109]. The research in [107] compares the PAPR performance of optical OFDM interleave division multiple access (O-OFDM-IDMA) with OOFDMA. The simulation results in this work suggest that the O-OFDM-IDMA is more power-efficient than O-OFDMA, especially for higher throughput at the cost of higher computational complexity. However, the CCDF curves for O-OFDM-IDMA and OOFDMA do not show much difference. The superiority of SC-FDMA over OOFDMA in WLED based communication system is outlined in [108]. The work in [109], proposes an improved frequency-domain decision feedback equalizer (FD-DFE) for SC-FDMA-based VLC system. This proposed structure remarkably reduces the decision error of FD-DFE and at the same time improves the BER performance as well as the transmission performance.

1.6 Synchronization in optical OFDM for IM/DD based VLC systems

For cost-effective realization of VLC systems which are based on white LEDs, IM/DD is the most preferable modulation format. However, without employing optical filtering and equalization, the modulation bandwidth of IM/DD based VLC systems is usually limited to several MHz. Particularly, it is mandated to have precise synchronization when VLC systems exploit highly spectral-efficient multicarrier modulation scheme like OFDM. In spite of its significance, the vulnerability of OFDM to the synchronization errors, represented by the so-called frequency and timing offsets results as the most vital principal disadvantages of OFDM.

Frequency offset (FO) leads to a reduction of desired signal amplitude level in the output decision variables besides, the small frequency mismatches between the transmitter and the receiver leads to the loss of orthogonality among the subcarrier components hence, inter carrier interference (ICI) emanates. Timing induced offsets results in the rotation of OFDM subcarrier constellation thereby hindering the recovery of the transmitted signal when high constellation order QAM is implemented. Predominantly, the synchronization process involved in OFDM can be divided into a coarse frequency and timing acquisition and a fine frequency and timing offsets estimation [110]. Generally, coarse frequency and timing synchronization at the receiving end can be achieved by correlating the received and the original synchronization preamble in the frequency and time domain respectively. Even though, theses offsets might be small, but due to the extremely high synchronization requirement of the system it is of paramount important to estimate and to compensate them. This could be done either by demodulating the OFDM synchronization preamble which is an OFDM symbol which is used for training purpose, or by inserting the pilot carriers within the OFDM symbols.

Several number of studies have been reported regarding OFDM synchronization [111–116]. Earlier studies reports that synchronization errors are due to three different effects i.e., carrier error, clock error and sampling timing error. The difference between the local oscillator in the receiver and the carrier frequency of the transmitting signal leads to carrier error. While, the difference in the sampling clock in the receiver and the transmitter is usually defined as clock error. Besides, the difference between the optimum sampling time in the receiver and the actual sampling time is called sampling timing error. In the literature, it is reported that carrier error and clock error together can be stated as FO, while sampling timing error is recognized as timing offset. Consequently, due to the high sensitivity of OFDM systems to different synchronization errors it is worthwhile to investigate the deleterious effects of these offsets when OFDM is adopted for IM/DD systems in VLC.

The synchronization problems encountered in optical OFDM are mainly focused on timing synchronization i.e., frame detection and frequency synchronization. It is well known that the advantages of OFDM can be utilized as long as the orthogonality among the subcarriers is maintained. The moment, the orthogonality is disrupted by any means then ICI and inter symbol interference (ISI) emanates. In general, the frequency offset in case of optical OFDM arises due to the occurrence of Doppler shift in a mobile environment. Moreover, the STO hinders the detection capability at the receiver side because due to improper frame misalignments, the current OFDM symbol overlaps with the previous and the next symbols thereby, eventually this leads to the emanation of ICI and ISI. Therefore, it is vital to estimate these offsets and then it is required to compensate them. Subsequently, this enforces to rely on several synchronization algorithms like Classen, Moose, Training symbol assisted, Minimum difference and Maximum Correlation methods. This augmenting technology like VLC provides the flexibility of creation of a small scale cellular communication network within an indoor room environment by making use of the already utilized LED lighting fixtures. In this scenario, each installed LED lighting fixture will act as an OAP rendering services to several roaming mobile stations which are within the vicinity of LEDs. Therefore, in this scenario it is vital to explore synchronization aspects when multiple access schemes are exploited for IM/DD systems.

1.7 Applications of VLC

This section interprets the applications of VLC for imparting vehicular communication as well as portrays the prominence of VLC in making a city to be evolved as a smart city.

1.7.1 Vehicle to Vehicle (V2V) and Vehicle to Infrastructure (V2I) communication using VLC technology

Enhancing the road safety in an effort of minimizing the victims who are prone to road accidents stems out to be the most indispensable aspect in the present days. Consequently, enabling the vehicles to experience a real time wireless exchange of data pertaining to heavy traffic areas and distance between vehicles will definitely help people to avoid road accidents. In [117], it is clearly stated that the vehicles are already embed-

Figure 1.4: Illustration of Vehicle to Vehicle (V2V) Communication

ded with sophisticated on-board driving equipment like control and information sources which enables the vehicle drivers to remain well-informed about the status of vehicles.

Moreover, the rapid availability of cameras, anti-lock braking systems, navigation units and sensors fitted to vehicles will definitely enable to capture relevant information which will notify the driver to take precautions to avoid road-accidents. Therefore, this sparked the attraction of various governmental bodies and scientific communities to join hands with the intelligent transportation system (ITS) for the provision of facilitating seamless wireless experience among moving vehicles i.e., imparting vehicle to vehicle (V2V) communication and vehicle to infrastructure (V2I) communication. Generally, imparting communication between the vehicles and the traffic infrastructural units forms a network which is known as Vehicle Ad-hoc Network (VANET) [118]. This sort of network provides a significant enhancement in road safety as it provides the flexibility in dispensing reliable transmission of data with minimal latency.

Pertaining to RF domain, dedicated short range communications (DSRC) can be contemplated as the propitious technology utilizing the 5.9 GHz radio spectrum for expediting V2V and V2I communication. However, this entails a complex design structure which is incurred in the deployment of the RF-based equipment. Eventually, with the omnipresence of white LEDs, and the prominence of enabling simultaneous ‘illumination’ and ‘communication’ which is aesthetically pleasing to the human eye has enabled VLC to be amalgamated with the ITS to help vehicles to exchange real-time information pertaining to different scenarios on traffic updates as well as to prevent congestion. In addition, the unique distinguished characteristics of the LEDs such as their high reliability, energy efficiency, long life expectancy (large amount of lighting hours) has created an enthusiasm for the car manufacturers to replace the classical halogen lamps by LED lighting systems [119]. Moreover, the high amount of efficiency offered by the LEDs sparked the attraction of the authorities to incorporate them in traffic lights as well. Several studies in the literature reveal that the traffic light system which is based on LEDs is substantially growing prevalent due to low maintenance and installation costs and at the same time good visibility is assured. With the emerging trends in the lighting industry, it is predicted that in the coming days, the entire street lighting will be replaced by the LED based lighting systems. As, per the authors in [120] and [121], communication can even be rendered with the assistance of road illumination. Under such scenarios, a high data rate transfer with good stability can be imparted by maintaining a constant short distance between street lighting units and vehicles.

Figure 1.5: Interface of LEDs lighting System as a part in Vehicles

Recently, particularly in the area of vehicular communication, much of the attention has been drawn by the research group to help people to prevent road accidents. Moreover, the vehicle safety communications consortium (VSCC) concludes that substantial increment in both efficiency and safety can be achieved in the transportation system if real time access and exchange of data between the traffic infrastructure especially between two vehicles is made possible [122]. Taking into consideration, the above said circumstances the area pertaining to V2V and I2V/V2I VLC will flourish at a rapid pace. In [123], it is predicted that upon combing V2V and I2V/V2I communications, 81 % of the vehicle crashes could be prevented. Fig. 1.5, 1.6 clearly illustrates several examples of the usage of LED as part of the transportation infrastructure. These above said examples clearly depict that in the near future the entire transportation system will be based on LED lighting because at present some of the vehicles and the infrastructure are already integrated with LEDs. Already being revolutionized by the solid-state lighting and moreover becoming a part of the transportation infrastructure such as vehicle lighting systems will definitely enable VLC to evolve as a global technology. A glimpse of the published

Figure 1.6: Integration of LED with the Transportation Infrastructure

works reveal the utilization of VLC technology to impart V2V/V2I communication. The authors in [124], employed image sensor based VLC for finding the distance between two vehicles. An automotive VLC system utilizing optical communication image sensor (OCI) was proposed in [125]. Here, DCO-OFDM was utilized for achieving an effective signal transmission. The experimental demonstrations of this work shows to achieve a data rate of 55 Mbps.

The prominence of VLC to impart V2V communication under adverse weather conditions like fog was experimentally demonstrated in [126]. Under heavy fog conditions, high Fresnel lens and multiple PDs were employed to focus the incoming light adequately. The work in [127] illustrates inter-vehicle communication by exploiting controller area network (CAN) which is already available in a car to generate control signals regarding the speed of the car, engine, etc. This work exploits the optical filters to address the PD saturation problem which arises due to the effects of sunlight. Much recent work which exploits VLC for enabling infrastructure-to-vehicle-to-vehicle (I2V2V) can be found in [128] where the designed system is fully complaint with the IEEE 802.15.7 standard.

1.7.2 VLC for Smart Cities

The main motive of a smart city is to acquire integration of both information and communication technology (ICT) and IoT for the purpose of managing city's assets and to ensure a better Quality of Service (QoS) for the well being of the people. The assets include almost several units namely educational institutions such as schools and colleges, libraries, local departments, information systems, transportation systems, hospitals, power plants, water supply networks, waste management, law enforcement and other community services. The tremendous development of communication and information technology originated a city to become smart. The objective of the smart city is to ensure seamless connectivity among the people, environment, government and every unit present in the city in order to intensify the quality of life and well being of the population. The features and overview of the smart city are illustrated in Fig. 1.7a and Fig. 1.7b.

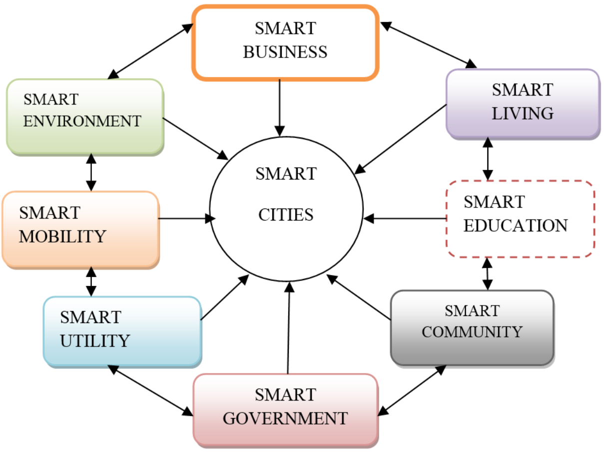

(a) FEATURES OF SMART CITY

(b) OVERVIEW OF SMART CITY

Figure 1.7: Features and Overview of Smart City

Regardless, many applications employing the RF technology for the purpose of facilitating data access to enable seamless communication throughout the smart city, it is revealed in many studies that it shall become as one of the inadequate resource in the near future. In this context, RF shall be no longer able to assure the QoS and the desired high data rate communication for the emerging smart city applications. Hence, as an intriguing alternative VLC technology has emerged out. This has gained tremendous attraction particularly of its nature to handle higher communication data rate demands and to enable a huge communication exploration for smart city applications i.e., providing simultaneous communication and illumination which is aesthetically pleasing to the human eye.

As already discussed, the prominent nature of VLC is not to interfere with the existing technologies and as a result it can be seamlessly amalgamated with almost every unit present in the city which includes the infrastructural units such as the public lighting system, transportation system, RSU, etc. The light-based communication architecture's design and its capability to allow intelligent transportation applications in smart cities was presented in [129]. Accordingly, the general architecture is shown in the Fig. 1.8 highlighting the various communication layers. Therefore, these communication layers can be broadly classified as:

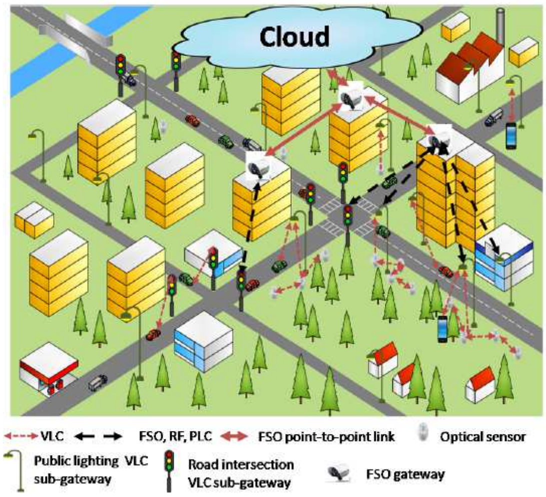

Figure 1.8: Communication architecture based on lighting system for smart cities [129]

- *LED-to-LED*
- *LED-to-VLC sub-gateway*
- *VLC sub-gateways-to-Free Space Optical Wireless Communication (FSO) gateway*
- *Inter FSO-gateways*

The methodology of imparting communication with the help of these layers is summarized below:

- LED can be modulated to be used both as a light source as well as a sensor. This sort of LED-to-LED communication lays the foundation for the emergence of wireless optical sensor networks to facilitate the collection of the real time information pertaining to road conditions such as congestion in a particular area and high accident prone areas. It even gathers information relating to the emergency issues such as availability of ambulance, fire-aids, etc.
- Later on, all the aforesaid sensed and tracked data is disseminated to a $VLC\ sub-gateway$.
- The crucial role of the $sub-gateway$ is to gather relevant data from various optical sensors and to draw remarkable conclusions regarding real-time situations such as transportation, emergency, etc.
- Furthermore, Fig. 1.8, clearly depicts that there are two kind of sub-gateways: The first is the *public lighting VLC sub-gateway* that is located in the lighting poles that are installed along the road. The second is the *road intersection VLC sub-gateway* which is meant to ensure full coverage of the road intersection.
- A $VLC\ sub-gateway$ allows for seamless communication between the smart city and other network service providers.
- By employing FSO point to point links, data can be communicated across several $VLC\ sub-gateways$ that span throughout the city.

By having an overview of the above lighting based architecture in smart cities, it is evident that smart cities can support many applications using the VLC technology namely the transportation, the public safety, government applications, etc. Listed below are a few applications which are used to design smart transportation systems:

- *Green Traffic Management*
- *Parking management*
- *Accident management*
- *Emergency case management*

- *Vehicle tracking*

Using the above approaches as stated, research is striving forward to enable communication everywhere and anywhere. One such approach has been carried out in [121], where several issues were briefed regarding the development of a smart city utilizing intelligent as well as energy effective public illumination system concurrently imparting high speed communication. The most significant nature to be noted is that this lighting system relies on LEDs and is thus able to adapt the light intensity upon sensing the neighbouring environmental conditions. A case scenario pertaining to road illumination is also discussed and from the simulation studies, it is revealed that data communication at high rate can be imparted using the lighting infrastructures.

A practical approach of integrating VLC and Power Line Communication (PLC) technology along with various applications of VLC were discussed in [130]. The integration of VLC technology with PLC emerges as an attractive solution for the new smart city applications and this approach makes VLC to become more practical, efficient and cost effective. The smart grid which is based on PLC can provide the broadband data access and power for the VLC node (bulb) to ensure both wireless data connectivity and illumination [131]. Utilizing the advantage of infinite bandwidth of VLC, one key concern is to develop a merging solution which provides both power and data from the same power line to the VLC node. It is also worthy in mentioning that the aforementioned solution has been recommended by the industry and there is an increasing interest in finding such fascinating solutions to promote VLC adequately.

In [132], the authors employed the usage of visible light communicating devices to serve as data access points in the smart city environment. Here, the primary aim of the authors is to facilitate smart tourism services. Hence, they have considered street lights as auxiliary points to provide basic information to everyone regarding the city. The information pertaining to the place, direction, nearby tourist places are of paramount important to the tourists visiting a new area. Smart city desires almost everything originating right from the infrastructure to the services to be smart, accurate and intelligent.

The design of smart city has become the focus of enormous interest in the present days which opened the gateway to explore many technical concepts pertaining to VLC. This section addresses the importance of integrating the public lighting systems with the infrastructures present in the smart city to enable data communication and as well as addresses how well this technology can be used for traffic management. Aiding to this, the system could offer wide-range communication by making use of this novel technology called VLC.

1.8 KEY CONTRIBUTIONS of this Thesis:

The summary of key contributions of this thesis is given as follows:

- **Contribution 1: Channel estimation in optical OFDM exploiting different transform techniques for VLC:**

  1. It is apparent that in conventional OFDM system, the modulation and demodulation exploit the advantages of IFFT and FFT transforms. However, in case of optical domain pertaining to IM/DD systems, the optical OFDM signal modulates the intensity of the signal, rather than the amplitude and phase information. Therefore, this affirms that the signal transmission has to be assured of its real and positive (i.e., unipolar) nature. Consequently, in order to accomplish a real valued signal transmission, the input signal to the IFFT block is constrained to satisfy Hermitian Symmetry criteria. Therefore, according to Hermitian Symmetry criteria, only half of the subcarriers are exploited for data transmission as the rest half are flipped complex conjugate versions of the previous ones. Consequently, this reduces the spectral efficiency as all of the subcarriers are not utilized. Moreover, this incurs additional digital signal processing circuitry for the computation of Hermitian Symmetry criteria. Additionally, the amount of power consumption increases as the size of IFFT increases. Hence, in order to overcome such drawbacks, it entails to exploit real transformation techniques like discrete Hartley transform (DHT), discrete cosine transform (DCT), discrete sine transform (DST), Hadamard coded modulation which is based on fast Walsh Hadamard transform (HCM-FWHT) and wavelet packet division multiplexing (WPDM).

  2. Mathematical modeling of the time-domain signal is performed for Hermitian

Symmetry imposed FFT-based optical OFDM system and is compared with other real transformation techniques like DCT, DST, DHT, HCM-FWHT and WPDM. The performance of the aforementioned real transform techniques based optical OFDM is analysed over dispersive optical channel environment. Furthermore, a thorough analysis of computational complexity is also the focus of this work.

3. Taking into consideration the multipath propagation scenario in an indoor room environment, in this work, a comb-type pilot arrangement based ACO-OFDM system which is employing different transforms namely Hermitian symmetry imposed IFFT, and real transformation technique like DHT are developed and further compared with other multicarrier modulation formats like HCM-based on FWHT and WPDM. Therefore, for the purpose of estimating the channel state information, channel estimation algorithms like LS and MMSE are employed. Based upon the channel state information at the pilots, the channel information at the data subcarriers is interpolated by using different interpolation channel estimation algorithms like Linear, Low-pass and natural cubic spline interpolation. This work derives the mathematical expressions for the overall system models developed and furthermore, their performances are analyzed through simulations using MATLAB software. From the simulated results, it can be inferred that to achieve the same BER curves as that of FFT-based optical OFDM, the same order real transformation techniques can be used with simple and real mapping schemes of lower constellation sizes.

- **Contribution 2a: PAPR analysis in DCT-based IM/DD systems for VLC.**

  1. Even though, OFDM is considered for high data rate transmission, the high peaks which arise due to super-imposition of huge number of subcarriers is inevitable. This situation is even more worsened in case of optical OFDM which is exploiting LEDs, because the limited dynamic range of LEDs, leads to clipping of the signal peaks of optical OFDM which doesn't fit within the LED linear range. Hence, there is a necessity to reduce PAPR in OFDM especially in the optical domain.

  2. This contribution highlights the different PAPR reduction schemes like spread-

ing, PTS, clipping and filtering in DCT-based OFDM which is also referred to as fast optical OFDM (FOOFDM).

3. For the purpose of reducing the amount of PAPR in FOOFDM system, this work proposes a DCT-based spreading to DCT-based multicarrier system (i.e., FOOFDM) and compares with other PAPR reduction schemes like PTS and clipping and filtering for the same system. Enforcing the PAPR reduction techniques in the optical domain is not straightforward due to real and positive signal transmission. Therefore, mathematical expressions for the time-domain signal formats are derived for the proposed systems.

4. Furthermore, the performance of different multiple access schemes are also analyzed. Mathematical expressions are derived for different subcarrier mapping strategies like DCT-based optical interleaved frequency division multiple access i.e., fast optical IFDMA (F-O-IFDMA), fast optical localized frequency division multiple access (F-O-LFDMA). Additionally, for the purpose of comparison with DCT-based multiple access schemes, this work imposes DFT-based spreading to optical frequency division multiple access (DFT-S-OOFDMA) and derives the mathematical expressions for it. Simulation results are presented for the proposed systems.

- **Contribution 2b: Performance analysis of DST-based IM/DD systems for VLC.**

  1. This work proposes a DST-based optical OFDM system and analyzes the performance of a DST-based ACO-OFDM and DST-DCO-OFDM system over VLC channel environment. Mathematical expressions are derived for the aforementioned system models.

  2. Furthermore, since DCO-OFDM system is power-inefficient, therefore to reduce the amount of PAPR in DCO-OFDM system, a DST-based spreading is proposed in this work. A thorough mathematical analysis is accomplished for the time-domain signal formats and furthermore, other PAPR reduction techniques like PTS, Clipping and filtering are imposed on the same system model and then compared with DST-based spreading.

  3. An uplink scenario is described and for enabling multiple access support, different multiple access strategies like DST-O-LFDMA, DST-O-IFDMA are employed. Mathematical expressions are derived for the time-domain signals and are verified through simulation results.
  4. Spectral efficiency and computational complexity are compared for DFT-based optical OFDM and DST-based optical OFDM.

- **Contribution 3: Synchronization in DCO-OFDM and DCO-OFDMA-based IM/DD systems for VLC.**
  1. Primarily, this contribution accomplishes the mathematical analysis for the time-domain signal formats in a multicarrier system like DCO-OFDM which is effected with FO and STO.
  2. Additionally, this contribution gives interference analysis for the multi-user scenario and gives the mathematical derivations of the received signal pertaining to the desired subscriber when effected with timing and frequency offsets in a multiple access system like DCO-OFDMA system.
  3. Mathematical expressions are derived depicting the degradation of the received signal in the presence of different interferences like ICI, multi user interference (MUI).
  4. Mathematical analysis is performed highlighting the performance of different synchronization algorithms and the simulated results are presented. The performance of the system models in the presence of these offsets are verified through simulations.
  5. Lastly, Cramer Rao Lower Bound (CRLB) is derived for the estimators and is verified through simulation results.

- **Contribution 4: Effects of timing and frequency offsets in DCT-based multiple access system for VLC.**
  1. In order to overcome the drawbacks associated with Hermitian Symmetry imposed optical multiple access system, this contribution proposes a multiple access system which is based on DCT. The major focus of this contribution is

to illustrate a simple uplink scenario in which the mobile and base stations are designed in accordant with IM/DD systems.

2. Mathematical expressions are derived by illustrating the deterioration of the received signal in the presence of frequency and timing offsets.
3. The deleterious impact of different probabilities of timing error on the received signal pertaining to a desired subscriber in DCO-fast-OFDMA (DCO-FOFDMA) system is elaborated through mathematical derivations.
4. This work highlights the performance of different synchronization algorithms for the estimation of these offsets in DCT-based multiple access system. Also, the CRLB for the estimation of FO and STO is derived for the aforementioned system and is verified through simulation results.

1.9 Thesis Organization

The thesis is organized into six chapters. The first chapter provides the introduction, background, motivation for the research work as well as details the literature survey discussing the current state of art aspects pertaining to VLC and organization of thesis. The second, third, fourth and fifth chapters provides the contributions of the research work. The sixth chapter provides the conclusions and future scope of the research work. The summary of each chapter is given below.

- **Chapter 1:** This chapter, as a start, gives the background of the emerging technology like VLC with major emphasis on several aspects which highlights that VLC is an intriguing alternative to RF-based wireless communication. Along with its several advantages, this chapter states several research challenges which needs to be addressed when exploiting VLC. Additionally, this chapter details the literature survey imparting focus on the VLC system model, different baseband modulation formats and multicarrier modulation schemes. The different variants of optical OFDM which were proposed in accordant with IM/DD systems are also discussed. Furthermore, the research done so far pertaining to several aspects like channel estimation in optical OFDM, PAPR analysis in multicarrier and multiple access systems as well as synchronization in optical OFDM compatible with IM/DD systems is also briefed. Lastly, the applications of VLC in the fields of vehicular communication and its usage in smart city is also the focus of this chapter.

- **Chapter 2:** Taking into consideration the requirements of IM/DD systems as stated in Chapter 1, an elaborate understanding about the unipolar OFDM is vital. Accordingly, this chapter gives a detailed mathematical description about the different unipolar optical OFDM systems with much stress on the drawbacks associated with imposing Hermitian Symmetry criteria for the purpose of fetching a real-valued signal. Several real transformation techniques which can be exploited in optical OFDM for the purpose of attaining a real-valued signal without the requirement of Hermitian Symmetry criteria are also underlined. This chapter gives the detailed analysis of VLC channel modeling scenario and proposes a comb-type pilot arrangement based ACO-OFDM system which is exploiting different transformation techniques like Hermitian Symmetry imposed IFFT, real transformation techniques like DHT. For the purpose of channel estimation, different channel estimation algorithms like LS, MMSE are utilized. By making use of these estimates, the channel state information at the data is interpolated by exploiting different interpolation algorithms like linear, low-pass and natural cubic spline. A thorough mathematical analysis of the different channel estimation techniques is given. Additionally, this chapter even verifies the performance of the aforementioned channel estimation algorithms in HCM-based on FWHT based optical OFDM (HCM-FWHT-based DCO-OFDM) system and WPDM-based DCO-OFDM system.

- **Chapter 3:** This chapter illustrates the most crucial aspect like PAPR which arises in a multicarrier system like DCT-based optical OFDM (i.e., fast optical OFDM (FOOFDM)). This work compares the proposed PAPR reduction technique like DCT-based spreading with other PAPR reduction techniques like PTS, clipping and filtering. Moreover, mathematical expressions are derived for the time-domain signal formats of FOOFDM system upon imposing these aforementioned PAPR reduction techniques. Further, the expressions of different time-domain signal formats for different subcarrier mapping strategies like F-O-IFDMA and F-O-LFDMA are derived and the superiority of F-O-IFDMA in terms of PAPR reduction than F-

O-LFDMA is verified through simulation results. Additionally, the performance of a DST-based ACO-OFDM and DST-DCO-OFDM system are delineated through mathematical expressions and the simulations are presented over dispersive VLC channel environment. For the purpose of effectively reducing the amount of PAPR in DST-DCO-OFDM system, the proposed DST-based spreading technique is presented along with derivations of the mathematical expressions of the time-domain signal formats. Additionally, the mathematical derivations for different multiple access schemes like DST-based O-IFDMA, DST-O-LFDMA are also depicted. The dominance of DST-based DCO and DST-ACO-OFDM system over Hermitian Symmetry imposed DCO-OFDM and ACO-OFDM system in terms of computational complexity, spectral efficiency are also presented.

- **Chapter 4:** This chapter elucidates the effects of FO and STO on the received signal and derives the mathematical expressions illustrating the deterioration of the overall system performance in the presence of these offsets in a multicarrier system like DCO-OFDM. Several synchronization algorithms like Classen, Moose, and training assisted are imposed in DCO-OFDM system with the intention to estimate these offsets. Moreover, the uplink environment for a multi-user scenario is also portrayed for DCO-OFDMA based multiple access system. Additionally, a thorough mathematical analysis is presented which intensifies the emanation of different sorts of interference like ICI and MUI in the presence of multi-user scenario.

- **Chapter 5:** Taking into consideration the drawbacks which are associated with Hermitian Symmetry imposed IFFT based multicarrier and multiple access systems, this contribution highlights the effects of timing and frequency offsets in DCT-based multiple access system.

- **Chapter 6:** Finally, this chapter presents the conclusions and the future scope of this work.

Chapter 2

Channel Estimation in optical OFDM for VLC

2.1 Introduction and Motivation

For the purpose of assuring a reliable reception of the transmitted data, it is vital to sense and to track the channel state information. In precise, wireless channel estimation can be performed by exploiting different channel estimation algorithms like LS, MMSE and different interpolation techniques like linear, spline and low-pass. It is to be noted that, channel modeling pertaining to optical domain is quite different with that of the conventional RF-based wireless communication. This chapter presents a detailed discussion on channel estimation in optical OFDM which is making use of different real transformation techniques like DHT, WPDM and HCM which is based on FWHT. Furthermore, computational complexity and spectral efficiency of optical OFDM which is based on real transformation techniques will be compared with traditional Hermitian Symmetry imposed IFFT based optical OFDM. In this chapter, a major emphasis is laid on VLC channel modeling along with the mathematical modeling of different channel estimation techniques in the developed system models.

2.2 Channel Estimation in Hermitian Symmetry imposed IFFT based optical OFDM

2.2.1 Channel Estimation in DCO-OFDM

A conventional optical OFDM system is delineated in Fig. 2.1. As depicted from the figure, the incoming high-speed data stream is being encoded into M-ary phase shift keying (M-PSK), M-QAM and M-ary pulse amplitude modulation (M-PAM) symbols where M signifies the constellation order which varies from 2, 4, 8, 16, 32, 64, 256 and 1024. For ensuring perfect reception of the transmitted data, estimation and tracking of the channel is of major requisite. Hence, pilot symbols are inserted based upon comb type pilot arrangement. Further, this stream of symbols are split into a large number of low-speed datasets with the help of a serial to parallel (S/P) converter.

Accordingly, the resultant signal can be expressed as

$$X\left[k\right] = X\left[mN_f + l\right] = \begin{cases} x_p\left[m\right], l = 0 \\ Data,\ l = 1, 2, 3, \cdots, N_f - 1 \end{cases} \tag{2.1}$$

From (2.1), N_f is the Pilot Symbol insertion Frequency, N denotes the total number of subcarriers, $m = 0, 1, 2, \cdots, N_P - 1$, N_P specifies the number of pilot subcarriers which can be obtained as $N_P = \frac{N}{N_f}$ and $X\left[k\right]$ is the frequency domain representation of the data symbols.

Thereupon, these frequency symbols are fed as input to the IFFT transformation block to yield the time-domain signal. It is apparent that, for complex mapping of the input data to the IFFT, the output of it will be definitely a complex-valued signal. Therefore, this necessitates to constrain the input to the IFFT module to satisfy the Hermitian Symmetry criteria. According to Hermitian Symmetry criteria, if there are a total of N number of subcarriers, only $\frac{N}{2}$ will be utilized for data transmission and the rest half are flipped complex conjugate versions of the previous ones. The pictorial representation of the phenomena involved behind the usage of Hermitian Symmetry criteria is illustrated in Fig. 2.2. Mathematically, this can be represented as:

$$X\left[N - k\right] = X^*\left[k\right],\ k = 1, 2, \cdots \frac{N}{2} \tag{2.2}$$

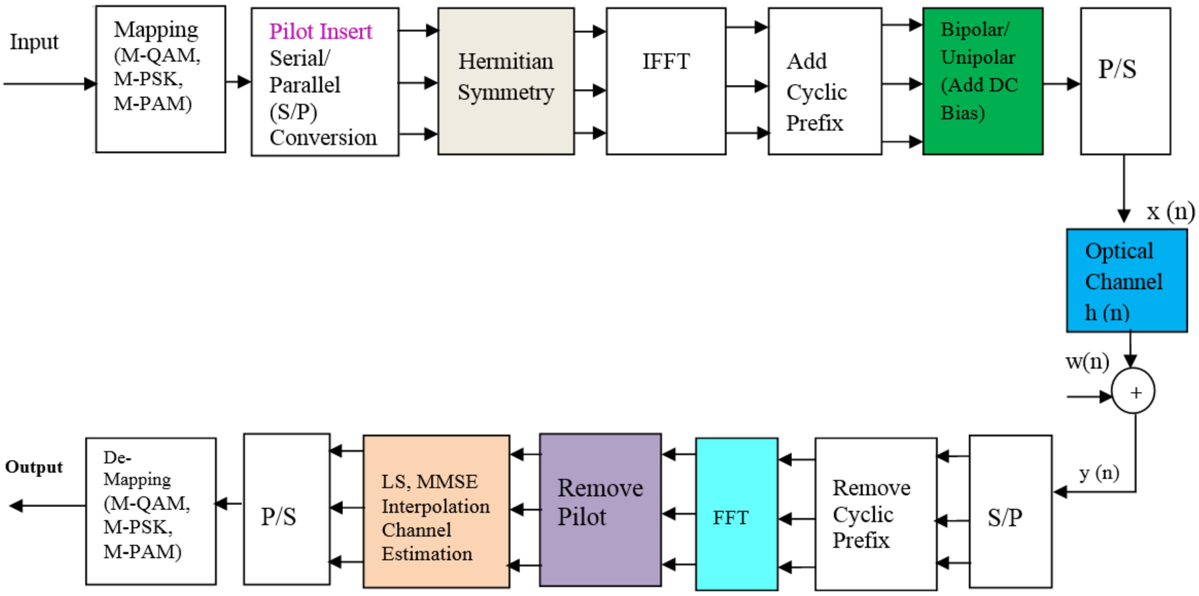

Figure 2.1: Schematic Block of channel estimation in Hermitian Symmetry imposed IFFT-based DCO-OFDM

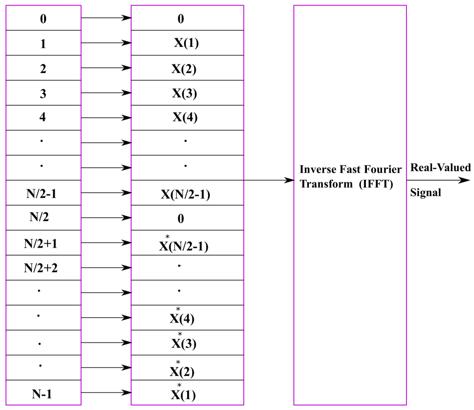

Figure 2.2: Hermitian Symmetry imposed IFFT

Generally, to avoid any imaginary part at the output, the first and the middle subcarrier are set to 0 i.e.,

$$X\left[0\right] = X\left[\frac{N}{2}\right] = 0 \tag{2.3}$$

Hence, the input to the IFFT module has got the following representation as shown by (2.4)

$$X = \left[0, X_1, X_2, X_3, \cdots X_{N/2-1}, 0, X^*_{N/2-1}, \cdots X^*_2, X^*_1\right]^T \tag{2.4}$$

From (2.4), it is evident that due to Hermitian Symmetry criteria, only first half of the subcarriers carry data while the second half are flipped complex conjugates of the first half i.e, out of N subcarriers only $\frac{N}{2}$ are utilized to carry data. The discretized signal at the output of the IFFT can be expressed as

$$x\left[n\right] = \frac{1}{N}\sum_{k=0}^{N-1} X\left[k\right] e^{\frac{j2\pi nk}{N}} \tag{2.5}$$

Therefore, (2.5) can be solved by incorporating the aforementioned constraints to obtain the time domain signal as

$$\begin{aligned} x\left[n\right] = \frac{1}{N}\Big[X\left[0\right] e^{\frac{j2\pi n(0)}{N}} + \sum_{k=1}^{\frac{N}{2}-1} X\left[k\right] e^{\frac{j2\pi nk}{N}} + \\ X\left[\frac{N}{2}\right] e^{\frac{j2\pi n\left(\frac{N}{2}\right)}{N}} + \sum_{k=\frac{N}{2}+1}^{N-1} X\left[k\right] e^{\frac{j2\pi nk}{N}} \Big] \end{aligned} \tag{2.6}$$

Incorporating (2.3) in (2.6), then (2.6) can be reduced to

$$x\left[n\right] = \frac{1}{N}\Big[\sum_{k=1}^{\frac{N}{2}-1} X\left[k\right] e^{\frac{j2\pi nk}{N}} + \sum_{k=\frac{N}{2}+1}^{N-1} X\left[k\right] e^{\frac{j2\pi nk}{N}} \Big] \tag{2.7}$$

Letting $N - k^{'} = k$ and changing the order of limits in (2.7), and re-arranging yields

$$x\left[n\right] = \frac{1}{N}\Big[\sum_{k=1}^{\frac{N}{2}-1} X\left[k\right] e^{\frac{j2\pi nk}{N}} + \sum_{k^{'}=1}^{\frac{N}{2}-1} X\left[N - k^{'}\right] e^{-\frac{j2\pi n\left[N-k^{'}\right]}{N}} \Big] \tag{2.8}$$

Making use of (2.2) in (2.8) and reordering

$$x\left[n\right] = \frac{1}{N}\Big[\sum_{k=1}^{\frac{N}{2}-1} X\left[k\right] e^{\frac{j2\pi nk}{N}} + \sum_{k=1}^{\frac{N}{2}-1} X^{*}\left[k\right] e^{-\frac{j2\pi nk}{N}} \Big] \tag{2.9}$$

Further, by making use of Euler's Identities $e^{j\theta} = cos\theta + jsin\theta$ and $e^{-j\theta} = cos\theta - jsin\theta$, (2.9) can be solved as

$$\begin{aligned} x\left(n\right) = \frac{1}{N}\left[\sum_{k=1}^{\frac{N}{4}-1} \left(X\left[k\right] + X^{*}\left[k\right]\right) cos\left(\frac{2\pi nk}{N}\right)\right] + \\ j\frac{1}{N}\left[\sum_{k=1}^{\frac{N}{4}-1} \left(X\left[k\right] - X^{*}\left[k\right]\right) sin\left(\frac{2\pi nk}{N}\right)\right] \end{aligned} \tag{2.10}$$

By utilizing the real and imaginary parts of the signal which are given as $\underset{RC}{x\left[t\right]} = \frac{x[t]+x^{*}[t]}{2}$ and the imaginary component is $\underset{IC}{x\left[t\right]} = \frac{x[t]-x^{*}[t]}{2j}$. Upon substitution of the above mentioned signal processing, (2.10) reduces to

$$x\left[n\right] = \frac{2}{N}\Big[\sum_{k=1}^{\frac{N}{2}-1} \underset{RC}{X\left[k\right]} cos\left(\frac{2\pi nk}{N}\right) - \sum_{k=1}^{\frac{N}{2}-1} \underset{IC}{X\left[k\right]} sin\left(\frac{2\pi nk}{N}\right) \Big] \tag{2.11}$$

where $\underset{RC}{X}[k]$ and $\underset{IC}{X}[k]$ in (2.11) denote the real and imaginary components of $X[k]$. Furthermore, from (2.11), it is clear that, upon enforcing Hermitian Symmetry criteria, a real valued signal is attained. To surpass the effects of ISI, a certain amount of cyclic prefix/guard interval is inserted. The cyclic prefix to be inserted is $\frac{1}{4}^{th}$ of the sub-carrier's size used and the cyclic prefix added discrete time-domain signal can be expressed mathematically as

$$x_{cp}[n] = x_g[n] = \begin{cases} x[N+n], & n = N_g, N_g - 1, \cdots, 1 \\ x[n], & n = 0, 1, 2, \cdots, N-1 \end{cases} \tag{2.12}$$

In (2.12), N_g is the number of samples in the guard interval. This parallelized signal is then converted into a serial signal for transmission through the channel. Generally, this cyclic prefix added signal (i.e., $x_{cp}[n]$) is real but not necessarily unipolar. Apparently, for the conversion of this bipolar signal into a positive (unipolar) signal, it entails to rely on bipolar to unipolar conversion strategies. One such straightforward approach for converting the bipolar signal into unipolar signal is DCO-OFDM methodology.

This variant of optical OFDM consists of addition of a certain amount of DC bias to the bipolar signal in order to convert it into a unipolar signal. To guarantee a non-negative signal, the required amount of DC bias which is to be added equals the absolute value of the maximum negative amplitude of the bipolar optical OFDM signal. In spite of offering significant advantages, the high peaks which arise due to superimposition of huge number of subcarriers make OFDM prone to high PAPR. Consequently, this high PAPR results in the increase of addition of DC bias for the purpose of assuring the non-negativity in the signal which is to be transmitted. In particular, for large values of the number of subcarriers, the optical OFDM signal amplitude can be approximated as a Gaussian distribution. Therefore, in order to circumvent the addition of surplus DC bias and at the same time to obtain a reduction in the required optical power, it is vital to utilize the DC bias B_{DC} proportional to the power of $x[n]$. The DC bias B_{DC} is usually relative to the electrical power of the signal $x_{cp}[n]$ and is represented as

$$B_{DC} = k\sqrt{E\left\{x_{cp}^2[n]\right\}} \tag{2.13}$$

Where, k is the proportionality constant in general, it is the clipping factor and $E\{\}$ denotes the Expectation operator.

However, the amount of DC bias which is to be added is given in the literature as [133]

$$B_{DC} = 10log_{10}\left(k^2+1\right)\ dB \tag{2.14}$$

The resultant discretized DC biased added signal can be expressed as

$$x_{DC}\left[n\right] = x_{cp}\left[n\right] + B_{DC} \tag{2.15}$$

In order to prevent the added DC bias to be excessive, the peaks of the negative signal must be clipped. Hence, this introduces a noise called as clipping noise which is denoted as η_{clip} [133]. Therefore, the resultant signal after the inclusion of clipping noise is represented as

$$x_{DC}\left[n\right] = x_{cp}\left[n\right] + B_{DC} + \eta_{clip} \tag{2.16}$$

Thus, it can be inferred from the aforementioned analysis that a real and unipolar signal is attained and this can be represented as

$$\underset{unipolar}{x\left[n\right]} = x_{DC}\left[n\right] = x_{cp}\left[n\right] + B_{DC} + \eta_{clip} \tag{2.17}$$

Primarily, PAPR of OFDM increases with the accumulation of subcarriers. Consequently, clipping noise can be minimized upon increasing B_{DC}. Aiding to this, in order to let the clipping noise to be small for higher orders of constellation like 64, 256 and 1024 PSK/PAM/QAM, the amount of DC Bias B_{DC} to be added must be large. One interesting fact to note is, in DCO-OFDM due to imposition of Hermitian Symmetry constraint on IFFT, out of N subcarriers only $^N/_2$ subcarriers are utilized for conveying the data and the rest half are flipped complex conjugates of the previous ones. Eventually, (2.13) clearly illustrates that a proportionality constraint exists between the optical power and the OFDM signal amplitude. In addition to, the electric signal modulates the intensity of the optical transmitter, therefore, this confirms that the required optical power is proportional to the OFDM signal amplitude. Hence, as a matter of fact, it can be affirmed that DCO-OFDM is afflicted due to addition of DC bias as there is a huge power inefficiency. But, in the literature, it is revealed that high amount of powers are desired to fulfil the illumination requirements [134], [135].

Thereupon, this real and unipolar signal is propagated through the optical wireless channel comprising of impulse response $h\left[n\right]$. The time-domain signal which is received can be expressed as

$$y\left[n\right] = R\ \underset{Unipolar}{x\left[n\right]} * h\left[n\right] + z\left[n\right] \tag{2.18}$$

Where, R is the photodetector responsivity in ${}^{Ampere}/_{Watt}$ (${}^{A}/_{W}$) and $z[n]$ is the total noise content which consists of both ambient light shot noise and thermal noise which is modelled as additive white Gaussian noise (AWGN). The VLC channel model used in [136] is considered and the received signal can be formulated as

$$y[n] = \sum_{l=0}^{L-1} h[l] \underset{Unipolar}{x[n-l]} + z[n] \tag{2.19}$$

From (2.19), the photodetector responsivity R is taken as unity and the total number of paths of the VLC channel are denoted by L. In particular, at the receiving end, reverse operations like serial to parallel conversion, removal of cyclic prefix and frequency domain processing of the received signal by passing through the FFT block are performed. Thus, the corresponding frequency domain signal can be put up as

$$Y[k] = X[k] H[k] + Z[k] \tag{2.20}$$

Later, upon removal of pilot tones, the channel is estimated by exploiting channel estimation algorithms like LS and MMSE. There upon, by using these estimates, the channel state information at the data is interpolated by exploiting interpolation algorithms like linear, spline and low-pass interpolation. Finally, the data is recovered by exploiting demapping schemes like M-PSK, M-PAM and M-QAM. It should be noted that the FFT operation reproduces the mirrored structure which was designed at the transmitter where the first half of the elements from 2 to ${}^{N}/_{2} - 1$ are retained as the valid result. Detailed mathematical description about VLC channel modeling and channel estimation techniques are detailed in the subsequent sections.

2.2.2 Channel Estimation in ACO-OFDM

Substantially, to overcome the drawback of power-inefficiency in DCO-OFDM, ACO-OFDM methodology can be employed to yield a positive-valued signal. Predominantly, a unipolar signal can be generated without the requirement of addition of DC bias. In contrast to DCO-OFDM methodology, a positive-valued signal is obtained by reliably choosing the subcarriers for data modulation. As evidenced from Fig. 2.3, the frequency domain representation of the signal follows equation (2.1). Here, only odd subcarriers are modulated and are assigned with Hermitian Symmetry while the even subcarriers are

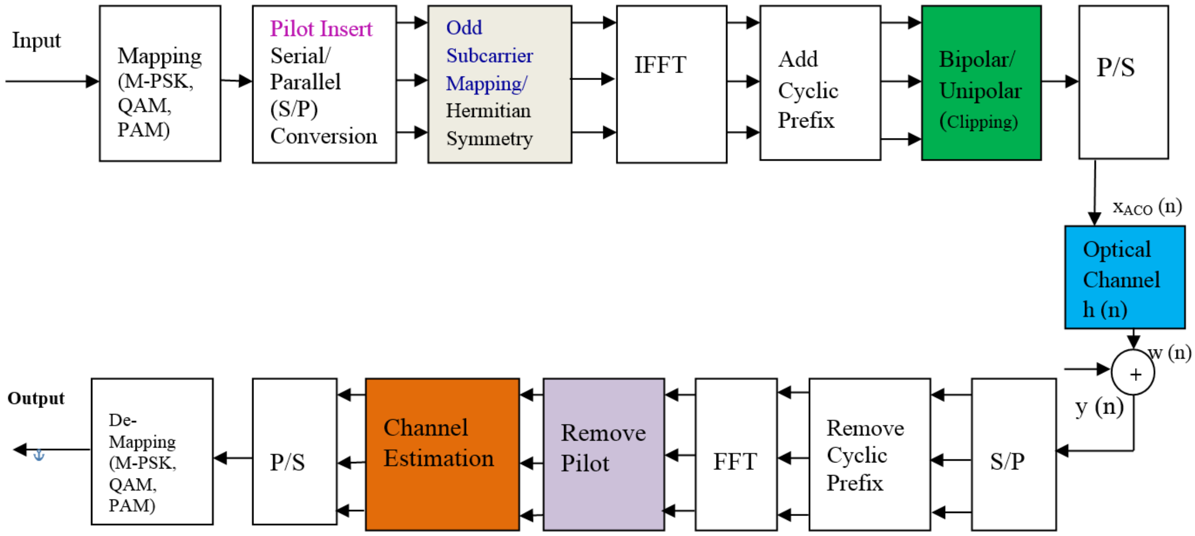

Figure 2.3: Schematic representation of channel estimation in Hermitian Symmetry imposed-IFFT based ACO-OFDM system

assigned zero. Thus, the resultant signal can be put up as

$$X\left[N-k\right]=\begin{cases} X^{*}\left[k\right] & k\ is\ odd \\ 0 & k\ is\ even \end{cases} \tag{2.21}$$

Hence, the input to the IFFT resembles as follows

$$X=\left[0, X_1, 0, X_3, \cdots X_{N/4-1}, 0, X^{*}_{N/4-1}, 0, \cdots X^{*}_{1}\right]^{T} \tag{2.22}$$

It is apparent that from (2.22) only odd subcarriers are modulated and the even subcarriers are set to zero. Hence, out of N subcarriers only $\frac{N}{2}$ are utilized and due to Hermitian Symmetry constraint only $\frac{N}{4}$ are meant for carrying data because, the rest $\frac{N}{4}$ are flipped complex conjugate versions of the previous ones. Therefore, (2.2) can be modified as

$$X\left[\frac{N}{2}-k\right]=X^{*}\left[k\right], \ k=1,2,\cdots\frac{N}{4} \tag{2.23}$$

By making use of (2.5), the discretized time-domain signal at the output of the IFFT can be solved as

$$\begin{aligned} x\left[n\right]=\frac{1}{N}\Bigg[X\left[0\right]e^{\frac{j2\pi n(0)}{N}}+\sum_{k=1}^{\frac{N}{4}-1}X\left[k\right]e^{\frac{j2\pi nk}{N}}+ \\ X\left[\frac{N}{4}\right]e^{\frac{j2\pi n\left(\frac{N}{4}\right)}{N}}+\sum_{k=\frac{N}{4}+1}^{\frac{N}{2}-1}X\left[k\right]e^{\frac{j2\pi nk}{N}}\Bigg] \end{aligned} \tag{2.24}$$

Upon further solving, (2.24) can be reduced as

$$x\left[n\right]=\frac{1}{N}\left[\sum_{k=1}^{\frac{N}{4}-1}X\left[k\right]e^{\frac{j2\pi nk}{N}}+\sum_{k=\frac{N}{4}+1}^{\frac{N}{2}-1}X\left[k\right]e^{\frac{j2\pi nk}{N}}\right] \tag{2.25}$$

Now applying change in variable transformation i.e., letting $\frac{N}{2}-k^{'}=k$ and the resultant expression is

$$x\left[n\right]=\frac{1}{N}\left[\sum_{k=1}^{\frac{N}{4}-1}X\left[k\right]e^{\frac{j2\pi nk}{N}}+\sum_{k^{'}=\frac{N}{4}-1}^{1}X\left[\frac{N}{2}-k^{'}\right]e^{\frac{j2\pi\left(\frac{N}{2}-k^{'}\right)n}{N}}\right] \tag{2.26}$$

Changing the limits in (2.26) yields the following expression

$$x\left[n\right]=\frac{1}{N}\left[\sum_{k=1}^{\frac{N}{4}-1}X\left[k\right]e^{\frac{j2\pi nk}{N}}+\sum_{k^{'}=1}^{\frac{N}{4}-1}X\left[\frac{N}{2}-k^{'}\right]e^{\frac{-j2\pi\left(\frac{N}{2}-k^{'}\right)n}{N}}\right] \tag{2.27}$$

By making use of (2.23) in (2.27) and then rearranging, the following expression can be attained

$$x\left[n\right]=\frac{1}{N}\left[\sum_{k=1}^{\frac{N}{4}-1}X\left[k\right]e^{\frac{j2\pi nk}{N}}+\sum_{k=1}^{\frac{N}{4}-1}X^{*}\left[k\right]e^{\frac{-j2\pi nk}{N}}\right] \tag{2.28}$$

Making use of Euler's Inequalities and signal processing identities, (2.28) can be derived as

$$x\left[n\right]=\frac{1}{N}\Big[\sum_{k=1}^{\frac{N}{4}-1}2X\underset{RC}{[k]}cos\left(\frac{2\pi nk}{N}\right)-\sum_{k=1}^{\frac{N}{4}-1}2X\underset{IC}{[k]}sin\left(\frac{2\pi nk}{N}\right)\Big] \tag{2.29}$$

(2.29), unveils that a real-valued signal is attained at the expense of reduced throughput as only $N/4$ subcarriers are involved for data transmission. Further, to this signal, cyclic prefix is added and the resultant signal $x_{cp}\left[n\right]$ is assured of its positivity by hard clipping the entire negative excursion and then transmitting only the positive signal. This operation can be represented as

$$\underset{Unipolar}{x\left[n\right]}=x_{ACO}\left[n\right]=\begin{cases} x_{cp}\left[n\right] & if\ x_{cp}\left[n\right]\geq 0\\ 0 & if\ x_{cp}\left[n\right]\leq 0\end{cases} \tag{2.30}$$

It is interesting to note that, this time domain signal has got an anti-symmetric property. The main reason involved behind employing odd subcarrier modulation and clipping the even subcarriers is to ensure that clipping noise falls only on the even subcarriers.

The anti-symmetric property can be proved mathematically as: Using the expression for discretized time-domain signal as shown in (2.5),

$$x\left[n+\frac{N}{2}\right]=\frac{1}{N}\sum_{k=0}^{N-1}X\left[k\right]e^{\frac{-j2\pi\left(n+\frac{N}{2}\right)k}{N}} \tag{2.31}$$

On further solving, (2.31) reduces as

$$x\left[n+\frac{N}{2}\right]=\frac{1}{N}\sum_{k=0}^{N-1}X\left[k\right]e^{\frac{-j2\pi nk}{N}}e^{j\pi k} \tag{2.32}$$

$e^{j\pi k}=\left(-1\right)^{k}$, therefore (2.32) can be reduced to

$$x\left[n+\frac{N}{2}\right]=\frac{1}{N}\sum_{k=0}^{N-1}X\left[k\right]e^{\frac{-j2\pi nk}{N}}\left(-1\right)^{k} \tag{2.33}$$

Since, only odd subcarriers are utilized for data modulation and the even subcarriers are set to zero. Hence, we can consider only odd subcarriers. Therefore, $\left(-1\right)^{k}=-1$ since our point of interest is only odd subcarriers.

$$x\left[n+\frac{N}{2}\right]=-\frac{1}{N}\sum_{k=0}^{N-1}X\left[k\right]e^{\frac{-j2\pi nk}{N}} \tag{2.34}$$

Subsequently from (2.34) it can be inferred that

$$x\left[n+\frac{N}{2}\right]=-x\left[n\right] \tag{2.35}$$

Therefore, it can be deduced that the time-domain signal has an anti-symmetry property. Even though the negative peaks are clipped, for each clipped negative peak a positive peak with the same absolute value will be transmitted. As a result, clipping doesn't lead to loss of information. However, clipping noise arises in ACO-OFDM.

2.3 Complexity involved in the computation of Hermitian Symmetry criteria

To be compatible with the characteristics of light sources, it is essential for the OFDM signal to be real and unipolar. One such prevailing approach to yield a real-valued signal is to oblige the frequency-domain symbols at the input of the IFFT module to comply with the Hermitian Symmetry criteria. Principally, this kind of modulation format is referred to as discrete multitone modulation (DMT). It is apparent that FFT and IFFT transformation modules are noteworthy in enabling OFDM modulation and demodulation. Consequently, with the increase in the size of IFFT, the power consumption as well as the area on chip increases significantly. On the other hand, pertaining to the optical OFDM system, for the purpose of accomplishing high data rate transmission, it requires double the size of IFFT and FFT blocks due to the enforcement of Hermitian Symmetry criteria on the frequency-domain symbols. Assuredly, it requires $2N$-point IFFT and FFT transform sizes for modulating the N frequency domain symbols.

The impact of the sizes of IFFT and FFT transforms on the performance of optical OFDM system is unveiled in [137]. As reported in [137], upon increasing the sizes of IFFT/FFT, the number of data subcarriers increase which in turn increases the dynamic range of the OFDM signal, thereby substantially resulting in the requirement of higher precision in the arithmetic operations. The result analysis as depicted in the aforementioned Fig. 2.4 was taken from [137]. This figure clearly indicates the effects of varying sizes of FFT/IFFT on the error vector magnitude (EVM) and the size of the FFT/IFFT is chosen from 32 to 1024. Indeed, it can be inferred from the figure that for a given FFT/IFFT bit precision, upon decreasing the sizes of FFT/IFFT, a reduction in the corresponding EVM is observed. As delineated in [138], for a radix-2 algorithm, the number of additions and multiplications which are required for the computation of real-valued FFT is given by

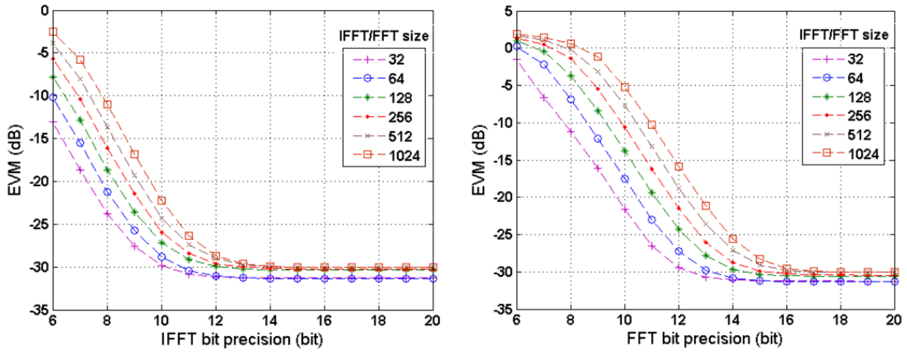

Figure 2.4: Error vector magnitude as a function of FFT and IFFT bit precession for the subcarriers varying from 32 to 1024 [137]

$$\underset{FFT}{Add} = 3Nlog_2N - 3N + 4 \tag{2.36}$$

$$\underset{FFT}{Mul} = Nlog_2N - 3N + 4 \tag{2.37}$$

Therefore, the parameters $\underset{FFT}{Add}$ and $\underset{FFT}{Mul}$ specify the total number of additions and multiplications for FFT transform. In practice, the computational complexity for any transform is defined in terms of the total number of additions and multiplications which are required to compute it. Table. 2.1 gives the total number of additions and multiplications required for different sizes of FFT varying from $8, 16, 32, \cdots, 2048$. Fig. 2.5 confirms the fact that upon increasing the sizes of FFT, computational complexity increases drastically for a DMT system.

Size of FFT	No of Additions	No of Multiplications
8	52	4
16	148	20
32	388	68
64	964	196
128	2308	516
256	5380	1284
512	12292	3076
1024	27652	7172
2048	61444	16388

Table 2.1: Illustration of total number of additions and multiplications required for the computation of different sizes of FFT

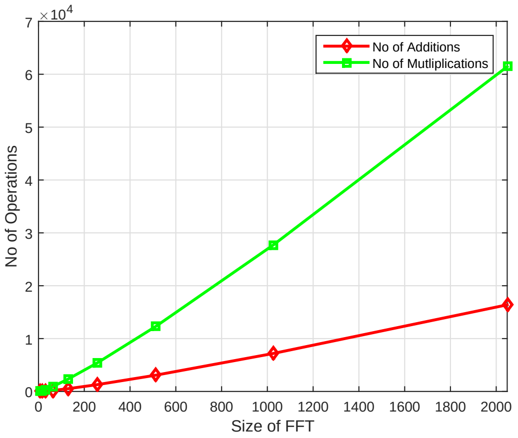

Figure 2.5: Illustration of computational complexity involved behind the split-radix FFT algorithm

The second important aspect which needs to be taken into account along with the computational complexity is power consumption. Therefore, for maximizing the system performance, Application Specific Integrated Circuits (ASICs) are widely deployed in networking devices [139]. The effects of increasing the size of FFT on the performance as well as the power consumption of real-time ASIC-based DMT transceivers was detailed in [137]. The result analysis of this work confirms the fact that upon increasing the size of FFT and IFFT, the cost as well as the power consumption increases drastically. This is more pronounced when the size of FFT/IFFT increases from 512 to 1024, where a 40% increase in the area of the chip and 38% increase in the power consumption at the receiver side can be observed .

2.4 Exploiting Real transformation techniques for optical OFDM

Subsequently, the aforementioned mathematical analysis clearly encapsulates the complexity involved behind enforcing the data input to the IFFT module to satisfy Hermitian Symmetry constraint. As a result, this has a huge impact in the requirement of additional resources as well as longer time is of essential prerequisite to compute the FFT operation thereby leading to the increase in latency. Moreover, for ensuring rapid deployment of real optical OFDM systems for the next generation of networks, it is mandatory to resolve the most vital aspects like cost and power consumption. Additionally, pertaining to real time applications, additional digital signal processing circuitry is required for the computation of Hermitian Symmetry criteria. Furthermore, the decrease in spectral efficiency can be clearly inferred from equations (2.11) and (2.29) since, out of N number of subcarriers, only $N/2$ subcarriers are transmitted in the former while, $N/4$ subcarriers are utilized in the later. This clearly emphasizes the necessity to exploit real transformation techniques. Hence, in this work the performance of the developed systems are evaluated by employing real transformations such as DHT, HCM which is based on FWHT as well as WPDM.

2.4.1 Channel Estimation in Discrete Hartley Transform (DHT)-based optical OFDM

A DHT-based optical OFDM has been proposed in [140] for the purpose of assuring a reduction in computational complexity as encountered in traditional Hermitian Symmetry imposed IFFT-based optical OFDM. Typically, Hartley transform is an attractive tool for enabling real signal processing and has gained tremendous popularity because it involves the same digital signal processing in the transmission and reception and works with real algebra. Moreover, Hartley transform is a real trigonometric transform where the forward/direct and inverse transforms are identical. This implies that it possesses self-inverse property. Inevitably, same digital signal processing device can be exploited for enabling the modulation and demodulation.

Being a real-valued trigonometric transform, it maps the input data using a real constellation such as BPSK and M-PAM to yield a real output. Furthermore, Hartley transform kernel differs from Fourier transform only in the imaginary part and the real and imaginary components of FFT coincide with the even and negative odd parts of DHT. Since it has got the same routine in terms of transmission and reception, we need not force its input to satisfy Hermitian Symmetry constraint. Using a simpler implementation scheme, it supports double the input symbols of a standard real-valued FFT. In OFDM, DFT is prominent in implementing OFDM modulation since it can be seen as a bank of modulators whose narrowband channels have mutually orthogonal subcarriers. In the same manner, the mirror-symmetric sub-bands of DHT guarantee for subcarrier orthogonality and the spectral behaviour of it enables to carry the data symbols for parallel processing. As a result, DHT can be envisaged to replace the FFT in optical OFDM and to embellish as an attractive modulation scheme to be employed for cost-effective IM/DD systems.

A schematic representation of channel estimation in ACO-OFDM which is making use of DHT over a dispersive VLC channel is presented in Fig. 2.6. As depicted, the incoming input data stream is encoded by utilizing real constellation mapping techniques like BPSK and M-PAM. It is evident from the figure that DHT is used for accomplishing the OFDM modulation and demodulation therefore, without enforcing the Hermitian Symmetry criteria, a real valued signal is obtained which is a primary requisite of IM/DD system.

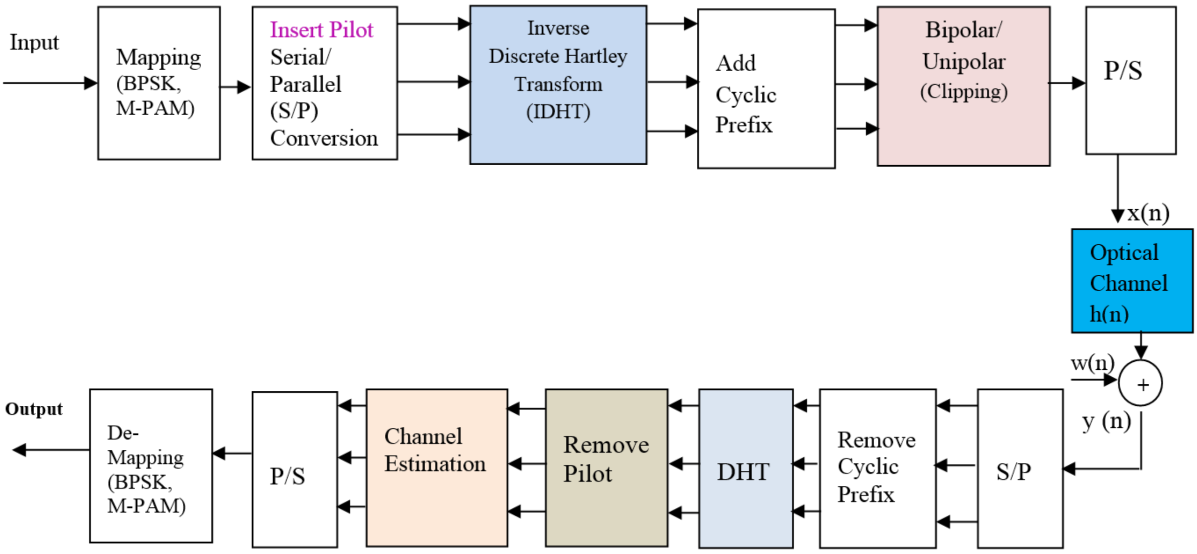

Figure 2.6: Schematic representation of Channel Estimation in ACO-OFDM using Discrete Hartley Transform (DHT) over VLC Channel

The signal processing operation involved behind the transmitter schematic is detailed while dealing with channel estimation in traditional DCO-OFDM and ACO-OFDM systems. Except the transform technique employed, rest of the operations are similar. Accordingly, the discrete time-domain signal at the output of IDHT is given by

$$x\left[n\right] = \frac{1}{\sqrt{N}} \sum_{k=0}^{N-1} X\left[k\right] \left[cos\left(\frac{2\pi nk}{N}\right) + sin\left(\frac{2\pi nk}{N}\right)\right] \tag{2.38}$$

This is equivalent to

$$x\left[n\right] = \frac{1}{\sqrt{N}} \sum_{k=0}^{N-1} X(K) \left[cas\left(\frac{2\pi nk}{N}\right)\right] \tag{2.39}$$

Where $cas\theta = cos\theta + sin\theta$. However, it is to be noted that since ACO-OFDM principality is employed, only odd subcarriers are employed for data transmission. Since, the forward and inverse transforms are identical, $X\left[k\right]$ can be expressed as

$$X\left[k\right] = \frac{1}{\sqrt{N}} \sum_{n=0}^{N-1} x\left[n\right] \left[cos\left(\frac{2\pi nk}{N}\right) + sin\left(\frac{2\pi nk}{N}\right)\right] \tag{2.40}$$

Similar to DFT-based ACO-OFDM, even while exploiting DHT, it is easy to demonstrate for odd subcarriers. Thus, equation (2.40) can be expressed as

$$X\left[k + \frac{N}{2}\right] = \frac{1}{\sqrt{N}} \sum_{n=0}^{N-1} x\left[n\right] \left[cos\left(\frac{2\pi n\left(k + \frac{N}{2}\right)}{N}\right) + sin\left(\frac{2\pi n\left(k + \frac{N}{2}\right)}{N}\right)\right] \tag{2.41}$$

Further, (2.41) can be solved as

$$X\left[k+\frac{N}{2}\right]=\frac{1}{\sqrt{N}}\sum_{n=0}^{N-1}x\left[n\right]\left[cos\left(\frac{2\pi nk}{N}\right)cos\pi n-sin\left(\frac{2\pi nk}{N}\right)sin\pi n+\right.$$
$$\left.sin\left(\frac{2\pi nk}{N}\right)cos\pi n+cos\left(\frac{2\pi nk}{N}\right)sin\pi n\right]\quad(2.42)$$

Therefore, (2.42) can be further reduced to

$$X\left[k+\frac{N}{2}\right]=\left(-1\right)^{n}\frac{1}{\sqrt{N}}\sum_{n=0}^{N-1}x\left[n\right]\left[cos\left(\frac{2\pi nk}{N}\right)+sin\left(\frac{2\pi nk}{N}\right)\right]\quad(2.43)$$

From (2.43), since we are interested in odd subcarriers, we can establish a relation that

$$X\left[k+\frac{N}{2}\right]=-X\left[k\right]\quad(2.44)$$

The symbol elements in the summation of (2.39) can be written as

$$x\left[n\right]=\frac{1}{\sqrt{N}}\sum_{k=0}^{\frac{N}{2}-1}\left[X\left[k\right]cas\left(\frac{2\pi nk}{N}\right)+X\left[k+\frac{N}{2}\right]cas\left(\frac{2\pi n\left(k+\frac{N}{2}\right)}{N}\right)\right]\quad(2.45)$$

By making use of (2.44), (2.45) can be expressed as

$$x\left[n\right]=\frac{2}{\sqrt{N}}\sum_{k=0}^{\frac{N}{2}-1}X\left[k\right]\left[cos\left(\frac{2\pi nk}{N}\right)+sin\left(\frac{2\pi nk}{N}\right)\right]\quad(2.46)$$

Thus, (2.46) can be further re-written as

$$x\left[n\right]=\frac{2}{\sqrt{N}}\sum_{k=0}^{\frac{N}{2}-1}X(K)\left[cas\left(\frac{2\pi nk}{N}\right)\right]\quad(2.47)$$

Thereupon, the negative peaks in the discretized time-domain signal are clipped and only a positive valued signal is intensity modulated through the LED. The rest of the operations, like pilot tone extraction and channel estimation are similar to that of the traditional optical OFDM. The detailed analysis could be found in subsequent sections.

Computational Complexity Analysis of DHT:

Several studies as stated in [141], [142], [143] reveal that FHT require about the same number of multiplications like that of the FFT transform when exploiting Hermitian Symmetry criteria. Pertaining to the number of additions, DHT require more number of additions than that of the FFT. Nevertheless, for the computation of real-valued FFT, it requires to rely on additional resources to calculate the complex-conjugate vector. Earlier studies as reported in [143] reveal that in the case of radix-2 algorithm, for both the decimation-in-time and decimation-in-frequency, DHT algorithm has got the same number of multiplications as that of the FFT but $N-2$ more number of additions than the corresponding FFT algorithm optimized for a real input vector.

Similarly, even for radix-4, split radix, prime factor and Winograd transform algorithms, as illustrated in [143], the requirement in the number of additions for DHT slightly exceeds than the ones required by FFT of a real valued sequence. However, with the proposal of fast algorithms for implementing DHT, much significant work in [144], [145] illustrate that there is a significant reduction in the number of additions. In precise, the improved version of the fastest algorithm as proposed in the aforementioned literature states that DHT algorithm requires only two more additions than that of the FFT algorithm for a real-valued signal thus assuring for a minimal arithmetic complexity as well as enhancing the computational speed of DSP devices.

According to these algorithms, the minimum number of multiplications required for both FFT and DHT is $^{(Nlog_2N-3N+4)}/_2$. While, the additions in case of FFT is $^{(3Nlog_2N-5N)}/_2+4$ and pertaining to DHT, the total number of additions required are $^{(3Nlog_2N-5N)}/_2+6$.

2.4.2 Channel Estimation in Hadamard Coded Modulation (HCM)-based optical OFDM

The most vital problem which is encountered with OFDM is that the transmitted signal have high peaks i.e., high PAPR which imposes as a serious signal distortion at the output of the non-linear channels. The authors in [146], proposed a supplementary to OFDM which is based on Hadamard transform that retains several advantages of OFDM and is notably more resilient against non-linearity. Predominantly, Hadamard matrices and Hadamard transform are prominent tools to be employed for communication systems. Particularly, much significant works in [147], [148], [149] reports that Hadamard matrices/transform have been proposed as a precoder technique to reduce the amount of PAPR in OFDM systems. Particularly, Hadamard transform is an orthogonal linear transform which is implemented by a butterfly structure in the FFT process and henceforth, it will not increase the overall computational complexity of the system. Earlier works pertaining to the utilization of Hadamard transform for VLC reports that, it has been exploited not as a precoder for the sake of reducing the PAPR, but as a modulation technique for encoding and transmitting the information. In [146], the authors have introduced this multilevel modulation technique called HCM which uses Hadamard matrices as a modulation technique rather than a precoder. This sort of modulation can be realized by using the fast Walsh-Hadamard transform (FWHT), which has got the same complexity as that of FFT which used in OFDM, i.e., $Nlog_2N$, where N is the size of the Hadamard matrix Channel Estimation using HCM which is based on FWHT is shown in Fig. 2.7. Similar

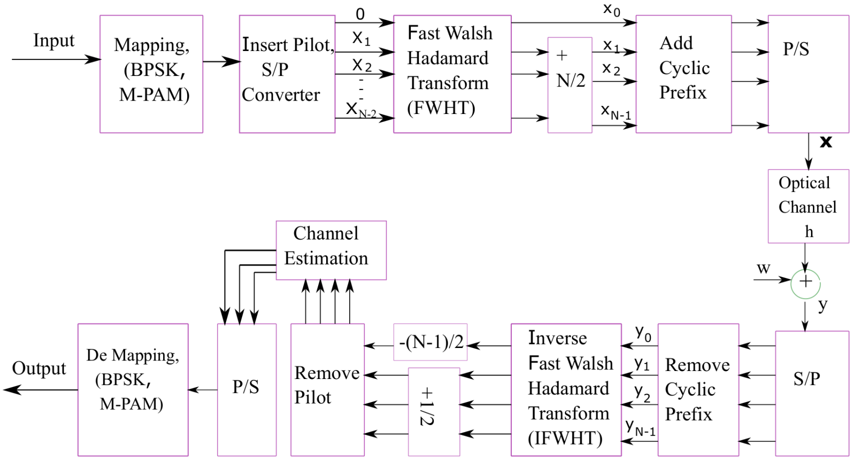

Figure 2.7: Schematic representation of Channel Estimation using Hadamard Coded Modulation (HCM) over VLC Channel

to DHT, FWHT being a real transform it works with real mapping signals such as BPSK and M-PAM. HCM employs FWHT at the transmitter side to modulate the data and IFWHT is used at the receiving end to decode the received data.

Followed by pilot insertion, the components of $\boldsymbol{X}$ i.e., $X_0, X_1, X_2 \cdots X_{N-1}$ are M-PAM modulated and the transmitted signal can be considered as a vector $\boldsymbol{x}$ and is given as [146]

$$\boldsymbol{x} = \left(\boldsymbol{X}\boldsymbol{H_N} + (1-\boldsymbol{X})\,\bar{\boldsymbol{H}}_{\boldsymbol{N}}\right) \tag{2.48}$$

Where, $\boldsymbol{H_N}$ in (2.48) represents a binary Hadamard matrix of order N which is obtained by replacing -1 by 0 in the original $\{-1,1\}$ Hadamard matrix and $\bar{\boldsymbol{H}}_{\boldsymbol{N}}$ denotes the complement of $\boldsymbol{H_N}$. (2.48), can be further expressed as

$$\boldsymbol{x} = \boldsymbol{X}\left(\boldsymbol{H_N} - \bar{\boldsymbol{H}}_{\boldsymbol{N}}\right) + \frac{N}{2}\,[0,1,1,\cdots 1] \tag{2.49}$$

The matrix $\left(\boldsymbol{H_N} - \bar{\boldsymbol{H}}_{\boldsymbol{N}}\right)$ as evidenced by equation (2.49) denotes the bipolar Hadamard matrix and hence the first term in (2.49) represents the Walsh-Hadamard transform of the data vector $\boldsymbol{X}$ while, the second term represents the product of a vector of $1 \times N$ all ones with $\bar{\boldsymbol{H}}_{\boldsymbol{N}}$ [146]. Therefore, the transmitter block can be replaced with fast Walsh Hadamard Transform (FWHT) as illustrated in Fig. 2.7. In brief, at the transmitter side, Hadamard transform using FWHT of size N is applied on the data stream and then a constant of $\frac{N}{2}$ is added to $N-1$ elements to generate the transmitted signal vector $\boldsymbol{x}$. In this way a real and unipolar signal is attained fulfilling the requirements of IM/DD systems. At the receiving end, inverse FWHT (IFWHT) is incorporated instead of FFT. Rest of the analysis is similar to the aforesaid system models.

2.4.3 Wavelet Packet Division Multiplexing (WPDM)-based optical OFDM

WPDM makes use of Inverse Discrete Wavelet Packet Transform (IDWPT) instead of IFFT at the transmitter side and DWPT at the receiving end. In order to compare WPDM-based multicarrier transmission system with aforementioned systems we employed real mapper 16-PAM, Daubechies *db*4 basis function. We followed the same methodology as used in [150] where DC bias of 7 dB is added to the bipolar signal to make it unipolar. WPDM is seen to have advantages over OFDM when used in RF. But, in case of VLC, in order to make the real bipolar signal as unipolar, some amount of DC bias is added. This addition of DC bias leads to power inefficiency. However, it assures spectral efficiency as there is no requirement of Hermitian Symmetry. Exploring novel methodologies to convert real and bipolar WPDM time domain signal as real and unipolar would be the future scope of research.

2.5 Channel Modeling for VLC

In order to model the channel environment, we employ a simple room environment comprising of dimensions $L \times W \times H$ m^3 where LEDs are mounted on the top of the ceiling and the signal from the transmitter LED reaches the receiver through both LOS as well as NLOS paths. In specific, in an indoor room environment, the NLOS paths arise due the reflections from the walls, floor and ceiling. Accordingly, if the transmitter LED employed is of Lambertian type source (i.e., a source which emits light uniformly in all directions), and at the receiving end, for the purpose of eliminating the ambient noise an optical band-pass filter of transmission $T_s(\psi)$ as well as a non-imagining concentrator with gain $g(\psi)$ can be utilized. Then, the impulse response corresponding to the LOS link can be expressed as [151], [152]

$$\underset{LOS}{h[n]} = \begin{cases} \frac{A_{pd}(m+1)}{2\pi d^2} cos^m(\phi) T_s(\psi) g(\psi) cos\psi \delta\left(n - \frac{d}{c}\right), & 0 \leq \psi \leq \psi_c \\ 0, & 0 \geq \psi_c \end{cases} \tag{2.50}$$

The Lambert's mode number is specified by m which is used for expressing the directivity of the LED and is related to the LED semi-angle at half power illumination $\phi_{\frac{1}{2}}$ ($\phi_{\frac{1}{2}}$ is taken as 70 deg) as [151]

$$m = \frac{-ln2}{ln\left(cos\phi_{\frac{1}{2}}\right)} \tag{2.51}$$

From (2.50), d refers to the direct LOS path i.e., the distance between the transmitting LED and the receiver, while A_{pd} corresponds to the area of the PD. The function $\delta\left(n - \frac{d}{c}\right)$ corresponds to the Dirac delta function indicating the signal propagation delay and c is the speed of light in free space. However, in case of diffuse link environment, the reflections need to be taken into consideration. Consequently, in order to consider the total number of reflections of the light in a given room, ray-tracing algorithm can be adopted to calculate the channel impulse response in case of NLOS scenario [153]. Therefore, when the light ray undergoes L reflections, then the channel impulse response can be expressed as

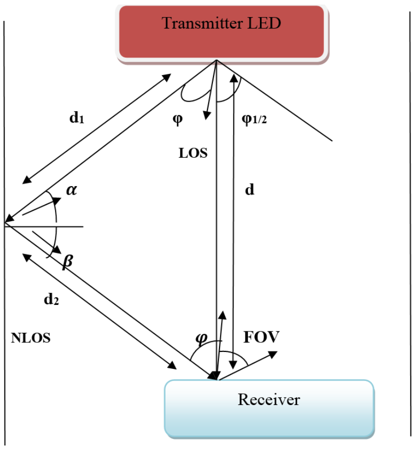

Figure 2.8: Propagation characteristics of VLC Channel

$$\underset{NLOS}{h[n]} = \sum_{L} \underset{NLOS}{h[n]} \tag{2.52}$$

The channel impulse response of the first bounce/reflection as depicted in Fig. 2.8 can be calculated as [151], [152]

$$\underset{NLOS}{h\left[n\right]} = \begin{cases} \frac{A_{pd}(m+1)\rho dA_{wall} cos^{m}(\phi) cos(\alpha) cos(\beta) T_{s}(\psi) g(\psi) cos(\psi)}{2\pi^{2} d_{1}^{2} d_{2}^{2}}, & 0 \leq \psi \leq \psi_{c} \\ 0, & \psi > \psi_{c} \end{cases} \tag{2.53}$$

From (2.53), the parameters d_1 specifies the distance from the transmitter LED to a certain reflective point situated on the wall, while d_2 signifies the distance from this reflective point to the receiver. The reflectance factor is denoted with ρ, while the reflective area of the small region is represented by dA_{wall}, ϕ and α gives the angle of irradiance to a particular reflective point. Whereas, the angle of irradiance to the receiver is denoted by β, the incident angle from the reflective surface is manifested by ψ and ψ_c implies the FOV of the PD.

It is to be noted that for the purpose of simulation, the gain of the optical filter $T_s\left(\psi\right)$ is taken as 1 while the gain of the optical concentrator with refractive index r is given as [151], [152]

$$g\left(\psi\right) = \begin{cases} \frac{r^{2}}{sin^{2}(\psi_{c})}, & 0 \leq \psi \leq \psi_{c} \\ 0, & 0 \geq \psi_{c} \end{cases} \tag{2.54}$$

r specifies the refractive index of the optical concentrator which is taken as 1.5, while the FOV ψ_c is taken as 60.0 deg, reflectance factor ρ is taken as 0.8 and the area of the PD A_{pd} considered is $1cm^2$.

2.6 Channel Estimation Techniques

The corresponding channel estimate at the pilot carriers is obtained as follows:

The resultant frequency domain signal is represented in (2.20). Since, we are interested to know the channel state at the pilots so we proceed further to get this pilot channel estimate by employing the approach of Maximum Likelihood estimate. The resultant signal can be expressed as

$$Y = XH + W \tag{2.55}$$

Since, W is random it is modelled as AWGN. Hence, $W \sim N\left(0, \sigma^2\right)$. Hence, Y is also random and is characterized as $Y \sim N\left(XH, \sigma^2\right)$. Every Gaussian random variable has got its corresponding Likelihood function which is represented as $P\left(Y;H\right)$

$$P\left(Y;H\right)=\frac{1}{\sqrt{2\pi\sigma^2}}e^{\frac{-(Y-XH)^2}{2\sigma^2}} \tag{2.56}$$

We are interested in maximizing this likelihood function. Simply put, maximizing this function is the same as maximizing the log likelihood function which is represented as $L\left(Y;H\right)$

$$L\left(Y;H\right)=-\frac{1}{2}ln\left(2\pi\sigma^2\right)-\frac{\left(Y-XH\right)^2}{2\sigma^2} \tag{2.57}$$

The maximum likelihood estimate of the parameter H is obtained by simple differentiation w.r.t H and then equating to 0.

$$\frac{\partial}{\partial H}L\left(Y;H\right)=0 \tag{2.58}$$

$$\frac{-2\left(Y-XH\right)\left(-X\right)}{\sigma^2}=0 \tag{2.59}$$

On solving, the estimate of the channel $\hat{H}$ is obtained as follows

$$\hat{H}=\frac{Y}{X} \tag{2.60}$$

In general, since we are interested in determining the response across the pilots. So, $\hat{H}$ can be represented as $H_p\hat{}(m)$ where, $m=0,1,2,\cdots N_p-1$ i.e., the frequency response of the channel at the corresponding pilot sub-carrier. (2.60) can be rewritten as

$$\hat{H}_p\left(m\right)=\frac{Y_p\left(m\right)}{X_p\left(m\right)} \tag{2.61}$$

Least Square (LS) Channel Estimation The LS channel estimation is obtained by means of simple division of the output pilots under the effect of optical channel over input pilots. i.e.,

$$\underset{\boldsymbol{LS\ Estimate}}{\hat{\boldsymbol{H}}}=\boldsymbol{X^{-1}Y} \tag{2.62}$$

Minimum Mean Square Error (MMSE) Channel Estimation

The other robust algorithm to predict the channel response is MMSE. The error of the channel estimate $\boldsymbol{e}$ is given by the following equation

$$\boldsymbol{e}=\boldsymbol{H}-\hat{\boldsymbol{H}} \tag{2.63}$$

Where $\boldsymbol{H}$ and $\hat{\boldsymbol{H}}$ are the actual and raw channel estimates respectively, and the MSE of the channel estimate is given as

$$E\left\{|\boldsymbol{e}|^2\right\}=E\left\{\left|\boldsymbol{H}-\hat{\boldsymbol{H}}\right|^{\boldsymbol{2}}\right\} \tag{2.64}$$

$E\{\}$ in (2.64) denotes the expectation operator. Since, the optical channel and the AWGN are not correlated with each other, the MMSE estimate of the channel is given as

$$\boldsymbol{H}_{\hat{\boldsymbol{M}}\boldsymbol{MSE}} = \boldsymbol{R_{HY}} \boldsymbol{R_{YY}}^{-1} \boldsymbol{Y} \tag{2.65}$$

The auto-covariance and cross-covariance matrices of H and Y are denoted by R_{YY} and R_{HY}. The auto-covariance and cross-covariance matrices are given as:

$$\boldsymbol{R_{YY}} = E\left\{\boldsymbol{Y}\boldsymbol{Y^H}\right\} \tag{2.66}$$

Upon substituting the received signal $\boldsymbol{Y} = \boldsymbol{XH} + \boldsymbol{Z}$ in the above equation gives the following representation

$$\begin{aligned}\boldsymbol{R_{YY}} =& E\big\{(\boldsymbol{HX} + \boldsymbol{Z})(\boldsymbol{HX} + \boldsymbol{Z})^{\boldsymbol{H}}\big\} && (2.67)\\ =& E\big\{(\boldsymbol{HXH^HX^H} + \boldsymbol{HXZ^H} + \boldsymbol{ZH^HX^H} + \boldsymbol{ZZ^H})\big\} && (2.68)\end{aligned}$$

Since the channel and AWGN are not correlated, the expectation of HZ as denoted by $E\{\boldsymbol{HZ}\}$ is zero i.e., $E\{\boldsymbol{HZ}\} = 0$

$$\begin{aligned}\boldsymbol{R_{YY}} =& E\left\{\boldsymbol{HH^H}\right\}\boldsymbol{XX^H} + 0 + 0 + E\left\{\boldsymbol{ZZ^H}\right\} && (2.69)\\ =& \boldsymbol{X}\boldsymbol{R_{HH}}\boldsymbol{X^H} + \boldsymbol{\sigma^2} I && (2.70)\end{aligned}$$

Similarly, the cross correlation matrix has got the following mathematical representation

$$\boldsymbol{R_{HY}} = E\left\{\boldsymbol{HY^H}\right\} = E\left\{\boldsymbol{HH^HX^H} + \boldsymbol{HZ^H}\right\} \tag{2.71}$$

$$\boldsymbol{R_{HY}} = E\left\{\boldsymbol{HH^H}\right\}\boldsymbol{X^H} = \boldsymbol{R_{HH}}\boldsymbol{X^H} \tag{2.72}$$

$$\begin{aligned}\hat{\boldsymbol{H}}_{\boldsymbol{MMSE}} =& \boldsymbol{R_{HY}}\boldsymbol{R_{YY}^{-1}}\boldsymbol{Y} && (2.73)\\ =& \boldsymbol{R_{HH}}\boldsymbol{X^H}(\boldsymbol{X}\boldsymbol{R_{HH}}\boldsymbol{X^H} + \boldsymbol{\sigma^2})^{-1}\hat{\boldsymbol{H}}_{\boldsymbol{LS}} && (2.74)\end{aligned}$$

Upon solving, the MMSE channel estimate is given as [136]

$$\hat{\boldsymbol{H}}_{\boldsymbol{MMSE}} = \boldsymbol{R_{HH}}(\boldsymbol{R_{HH}} + \boldsymbol{\sigma^2}(\boldsymbol{X^HX})^{-1})^{-1}\hat{\boldsymbol{H}}_{\boldsymbol{LS}} \tag{2.75}$$

Linear Interpolation

In the case of linear interpolation, the channel estimation at the data sub-carrier is obtained by estimation of response of two adjacent pilot subcarriers. The linear interpolation is a simple means of channel estimation and is given as below

$$\hat{H}(k) = \hat{H}(mN_f + l) = \left(\hat{H}_p(m+1) - \hat{H}_p(m)\right)\frac{1}{N_f} + \hat{H}_p(m) \tag{2.76}$$

Spline Interpolation

The spline interpolation gives a better smooth and continuous polynomial fitted to given data points. However, this is obtained by employing *spline* function in matlab.

Mathematical Description

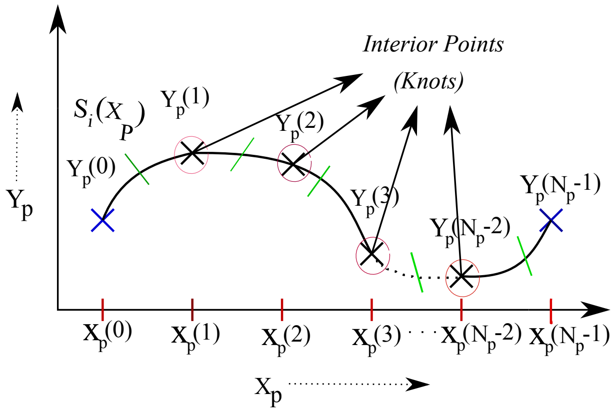

Figure 2.9: Spline Interpolation

A rough schematic of spline interpolation is illustrated in Fig. 2.9. For a given set of transmitted pilots $X_p\left(0\right), X_p\left(1\right), X_p\left(2\right) \cdots X_p\left(N_p-1\right)$, a cubic spline with the function S_i can be defined in the piecewise interval $X_p\left(i\right) \leq X_p \leq X_p\left(i+1\right)$.

To be more precise, $S\left(X_p\right) = S_i\left(X_p\right)$ for $X_p\left(i\right) \leq X_p \leq X_p\left(i+1\right)$. Since, each value of S_i should be a cubic polynomial, in general, we can write in the form

$$S_i\left(X_p\right) = a_i X_p^3 + b_i X_p^2 + c_i X_p + d_i \tag{2.77}$$

The interval i in (2.77) is ranging from $i = 0, 1, 2, \cdots N_p - 2$. For each i, there are 4 unknowns and the interval i runs from $0, 1, 2, \cdots N_p - 2$. So, there are $N_p - 1$ intervals. Therefore, the total number of unknowns are $4\left(N_p-1\right)$.

We have a set of requirements which needs to be satisfied: The spline itself, its first order derivative and the second order derivative must be continuous i.e, S, S' and S'' must be continuous. Further, $S\left(X_p\right)$ must interpolate the data at the interior knots. Since, we have $4\left(N_p-1\right)$ unknowns, we need to set up $4\left(N_p-1\right)$ equations to solve. These set of equations are listed below:

$$S_i\left(X_p\left(i\right)\right) = Y_p\left(i\right), \quad i = 0, 1, \cdots N_p - 2 \qquad N_p - 1 \textit{ equations} \tag{2.78}$$

(2.78) specifies there are $N_p - 1$ *equations*

$$S_i\left(X_p\left(i+1\right)\right) = Y_p\left(i+1\right), \ i = 0, 1, \cdots N_p - 2 \qquad N_p - 1 \textit{ equations} \tag{2.79}$$

(2.79) specifies there are $N_p - 1$ *equations*

$$S_i^{'}\left(X_p\left(i+1\right)\right) = S_{i+1}^{'}\left(X_p\left(i+1\right)\right),\ i = 0, 1, \cdots N_p - 3 \quad N_p - 2 \text{ } equations \tag{2.80}$$

(2.80) specifies there are $N_p - 2$ *equations*

$$S_i^{''}\left(X_p\left(i+1\right)\right) = S_{i+1}^{''}\left(X_p\left(i+1\right)\right), i = 0, 1, \cdots N_p - 3 \quad N_p - 2 \text{ } equations \tag{2.81}$$

(2.81) specifies there are $N_p - 2$ *equations*

$$S_0^{''}\left(X_p\left(0\right)\right) = 0, \qquad 1 \text{ } equation \tag{2.82}$$

$$S_{N_p-2}^{''}\left(X_p\left(N_p - 1\right)\right) = 0, \qquad 1 \text{ } equation \tag{2.83}$$

(2.82) and (2.83) together represent 2 equations. The equations (2.82) and (2.83) denotes that we are interested in computing the natural cubic spline. Hence, there are a total of $4N_p - 4$ equations to be solved to attain $S_i\left(X_p\right)$. It is apparent that each S_i is a polynomial of degree 3. On differentiation, it yields $S_i^{'}$ which is of degree 2 and further differentiation obtains $S_i^{''}$ which is of degree 1. It is to be noted that $S_i^{''}$ is a piecewise linear polynomial and is also continuous. So, $S_i^{''}$ can be claimed as a linear spline.

In order to evaluate the value of $S_i\left(X_p\right)$ we proceed from the backward direction where we start with $S_i^{''}\left(X_p\right)$, as it is linear we can incorporate Lagrange form. Followed by integration of $S_i^{''}\left(X_p\right)$ twice, we get two integration constants. Let us define $r_i = S^{''}\left(X_p\left(i\right)\right),\ i = 1, 2, \cdots N_p - 2$. It is to be noted that these set of r_i's are primary unknowns. Let's use the notation q_i to denote the length of the interval

$$q_i = X_p\left(i+1\right) - X_p\left(i\right) \tag{2.84}$$

Using (2.84), we can describe the Lagrange form for $S_i^{''}\left(X_p\right)$ on the i^{th} interval where, $S_i^{''}\left(X_p\right)$ is a linear polynomial and is a straight line passing through r_i to r_{i+1} from $X_p\left(i\right)$ to $X_p\left(i+1\right)$. So its Lagrange's form can be represented as:

$$S_i^{''}\left(X_p\right) = \frac{r_{i+1}}{q_i}\left(X_p - X_p\left(i\right)\right) - \frac{r_i}{q_i}\left(X_p - X_p\left(i+1\right)\right) \tag{2.85}$$

Integrating (2.85), obtains

$$S_i^{'}\left(X_p\right) = \frac{r_{i+1}}{2q_i}\left(X_p - X_p\left(i\right)\right)^2 - \frac{r_i}{2q_i}\left(X_p - X_p\left(i+1\right)\right)^2 + C_i - D_i \tag{2.86}$$

Where, C_i and D_i represents the arbitrary constants. On further integration of (2.86) obtains

$$\begin{aligned}S_i\left(X_p\right) = \frac{r_{i+1}}{6q_i}\left(X_p - X_p\left(i\right)\right)^3 - \frac{r_i}{6q_i}\left(X_p - X_p\left(i+1\right)\right)^3 + \\ C_i\left(X_p - X_p\left(i\right)\right) - D_i\left(X_p - X_p\left(i+1\right)\right)\end{aligned} \tag{2.87}$$

Incorporating the properties to be satisfied by cubic spline i.e, making use of (2.78) in (2.87) can obtain the arbitrary constant D_i

$$D_i = \frac{Y_p\left(i\right)}{q_i} - \frac{q_i}{6}r_i \tag{2.88}$$

Similarly using (2.79) in (2.87) obtains the second arbitrary constant C_i which is given as

$$C_i = \frac{Y_p\left(i+1\right)}{q_i} - \frac{q_i}{6}r_{i+1} \tag{2.89}$$

A conclusion can be drawn that once r_i's are known, then (C_i, D_i)'s will be known which will help to compute S_i. On substitution of (2.88) and (2.89) in (2.87) will obtain the following representation

$$\begin{aligned}S_i^{'}\left(X_p\right) = \frac{r_{i+1}}{2q_i}\left(X_p - X_p\left(i\right)\right)^2 - \frac{r_i}{2q_i}\left(X_p - X_p\left(i+1\right)\right)^2 + \\ \frac{Y_p\left(i+1\right) - Y_p\left(i\right)}{q_i} - \frac{q_i\left(r_{i+1} - r_i\right)}{6}\end{aligned} \tag{2.90}$$

$S^{'}$ must be a continuous function so, at any inner point $X_p\left(i\right)$ approaching from the left must be equal to the value approaching from the right to $X_p\left(i\right)$ i.e.,

$$S_{i-1}^{'}\left(X_p\left(i\right)\right) = S_i^{'}\left(X_p\left(i\right)\right) \tag{2.91}$$

Upon solving, we get the value approaching from the right as

$$S_i^{'}\left(X_p\left(i\right)\right) = \frac{-r_iq_i}{2} + \frac{Y_p\left(i+1\right) - Y_p\left(i\right)}{q_i} - \frac{r_{i+1} - r_i}{6}q_i \tag{2.92}$$

The second term in (2.92) denotes the known data and let it be represented as b_i, then after rearranging, (2.92) can be reduced to

$$S_i^{'}\left(X_p\left(i\right)\right) = \frac{-1}{6}r_{i+1}q_i - \frac{1}{3}r_iq_i + b_i \tag{2.93}$$

Similarly, we get the value approaching from the left as

$$S_{i-1}^{'}\left(X_p\left(i\right)\right) = \frac{1}{6}r_{i-1}q_{i-1} + \frac{1}{3}r_iq_{i-1} + b_{i-1} \tag{2.94}$$

According to (2.91), equating (2.93) and (2.94) will obtain the following conditions:

$$q_{i-1}r_{i-1} + 2\left(q_{i-1} + q_i\right) r_i + q_i r_{i+1} = 6\left(b_i - b_{i-1}\right) \tag{2.95}$$

(2.95) can be represented in the form of a Matrix-Vector form as $Q.\vec{r} = \vec{b}$

$$Q = \begin{bmatrix} 2\left(q_0+q_1\right) & q_1 & & & & \\ q_1 & 2\left(q_0+q_1\right) & q_2 & & & \\ & q_2 & 2\left(q_2+q_3\right) & q_3 & & \\ & \ddots & \ddots & & & \\ & & q_{N_p-4} & 2\left(q_{N_p-4}+q_{N_p-3}\right) & q_{N_p-2} \\ & & & q_{N_p-3} & 2\left(q_{N_p-3}+q_{N_p-2}\right) \end{bmatrix} \tag{2.96}$$

The unknown parameter matrix and the data matrix are given by

$$\vec{r} = \begin{bmatrix} r_1 \\ r_2 \\ r_3 \\ \vdots \\ r_{N_p-3} \\ r_{N_p-2} \end{bmatrix} \tag{2.97}$$

$$\vec{b} = \begin{bmatrix} 6\left(b_1 - b_0\right) \\ 6\left(b_2 - b_1\right) \\ 6\left(b_3 - b_2\right) \\ \vdots \\ 6\left(b_{N_p-3} - b_{N_p-2}\right) \\ 6\left(b_{N_p-2} - b_{N+p-1}\right) \end{bmatrix} \tag{2.98}$$

In this approach after computing $\vec{r}$ using Q and $\vec{b}$, then the Spline can be interpreted.

Low Pass Interpolation

The low-pass interpolation is performed by inserting zeros into the original sequence and then applying a lowpass finite impulse response (FIR) filter that allows the original data to pass through unchanged and interpolates between such that the mean-square error between the interpolated points and their ideal values is minimized. Based on the interpolation factor L, $L-1$ zeros are inserted between each pair of input sample values as illustrated in Fig. 2.10.

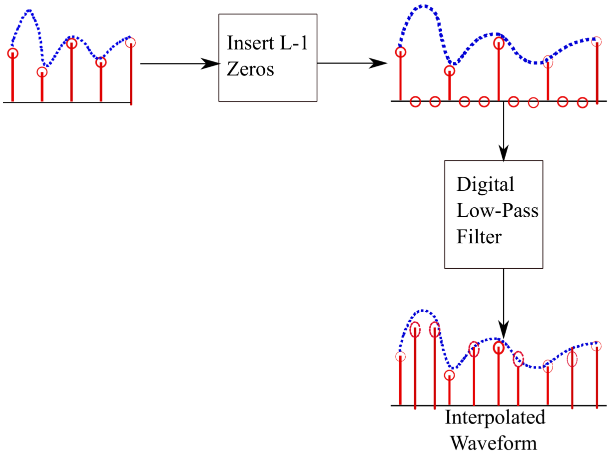

Figure 2.10: Low-Pass Interpolation

2.7 Cramer Rao Lower Bound (CRLB) for channel estimation error

In this section, we derive the CRLB [154] for channel estimation error. Principally, CRLB gives the minimum variance of any unbiased estimation. Usually, in its simplest form, the bound states that the variance of any unbiased estimator is high as the inverse of the Fisher Information Matrix. In general, the received signal in the presence of channel effect can be represented as

$$\begin{aligned} y\left[n\right] =& IFFT\left\{Y\left[k\right]\right\} = IFFT\left\{X\left[k\right]H\left[k\right] + W\left[k\right]\right\} \\ &= IFFT\left\{X\left[k\right]H\left[k\right]\right\} + IFFT\left\{W\left[k\right]\right\} \end{aligned} \tag{2.99}$$

Consequently, the received signal can be expressed as

$$y\left[n\right] = \frac{2}{N}\sum_{k=1}^{\frac{N}{4}-1}\left(\underset{RC}{X}\left[k\right]cos\left(\frac{2\pi nk}{N}\right) - \underset{IC}{X}\left[k\right]sin\left(\frac{2\pi nk}{N}\right)\right)H\left[k\right] + w\left[n\right] \tag{2.100}$$

Since we are interested in estimation of the channel coefficients, for the ease of simplification let it be denoted as h. It is apparent that, if $w\left[n\right]$ is random with mean 0 and variance σ^2 and hence it is characterized as $w \sim N\left(0,\sigma^2\right)$. This implies that $y\left[n\right]$ is also random in nature and is characterized as $y\left[n\right] \sim N\left(\frac{2}{N}\sum_{k=1}^{\frac{N}{4}-1}\left(\underset{RC}{X}\left[k\right]cos\left(\frac{2\pi nk}{N}\right) - \underset{IC}{X}\left[k\right]sin\left(\frac{2\pi nk}{N}\right)\right)h, \sigma^2\right)$. Its corresponding likelihood function can be expressed as

$$P\left(Y;h\right) = \frac{1}{\left(2\pi\sigma^2\right)^{\frac{N}{2}}}e^{-\frac{\sum_{n=0}^{N-1}\left(y[n]-\frac{2}{N}\sum_{k=1}^{\frac{N}{4}-1}\left(\underset{RC}{X}[k]cos\left(\frac{2\pi nk}{N}\right)-\underset{IC}{X}[k]sin\left(\frac{2\pi nk}{N}\right)\right)h\right)^2}{2\sigma^2}} \tag{2.101}$$

The log likelihood function which is denoted as $L\left(Y;h\right)$ corresponding to (2.101) can be calculated as

$$L\left(Y;H\right) = lnP\left(Y;h\right) =$$

$$-\frac{N}{2}ln\left(2\pi\sigma^2\right) - \frac{\sum_{n=0}^{N-1}\left(y\left[n\right] - \frac{2}{N}\sum_{k=1}^{\frac{N}{4}-1}\left(\underset{RC}{X}\left[k\right]cos\left(\frac{2\pi nk}{N}\right) - \underset{IC}{X}\left[k\right]sin\left(\frac{2\pi nk}{N}\right)\right)h\right)^2}{2\sigma^2} \tag{2.102}$$

According to CRLB,

$$V\left(\hat{h}\right) \geq \frac{1}{-E\left[\frac{\partial^2}{\partial h^2}lnP\left(Y;h\right)\right]} \tag{2.103}$$

On further solving, the second order derivative pertaining to the log likelihood estimate of h which is denoted as $\frac{\partial^2}{\partial h^2}lnP\left(Y;h\right)$ is attained as follows

$$\frac{\partial^2}{\partial h^2}lnP\left(Y;h\right) = \frac{-4}{N^2\sigma^2}\sum_{n=0}^{N-1}\left[\sum_{k=1}^{\frac{N}{4}-1}\left(\underset{RC}{X}\left[k\right]cos\left(\frac{2\pi nk}{N}\right) - \underset{IC}{X}\left[k\right]sin\left(\frac{2\pi nk}{N}\right)\right)\right]^2 \tag{2.104}$$

Using certain assumptions that for higher values of θ, $sin\theta \simeq \theta$ and $cos\theta = 0$, (2.104) can be reduced as

$$\frac{\partial^2}{\partial h^2}lnP\left(Y;h\right) = -\frac{32\pi^2}{2\sigma^2N^4}\sum_{n=0}^{N-1}n^2\left[\sum_{k=1}^{\frac{N}{4}-1}k\underset{IC}{X}\left[k\right]\right]^2 \tag{2.105}$$

On further solving (2.105), by making use $\sum_{n=0}^{N-1}n^2 = \frac{N(N+1)(2N+1)}{6}$, (2.105) can be further reduced as

$$\frac{\partial^2}{\partial h^2}lnP\left(Y;h\right) = -\frac{8\pi^2\left(N+1\right)\left(2N+1\right)}{3\sigma^2N^3}\left[\sum_{k=1}^{\frac{N}{4}-1}k\underset{IC}{X}\left[k\right]\right]^2 \tag{2.106}$$

Finally, upon enforcing the Expectation operator to (2.106), $V\left(\hat{h}\right)$ can be obtained as

$$V\left(\hat{h}\right) \geq \frac{144\sigma^2N^2}{\pi^2\left(N+1\right)\left(2N+1\right)\left(N-4\right)} \tag{2.107}$$

The simulated result as evidenced from results and discussions section clearly illustrate that CRLB attains the minimum variance when compared with other channel estimation algorithms.

2.8 Results and Discussions

The simulated results for the proposed systems are presented over VLC channel environment. The channel estimation techniques such as LS, MMSE and interpolation

Table 2.2: System Parameters for Simulation

Parameter	Value
No of OFDM symbols	512
Total Number of Subcarriers	1024
Pilot Insertion interval	$\frac{1}{8}$th the subcarriers size
Total Number of Pilot carriers	128
Type of the transform techniques employed	FFT, DHT, FWHT
Variants of optical OFDM employed	DCO-OFDM, ACO-OFDM
Cyclic Prefix	$\frac{1}{4}$th subcarriers size
Orders of Modulation	M-QAM, M-PSK, M-PAM
Dimensions of the Room	$6 \times 6 \times 3$
Total number of LEDs	1200
Power of each LED	20mW
LED semi-angle	70 degrees
FOV of the photodiode ψ_c	60 degrees
Area of the Photodiode A_{pd}	1 cm^2
Optical Filter Co-efficient $T_s(\psi)$	1
Refractive index	1.5
Reflectance factor ρ	0.8
Channel estimation algorithms	LS, MMSE, Interpolation

for comb type pilot arrangement are simulated. Here, for the proposed system models, 1024 subcarriers are considered and pilot symbol insertion was done at an interval of $\frac{1}{8}$, therefore, the no of pilot carriers employed are 128. The parameters which are employed for simulation are detailed in Table. 2.2.

Fig. 2.11, illustrates the simulated BER performance considering LOS VLC channel environment for ACO-OFDM using M-QAM. Here, as the order of modulation increases, SNR also increases to achieve BER of 10^{-4}. At SNR of 8 dB, the achieved BER is 1.538×10^{-4} for 4 QAM, whereas, while employing 1024 QAM, the achievable BER is 2.991×10^{-4} at SNR of 28 dB. However, when the number of NLOS components increase,

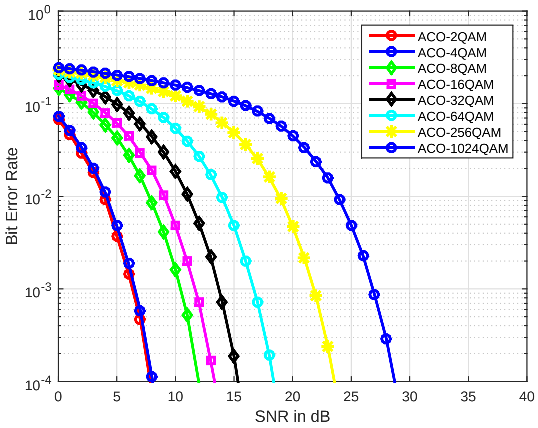

Figure 2.11: BER Comparison of ACO-OFDM for M-QAM considering LOS Component over VLC Channel

the SNR should be increased to achieve the same BER. This is clearly depicted in Fig. 2.12. Because, for 4 QAM at the same SNR of 8 dB, the achievable BER is 4.831×10^{-3}. It requires approximately 15 dB of SNR to achieve a BER of 1.474×10^{-4} for the same order of modulation.

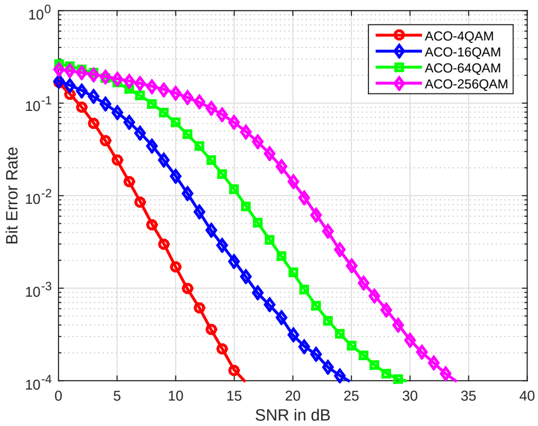

Figure 2.12: BER Comparison of ACO-OFDM for M-QAM considering NLOS Components over VLC channel

Fig. 2.13 and Fig. 2.14, shows the BER performance for ACO-OFDM employing FFT with Hermitian Symmetry using M-PSK and M-PAM considering a single NLOS component in VLC channel environment. The results show that both the orders of modulation i.e., M-PSK and M-PAM require more amount of SNR to achieve the same BER and for the higher order modulation like 64, 256 and 1024 PAM the BER deteriorates. This is valid because, for higher orders of modulation clipping noise in ACO-OFDM system

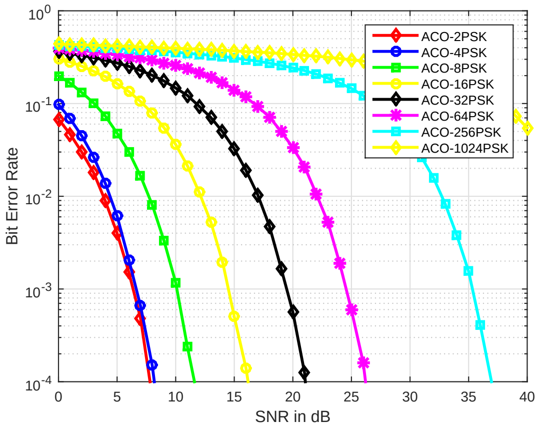

Figure 2.13: BER comparison of ACO-OFDM (employing Hermitian Symmetry imposed FFT) for M-PSK considering a single NLOS Component over VLC channel

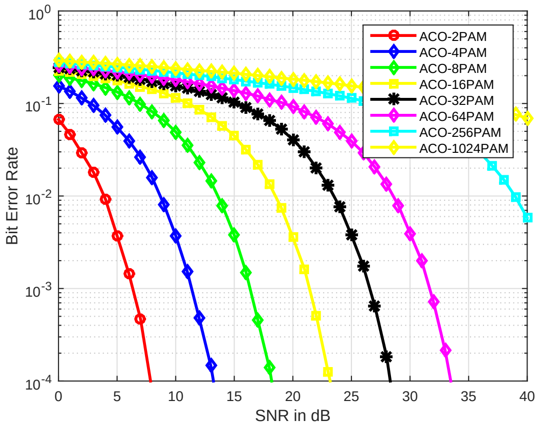

Figure 2.14: BER comparison of ACO-OFDM (employing Hermitian Symmetry imposed FFT) for M-PAM considering a single NLOS Component over VLC channel

is more dominant. When the VLC channel model which consists of NLOS components due to reflections from walls, ceiling, etc is incorporated in the system, then ISI plays a major role to introduce the bit errors. So, LS, MMSE and interpolation plays a major role to combat the channel effect. Fig. 2.15, depicts the different channel estimation techniques such as LS and MMSE employing M-QAM modulation scheme for ACO-OFDM system over VLC channel environment. It can be seen that, for instance, for 4-QAM the MMSE channel estimation performs better than LS. At SNR of 8 dB the obtained BER is 5.61×10^{-4} employing MMSE for 4 QAM. However, as the order of modulation increases, LS channel estimate is more susceptible to the noise which is mainly due to consideration of NLOS components. Spline interpolation based channel estimation techniques outper-

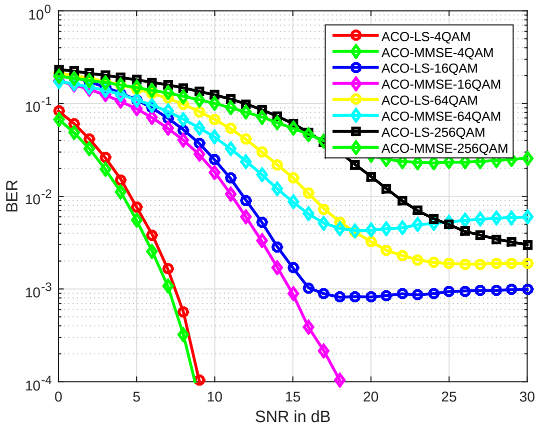

Figure 2.15: Channel estimation using LS and MMSE algorithms over VLC Channel

forms the other interpolation techniques like linear and low-pass in terms of BER. This is clearly observed from Fig. 2.16, at SNR of 11 dB the targeted BER is 3.946×10^{-5} for spline interpolation, 1.973×10^{-4} for linear and 5.04×10^{-3} for low-pass.

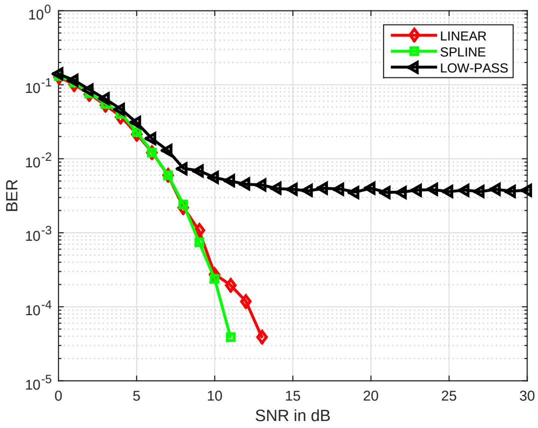

Figure 2.16: Interpolation Channel estimation in ACO-OFDM for 4-QAM over VLC Channel

In order to compare the performance of traditional Hermitian Symmetry imposed FFT-based ACO-OFDM system, we analyze the performance of ACO-OFDM system which is based on DHT over dispersive VLC channel. We compare the performance of different channel estimation algorithms in DHT-based ACO-OFDM system by considering the modulation formats like BPSK and M-PAM. In order to exploit the advantages of real-signal processing offered by Hartley transform, only real constellation can be supported. Therefore, we analyze the performance for BPSK and M-ary PAM. Fig. 2.17, represents the BER performance analysis of DHT-based ACO-OFDM system using BPSK

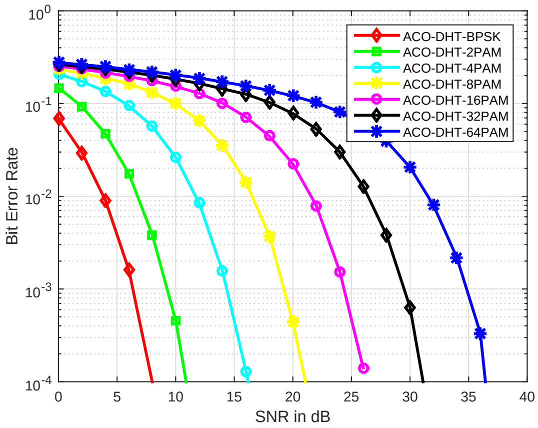

Figure 2.17: BER performance analysis of Discrete Hartley Transform (DHT)-based ACO-OFDM using BPSK Modulation and M-PAM over VLC Channel

and M-PAM over VLC channel model. From the figure, it can be evidenced that as the SNR increases better BER is obtained. However, with the increase in order of modulation, SNR also increases to attain a reduced error floor. It is interesting to note that Hermitian Symmetry imposed FFT-based ACO-OFDM system requires about 4, 16, 64, 256 and 1024 QAM in order to achieve the same amount of performance as that of DHT-based ACO-OFDM which is employing $2, 4, 16$ and 32 PAM respectively. This confirms that by using a simpler system like DHT-based ACO-OFDM, the same data sequence is transmitted without the requirement of Hermitian Symmetry as well as lower orders of modulation format is sufficient. The performance of channel estimation algorithms

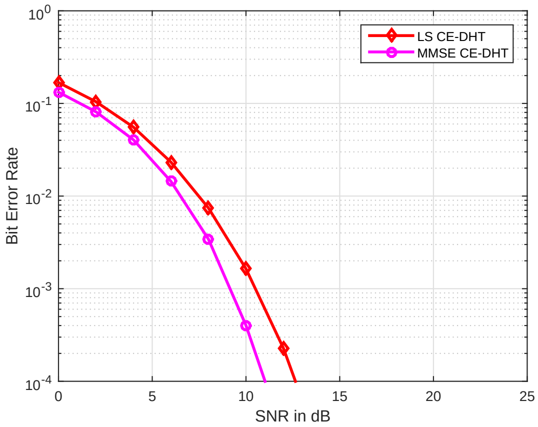

Figure 2.18: Channel estimation in Discrete Hartley Transform (DHT)-based ACO-OFDM using BPSK Modulation over VLC Channel

like LS and MMSE for DHT-based ACO-OFDM system employing BPSK and M-PAM is elucidated in figures 2.18 and 2.19. It can be seen from Fig. 2.18, LS and MMSE channel estimation algorithms are compared for the same system model using BPSK modulation scheme. Here, MMSE gives good performance over LS for BPSK modulation scheme. For 10 dB of SNR, the achievable BER is around 10^{-4}. For higher constellation orders, the results show that MMSE outperforms than LS but at the cost in increase in SNR. This is clearly depicted from Fig. 2.19, where LS and MMSE channel estimation was done for M-PAM using DHT for optical (VLC) channel environment.

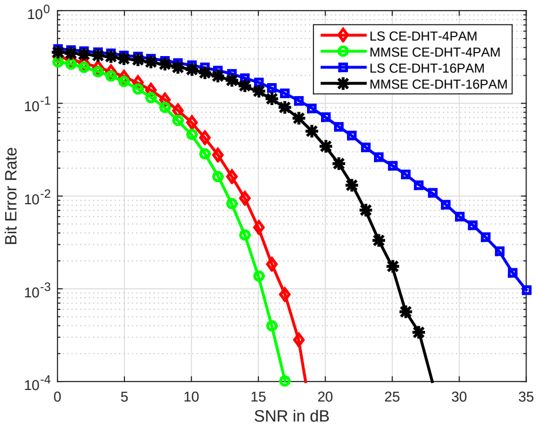

Figure 2.19: Channel estimation in Discrete Hartley Transform (DHT)-based ACO-OFDM using M-PAM over VLC Channel

Table 2.3: Comparison between DHT-optical OFDM and DFT-optical OFDM

Type of OFDM	DHT-ACO-OFDM and DHT-DCO-OFDM	DFT-ACO-OFDM and DFT-DCO-OFDM
Hermitian Symmetry	Not-required	Required
Constellation	Real (BPSK, M-PAM)	Complex (M-QAM)
Constellation Size	M=L	M=L^2
Self-Inverse Property	Self-Inversive	Not-Self-Inversive
Subcarriers-Utilized	$\frac{N}{2}$ for DHT-ACO-OFDM N for DHT-DCO-OFDM	$\frac{N}{4}$ for DFT-ACO-OFDM $\frac{N}{2}$ for DFT-DCO-OFDM
No of Multiplications	$(3Nlog_2N-3N+4)/2$	$(3Nlog_2N-3N+4)/2$
No of Additions	$(3Nlog_2N-5N)/2+6$	$(3Nlog_2N-5N)/2+4$

Table 2.3 summarizes the difference between DFT-based and DHT-based optical

OFDM system. As represented in the table, Hartley transform replaces the Fourier signal processing. Additionally, the self-inversive property of DHT enables the exploitation of same digital signal processing for both modulation and demodulation. Moreover, a DHT-based optical system supports double the number of subcarriers for data transmission when compared with DFT-based optical OFDM system. Fig. 2.20, depicts the theoretical and simulated analysis for ACO-OFDM using LS channel estimation. It is apparent that, the probability of error for M-PAM is given by [155]

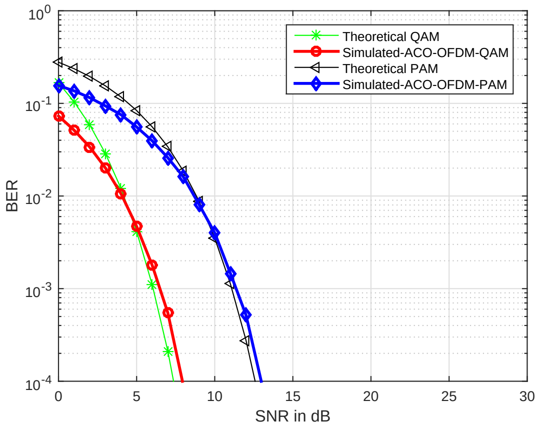

Figure 2.20: Theoretical and Simulation Analysis of ACO-OFDM over VLC Channel

$$P_e = \frac{2\left(M-1\right)}{M} Q\left(\sqrt{\frac{\left(6log_2^M\right)E_b}{\left(M^2-1\right)N_0}}\right) \tag{2.108}$$

Making use of the relation between $Q - function$ and $errorfunction$ [155]

$$Q\left(z\right) = \frac{1}{2} erfc\left(\frac{z}{\sqrt{2}}\right) \tag{2.109}$$

Finally, the probability of error for $4 - PAM$ is obtained as

$$P_e = \frac{3}{4} erfc\left(\sqrt{\frac{2E_b}{5N_0}}\right) \tag{2.110}$$

Similarly, the error probability for M-QAM is given as

$$P_e = 4Q\left(\sqrt{\frac{3kE_b}{\left(M-1\right)N_0}}\right) \tag{2.111}$$

where $M = 2^k$.

With a slight variation, the simulated results follows the theoretical results. Similarly, the analytical analysis has been carried out for DCO-OFDM system with the assumption that the signal which is received in the presence of noise is represented by

$$Y = X + B_{DC} + W \tag{2.112}$$

B_{DC} in (2.112) is the amount of DC bias which is added to guarantee a positive (unipolar) signal and W is the combination of thermal noise and shot noise which is modelled as AWGN. So, W has got the representation as $W \sim N\left(0, \sigma^2\right)$. Since, the type of modulation considered is M-QAM, firstly, it is essential to derive the expression for probability of error which is denoted as P_e for M-PAM and then evaluate for M-QAM. The P_e for M-PAM is expressed as

$$P_e = 2\left(\frac{M-1}{M}\right) Q\left(\sqrt{\frac{6log_2^M E_b}{\left(M^2-1\right) N_0}} - \frac{B_{DC}}{\sqrt{\sigma^2}}\right) \tag{2.113}$$

Using the relation between Q function and error function as stated in (2.109), (2.113) can be reduced as

$$P_e = \left(\frac{M-1}{M}\right) erfc\left(\sqrt{\frac{3log_2^M E_b}{\left(M^2-1\right) N_0}} - \frac{B_{DC}}{\sqrt{2\sigma^2}}\right) \tag{2.114}$$

Therefore, the P_e employing M-QAM reduces to

$$P_e = 2erfc\left(\sqrt{\frac{1.5log_2^M E_b}{\left(M-1\right) N_0}} - \frac{B_{DC}}{\sqrt{2\sigma^2}}\right) \tag{2.115}$$

Fig. 2.21, represents the BER performance for the analytical analysis as shown. From the results it can be inferred that, the addition of DC-bias enables unipolar DCO-OFDM

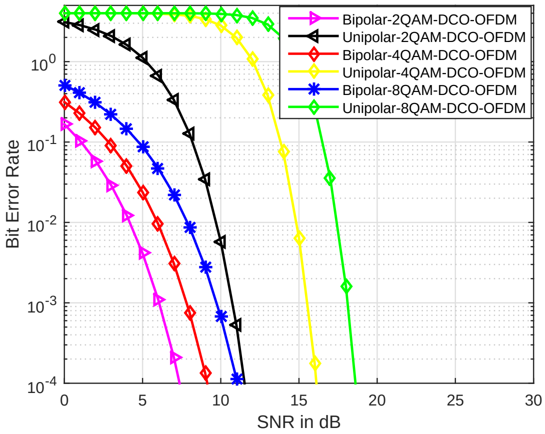

Figure 2.21: Comparision of Unipolar-DCO-OFDM and Bipolar OFDM system using M-QAM

system to consume more SNR than bipolar DCO-OFDM system. However, large amount of SNR is preferred for illumination requirements.

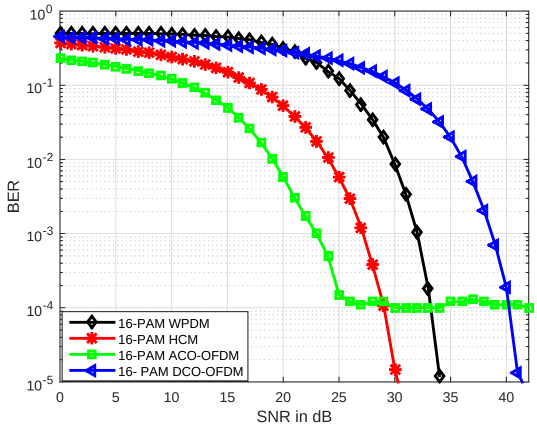

Figure 2.22: BER Performance of ACO-OFDM, DCO-OFDM, WPDM and HCM over dispersive VLC Channel

Fig. 2.22, shows the comparison analysis of HCM, ACO-OFDM, WPDM and DCO-OFDM over dispersive VLC channel environment. From the result analysis it can be depicted that, ACO-OFDM gives better BER than HCM at lower SNRs but as the SNR increases, the performance of ACO-OFDM deteriorates due to clipping noise. While, at higher SNRs, HCM dominates ACO-OFDM. This is justified because HCM exhibits better performance at higher average optical powers because of its low PAPR. The power inefficiency of DCO-OFDM is clearly illustrated, because the added DC bias leads to consumption of huge amount of SNR to achieve a desired BER. The same can be implied to WPDM also. At SNR of 25 dB, ACO-OFDM gives a BER of 1.5×10^{-4} and HCM gives 5.731×10^{-3} while WPDM gives 0.1234 and DCO-OFDM gives 0.2136. While at SNR of 30 dB, HCM achieves a BER of 1.766×10^{-5} and ACO-OFDM attains 1.000×10^{-4} whereas, WPDM and DCO-OFDM achieves a BER of $8.667 \times 10^{-3}$and 0.1083 respectively. This analysis depicts the power inefficiency of adding DC bias.

Fig. 2.23, shows LS and MMSE channel estimation in HCM system over VLC channel. It is evident from the figure that, LS channel estimation is more vulnerable to noise because it has an irreducible error floor at higher SNRs. MMSE algorithm outperforms LS and this is similar to DHT-based ACO-OFDM. At SNR of 17 dB, MMSE algorithm using 4 PAM achieved targeted BER of 7.262×10^{-5} while with LS, it is 7.339×10^{-4}. It can be observed that as the order of modulation increases, MMSE requires higher SNR to

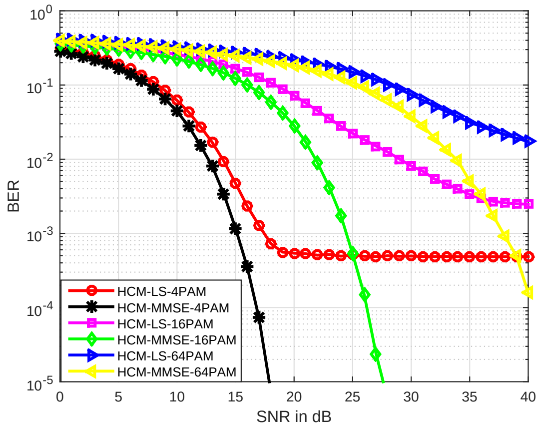

Figure 2.23: Comparison of LS and MMSE Channel Estimation in HCM System over dispersive VLC Channel

obtain the desired BER. For 16 PAM, MMSE requires 27dB of SNR to achieve BER of 2.389×10^{-5} and using 64 PAM, MMSE needs 40 dB of SNR to attain a BER of 1.573×10^{-4}.

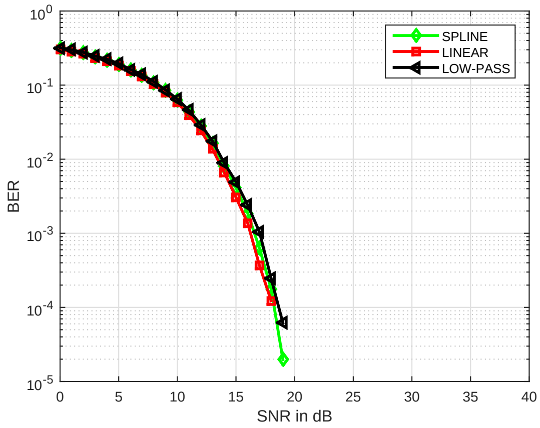

Figure 2.24: Comparison of Interpolation Channel estimation in HCM system over dispersive VLC Channel

Channel estimation in HCM exploiting interpolation techniques is elucidated in Fig. 2.24. The figure emphasizes that, interpolation techniques namely spline, linear and low-pass outperforms MMSE and LS channel estimation techniques for the same order of modulation i.e, 4 PAM. However, when compared with ACO-OFDM and DHT-based ACO-OFDM, HCM requires higher SNR to acquire a reducible error floor. It can be seen that spline requires SNR of 19 dB to acquire BER of 1.973×10^{-5} whereas, at SNR of 18 dB, linear and low-pass interpolation obtains BER of 1.23×10^{-4} and 2.461×10^{-4} respectively.

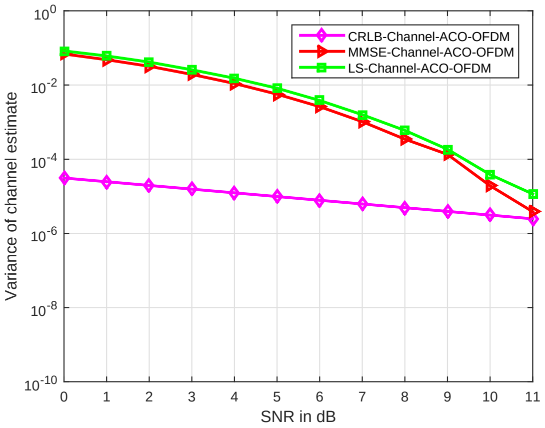

Figure 2.25: MSE Comparison for CRLB, LS and MMSE based channel estimation in ACO-OFDM system

Fig. 2.25 compares the MSE vs SNR for LS, MMSE channel estimation algorithms with the derived CRLB. From the figure, it can be inferred that, CRLB attains the minimum variance when compared with other estimation algorithms. At SNR of 11 dB, CRLB achieves MSE of 2.468×10^{-6}, while MMSE and LS achieves MSE of 3.845×10^{-6} and 1.153×10^{-5} respectively.

2.9 Conclusion

This chapter focuses on comb type pilot arrangement based channel estimation for traditional Hermitian Symmetry imposed IFFT-based ACO-OFDM and different multicarrier transmission systems like DHT-based ACO-OFDM and HCM employing FWHT over VLC channel environment. Various channel estimation algorithms like LS, MMSE and interpolation techniques such as linear, spline and low-pass are analyzed and compared for the aforementioned systems using different orders of modulation such as M-PSK, M-QAM and M-PAM. The simulated results depicts that, MMSE channel estimation algorithm in ACO-OFDM, DHT-based ACO-OFDM and HCM systems has reducible error floor as the order of modulation increases when compared with LS channel estimation algorithm. This is certain that due to dispersive nature of channel, LS is more susceptible to noise than MMSE. However, among spline, linear and low-pass interpolation techniques, spline interpolation has improvement in terms of BER over the others in all the multicarrier systems.

DHT-based ACO-OFDM ensures higher spectral efficiency and ease of implementation when compared with conventional Hermitian Symmetry imposed FFT-based ACO-OFDM. While, HCM gives better BER performance when compared with ACO-OFDM at the cost of increased SNR of around 6 dB. However, desired amount of signal power is essential for fulfilling illumination requirements for VLC. Eventually, DHT-based ACO-OFDM system is both spectral and power efficient as well as simple to implement whereas, HCM which is based on FWHT is spectrally efficient but consumes high SNRs to achieve the desired BER. Due to their ease of implementation without relying on Hermitian Symmetry as well as assuring improved spectral efficiency both these multicarrier transmission systems which are based on different transformation techniques namely DHT and FWHT can be envisaged for the realization of cost-effective IM/DD system for VLC.

Chapter 3

On the performance of DCT/DST-based multicarrier and multiple access schemes for VLC

3.1 Introduction and Motivation

Owing to its remarkable advantages and with the advancements of digital signal processing technology, OFDM has been applied to OWC. With its spectral efficiency feature and resilience against narrow band interference, it sparked a considerable amount of interest in the research community. The underlying physics involved behind the suitability of OFDM technique for transmission over a dispersive fading channel environment is that it splits a high-speed data stream into several low-speed data streams in such a way that each low-speed data stream can be concurrently transmitted over a number of harmonically related narrowband subcarriers [156]. An improvement in bandwidth efficiency can be achieved by reducing the spacing between the number of subcarriers. With this motive, as well as to emerge as a competitive solution in the market, fast optical OFDM (FOOFDM) has been proposed by setting its target to minimize the transceiver components cost [157].

The architectural design of FOOFDM reduces hardware and software engineering effort, while reducing the computational complexity by employing real signal processing without sacrificing the overall system performance. In contrast to conventional optical OFDM which employs Hermitian Symmetry imposed IFFT for accomplishing a real-valued signal transmission, FOOFDM system exploits real trigonometric transform like discrete cosine transform (DCT) for accomplishing OFDM modulation and demodulation. It is reported in the literature that, a DCT based optical OFDM which is also referred to as FOOFDM has been investigated for IM/DD optical transmission systems [158], [159], [160]. In FOOFDM, the spacing of the neighbouring subcarrier is half of the symbol rate per subcarrier. It uses simple, real and one-dimensional mapping schemes where only in-phase component is exploited. FOOFDM exhibits an improved system performance in channel estimation and exhibits enhanced robustness to FO and chromatic dispersion [161], [162], [163]. This is due to its excellent energy compaction property.

When compared with traditional Hermitian Symmetry imposed IFFT-based optical OFDM, FOOFDM exhibits lower computational complexity because without the requirement of Hermitian Symmetry criteria, a real-valued signal is attained as well as the operation count in terms of number of additions and multiplications for DCT is less than that of the DFT. As shown in Fig. 3.1, the minimum subcarrier spacing which is required by FOOFDM is just half of that of the DFT-based OFDM. Aiding to this, another real trigonometric transform which can be exploited in optical OFDM is discrete sine transform (DST). In generality, DST belongs to the family of sinusoidal unitary transforms. In particular, a sinusoidal unitary transform is an invertible linear transform whose kernel is described by a set of orthogonal discrete sine basis functions [165].

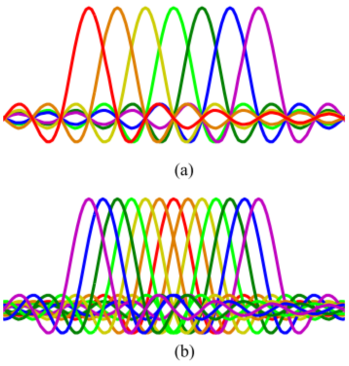

Figure 3.1: Illustration of Spectrum of DFT-based OFDM and FOOFDM (a) DFT-based OFDM (b) DCT-based OFDM [164]

DSTs, which are ably called as discrete trigonometric transforms consists of 8 versions of DST where each transform is classified as even or odd of type I, II, III and IV [165], [166], [167], [168]. In general, even types of DSTs i.e., DST-I, DST-II, DST-III and DST-IV are widely defined in the literature due to their utilization in several digital signal processing and image processing applications. For a transform of size N, the corresponding 4 even types of DST as defined in [167] can be expressed as:

$$DST-I=\sqrt{\frac{2}{N}}\left[sin\left(\frac{\pi\left(n+1\right)\left(k+1\right)}{N}\right)\right],n,k=0,1,2,\cdots N-2 \tag{3.1}$$

$$DST-II=\sqrt{\frac{2}{N}}\left[\epsilon_k sin\left(\frac{\pi\left(2n+1\right)\left(k+1\right)}{2N}\right)\right],n,k=0,1,2,\cdots N-1 \tag{3.2}$$

$$DST-III=\sqrt{\frac{2}{N}}\left[\epsilon_n sin\left(\frac{\pi\left(2k+1\right)\left(n+1\right)}{2N}\right)\right],n,k=0,1,2,\cdots N-1 \tag{3.3}$$

From (3.2) and (3.3), the value ϵ_r can be defined as

$$\epsilon_r=\begin{cases}\frac{1}{\sqrt{2}}, & r=N-1\\ 1, & Otherwise\end{cases} \tag{3.4}$$

$$DST-IV=\sqrt{\frac{2}{N}}\left[sin\left(\frac{\pi\left(2n+1\right)\left(2k+1\right)}{4N}\right)\right],n,k=0,1,2,\cdots N-1 \tag{3.5}$$

The noteworthy feature is that the existence of fast algorithms allows for the efficient computation of DST. Moreover, these different versions of DST have profound use in the diverse areas of digital signal processing. DST-IV which is used in this work has profound applicability in the fast implementation of lapped orthogonal transforms and sine modulated filter banks for the purpose of efficient subband coding [169]. Eventually, these kind of real trigonometric transforms like DCT and DST can be utilized in optical OFDM systems to enable modulation and demodulation process. Consequently, such kind of systems can be envisaged to be realized as cost-effective solutions for IM/DD systems.

In spite of offering several noteworthy benefits, the high peaks which arise due to superimposition of huge number of subcarriers is inevitable in OFDM. In precise, due to increase in the number of subcarriers, high PAPR occurs in OFDM. This scenario is even more worsened in case of IM/DD systems exploiting LEDs. This is due to the fact that in VLC, LED is the main source of non-linearity. Moreover, the limited dynamic range of LEDs leads to clipping of the peaks of the optical time-domain signal which doesn't fit within the linear range of LEDs. Hence, there is an urge to address the PAPR issue especially in optical domain.

This chapter analyses the performance of FOOFDM system i.e., a multicarrier system which is exploiting DCT as well as a DST-based optical OFDM system over dispersive VLC channel environment. Furthermore, the PAPR analysis is carried out in the aforementioned multicarrier systems by exploiting different PAPR reduction schemes like spreading, multiple probabilistic and signalling technique like PTS and signal distortion technique like clipping with filtering. In addition to this, mathematical expressions are derived for the time-domain signal formats which are complying with the requirements of IM/DD systems for the developed systems. Further, PAPR analysis for different subcarrier mapping strategies corresponding to the multiple access schemes which are based on DCT and DST is also the focus of this chapter.

3.2 Performance analysis of FOOFDM system

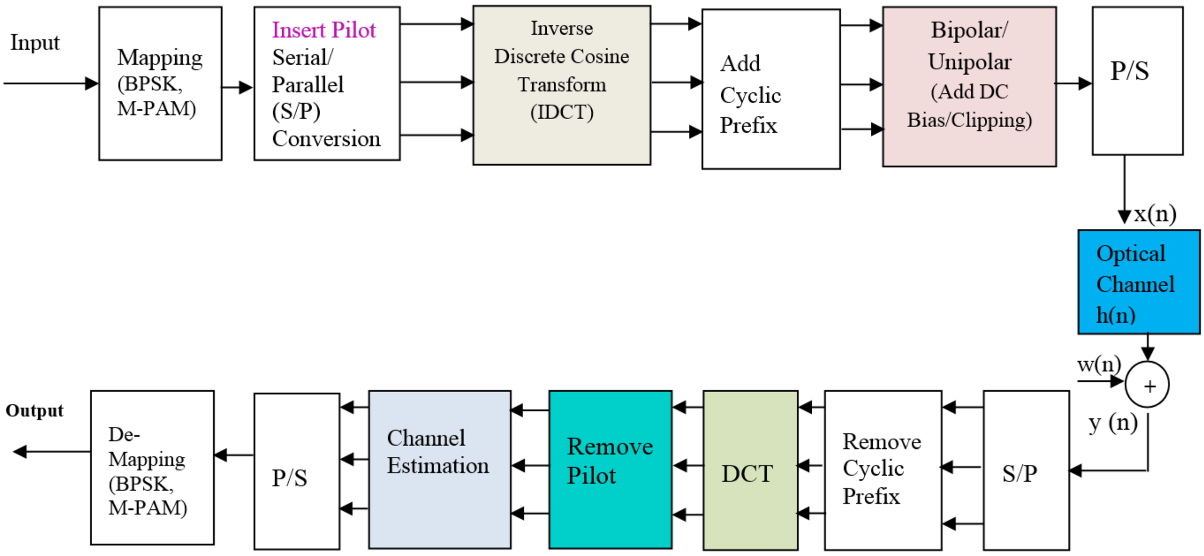

Figure 3.2: Schematic representation for FOOFDM System

The schematic representation of DCO-OFDM system model which is based on DCT is delineated in Fig. 3.2. The N point DCT and its inverse (IDCT) for a data sequence $m = 0, 1, 2, \cdots N - 1$ as defined in [170], [171] are given as:

$$X_k = \sqrt{\frac{2}{N}} C_k \sum_{m=0}^{N-1} x_m cos\left(\frac{\pi\left(2m+1\right)k}{2N}\right), 0 \leq k \leq N-1 \tag{3.6}$$

$$x_m = \sqrt{\frac{2}{N}} \sum_{k=0}^{N-1} C_k X_k cos\left(\frac{\pi\left(2m+1\right)k}{2N}\right), 0 \leq m \leq N-1 \tag{3.7}$$

Where,

$$C_k = \begin{cases} \frac{1}{\sqrt{2}}, & k = 0 \\ 1, & k = 1, 2, 3, \cdots N-1 \end{cases} \tag{3.8}$$

where X_k and x_m represents the frequency-domain and time-domain samples. As evident from the block diagram, DCT and IDCT plays the role of data modulation and de-modulation. In general, the pilot tones are inserted based upon comb-type pilot arrangement pattern into each FOOFDM symbol based upon a specific period. The input vector to the transformation module is mapped by employing real-mapping schemes like BPSK and M-PAM. It is to be noted that without the requirement of Hermitian Symmetry, a real-valued signal is attained. However, in order to assure for non-negativity of the signal, a suitable amount of DC-bias is added to bipolar FOOFDM signal and the remaining negative peaks are clipped to result into a positive DCO-FOOFDM signal. Therefore, the DCO-FOOFDM signal can be expressed as

$$s(n) = \begin{cases} x(n) + \beta_{DC}, & x(n) > \beta_{DC} \\ 0, & x(n) < \beta_{DC} \end{cases} \tag{3.9}$$

The basic principle of DCO-OFDM which includes the addition of DC bias is stated in previous chapter i.e. chapter 2. Therefore, this real and positive-valued signal is propagated through the optical channel environment. Thus, the received signal can be expressed as

$$y(n) = Rs(n) \circledast h(n) + w(n) \tag{3.10}$$

Where R in (3.10) signifies the Responsivity of the PD in $Ampere/Watts$, $\circledast$ specifies the convolution operator and $w(n)$ represents the thermal and shot noise which is modeled as AWGN. For ease of simplicity the value of R is taken as 1. (3.10) can be solved to attain

$$y(n) = \sum_{l=0}^{L-1} s(n-l)\, h(l) + w(n) \tag{3.11}$$

L in (3.11) represents the total number of paths. At the receiving end, this huge stream of serialized data is converted into parallel by employing S/P converter. Thereupon, pilot tones are extracted and then channel estimation is enforced where, the transmitted pilots and the received pilots are compared to determine the deterioration of the received signal under the channel effects. Lastly, the signal is processed to obtain the final output.

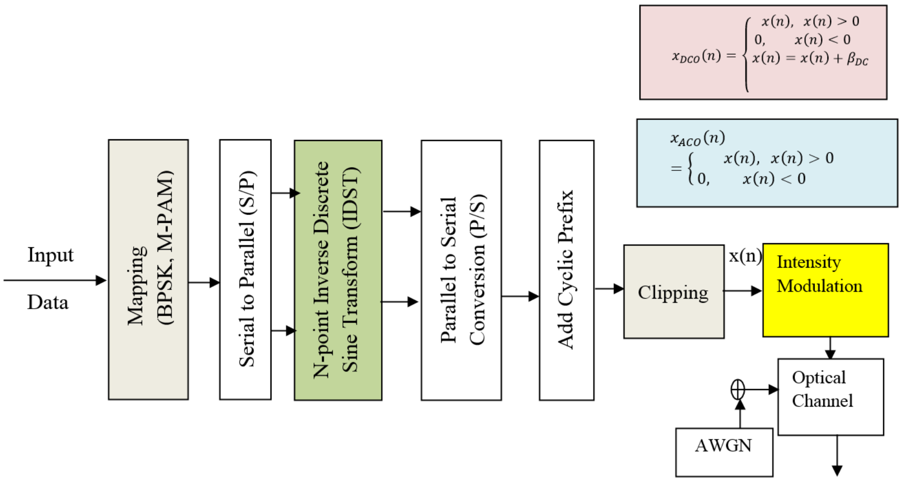

(a) Transmitter of DST-DCO/ACO-OFDM system for VLC

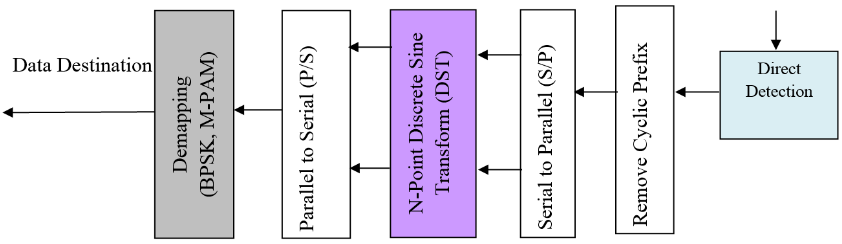

(b) Receiver of DST-DCO/ACO-OFDM system for VLC

Figure 3.3: DST-based DCO-OFDM/ACO-OFDM system model for VLC

3.3 Performance analysis of DST-based multicarrier systems

The combination of multicarrier transmission techniques with higher orders of modulation emerged as the most appealing solution for cost-effective and gigantic speed IM/DD systems. Fig. 3.3a and 3.3b delineates the developed system model which includes both the transmitter and receiver modules in accordant with IM/DD systems for VLC. As depicted from the transmitter and receiver modules, DST is employed to accomplish the modulation and demodulation rather than the FFT transform as used in traditional OFDM system. In specific, the N-point DST and its inverse are given by [169]

$$X_k = \sqrt{\frac{2}{N}} \sum_{n=0}^{N-1} x_n sin\left[\frac{\pi\left(2n+1\right)\left(2k+1\right)}{4N}\right] \quad k = 0, 1, 2, 3, \cdots N-1 \tag{3.12}$$

$$x_n = \sqrt{\frac{2}{N}} \sum_{k=0}^{N-1} X_k sin\left[\frac{\pi\left(2n+1\right)\left(2k+1\right)}{4N}\right] \quad n = 0, 1, 2, 3, \cdots N-1 \tag{3.13}$$

X_k and x_n in (3.12) and (3.13) represents the frequency and time-domain signal and furthermore it can be inferred that a real valued signal is attained without enforcing

Hermitian Symmetry criteria as required in DFT-based DCO-OFDM/ACO-OFDM system. DST being a real transformation technique, enables the huge sets of incoming data stream to be mapped by exploiting real and simple one-dimensional mapping like BPSK and M-PAM. In particular, the optical OFDM system which is based on N-point FFT, for each stage of parallel processing, the input information bit sequence which is mapped by employing M-QAM requires $^{N}/_{2}$ total number of subcarriers for data transmission due to Hermitian Symmetry constraint (i.e., according to Hermitian Symmetry criteria, only half of the inputs carry the data while the other half are flipped complex conjugate versions of the previous ones). While, the N-point DST as depicted in equations (3.12) and (3.13) employs all of the transform points i.e., subcarriers for data transmission therefore, assuring double the data rate.

Therefore, as depicted in the figure, the stream of modulated data symbols are transmitted in parallel by employing a S/P. Furthermore, in order to prevent ISI which generally prevails in a multipath environment, cyclic prefix or guard interval is added to this time-domain signal. Prior to intensity modulation of this real valued time-domain signal through the LED, it should be assured of its positivity. Hence, this necessitates to employ DCO-OFDM and ACO-OFDM methodologies.

Pertaining to DST-DCO-OFDM system, in order to assure the signal positivity, instead of adding a fixed amount of DC bias, it is convenient to add the DC bias per symbol basis as [172]

$$\beta_{DC} = |min\{x_n, n = 0, 1, 2, 3, \cdots N-1\}| + V_{TOV} \tag{3.14}$$

In (3.14), V_{TOV} represents the LED turn on voltage i.e., the amount of voltage required for the LED to enter into conduction region. Thus, the transmitted signal in case of DST-DCO-OFDM system after the addition of DC bias can be represented as

$$\underset{Unipolar}{x(n)} = \underset{DCO}{x(n)} = x_n + \beta_{DC} \tag{3.15}$$

Where $\underset{DCO}{x(n)}$ in (3.15) denotes the transmitted signal in DST-DCO-OFDM system. In case of DST-ACO-OFDM system, the time-domain signal can be mathematically formulated as: since, only odd subcarriers are modulated therefore, out of N number of subcarriers only $\frac{N}{2}$ are meant for data transmission. Hence, by making use of (3.13), the expression for time-domain signal i.e., the output of the IDST transformation block can be obtained as:

$$x_{n+\frac{N}{2}} = \sqrt{\frac{N}{2}} \sum_{k=0}^{\frac{N}{2}-1} X_k sin\left[\frac{\pi}{N}\left(n+\frac{N}{2}+\frac{1}{2}\right)\left(k+\frac{1}{2}\right)\right] \tag{3.16}$$

$$x_{n+\frac{N}{2}} = \frac{2}{N} \sum_{k=0}^{\frac{N}{2}-1} X_k sin\left[\frac{\pi}{N}\left(n+\frac{1}{2}\right)\left(k+\frac{1}{2}\right)+\frac{\pi}{2}\left(k+\frac{1}{2}\right)\right] \tag{3.17}$$

(3.17) can be further solved to attain

$$\begin{aligned} x_{n+\frac{N}{2}} = \frac{2}{N} \sum_{k=0}^{\frac{N}{2}-1} X_k sin\left[\frac{\pi}{N}\left(n+\frac{1}{2}\right)\left(k+\frac{1}{2}\right)\right] cos\left[\frac{\pi}{2}\left(k+\frac{1}{2}\right)\right] + \\ \frac{2}{N} \sum_{k=0}^{\frac{N}{2}-1} X_k cos\left[\frac{\pi}{N}\left(n+\frac{1}{2}\right)\left(k+\frac{1}{2}\right)\right] sin\left[\frac{\pi}{2}\left(k+\frac{1}{2}\right)\right] \\ where\ k\ is\ odd \end{aligned} \tag{3.18}$$

Finally, only the positive part of the time-domain signal is transmitted and can be expressed as

$$\underset{Unipolar}{x(n)} = \underset{ACO}{x(n)} = \begin{cases} x_{n+\frac{N}{2}} & if\ x_{n+\frac{N}{2}} > 0 \\ 0 & if\ x_{n+\frac{N}{2}} \leq 0 \end{cases} \tag{3.19}$$

The obtained time-domain signals pertaining to DST-DCO-OFDM and DST-ACO-OFDM systems as shown by (3.15) and (3.19) are propagated through the channel and at the receiving side, a PD is employed to convert the light signal to electrical form and then inverse operations like removal of cyclic prefix, N-point DST, and then demapping are performed to transmit the data to the desired destination. In particular, the obtained real and positive-valued time-domain signals for both the scenarios i.e., DST-DCO-OFDM and DST-ACO-OFDM as represented by (3.15) and (3.19) are passed through the channel comprising of channel impulse response $h(n)$. Furthermore, the received electrical time-domain signal can be expressed as:

$$y(n) = R \underset{Unipolar}{x(n)} \circledast h(n) + w(n) \tag{3.20}$$

(3.20) can be solved to attain

$$y(n) = \sum_{l=0}^{L-1} \underset{Unipolar}{x(n-l)} h(l) + w(n) \tag{3.21}$$

L in (3.21) represents the total number of paths, and in general for a VLC system, the channel environment is modeled taking into consideration both the LOS and NLOS scenarios. The details of channel modeling is given in chapter 2. It is to be noted that, while dealing with DST-DCO-OFDM all of the subcarriers are utilized and the corresponding frequency-domain signal is passed through the BPSK/M-PAM demapping blocks for the purpose of recovering the data signal. Whereas, in case of DST-ACO-OFDM system, since only odd subcarriers are modulated, the data is extracted corresponding to the odd subcarrier positions.

3.4 Statistical Characterization of DCO-OFDM system

In this section, we statistically characterize the DCO-OFDM system exploiting DCT i.e., FOOFDM system, the same phenomena holds good for DST-DCO-OFDM system. Principally, for any choice of subcarrier number, an FOOFDM symbol (in general, a DCO-OFDM symbol) can be treated as the sum of a group of identically, independent distributed (i.i.d) samples. By utilizing central limit theorem, the FOOFDM symbol approximately becomes Gaussian. The mean of the FOOFDM symbol is equal to zero. The FOOFDM signal $s\left(n\right)$ can be modeled as an independent and identically distributed (i.i.d.) Gaussian process with probability density function (PDF) $P_{DCO}\left(s\right)$ which is given as

$$P_{DCO}\left(s\right) = N\left(s;\beta_{DC},\sigma^2\right) \tag{3.22}$$

Where $N(s;\beta_{DC},\sigma^2)$ is Gaussian and is given as

$$N\left(s;\beta_{DC},\sigma^2\right) = \frac{1}{\sqrt{2\pi\sigma^2}}e^{-\frac{\left(s-\beta_{DC}\right)^2}{2\sigma^2}} \tag{3.23}$$

The optical power is given as

$$\underset{optical}{P_{DCO}}\left(s\right) = \int_{-\infty}^{\infty} sP_{DCO}\left(s\right)ds \tag{3.24}$$

Upon substitution of (3.23) into (3.24)

$$\underset{optical}{P_{DCO}}\left(s\right) = \int_{0}^{\infty} s\frac{1}{\sqrt{2\pi\sigma^2}}e^{-\frac{\left(s-\beta_{DC}\right)^2}{2\sigma^2}}ds \tag{3.25}$$

Solving for the terms in integral by assuming $\frac{s-\beta_{DC}}{\sigma} = t$, then equation (3.25) reduces to

$$\underset{optical}{P_{DCO}}\left(s\right) = \frac{\sigma}{\sqrt{2\pi\sigma^2}}\int_{-\frac{\beta_{DC}}{\sigma}}^{\infty}\left(\sigma t+\beta_{DC}\right)e^{-\frac{t^2}{2}}dt \tag{3.26}$$

(3.26) can be further solved to attain

$$P_{\underset{optical}{DCO}}\left(s\right)=\frac{\sigma}{\sqrt{2\pi}}\int_{-\frac{\beta_{DC}}{\sigma}}^{\infty}te^{-\frac{t^2}{2}}dt+\frac{\beta_{DC}\sigma}{\sqrt{2\pi\sigma^2}}\int_{-\frac{\beta_{DC}}{\sigma}}^{\infty}e^{-\frac{t^2}{2}}dt \tag{3.27}$$

The integral in the first term of (3.27) can be solved by assuming $t^2=u$

$$P_{\underset{optical}{DCO}}\left(s\right)=\frac{\sigma}{\sqrt{2\pi}}\int_{\left(\frac{\beta_{DC}}{\sigma}\right)^2}^{\infty}\frac{1}{2}e^{-\frac{u}{2}}du+\beta_{DC}\frac{1}{\sqrt{2\pi}}\int_{-\frac{\beta_{DC}}{\sigma}}^{\infty}e^{-\frac{t^2}{2}}dt \tag{3.28}$$

Upon solving the integral in the first term and by writing the integral in the second term by means of Q-function as

$$Q\left(z\right)=\frac{1}{\sqrt{2\pi}}\int_{z}^{\infty}e^{-\frac{x^2}{2}}dx \tag{3.29}$$

Thus, the optical power in (3.28) can be obtained as

$$P_{\underset{optical}{DCO}}\left(s\right)=\frac{\sigma}{\sqrt{2\pi}}e^{-\frac{\beta_{DC}^2}{2\sigma^2}}+\beta_{DC}Q\left(-\frac{\beta_{DC}}{\sigma}\right) \tag{3.30}$$

When less amount of bias β_{DC} is added, i.e., when β_{DC} is small, then it results in clipping of lots of signal power, thereby leading to the emanation of clipping noise. Therefore, in order to overcome clipping noise, β_{DC} should be large enough. So, when β_{DC} is sufficiently large enough, then the optical power as represented in (3.30) is approximately equal to β_{DC}. Then,

$$P_{\underset{optical}{DCO}}\left(s\right)\sim\beta_{DC} \tag{3.31}$$

From (3.31), it is obvious that the optical power increases with the increase in added bias value. Thereby, this corresponds to reduction in power efficiency. Thus, it is vital to reduce the amount of PAPR in such systems.

3.5 PAPR analysis in DCT/DST-based multicarrier system

3.5.1 DCT-Spread-FOOFDM

The proposed DCT Spread (DCT-S) FOOFDM system incorporates the DCT algorithm for multiplexing and demultiplexing. DCT is a real trigonometric transform with an eminent energy concentration property and satisfies the requirements of IM/DD system by fetching a real output signal. It is imperative that, spreading the input sequence can effectively reduce the PAPR to the level of a single carrier transmission system [173], [174].

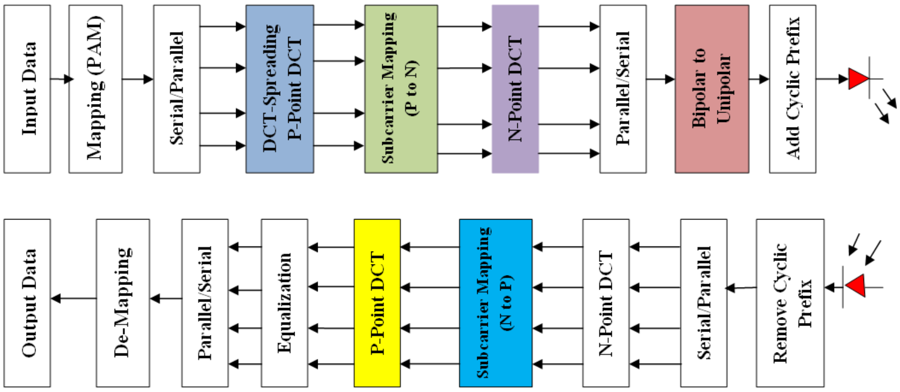

Figure 3.4: DCT-Spread FOOFDM for VLC

The schematic representation of DCT-S-FOOFDM is delineated in Fig. 3.4. While, working with the IM/DD system it is obligatory for the time domain signal to be both real and unipolar. A real signal can be obtained by enabling the DCT transform, but the obtained signal cannot be assured for its unipolarity. So, in order to transform this real bipolar signal to real unipolar signal emphasizes the dependency on ACO-OFDM methodology. Fig. 3.4, clearly illustrates that, at the transmitting end, the incoming bit stream of data is parallelized and then mapped using real constellation technique such as M-PAM. The obtained symbols are passed through the P-point DCT to accomplish the DCT-S-FOOFDM.

Let the output of the P-point DCT be defined as

$$x_m = \sqrt{\frac{2}{P}} \sum_{p=0}^{P-1} C_p X_p cos\left(\frac{\pi\left(2m+1\right)p}{2P}\right), \; 0 \leq m \leq P-1 \tag{3.32}$$

Here, it should be noted that x_m is assigned to odd subcarriers of N-point DCT operation i.e., $N = 2P$. The representation can be treated as a vector of the form

$$\boldsymbol{Y} = [0, x_0, 0, x_1, \cdots x_{m-1}] \tag{3.33}$$

On performing the N-point DCT operation, the generated FOOFDM sequence Y_i can be expressed as:

$$\begin{aligned} Y_i &= \sqrt{\frac{2}{2P}} C_i \sum_{h=0}^{2P-1} y_h cos\left(\frac{\pi\left(2h+1\right)i}{4P}\right) \\ &= \sqrt{\frac{1}{P}} C_i \sum_{j=0}^{P-1} y_{2j+1} cos\left(\frac{\pi\left(2\left(2j+1\right)+1\right)i}{4P}\right) \end{aligned} \tag{3.34}$$

From (3.33), $y_{2j+1} = x_j$ [175]. So, on substitution in (3.34) yields

$$Y_i = \sqrt{\frac{1}{P}} C_i \sum_{j=0}^{P-1} x_j cos\left(\frac{\pi\left(4j+3\right)i}{4P}\right) \tag{3.35}$$

Where,

$$x_j = \sqrt{\frac{2}{P}} \sum_{p=0}^{P-1} C_p X_p cos\left(\frac{\pi\left(2j+1\right)p}{2P}\right) \tag{3.36}$$

Upon substituting (3.36) in (3.35), the output sequence is obtained as

$$Y_i = \frac{\sqrt{2}}{P} C_i \sum_{j=0}^{P-1} \sum_{p=0}^{P-1} C_p X_p cos\left(\frac{\pi\left(2j+1\right)p}{2P}\right) cos\left(\frac{\pi\left(4j+3\right)i}{4P}\right) \tag{3.37}$$

On solving (3.37), we get

$$\begin{aligned} Y_i = \frac{1}{\sqrt{2}P} C_i \sum_{j=0}^{P-1} \sum_{p=0}^{P-1} C_p X_p \Big[& cos\left(\frac{4\pi\left(i-p\right)j + \pi\left(3i-2p\right)}{4P}\right) + \\ & cos\left(\frac{4\pi\left(i+p\right)j + \pi\left(3i+2p\right)}{4P}\right)\Big] \end{aligned} \tag{3.38}$$

The negative components in Y_i are clipped to zero to yield a unipolar real valued signal $\underset{unipolar}{y}$ given as

$$\underset{unipolar}{y} = \begin{cases} Y_i, & Y_i > 0 \\ 0, & Y_i \leq 0 \end{cases} \tag{3.39}$$

In order to prevent the ISI, cyclic prefix is inserted at a rate of $\frac{1}{4}$th of the subcarriers size. Then this, time domain real valued and unipolar signal is transmitted using optical channel. At, the receiver inverse operations are performed to ensure perfect recovery of the transmitted data stream. Few such operations are removal of cyclic prefix, N-Point DCT, P-Point DCT, de-mapping etc. Since, the cyclic prefix/guard interval converts the linear convolution of the FOOFDM signal with the channel into circular convolution, so a fundamental frequency domain equalizer like zero-forcing can be employed.

Complementary Cumulative Distribution Function (CCDF) for PAPR: The PAPR is generally the ratio between the maximum peak power and the average power of the discretized OFDM signal and is represented as

$$PAPR = 10log_{10}\left(\frac{Max\left\{\left|\underset{unipolar}{y}\right|^2\right\}}{E\left\{\left|\underset{unipolar}{y}\right|^2\right\}}\right) \tag{3.40}$$

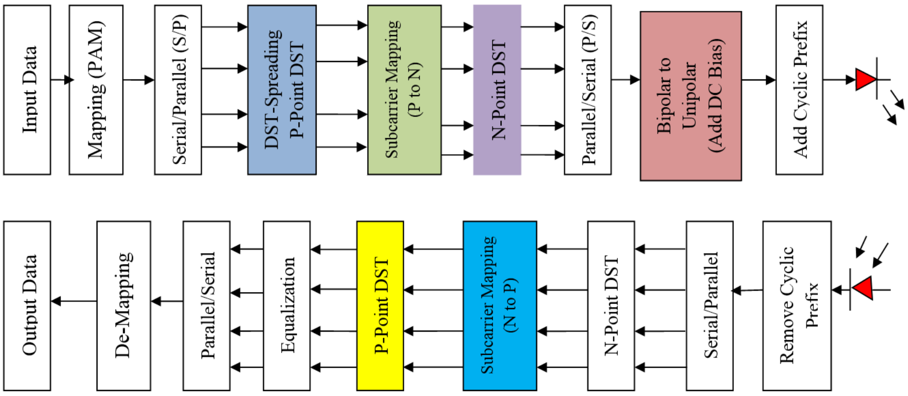

Figure 3.5: DST-Spread-DCO-OFDM (DST-S-DCO-OFDM) system for VLC

From (3.40), $E\{\}$ denotes the Expectation operator. One is familiar that, CCDF is used for evaluating the probability that PAPR of a particular OFDM time-domain symbol exceeds a certain value of threshold PAPR$_0$ which is given as

$$CCDF = Pr\left(PAPR > PAPR_0\right) \tag{3.41}$$

3.5.2 DST-based Spreading technique for PAPR reduction in DST-DCO-OFDM system

Since, the addition of DC bias in DCO-OFDM system has resulted it is a power-inefficient scheme, hence, there is a necessity to reduce the amount of PAPR in DCO-OFDM system. Consequently, this work enforces the PAPR reduction techniques to DST-based DCO-OFDM system. The block diagram of DST-based spreading in DST-based DCO-OFDM system is represented in Fig. 3.5. In contrast to Hermitian Symmetry imposed IFFT and FFT, this system incorporates the DST transformation module for both multiplexing and de-multiplexing. The M-PAM mapped data is loaded into the P-point DST block to accomplish the DST-Spreading operation. Therefore, the output of the P-point DST can be expressed as

$$x_m = \sqrt{\frac{2}{P}} \sum_{p=0}^{P-1} X_p sin\left[\frac{\pi\left(2m+1\right)\left(2p+1\right)}{4P}\right], 0 \leq m \leq P-1 \tag{3.42}$$

Since, DCO-OFDM methodology is incorporated to fetch a positive signal, it should be noted that all of the subcarriers are involved in data transmission i.e., x_m is assigned to all of the subcarriers of N-point DST. Therefore, this can be mathematically represented as

$$\boldsymbol{y} = [x_0, x_1, x_2, x_3, \cdots x_{P-1}] \tag{3.43}$$

Accordingly, after computation of N-point DST, the output signal appears like

$$Y_i = \sqrt{\frac{2}{N}} \sum_{h=0}^{N-1} y_h sin\left[\frac{\pi\left(2h+1\right)\left(2i+1\right)}{4N}\right] \tag{3.44}$$

From (3.43), we can tell $N = P$ and $y_h = x_h$ as all of the subcarriers are involved for transmission of data. Hence, (3.44) can be modified as

$$Y_i = \sqrt{\frac{2}{P}} \sum_{h=0}^{P-1} x_h sin\left[\frac{\pi\left(2h+1\right)\left(2i+1\right)}{4P}\right] \tag{3.45}$$

x_h can be expressed as

$$x_h = \sqrt{\frac{2}{P}} \sum_{p=0}^{P-1} X_p sin\left[\frac{\pi\left(2h+1\right)\left(2p+1\right)}{4P}\right] \tag{3.46}$$

The final DST-S-DCO-OFDM signal can be obtained by substituting (3.46) into (3.45).

$$Y_i = \frac{2}{P} \sum_{h=0}^{P-1} \sum_{p=0}^{P-1} X_p sin\left[\frac{\pi\left(2h+1\right)\left(2p+1\right)}{4P}\right] sin\left[\frac{\pi\left(2h+1\right)\left(2i+1\right)}{4P}\right] \tag{3.47}$$

Using simple trigonometric inequalities, (3.47) can be reduced to

$$Y_i = \frac{1}{P} \sum_{h=0}^{P-1} \sum_{p=0}^{P-1} X_p cos\left[\frac{\pi\left(2h+1\right)2\left(i-p\right)}{4P}\right] - \frac{1}{P} \sum_{h=0}^{P-1} \sum_{p=0}^{P-1} X_p cos\left[\frac{\pi\left(2h+1\right)2\left(i+p\right)}{4P}\right] \tag{3.48}$$

The obtained signal as depicted in (3.48) cannot be assured of its positivity. Therefore, as stated earlier, in order to attain a positive signal some amount of DC bias is added.

$$\underset{Tx}{Y_i} = Y_i + \beta_{DC} \tag{3.49}$$

Finally, PAPR is computed to this transmitted time-domain signal which is denoted as $\underset{Tx}{Y_i}$. The PAPR of the time-domain signal is given as the ratio of the maximum peak power to average power.

$$PAPR = 10log_{10}\left(\frac{Max\left\{\left|\underset{Tx}{Y_i}\right|^2\right\}}{E\left\{\left|\underset{Tx}{Y_i}\right|^2\right\}}\right) \tag{3.50}$$

3.5.3 Exploitation of PTS technique in DCT/DST-based optical OFDM

In general, PTS is one of the multiple signalling and probabilistic technique which is widely employed in RF-based traditional OFDM system to reduce the amount of PAPR. The basic principle methodology involved behind the implementation of PTS technique is that the incoming huge stream of data is partitioned into sub-blocks before getting applied to the transformation module i.e., the transformation operation is computed individually to each subblock and then weighted by a phase factor. However, this technique is incorporated to reduce the levels of PAPR in DCT and DST-based optical OFDM system in accordant with IM/DD systems and is elucidated in Fig. 3.6 and 3.7. In order to show the difference between the mathematical expressions, we have enforced PTS technique to DCT-based ACO-OFDM and DST-based DCO-OFDM system.

PTS technique in DCT-based ACO-OFDM system

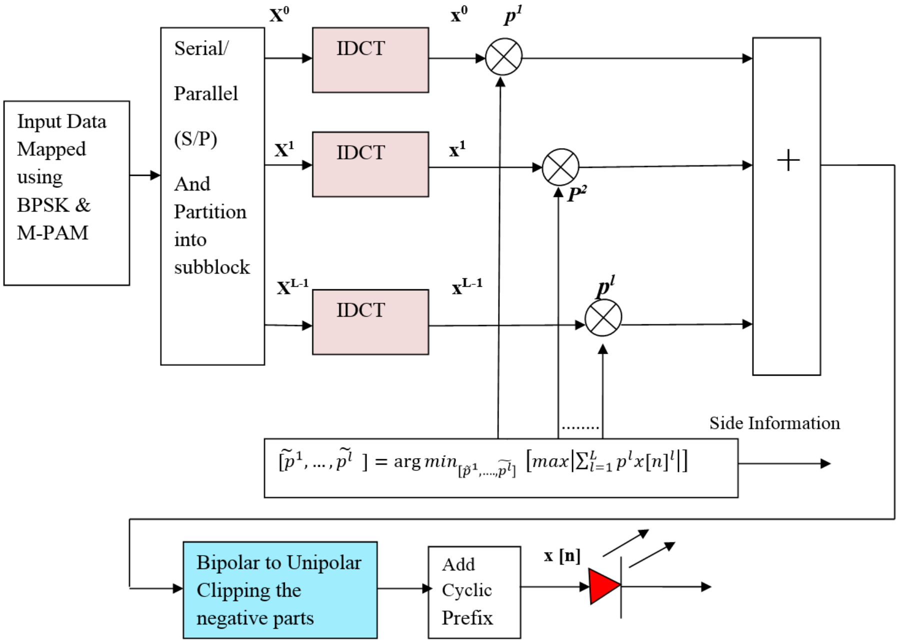

Figure 3.6: PAPR reduction in FOOFDM using Partial Transmit Sequence (PTS)

The schematic representation of FOOFDM VLC transmitter employing conventional PTS technique for PAPR reduction is illustrated in Fig. 3.6. The serialized BPSK/M-PAM mapped data stream is parallelized and then partitioned into L disjoint subblocks of equal size in a manner as depicted in (3.51).

$$\boldsymbol{X} = \left[\boldsymbol{X^{0}}, \boldsymbol{X^{1}}, \boldsymbol{X^{2}}, \boldsymbol{X^{3}}, \cdots \boldsymbol{X^{L-1}}\right]^{T} \tag{3.51}$$

Similar to ACO-OFDM methodology, the arrangement in each subblock $\boldsymbol{X^{l}}$ for $0 \leq l \leq L-1$ is made in such a way that only odd subcarriers are modulated setting the even subcarriers to zero. So, if there are N subcarriers only $\frac{N}{2}$ are utilized due to inclusion of odd subcarriers. Hence, the representation looks like

$$\boldsymbol{X}^{l}_{PTS} = \left[\left\{\boldsymbol{X}^{l}_{PTS}\left[1\right]\right\}, 0, \left\{\boldsymbol{X}^{l}_{PTS}\left[3\right]\right\}, 0, \cdots \left\{\boldsymbol{X}^{l}_{PTS}\left[\frac{N}{2}-1\right]\right\}\right]^{T} \tag{3.52}$$

Therefore, this signal is fed to the input of the IDCT to yield the time-domain signal which can be expressed as

$$\underset{DCT-ACO}{x^{l}_{PTS}\left[n\right]} = \sum_{l=0}^{L-1}\left\{\sqrt{\frac{2}{N}}\sum_{k=0}^{\frac{N}{2}-1} C^{l}\left[k\right] X^{l}_{PTS}\left[k\right] cos\left(\frac{\pi\left(2n+1\right)k}{2N}\right)\right\} \tag{3.53}$$

The obtained time-domain signal $\boldsymbol{x}^{l}_{PTS}\left[n\right]$ is phase rotated independently by getting multiplied with the corresponding complex phase factor $p^{l} = e^{j\phi_{l}}$ where $l = 0, 1, 2, 3, \cdots L-1$ and $\phi_{l} = [0, 2\pi)$ to yield the combined time-domain signal with the lowest PAPR as follows:

$$\widetilde{x_{PTS}} = \sum_{l=0}^{L-1} p^{l} \underset{DCT-ACO}{x^{l}_{PTS}\left[n\right]} \tag{3.54}$$

Therefore, the PAPR of the transmitted signal is given as

$$PAPR = 10log_{10}\left(\frac{Max\left\{\left|\widetilde{x_{PTS}}\right|^{2}\right\}}{E\left\{\left|\widetilde{x_{PTS}}\right|^{2}\right\}}\right) \tag{3.55}$$

Finally, the composite time-domain real and bipolar signal is transformed into a pure real and unipolar signal by clipping the negative components. After addition of cyclic prefix and then this parallel data stream is serialized and then intensity modulated through the LED. Here, the phase vector is chosen in a manner to minimize the PAPR of the combined time-domain signal obtained from all subblocks. This is given by the following representation

$$\left[\tilde{p}^{1}, \tilde{p}^{2}, \cdots \tilde{p}^{l}\right] = \underset{\left[\tilde{p}^{1}, \tilde{p}^{2}, \cdots \tilde{p}^{l}\right]}{arg\ min}\left(\underset{0,1,2,\cdots N-1}{max}\left|\sum_{l=0}^{L-1} p^{l} \underset{DCT-ACO}{x^{l}_{PTS}\left[n\right]}\right|\right) \tag{3.56}$$

Generally, the selection of phase vectors $\left\{p^l\right\}_{l=0}^{L-1}$ is limited to a finite set of elements for reducing the search complexity. Let these set of allowed phase vectors be defined as

$$\boldsymbol{p^l} = e^{\frac{j2\pi q}{W}}, for\ q = 0, 1, 2, \cdots W-1 \tag{3.57}$$

In (3.57), the total number of allowed phase vectors is denoted by W. If the first phase factor p^1 is set to 1, without any loss of information, then there are a total of $L-1$ phase factors to be found by exhaustive search. Therefore, a total of W^{L-1} sets of phase factors are to be searched to find the optimum one. It is to be taken into consideration that the amount of PAPR reduction has got a direct relationship between the phase factors W and the number of subblocks L. So here, it could be evidenced that, with the increase in the number of subblocks, the PAPR of the overall system decreases significantly but at the expense of exponential increase in search complexity. Moreover, L number of IDCT's are involved for each data subblock so, it requires $log_2 W^{L-1}$ bits of side information to be transmitted.

In order to reduce the amount of PAPR as well as to substantially reduce the search complexity of the phase vectors, a sub-optimal way of choosing the phase factors is proposed in the literature. Accordingly, all the phase factors are initially set to 1 followed by the computation of PAPR. It is to be noted that, p^1 remains 1 and the values of other phase factors are chosen among W possible sets. Then in the next iteration, the second phase factor is changed to p^2 and then PAPR is computed. Therefore, if the PAPR computed upon choosing p^2 is less than the previous one, then this phase factor is chosen as the part of the final set of phase factors. This procedure repeats until all the phase factors are explored.

The computational complexity incurred with the imposition of DCT when compared with Hermitian Symmetry-based DFT is quite less. This is because, DCT requires less number of multiplications and additions when compared with DFT. The computational analysis is summarized in Table. 3.1

Table 3.1: Comparison of Computational Complexity [176]

Transform	**Additions**	**Multiplications**
DCT	$(3Nlog_2N-2N+2)/2$	$Nlog_2N/2$
DFT	$3Nlog_2N-3N+4$	$Nlog_2N-3N+4$

From the table it is evident that, DFT requires ${}^{(3Nlog_2N)}/_2 - 2N + 3$ more number of additions and ${}^{(Nlog_2N)}/_2 - 3N + 4$ more number of multiplications than that of the DCT. Moreover, for PAPR reduction using PTS, every subblock should imbibe the Hermitian Symmetry criteria to meet the requirements of IM/DD systems. Eventually, this incurs a lot of additional complexity overhead.

Hence, this necessitates to stress on real transformation techniques like DCT and DST.

PTS technique in DST-based DCO-OFDM system

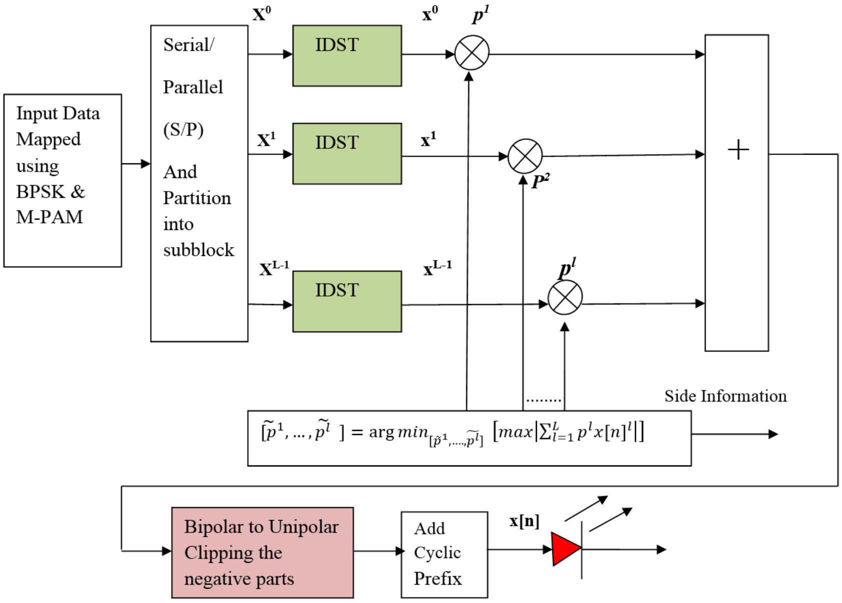

Figure 3.7: PAPR reduction in DST-DCO-OFDM system using PTS

As evident from the figure, the incoming huge stream of mapped data is partitioned into L disjoint subblocks as delineated in (3.51). In particular, these sub-blocks $\boldsymbol{X}^l$ where l lies in the interval $0 \leq l \leq L-1$ are of equal size and are sequentially located. Now, IDST operation is computed individually for each sub-block to attain the time-domain signal and the mathematical representation looks as follows:

$$\underset{DST-DCO}{x^l_{PTS}}[n] = \sum_{l=0}^{L-1}\left\{\sqrt{\frac{2}{N}}\sum_{k=0}^{N-1}\boldsymbol{X}^l_{PTS}[k]\, sin\left[\frac{\pi\,(2n+1)\,(2k+1)}{4N}\right]\right\} n = 0,1,2,3,\cdots N-1 \tag{3.58}$$

Now, signal scrambling is applied individually to each sub-block, i.e., each block of time-domain signal as depicted in (3.58) is individually weighted by a phase factor. Therefore, the representation looks like

$$\widetilde{x_{PTS}} = \sum_{l=0}^{L-1} p^l \, x^l_{\underset{DST-DCO}{PTS}}[n] \tag{3.59}$$

The primary motive of PTS technique is to reduce the PAPR of the combined time-domain signal as represented in (3.59), by carefully selecting the phase factors which is given mathematically as

$$\left[\tilde{p}^1, \tilde{p}^2, \cdots \tilde{p}^l\right] = \underset{\left[\tilde{p}^1, \tilde{p}^2, \cdots \tilde{p}^l\right]}{arg\ min} \left(\underset{0,1,2,\cdots N-1}{max} \left| \sum_{l=0}^{L-1} p^l \, x^l_{\underset{DST-DCO}{PTS}}[n] \right| \right) \tag{3.60}$$

The selection of the phase vectors is detailed in the previous sub-section i.e., PTS technique for DCT-ACO-OFDM system. The rest of the operations like addition of DC bias to assure the signal positivity as well as to prevent ISI, suitable amount of cyclic prefix is added. Finally, this low PAPR signal is intensity modulated through the LED. Thanks to the real transformation techniques like DCT/DST which relieves the burden of Hermitian Symmetry imposed IFFT sub-blocks.

3.5.4 Clipping and Filtering

This is one of the fundamental signal distortion technique where the highest peaks of the FOOFDM signal/DST-based optical OFDM signal are clipped. But, in doing so, this induces both in-band and out-of-band distortions. Generally, clipping can be associated as a non-linear process, where the former distortion leads to a significant decrease in the BER performance, while the latter leads to spectral spreading. However, out-of-band distortion can be reduced by filtering, but at the expense of increase in peak power growth. In this work, we have assimilated this technique in conventional FOOFDM system as well as DST-based DCO-OFDM system for comparing with DCT-Spread FOOFDM (DCT-S-FOOFDM) and DST-Spread DCO-OFDM system.

The fundamental principle behind this clipping and filtering is that clipping the optical OFDM signal will lead the entire clipping noise to fall in-band and becomes a tedious task to remove it by filtering. Hence, in order to combat such effects, oversampling the optical OFDM signal is imperative. In this work, we have evaluated the system performance by P times oversampling the optical OFDM signal. Therefore, the resultant time-domain signal at the output of IDCT in case of FOOFDM system can be proclaimed as

$$x_m^{'} = \underset{FOOFDM}{x_m^{'}} = \sqrt{\frac{2}{PN}} \sum_{k=0}^{PN-1} C_k X_k^{'} cos\left(\frac{\pi\left(2m+1\right)k}{2PN}\right) \tag{3.61}$$

While, the time-domain signal corresponding to DST-based DCO-OFDM system is given as

$$x_m^{'} = \underset{DST-DCO}{x_m^{'}} = \sqrt{\frac{2}{PN}} \sum_{k=0}^{PN-1} X_k^{'} sin\left[\frac{\pi\left(2m+1\right)\left(2k+1\right)}{4PN}\right], \qquad m = 0,1,2,3,\cdots PN-1 \tag{3.62}$$

where $x_m^{'}$ in (3.61) and (3.62) represents the discretized time-domain of FOOFDM and DST-DCO-OFDM signal and P denotes the oversampling factor. In this work, oversampling is implemented by affixing $N.\left(P-1\right)$ zeros in the frequency domain.

Since, the physical characteristics of opto-electronic devices oblige the VLC system to exploit IM to drive the LED, subsequently, this necessitates the transmitted signal to be both real and unipolar. Hence, in this scenario a desired amount of upper clipping and lower clipping followed by the addition of DC bias to fetch a unipolar signal is illustrated mathematically as given below.

$$\underset{clip}{x_m^{'}} = \begin{cases} A_u, & if\ x_m^{'} \geq A_u \\ x_m^{'}, & -A_l < x_m^{'} < A_u \\ -A_u, & if\ x_m^{'} \leq -A_l \end{cases} \tag{3.63}$$

where A_u and A_l in (3.63) denote the upper and lower clipping level respectively. Therefore, the upper and lower clipping ratios can be defined as

$$Upper\ Clipping\ Ratio = \frac{A_u^2}{\sigma^2} \tag{3.64}$$

$$Lower\ Clipping\ Ratio = \frac{A_l^2}{\sigma^2} \tag{3.65}$$

where σ^2 is the variance of the time domain signal. The simulated results evidences a significant decrease in PAPR by incorporation of this technique, but the decrease is not predominant when compared with DCT-Spreading in FOOFDM system as well as DST-Spreading in DST-DCO-OFDM system.

3.6 Optical Orthogonal Frequency Division Multiple Access (OOFDMA)

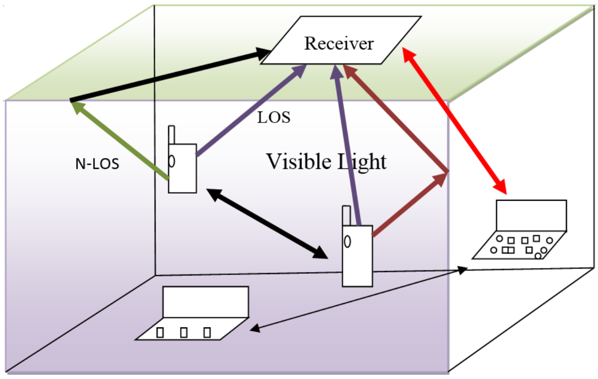

Figure 3.8: Illustration of Uplink scenario using Visible Light

Fig. 3.8, interprets an uplink transmission scenario using visible light in an indoor environment emphasizing that the channel consists of both LOS as well as NLOS components. This growing technology like VLC provides the flexibility for creation of a small scale communication network in an indoor room environment where each installed LED can act as a base station rendering services to multiple mobile terminals which are within the vicinity of LED lighting fixtures. In this regard, it is vital to exploit multiple access schemes for imparting high data rate communication. OFDM is one straightforward technique which is easily reconcilable with multiple access schemes giving rise to OFDMA. While, exploiting OFDMA to optical domain, it can be called as optical OFDMA (OOFDMA).

It is imperative that, in case of OFDMA system, the subcarriers are partitioned and are assigned to multiple mobile users. In precise, OFDMA facilitates the subcarriers belonging to each OFDM symbol to be divided orthogonally among multiple users. However, OFDMA waveform exhibits rapid envelope fluctuations resulting in high amount of PAPR. Therefore, in order to reduce the amount of PAPR in a multicarrier system, SC-FDMA can be expedited for the reduction of PAPR. This is implemented by enforcing M-point DFT spreading before the N-point IDFT operation at the transmitting end. In case of SC-FDMA, each of the terminal in the uplink employ a certain set of subcarriers to transmit its own data. While, the subcarriers which are not involved in data transmission will be filled with zeros. Further, upon incorporating DFT-Spreading, there exists different ways of allocating subcarriers to a specific user. Based upon the way of this assignment of subcarriers to each terminal there is a profound effect in PAPR reduction. Accordingly, the most remarkable ones are:

- IFDMA
- LFDMA

Interleaved Frequency Division Multiple Access

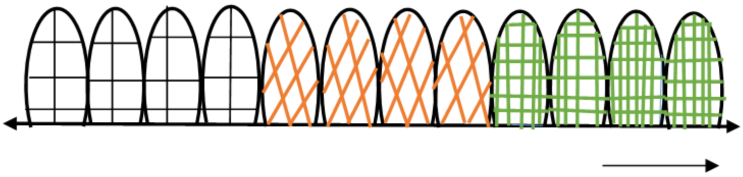

Localized Frequency Division Multiple Access

Figure 3.9: Different mapping strategies

Fig. 3.9. portrays the allocation of subcarriers to different users. In order to clearly illustrate the subcarrier mapping strategies, this figure employs 3 users, the sizes of N and M are 12 and 4 respectively. While, the spreading factor S is 3. The detailed derivations of the mathematical expressions relevant to these multiple access strategies will be given in the subsequent sections. In order to emphasize the benefits of enforcing real trigonometric transforms like DCT and DST to the aforesaid multiple access schemes, we carried out derivations of mathematical expressions pertaining to the Hermitian Symmetry imposed IFFT based multiple access schemes like DFT-OIFDMA, DFT-OLFDMA.

3.6.1 DST-based Multiple access schemes

The scenario of uplink transmission employing DST-based spreading in optical IFDMA/LFDMA (OIFDMA/OLFDMA) is delineated in Fig. 3.10. As evident from the figure, real modulation formats like BPSK and M-PAM are utilized to map the huge

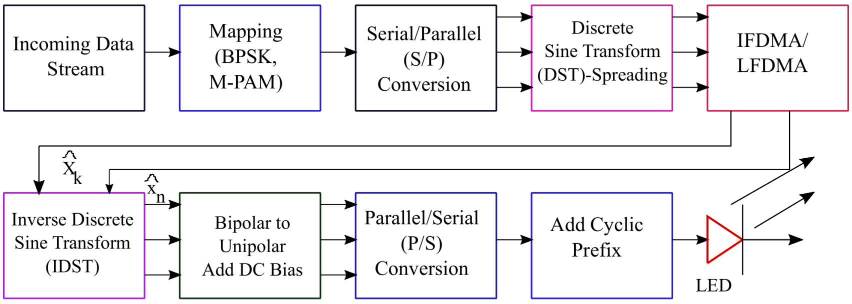

Figure 3.10: Illustration of Uplink transmission employing DST-Spreading in optical IFDMA/LFDMA (OIFDMA/OLFDMA)

stream of input data. In general, a S/P converter is employed to transmit these sets of modulated symbols in parallel. Then predominantly, this set of data is DST-spread by using M-point DST to obtain the frequency domain representation of the input data. Followed up by mapping, IFDMA and LFDMA subcarrier mapping strategies are exploited as illustrated in Fig. 3.11 and 3.12 respectively. In precise, the outputs of the DST are mapped to the N-point IDST where ($N > M$).

DST-OIFDMA:

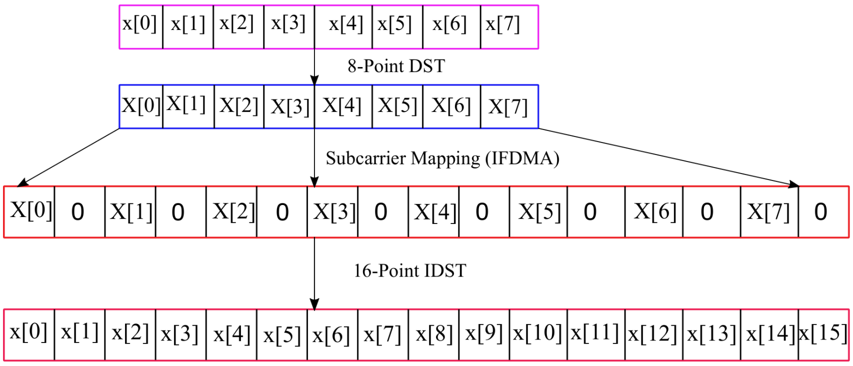

Figure 3.11: Signal Format depicting optical IFDMA (OIFDMA) mapping strategy.

Fig. 3.11 represents the subcarrier mapping utilizing 8-point DST and 16-point IDST. It is to be noted that, the outputs of DST are allocated in an equidistant manner as $\frac{N}{M} = S$, where S represents the bandwidth spreading factor. Therefore, mathematically this can be represented as [177]

$$\tilde{X}\left[k\right] = \begin{cases} X\left[\frac{k}{S}\right], & k = Sm_1, \quad m_1 = 0, 1, 2, 3, \cdots M-1 \\ 0, & Otherwise \end{cases} \tag{3.66}$$

Where $\tilde{X}\left[k\right]$ specifies the input of the IDST module and the output sequence of IDST which is denoted as $\tilde{x}\left[n\right]$ with $n = Ms + m$ for $s = 0, 1, 2, 3, \cdots S - 1$ and $m = 0, 1, 2, 3, \cdots M - 1$ can be formulated as

$$\tilde{x}\left[n\right] = \sqrt{\frac{2}{N}} \sum_{k=0}^{N-1} \tilde{X}\left[k\right] sin \left[\frac{\pi\left(2n+1\right)\left(2k+1\right)}{4N}\right] \tag{3.67}$$

Upon substitution of the aforementioned conditions, the following expression is attained

$$\tilde{x}\left[n\right] = \sqrt{\frac{2}{SM}} \sum_{m_1=0}^{M-1} X\left[m_1\right] sin \left[\frac{\pi\left(2Ms+2m+1\right)\left(2Sm_1+1\right)}{4MS}\right] \tag{3.68}$$

(3.68) can be further rearranged to obtain the resultant expression as

$$\tilde{x}\left[n\right] = \frac{1}{\sqrt{S}}\sqrt{\frac{2}{M}} \sum_{m_1=0}^{M-1} X\left[m_1\right] sin \Big[\frac{\pi\left(2m+1\right)m_1}{2M} + \frac{\pi\left(2\left(m+Ms\right)+1\right)}{4MS} + \pi k\Big] \tag{3.69}$$

Further, (3.69) can be solved to yield (taking into consideration that $sin\ \pi k = 0$)

$$\tilde{x}\left[n\right] = \frac{1}{\sqrt{S}}\sqrt{\frac{2}{M}} \sum_{m_1=0}^{M-1} X\left[m_1\right] sin \left[\frac{\pi\left(2m+1\right)m_1}{2M} + \frac{\pi\left(2\left(m+Ms\right)+1\right)}{4MS}\right] \times cos\ \pi k \tag{3.70}$$

Accordingly, the time-domain output signal can be derived as

$$\tilde{x}\left[n\right] = \begin{cases} \frac{1}{\sqrt{S}}\frac{2}{M} \sum_{m_1=0}^{M-1} X\left[m_1\right] sin \left[\frac{\pi(2m+1)m_1}{2M} + \frac{\pi(2(m+Ms)+1)}{4MS}\right] \left(-1\right)^k, \\ \quad if\ k\ is\ odd \\ \frac{1}{\sqrt{S}}\frac{2}{M} \sum_{m_1=0}^{M-1} X\left[m_1\right] sin \left[\frac{\pi(2m+1)m_1}{2M} + \frac{\pi(2(m+Ms)+1)}{4MS}\right], \\ \qquad if\ k\ is\ even \end{cases} \tag{3.71}$$

The rest of the analysis like addition of DC bias and cyclic prefix is stated in the earlier section. The achieved time-domain signal as shown in (3.71) is scaled by a factor of $\frac{1}{\sqrt{S}}$.

DST-OLFDMA:

In case of DST-OLFDMA, the DST outputs are allocated to M consecutive subcarriers out of N subcarriers of the IDST transformation block. The pictorial representation is depicted in Fig. 3.12. The input signal to the IDST block has got the following representation as [177]

$$\tilde{X}\left[k\right] = \begin{cases} X\left[k\right], & k = 0, 1, 2, 3, \cdots M - 1 \\ 0, & k = M, M+1, \cdots N - 1 \end{cases} \tag{3.72}$$

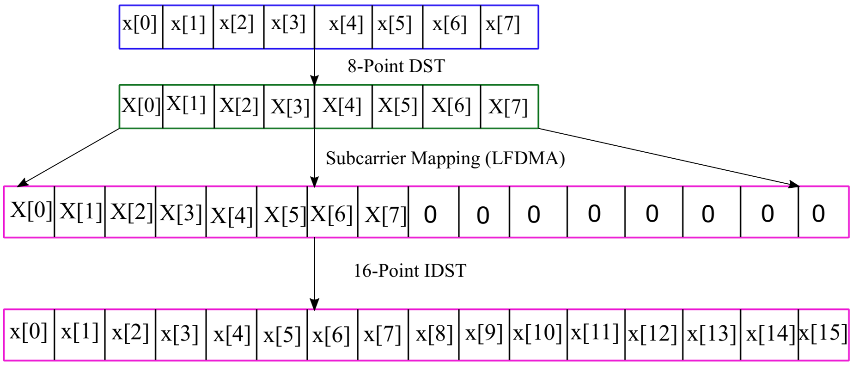

Figure 3.12: Signal Format depicting optical LFDMA (OLFDMA) mapping strategy.

The time-domain output sequence of the IDST transformation block which is denoted as $\tilde{x}\left[n\right]$ with $n = Sm + s$ for $s = 0, 1, 2, 3, \cdots S - 1$ can be represented as:

$$\tilde{x}\left[n\right] = \tilde{x}\left[Sm+s\right] = \sqrt{\frac{2}{MS}} \sum_{k=0}^{M-1} X\left[k\right] sin\left[\frac{\pi\left(2\left(Sm+s\right)+1\right)\left(2k+1\right)}{4MS}\right] \tag{3.73}$$

(3.73) can be further solved as

$$\tilde{x}\left[n\right] = \tilde{x}\left[Sm+s\right] = \sqrt{\frac{1}{S}}\sqrt{\frac{2}{M}} \sum_{k=0}^{M-1} X\left[k\right] sin\left[\frac{\pi S\left(2m+\frac{2s}{S}+\frac{1}{S}\right)\left(2k+1\right)}{4MS}\right] \tag{3.74}$$

We proceed to solve for two scenarios:

Case a: when $s = 0$, the output sequence can be obtained as

$$\tilde{x}\left[n\right] \; = \; \tilde{x}\left[Sm\right] \; = \; \frac{1}{\sqrt{S}}\sqrt{\frac{2}{M}} \sum_{k=0}^{M-1} X\left[k\right] sin\Big[\frac{\pi\left(2m+1\right)\left(2k+1\right)}{4M} - \frac{\pi\left(1-\frac{1}{S}\right)\left(2k+1\right)}{4M}\Big] \tag{3.75}$$

Further, (3.75) can be solved as

$$\begin{aligned} &\tilde{x}\left[n\right] = \tilde{x}\left[Sm\right] = \\ &\qquad \frac{1}{\sqrt{S}}\sqrt{\frac{2}{M}} \sum_{k=0}^{M-1} X\left[k\right] sin\left[\frac{\pi\left(2m+1\right)\left(2k+1\right)}{4M}\right] cos\left[\frac{\pi\left(1-\frac{1}{S}\right)\left(2k+1\right)}{4M}\right] - \\ &\qquad\quad \frac{1}{\sqrt{S}}\sqrt{\frac{2}{M}} \sum_{k=0}^{M-1} X_k cos\left[\frac{\pi\left(2m+1\right)\left(2k+1\right)}{4M}\right] sin\left[\frac{\pi\left(1-\frac{1}{S}\right)\left(2k+1\right)}{4M}\right] \end{aligned} \tag{3.76}$$

Case b: when $s \neq 0$, the output sequence can be derived as:

Let $X\left[k\right] = \sqrt{\frac{2}{M}} \sum_{p=0}^{M-1} x\left[p\right] sin\left[\frac{\pi(2p+1)(2k+1)}{4M}\right]$, then (3.74) can be solved as

$$\tilde{x}\left[Sm+s\right] = \sqrt{\frac{2}{MS}} \sum_{k=0}^{M-1} X\left[k\right] sin\left[\frac{\pi\left(2\left(Sm+s\right)+1\right)\left(2k+1\right)}{4MS}\right] \tag{3.77}$$

$$\tilde{x}[n] = \tilde{x}[Sm+s] = \sqrt{\frac{2}{MS}} \sum_{k=0}^{M-1} \left(\sqrt{\frac{2}{M}} \sum_{p=0}^{M-1} x[p]\, sin \left[\frac{\pi (2p+1)(2k+1)}{4M} \right] \right) \times \underbrace{sin \left[\frac{\pi (2Sm+2s+1)(2k+1)}{4MS} \right]}_{} \tag{3.78}$$

Therefore, in (3.78) the term under the brace can be rearranged to attain

$$sin \left[\frac{\pi \left(2m+\frac{1}{S}\right)(2k+1)}{4M} + \frac{\pi s (2k+1)}{2MS} \right] \tag{3.79}$$

Upon substituting in (3.78), the following time-domain signal is attained as

$$\begin{aligned} \tilde{x}[n] = \tilde{x}[Sm+s] = \frac{1}{\sqrt{S}} \frac{2}{M} \sum_{k=0}^{M-1} \sum_{p=0}^{M-1} x[p]\, sin \left[\frac{\pi (2p+1)(2k+1)}{4M} \right] \\ \times \Bigg[sin \left(\frac{\pi \left(2m+\frac{1}{S}\right)(2k+1)}{4M} \right) cos \left(\frac{\pi s (2k+1)}{2MS} \right) - \\ \Bigg[cos \left(\frac{\pi \left(2m+\frac{1}{S}\right)(2k+1)}{4M} \right) sin \left(\frac{\pi s (2k+1)}{2MS} \right) \Bigg] \Bigg] \end{aligned} \tag{3.80}$$

Therefore, the time-domain DST-OLFDMA signals as represented by (3.76) and (3.80) depicts that the time-domain signal is multiplied by additional weighing factors thereby contributing to the increase in PAPR when compared with DST-OIFDMA. This mathematical analysis is confirmed through simulation results.

3.6.2 Fast optical IFDMA (F-O-IFDMA) and Fast optical LFDMA (F-O-LFDMA)

In this section, the proposed uplink fast optical IFDMA (F-O-IFDMA) and fast optical LFDMA (F-O-LFDMA) transmitter block diagram along with the time-domain signal representation is presented. Fig. 3.13, illustrates the uplink transmitter employing DCT-Spreading for both the subcarrier mapping schemes i.e., interleaved and localized FDMA.

F-O-IFDMA

The M-PAM mapped data is spread using DCT and then allocated (subcarrier mapping) using (3.66). After subcarrier mapping, this sequence $\tilde{X}[k]$ is fed to the IDCT

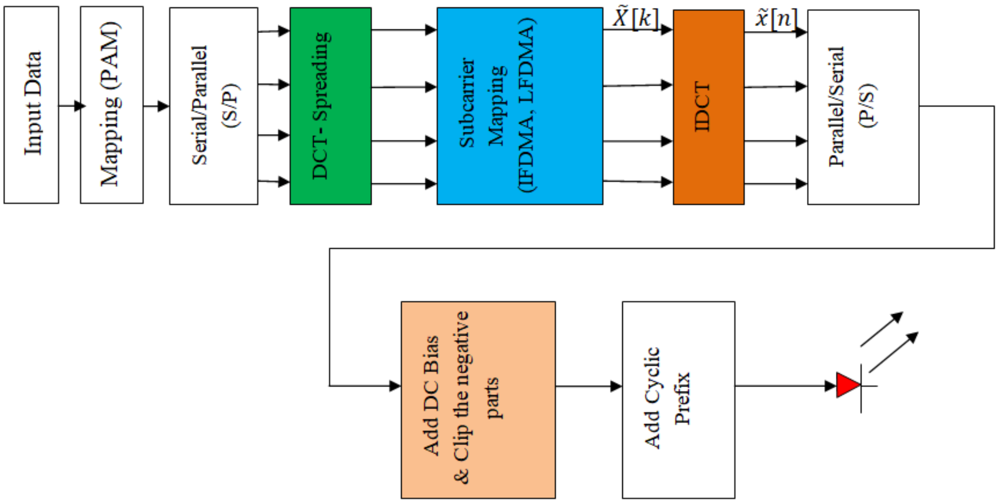

Figure 3.13: Uplink transmitter utilizing DCT-Spreading for F-O-IFDMA and F-O-LFDMA

to yield the time domain signal $\tilde{x}[n]$. The IDCT output sequence $\tilde{x}[n]$ with $n = Ms + m$ for $s = 0, 1, 2, 3 \cdots S - 1$ and $m = 0, 1, 2, 3, \cdots M - 1$ can be solved to attain as follows: Upon substitution of the subcarrier mapped sequence $\tilde{X}[k]$ as represented in (3.66) into (3.7) obtains

$$\tilde{x}[n] = \sqrt{\frac{2}{SM}} \Big[\sum_{m_1=0}^{M-1} C\left[\frac{k}{S}\right] X\left[\frac{k}{S}\right] cos\left(\frac{\pi(2Ms + 2m + 1)}{2N} k\right) \Big] \tag{3.81}$$

From (3.66), since, $k = Sm_1$ so, on substitution in (3.81), we obtain

$$\tilde{x}[n] = \frac{1}{\sqrt{S}} \sqrt{\frac{2}{M}} \Big[\sum_{m_1=0}^{M-1} C[m_1] X[m_1] cos\left(\frac{\pi(2(Ms + m) + 1) Sm_1}{2N}\right) \Big] \tag{3.82}$$

Further, since $S = \frac{N}{M}$ therefore, upon substitution in the argument value of the cosine term, equation (3.82) reduces to

$$\tilde{x}[n] = \frac{1}{\sqrt{S}} \sqrt{\frac{2}{M}} \Big[\sum_{m_1=0}^{M-1} C[m_1] X[m_1] cos\left(\frac{\pi(2(Ms + m) + 1) m_1}{2M}\right) \Big] \tag{3.83}$$

Upon rearranging the argument term of cosine in (3.83), the corresponding representation is illustrated in (3.84)

$$\tilde{x}[n] = \frac{1}{\sqrt{S}} \sqrt{\frac{2}{M}} \Big[\sum_{m_1=0}^{M-1} C[m_1] X[m_1] cos\left(\frac{\pi(2m + 1) m_1}{2M} + \frac{\pi(2Ms) m_1}{2M}\right) \Big] \tag{3.84}$$

On solving (3.84), by letting $k = sm_1$ as $s = 0, 1, 2, \cdots S-1$, the following expression can be obtained

$$\tilde{x}[n] = \frac{1}{\sqrt{S}}\sqrt{\frac{2}{M}}\Big[\sum_{m_1=0}^{M-1} C[m_1] X[m_1] cos\left(\frac{\pi(2m+1)m_1}{2M} + \pi k\right)\Big] \tag{3.85}$$

Using the identity

$cos(A+B) = cos(A)\,cos(B) - sin(A)\,sin(B)$ in (3.85) to attain

$$\tilde{x}[n] = \frac{1}{\sqrt{S}}\sqrt{\frac{2}{M}}\Big[\sum_{m_1=0}^{M-1} C[m_1] X[m_1] cos\left(\frac{\pi(2m+1)m_1}{2M}\right) cos(\pi k)\Big] \tag{3.86}$$

(3.86) can be solved to attain the time-domain F-O-IFDMA signal as

$$\tilde{x}[n] = \begin{cases} \frac{1}{\sqrt{S}}\sqrt{\frac{2}{M}}\sum_{m_1=0}^{M-1} C[m_1] X[m_1] cos\left(\frac{\pi(2m+1)m_1}{2M}\right)(-1)^k, \\ \qquad if\ k\ is\ odd \\ \frac{1}{\sqrt{S}}\sqrt{\frac{2}{M}}\sum_{m_1=0}^{M-1} C[m_1] X[m_1] cos\left(\frac{\pi(2m+1)m_1}{2M}\right), \\ \qquad if\ k\ is\ even \end{cases} \tag{3.87}$$

F-O-LFDMA

Here, the signal representation is dealt in the previous section which is given by (3.72). The IDCT output sequence $\tilde{x}[n]$ with $n = Sm + s$ for $s = 0, 1, 2, 3, \cdots S-1$ can be expressed as follows:

$$\tilde{x}[n] = \tilde{x}[Sm+s] = \sqrt{\frac{2}{MS}}\sum_{k=0}^{M-1} C[k] X[k] cos\left(\frac{\pi(2(Sm+s)+1)k}{2SM}\right) \tag{3.88}$$

In order to view the time-domain signal, we shall see for the case when $s = 0$

$$\tilde{x}[n] = \tilde{x}[Sm] = \frac{1}{\sqrt{S}}\left\{\sqrt{\frac{2}{M}}\sum_{k=0}^{M-1} C[k] X[k] cos\left(\frac{\pi(2Sm+1)k}{2SM}\right)\right\} \tag{3.89}$$

Upon solving we obtain

$$\tilde{x}[n] = \tilde{x}[Sm] = \frac{1}{\sqrt{S}}\left\{\sqrt{\frac{2}{M}}\sum_{k=0}^{M-1} C[k] X[k] cos\left(\frac{\pi S\left(2m+\frac{1}{S}\right)k}{2SM}\right)\right\} \tag{3.90}$$

On rearranging (3.90), yields the following representation

$$\tilde{x}[n] = \tilde{x}[Sm] = \frac{1}{\sqrt{S}}\Big\{\sqrt{\frac{2}{M}}\sum_{k=0}^{M-1} C[k] X[k] cos\left(\frac{\pi(2m+1)k}{2M}\right) cos\left(\frac{\pi\left(1-\frac{1}{S}\right)k}{2M}\right)\Big\} \tag{3.91}$$

If $s \neq 0$,

then let us consider $X\left[k\right] = \sqrt{\frac{2}{M}} C\left[k\right] \sum_{q=0}^{M-1} x\left[q\right] cos\left(\frac{\pi(2q+1)k}{2M}\right)$ and upon substituting in (3.91) yields

$$\tilde{x}\left[n\right] = \tilde{x}\left[Sm+s\right] = \frac{1}{\sqrt{S}}\frac{2}{M}\sum_{k=0}^{M-1} C\left[k\right]^2 \left\{\sum_{q=0}^{M-1} x\left[q\right] cos\left(\frac{\pi\left(2q+1\right)k}{2M}\right)\right\}\times$$
$$cos\left(\pi\left(\frac{Sm+s}{SM}\right)k + \frac{\pi k}{2SM}\right) \quad (3.92)$$

(3.91) and (3.92) reinforces that, the time-domain F-O-LFDMA signal represents that the input signal is scaled by a factor of $\frac{1}{S}$ and moreover, they are getting multiplied with the real weighting factors. Hence, this results in significant increase in PAPR for F-O-LFDMA when compared with F-O-IFDMA. This is verified through simulation results. Furthermore, an inference can be drawn by making use of (3.87), (3.91) and (3.92), where the real time-domain signals are fetched with good spectral efficiency as all of the subcarriers are utilized for data transmission. Based on the aforementioned arrangement of subcarriers, PAPR reduces accordingly and the simulation results are detailed next.

3.6.3 DFT-based DCO-aided Multiple Access System

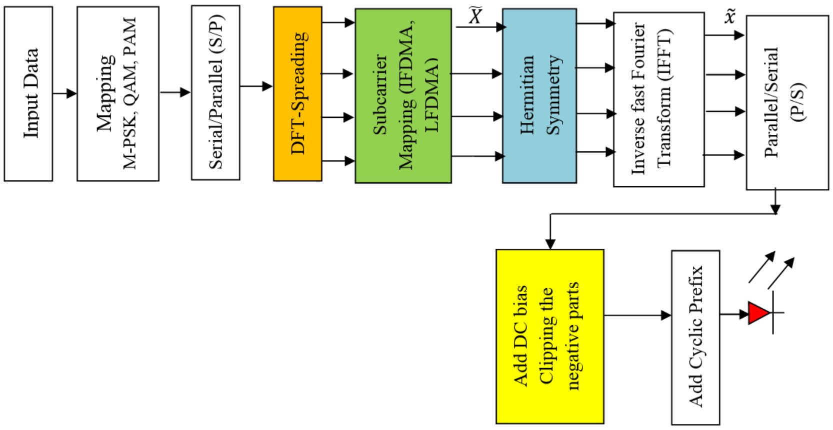

Figure 3.14: Illustration of Uplink transmission employing DFT-Spreading in optical IFDMA/LFDMA (OIFDMA/OLFDMA)

As discussed in the aforesaid section, this section highlights the mathematical analysis of the time-domain signal for DFT-based multiple access system. Moreover, due to the constraint of Hermitian Symmetry criteria, even the subcarrier mapping strategies are varied when compared with conventional RF domain.

DFT-OIFDMA

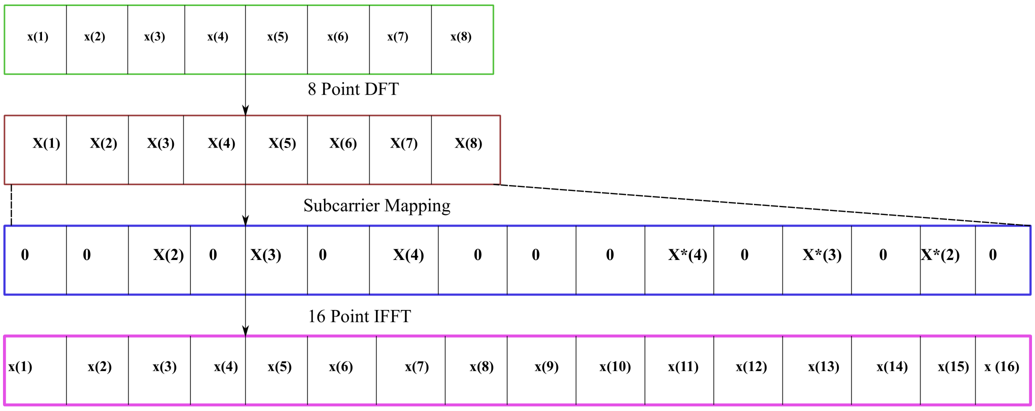

Figure 3.15: DFT-OIFDMA Subcarrier Mapping Format

As depicted in Fig. 3.14, the subcarrier mapped data is constrained to satisfy HS criteria before getting applied to the IDFT transformation block. The detailed description of the subcarrier mapping is outlined in Fig. 3.15. For the input sequence $\tilde{X}[k]$, the N-point IDFT output sequence can be represented as $\tilde{x}[n]$ with $n = Ms + m$ for $s = 0, 1, 2, 3, \cdots S - 1$ and $m = 0, 1, 2, 3, \cdots M - 1$ can be obtained as

$$\tilde{x}[n] = \frac{1}{N} \sum_{k=0}^{N-1} \tilde{X}[k]\, e^{\frac{j2\pi nk}{N}} \tag{3.93}$$

Upon substituting the aforementioned constraints as well as rearranging, (3.93) can be reduced as

$$\tilde{x}[n] = \frac{1}{SM} \sum_{m_1=0}^{M-1} X[m_1]\, e^{\frac{j2\pi nm_1}{M}} \tag{3.94}$$

However, $X[m_1]$ is constrained to satisfy Hermitian Symmetry criteria. As already seen in the prior chapter, according to Hermitian Symmetry criteria, the first and the middle subcarriers are set to zero as

$$X[0] = X\left[\frac{M}{2}\right] = 0 \tag{3.95}$$

In order to avoid the presence of any complex part of the signal at the output of IDFT block, the arrangement is made in such a manner that, all of the inputs are not utilized for data transmission, i.e., out of N subcarriers only $\frac{N}{2}$ are exploited for data transmission and the rest $\frac{N}{2}$ are flipped complex conjugate versions of the previous ones. Therefore, the arrangement looks like

$$X[M-k] = X^*[k], \quad k = 1, 2, 3, \cdots \frac{M}{2} \tag{3.96}$$

Accordingly, (3.94) can be re-arranged as

$$\tilde{x}[n] = \frac{1}{S}\frac{1}{M}\Big[X[0]\,e^{\frac{j2\pi(0)m}{M}} + \sum_{m_1=1}^{\frac{M}{2}-1} X[m_1]\,e^{\frac{j2\pi m_1 m}{M}} + X\left[\frac{M}{2}\right]e^{\frac{j2\pi\left(\frac{M}{2}\right)m}{M}} + \sum_{m_1=\frac{M}{2}+1}^{M-1} X[m_1]\,e^{\frac{j2\pi m_1 m}{M}}\Big] \tag{3.97}$$

Since, the first and the middle subcarriers are set to zero, (3.97) can be reduced to

$$\tilde{x}[n] = \frac{1}{S}\frac{1}{M}\left[\sum_{m_1=1}^{\frac{M}{2}-1} X[m_1]\,e^{\frac{j2\pi m_1 m}{M}} + \sum_{m_1=\frac{M}{2}+1}^{M-1} X[m_1]\,e^{\frac{j2\pi m_1 m}{M}}\right] \tag{3.98}$$

Upon applying change in variable transformation as $M - m_1^{'} = m_1$

$$\tilde{x}[n] = \tilde{x}[Ms+m] = \frac{1}{S}\frac{1}{M}\left[\sum_{m_1=1}^{\frac{M}{2}-1} X_{m_1}e^{\frac{j2\pi m_1 m}{M}} + \sum_{m_1^{'}=1}^{\frac{M}{2}-1} X\left[M - m_1^{'}\right]e^{\frac{-j2\pi\left(M-m_1^{'}\right)m}{M}}\right] \tag{3.99}$$

Therefore, by employing (3.96), as well as rearranging (3.99), the following expression can be obtained

$$\tilde{x}[n] = \tilde{x}[Ms+m] = \frac{1}{S}\frac{1}{M}\left[\sum_{m_1=1}^{\frac{M}{2}-1} X[m_1]\,e^{\frac{j2\pi m_1 m}{M}} + \sum_{m_1=1}^{\frac{M}{2}-1} X^{*}[m_1]\,e^{\frac{-j2\pi m_1 m}{M}}\right] \tag{3.100}$$

By using Euler inequalities, (3.100) can be re-arranged as

$$\tilde{x}[n] = \tilde{x}[Ms+m] = \frac{1}{S}\left[\frac{2}{M}\sum_{m_1=1}^{\frac{M}{2}-1} \underset{RC}{X[m_1]}cos\left(\frac{2\pi m_1 m}{M}\right) - \underset{IC}{X[m_1]}sin\left(\frac{2\pi m_1 m}{M}\right)\right] \tag{3.101}$$

where $\underset{RC}{X[m_1]}$ and $\underset{IC}{X[m_1]}$ in (3.101) represents the real and imaginary components. (3.101), clearly illustrates that there is a loss in spectral efficiency as all of the subcarriers are not utilized for data transmission. This is because, out of N subcarriers only $\frac{N}{2}$ are involved for transporting data.

3.6.4 DFT-OLFDMA

Elaborate signal format representation is shown in Fig. 3.16. Taking into consideration the signal representation as given by (3.72), the time-domain signal $\tilde{x}[n]$ with $n = Sm + s$ and $s = 0, 1, 2, 3, \cdots S-1$ can be represented as

$$\tilde{x}[n] = \tilde{x}[Sm+s] = \frac{1}{MS}\sum_{k=0}^{M-1} X[k]\,e^{\frac{j2\pi(Sm+s)k}{MS}} \tag{3.102}$$

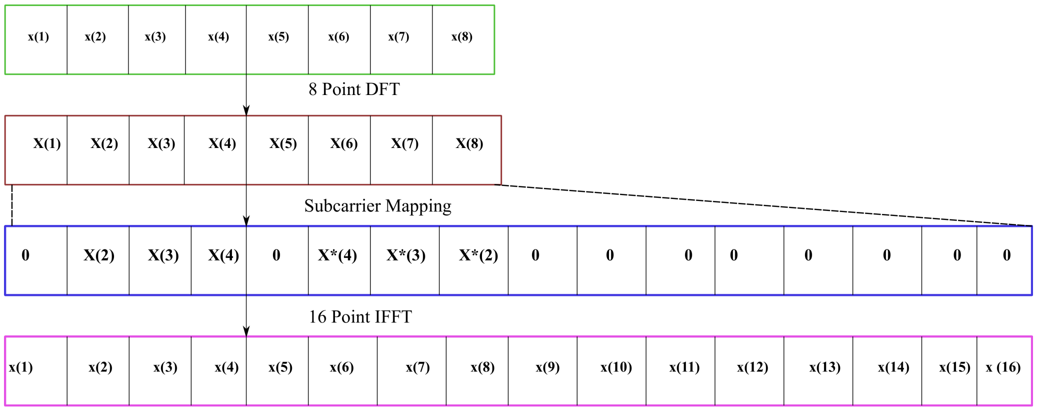

Figure 3.16: Signal format for DFT-OLFDMA

Furthermore, (3.102) can be solved by considering two scenarios:

When $s = 0$:

The time-domain analysis and the signal representation is similar to that obtained in the previous scenario DFT-OIFDMA. Therefore, the time-domain signal can be represented as

$$\tilde{x}[n] = \tilde{x}[Sm] = \frac{1}{S}\left[\frac{2}{M}\sum_{k=1}^{\frac{M}{2}-1} \underset{RC}{X}[k]cos\left(\frac{2\pi mk}{M}\right) - \underset{IC}{X}[k]sin\left(\frac{2\pi mk}{M}\right)\right] \tag{3.103}$$

When $s \neq 0$:

Let us substitute $X[k] = \sum_{p=0}^{M-1} x[p]\, e^{\frac{-j2\pi pk}{M}}$ in (3.102), then the following representation is attained

$$\tilde{x}[n] = \tilde{x}[Sm+s] = \frac{1}{MS}\sum_{k=0}^{M-1}\sum_{p=0}^{M-1} x[p]\, e^{\frac{-j2\pi pk}{M}} e^{\frac{j2\pi(Sm+s)k}{MS}} \tag{3.104}$$

However, $x[p]$ in (3.104) represents the time-domain signal at the output of IDFT transformation block and this is constrained to satisfy Hermitian Symmetry criteria and is given as

$$x[p] = \frac{2}{M}\sum_{k=1}^{\frac{M}{2}-1}\left(\underset{RC}{X}[k]cos\left(\frac{2\pi pk}{M}\right) - \underset{IC}{X}[k]sin\left(\frac{2\pi pk}{M}\right)\right) \tag{3.105}$$

Upon substituting, (3.105) in (3.104), the resultant expression can be obtained as

$$\begin{aligned}\tilde{x}[n] = \tilde{x}[Sm+s] = \frac{1}{S}\sum_{k=0}^{M-1}\sum_{p=0}^{M-1}\left[\frac{2}{M}\sum_{k=1}^{\frac{M}{2}-1}\left(\underset{RC}{X}[k]cos\left(\frac{2\pi pk}{M}\right) - \underset{IC}{X}[k]sin\left(\frac{2\pi pk}{M}\right)\right)\right] \\ \times \frac{1}{M}\sum_{k=0}^{M-1} e^{j2\pi\left(\frac{-p}{M}+\frac{m}{M}+\frac{s}{MS}\right)k}\end{aligned} \tag{3.106}$$

Further, (3.106) can be solved as

$$\tilde{x}\left[n\right] = \tilde{x}\left[Sm+s\right] = \frac{1}{S}\sum_{k=0}^{M-1}\sum_{p=0}^{M-1}\left[\frac{2}{M}\sum_{k=1}^{\frac{M}{2}-1}\left(\underset{RC}{X}[k]cos\left(\frac{2\pi pk}{M}\right) - \underset{IC}{X}[k]sin\left(\frac{2\pi pk}{M}\right)\right)\right]$$
$$\times\frac{sin\pi\left(\frac{(m-p)S+s}{S}\right)}{Msin\pi\left(\frac{(m-p)S+s}{MS}\right)}e^{j\pi\left(\frac{(m-p)S+s}{S}\right)\left(\frac{M-1}{M}\right)} \quad (3.107)$$

Therefore, upon comparison of (3.101), (3.103) and (3.107) with (3.71), (3.76) and (3.80) confirms the fact that DFT-based multiple access strategies results in a decrease in throughput.

3.7 Complexity Analysis

The work in [178] reports that recursive algorithms have been proposed for DST-IV of power-of-two transform size N which requires fewer total real additions and multiplications that can be called as flops. The fast algorithms computed in this work makes use of the FFT algorithm which reduced the operation count of discrete Fourier transform (DFT) of size N where the flop count was reduced from $4Nlog_2N$ to [179]

$$\frac{34}{9}Nlog_2N - \frac{124}{27}N - 2logN - \frac{2}{9}\left(-1\right)^{logN}logN + \frac{16}{27}\left(-1\right)^{logN} + 8 \quad (3.108)$$

Using the FFT as computed in [179], the number of flops (i.e., the total number of real additions and multiplications) for DST-IV in [178] were reduced from $2Nlog_2N+N$ to

$$\frac{17}{9}Nlog_2N + \frac{31}{37}N + \frac{2}{9}\left(-1\right)^{log_2N}log_2N - \frac{4}{27}\left(-1\right)^{log_2N} \quad (3.109)$$

Finally, it can be inferred that by using the improved FFT algorithm where the flop count reduced from $\sim 4Nlog_2N$ to $\sim \frac{34}{9}Nlog_2N$ (i.e., the algorithm where the total number of additions and multiplications are reduced to a significant amount), the earlier works report that new recursive algorithms can be derived for DST-IV to substantially reduce the total number of additions and multiplications for a transform of size $N = 2^m$ from $\sim 2Nlog_2N + N$ to $\sim \frac{17}{9}Nlog_2N$.

3.8 Comparisons between DFT-based optical-OFDM and DCT/DST-based optical-OFDM system

Table 3.2: Comparison between DCT/DST-optical OFDM and DFT-optical OFDM

Type of OFDM	DCT/DST-ACO-OFDM and DCT/DST-DCO-OFDM	DFT-ACO-OFDM and DFT-DCO-OFDM
Hermitian Symmetry	Not-required	Required
Constellation	Real (BPSK, M-PAM)	Complex (M-QAM)
Constellation Size	M=L	M=L^2
Self-Inverse Property	Self-Inversive	Not-Self-Inversive
Subcarriers-Utilized	$\frac{N}{2}$ for DCT/DST-ACO-OFDM N for DCT/DST-DCO-OFDM	$\frac{N}{4}$ for DFT-ACO-OFDM $\frac{N}{2}$ for DFT-DCO-OFDM

In case of DFT-based DCO-OFDM system, in order to generate a real valued signal, the huge stream of input data which is mapped by employing complex constellations like M-QAM is compelled to satisfy Hermitian Symmetry criteria before getting applied to the IFFT block. However, in doing so, only half of the subcarriers i.e., IFFT points are utilized for data transmission while, the rest half are flipped complex conjugate versions of the previous ones. Thus, there is a decrease in throughput. Therefore, the bandwidth efficiency (BE) pertaining to DFT-DCO-OFDM can be mathematically expressed as [180]

$$BE_{DFT-DCO-OFDM} = \left(\frac{{}^{N}\!/\!{}_{2} - 1}{N + N_G}\right) Blog_2 M \quad {}^{(bits/sec)}\!/\!{}_{Hz} \tag{3.110}$$

Consequently, to address the reduced bandwidth efficiency which is encountered when relying on Hermitian Symmetry imposed IFFT, real transformation techniques like DST can be exploited for DCO-OFDM system. Moreover, the aforementioned mathematical analysis clearly confirms the fact that, DST-based DCO-OFDM system involves all of the subcarriers for data transmission. This can be mathematically represented as

$$BE_{DST-DCO-OFDM} = \left(\frac{N - 1}{N + N_G}\right) Blog_2 M \quad {}^{(bits/sec)}\!/\!{}_{Hz} \tag{3.111}$$

While, with the case of DFT-ACO-OFDM system, due to Hermitian Symmetry criteria, out of N subcarriers, only $\frac{N}{2}$ subcarriers are exploited for the transmission of data and furthermore, due to the modulation of only odd subcarriers, (since, even subcarriers are set to zero) out of $\frac{N}{2}$ subcarriers, only $\frac{N}{4}$ subcarriers are involved for data transmission. While, DST-ACO-OFDM system doesn't rely on Hermitian Symmetry criteria for yielding a real valued signal. Therefore, out of N subcarriers, $\frac{N}{2}$ odd subcarriers are employed for the transmission of data. Mathematically, this can be expressed as [180]

$$BE_{DFT-ACO-OFDM} = \left(\frac{N/4 - 1}{N + N_G}\right) Blog_2M \quad {}^{(bits/sec)}/_{Hz} \tag{3.112}$$

$$BE_{DST-ACO-OFDM} = \left(\frac{N/2 - 1}{N + N_G}\right) Blog_2M \quad {}^{(bits/sec)}/_{Hz} \tag{3.113}$$

From (3.110), (3.111), (3.112) and (3.113), it can be deduced that, DST based optical-OFDM system achieves double the spectral efficiency when compared with traditional DFT-based optical-OFDM system. The parameters N, N_G, B, M in (3.110), (3.111), (3.112) and (3.113) denotes the total number of subcarriers, guard interval, the channel bandwidth and the constellation size. Table. 3.2, gives the comparison between DST-based optical OFDM (DST-ACO-OFDM, DST-DCO-OFDM) and DFT-based optical OFDM (DFT-ACO-OFDM, DFT-DCO-OFDM).

3.9 Results and Discussions

This section evaluates the performance of the proposed multicarrier and multiple access transmission schemes in terms of BER and PAPR reduction through simulation results. For the simulation purpose, the number of subcarriers taken into consideration are 512. The added cyclic prefix is $\frac{1}{4}$th of the subcarriers size to countervail the effects of ISI. The simulation parameter set-up is illustrated in Table. 3.3. The performance of FOOFDM system which is utilizing M-PAM modulation scheme is shown in Fig. 3.17. This result evidences that FOOFDM system which is based on the addition of DC bias requires higher SNRs to achieve the desired BER for $2, 4, 16$ and 64 PAM respectively. This is because, in case of DCO-FOOFDM, the clipping operation results in clipping-induced distortion which reduces the BER performance. Moreover, in order for the BER to reach the forward error correction limit of 10^{-3}, a fixed amount of DC bias addition is not sufficient for all the constellations in DCO-FOOFDM system.

Fig. 3.18, depicts the CCDF curves for DCT-Spread-FOOFDM system employing M-

Table 3.3: Simulation Parameters

Parameter	Value
No of OFDM symbols	512
Total Number of Subcarriers	512-DCO-OFDM, 1024-ACO-OFDM
Pilot Insertion interval	$\frac{1}{8}$th the subcarriers size
Total Number of Pilot carriers	64, 128
Type of the transform techniques employed	DFT, DCT, DST
Variants of optical OFDM employed	DCO-OFDM, ACO-OFDM
Cyclic Prefix	$\frac{1}{4}$th subcarriers size
Orders of Modulation	M-QAM, M-PAM
Dimensions of the Room	$6 \times 6 \times 3$
Total number of LEDs	1200
Power of each LED	20mW
LED semi-angle	70 degrees
FOV of the photodiode ψ_c	60 degrees
Area of the Photodiode A_{pd}	1 cm^2
Optical Filter Co-efficient $T_s\left(\psi\right)$	1
refractive index	1.5
reflectance factor ρ	0.8
Size of the IDST/IDCT (N)	512
Size of M	[8, 16, 32, 64, 128]
Orders of Modulation	M-PAM, M=[2, 4, 8, 16, 32, 64, 256]
Spreading Factor	$N/M = \{\frac{512}{8}, \frac{512}{16}, \frac{512}{32}, \frac{512}{64}, \frac{512}{128}\}$
Sub-blocks for PTS scheme	[4, 8, 16, 32]

PAM modulation format and conventional FOOFDM system. It is clearly evidenced that, when DCT-Spreading is employed using 4-PAM, the PAPR of conventional FOOFDM is significantly decreased. At a CCDF of 2×10^{-4}, PAPR of DCT-S-FOOFDM is 3.9 dB whereas, for conventional FOOFDM, it is around 13 dB. This clearly emphasizes that, upon exploiting DCT-spreading, there is a drastic decrease in PAPR by approxiamtely

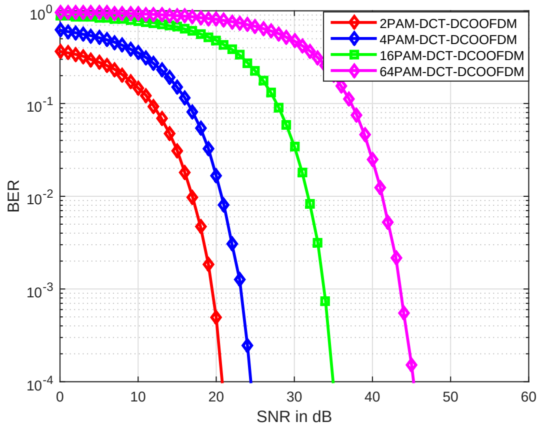

Figure 3.17: BER vs SNR performance analysis of FOOFDM system using M-PAM

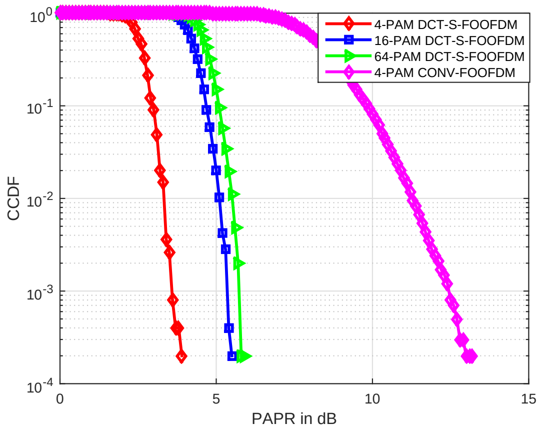

Figure 3.18: CCDF curves depicting PAPR reduction for DCT-S-FOOFDM using M-PAM

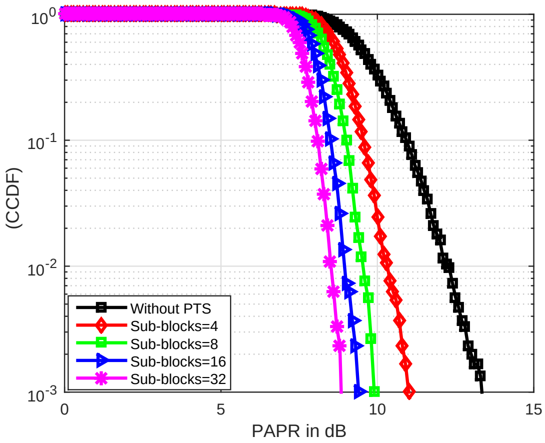

Figure 3.19: PAPR reduction in FOOFDM using Partial Transmit Sequence

10.9 dB. Further, this figure even depicts DCT-S-FOOFDM employing 16-PAM and 64-PAM. At the same probability of 2×10^{-4}, when 16-PAM and 64-PAM are modulated,

PAPR has been decreased by an amount of 7.5 dB and 7.2 dB respectively.
Fig. 3.19, reveals the effect of applying PTS technique for PAPR reduction in FOOFDM system employing 16-PAM order of modulation and the number of subcarriers used are 512. As illustrated in the figure, PAPR reduces significantly when the number of subblocks increase from $4, 8, 16$ and 32. Here, for a probability of 10^{-3}, when the number of subblocks are 32, there is a decrease in PAPR of around 4.5 dB when compared with FOOFDM without imposing PTS technique. The same can be inferred for the subblocks 16, 8 and 4 where the PAPR reduces by 3.9 dB, 3.4 dB and 2.1 dB respectively. This analysis clearly depicts the advantage of bestowing PTS technique for PAPR reduction. However, DCT-Spreading technique outperforms PTS technique for PAPR reduction in FOOFDM system.

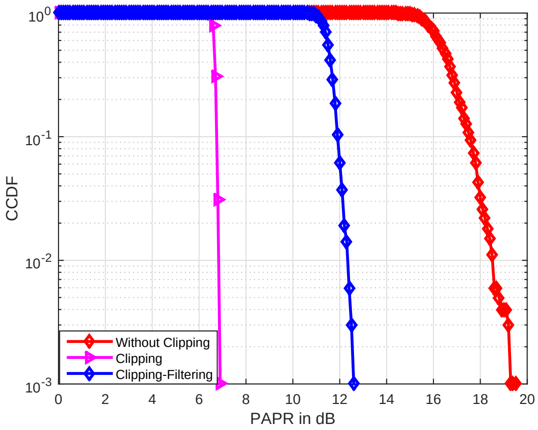

Figure 3.20: PAPR Performance of FOOFDM using Clipping and Filtering Technique

Fig. 3.20, manifests PAPR reduction in FOOFDM using clipping and filtering technique. The simulated results clearly depicts that PAPR reduction using clipping is better when compared to incorporation of filtering operation. When employing 4-PAM modulation scheme and utilizing 512 subcarriers, at CCDF of 10^{-3}, the attained PAPR for clipping, clipping and filtering as well as traditional FOOFDM system is 6.9 dB, 12.6 dB and 19.3 dB respectively. This huge increase in PAPR for conventional FOOFDM system is valid because of the addition of 7 dB of DC bias. However, DCT-Spreading technique dominates clipping and filtering technique.

The CCDF curves for PAPR reduction in multiple access system which are in accordant with IM/DD systems for VLC is delineated in Fig. 3.21 and 3.22. The figures

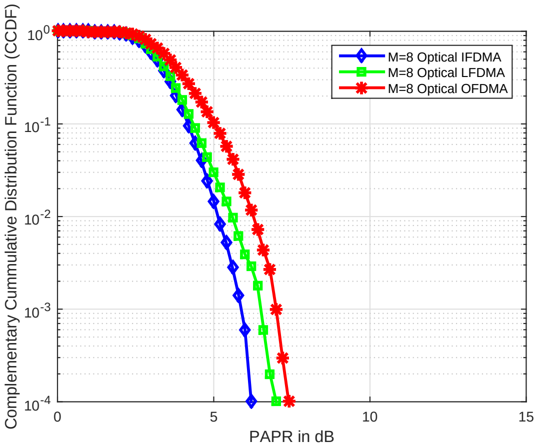

(a) CCDF vs PAPR employing M=8 for F-O-IFDMA, F-O-LFDMA and F-OOFDMA

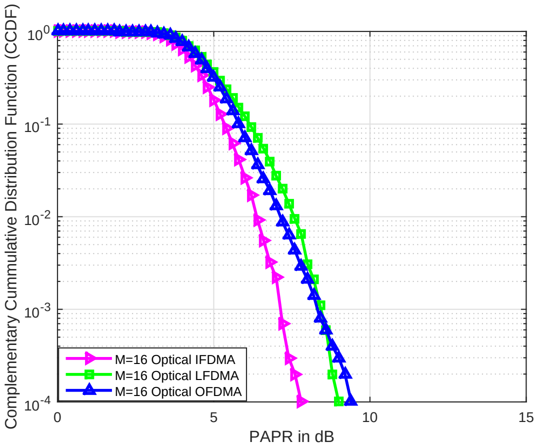

(b) CCDF vs PAPR employing M=16 for F-O-IFDMA, F-O-LFDMA and F-OOFDMA

Figure 3.21: Comparison of PAPR performance for F-O-IFDMA, F-O-LFDMA and F-OOFDMA when M varies from 8 and 16 employing 16-PAM

reconciles with the fact that, the reduction in PAPR is dependent on the way of allocating the subcarriers to each mobile terminal. Accordingly, the distribution of PAPR for different mapping strategies like F-OOFDMA, F-O-IFDMA ad F-O-LFDMA is delineated in Fig. 3.21a, 3.21b, 3.22a and 3.22b respectively. From the figures it can be affirmed that, PAPR performance has a direct relation with the number of subcarriers M that are devoted to each user/subscriber. Upon increasing the number of subcarriers from $M = 4, 8, \cdots, 128$, the PAPR performance deteriorates. In order to evaluate the performances of OIFDMA, OLFDMA and OOFDMA, a comparison analysis of their PAPR is carried out by fixing the number of subcarriers. Employing 16-PAM modulation scheme,

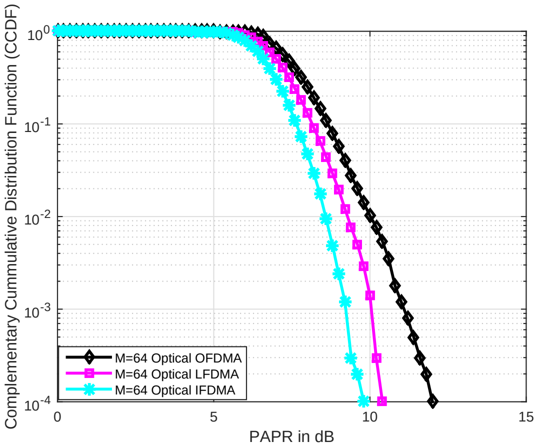

(a) CCDF vs PAPR employing M=64 for OIFDMA, OLFDMA and OOFDMA

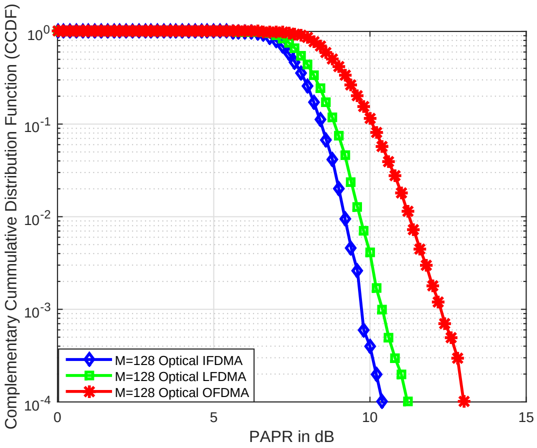

(b) CCDF vs PAPR employing M=128 for OIFDMA, OLFDMA and OOFDMA

Figure 3.22: Comparison of PAPR performance for OIFDMA, OLFDMA and OOFDMA for higher order of M employing 16-PAM

for $N = 512$-point IDCT, at a probability of 10^{-4}, the attained PAPR for F-O-IFDMA, F-O-LFDMA and F-OOFDMA using 8 subcarriers is 6.2 dB, 7 dB and 7.4 dB, while, for the same mapping strategies, utilizing 16 subcarriers, the obtained PAPR is 9 dB, 9.4 dB, and 13 dB respectively. This is clearly detailed in Fig. 3.21a and 3.21b. The performance analysis of F-O-IFDMA, F-O-LFDMA and F-OOFDMA for higher orders of M i.e., $M = 64$ and 128 is represented in Fig. 3.22a and 3.22b. For $M = 64$, at a CCDF of 10^{-4}, the obtained PAPR for F-O-IFDMA, F-O-LFDMA and F-OOFDMA is 9.8dB, 10.4 dB and 12 dB. Whereas, for $M = 128$, at a CCDF of 10^{-4}, the achievable PAPR for F-O-IFDMA, F-O-LFDMA and F-OOFDMA is 10.4dB, 11.2 dB and 13 dB respectively.

Together, the amount of PAPR in F-O-IFDMA and F-O-LFDMA is inferior than F-OOFDMA. Moreover, PAPR incurred in F-O-IFDMA is significantly less when compared with F-O-LFDMA and F-OOFDMA. In addition, F-O-LFDMA attains a higher PAPR than F-O-IFDMA, but, compared to F-OOFDMA it is lower. Therefore, this analysis confirms that F-O-IFDMA is more appealing in terms of PAPR reduction and power efficiency. The computation complexity involved behind the two transform techniques namely DCT and DFT is exemplified in Fig. 3.23. This figure clearly manifests that the computational complexity which is generally calculated in terms of total number of additions and multiplications of DCT transform is quite less than that of the DFT transform technique and this is mathematically confirmed by the analytical expressions as described in Table. 3.1. Therefore, DCT transform technique can be envisaged to be exploited for the cost-effective realization of IM/DD systems for VLC.

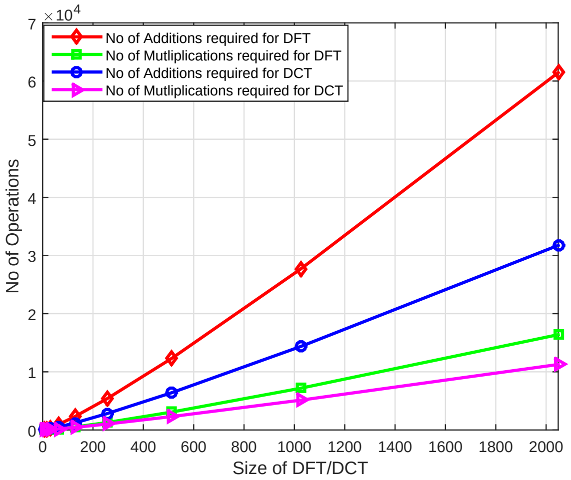

Figure 3.23: Comparison of Computational Complexity of DCT/DFT transformation techniques

Further, the BER vs SNR performance is evaluated for DST-based DCO-OFDM and ACO-OFDM i.e., (DST-DCO-OFDM) and (DST-ACO-OFDM) systems. It is to be noted that, for the purpose of simulation, the total number of subcarriers employed in case of DST-DCO-OFDM are 512. Pertaining to DST-ACO-OFDM since, there is a decrease in throughput, 1024 subcarriers are utilized and the cyclic prefix is chosen as $\frac{1}{4}$th the subcarriers size. Fig. 3.24a gives the magnitude of the time-domain signal for DST based OOFDM system employing $N = 64$ subcarriers and 4-PAM modulation scheme. While, Fig. 3.24b and 3.24c represent the magnitude plots of DCO-OFDM and

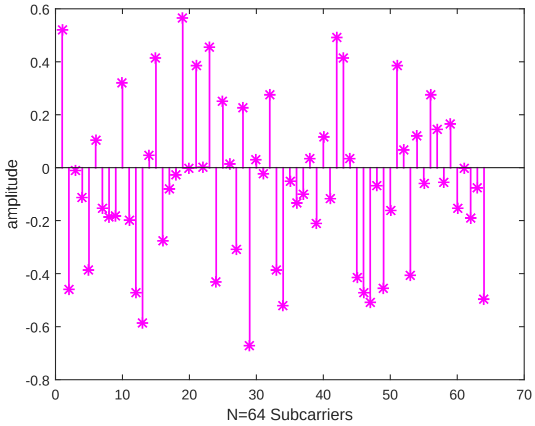

(a) Magnitude-Plot of DST-optical-OFDM (DST-OOFDM) system using 4-PAM modulation

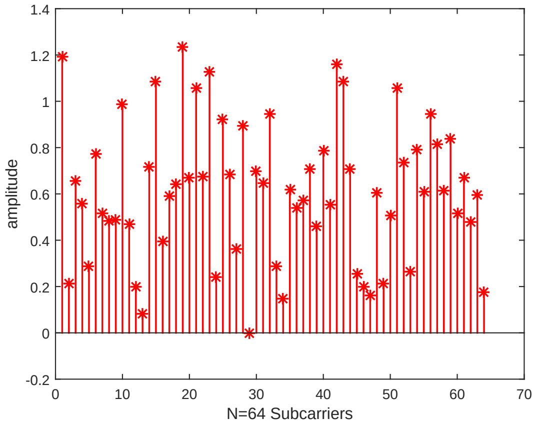

(b) Magnitude-Plot of DST-DCO-OFDM system using 4-PAM modulation

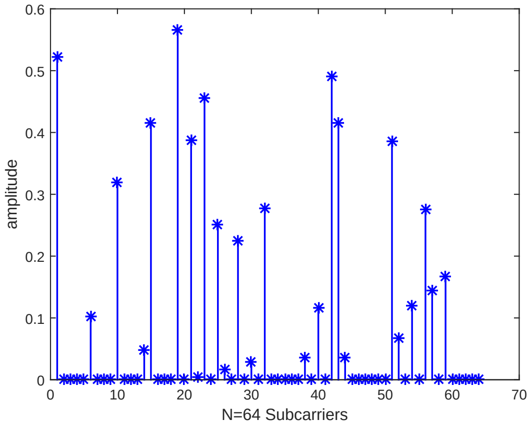

(c) Magnitude-Plot of DST-ACO-OFDM using 4-PAM modulation

Figure 3.24: Comparison of time-domain signal for DST-DCO-OFDM and DST-ACO-OFDM

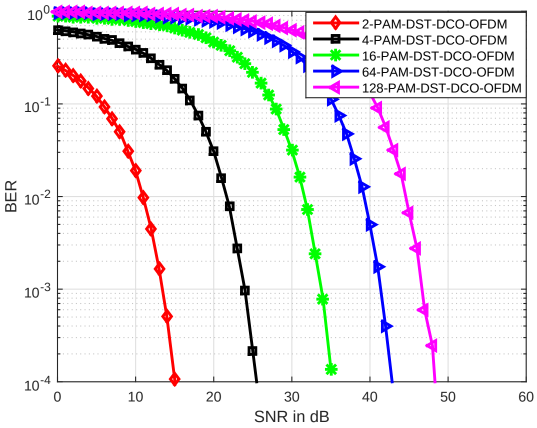

Figure 3.25: Performance analysis of DST-based DCO-OFDM (DST-DCO-OFDM) for VLC

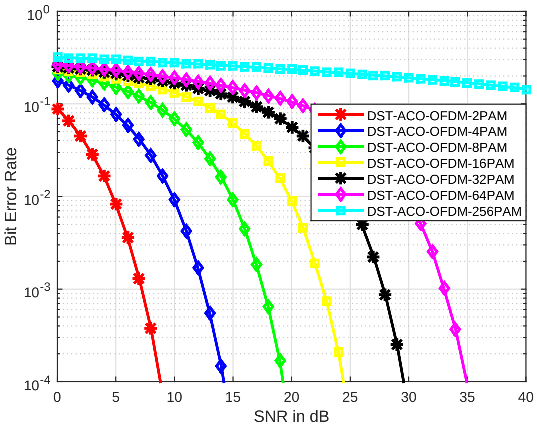

Figure 3.26: Performance analysis of DST-based ACO-OFDM (DST-ACO-OFDM) for VLC

ACO-OFDM methodologies, where the former represents the addition of DC bias while the later represents the effect of clipping of the negative part of the signal. BER vs SNR for DST-DCO-OFDM system which is compatible with IM/DD systems for VLC is illustrated in Fig. 3.25. It is evident from the figure that the performance is analysed by varying the size of the constellation of M-ary PAM. For higher orders, the BER performance deteriorates and even high amount of SNR is desired to achieve a reduced probability of error floor. This is valid because the addition of DC bias leads to increase in the power levels. Approximately in order to achieve a BER of 1.68×10^{-4}, the amount of SNR required by $2, 4, 16, 64$ and 128 PAM is $15, 25, 35, 42$ and 48 dB respectively. Similarly, the BER performance of DST-ACO-OFDM is depicted in Fig. 3.26. As evident

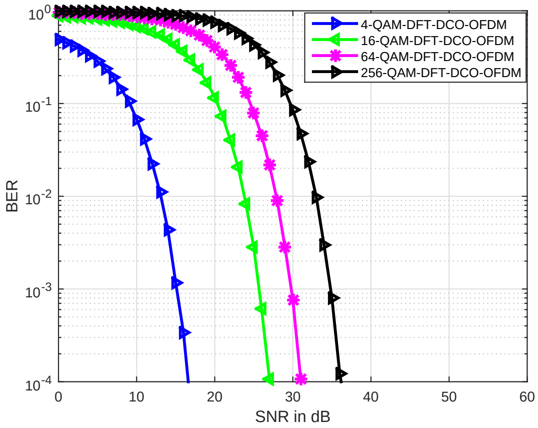

Figure 3.27: Performance analysis of DFT-based DCO-OFDM/Conventional Optical OFDM (DFT-DCO-OFDM) using M-QAM

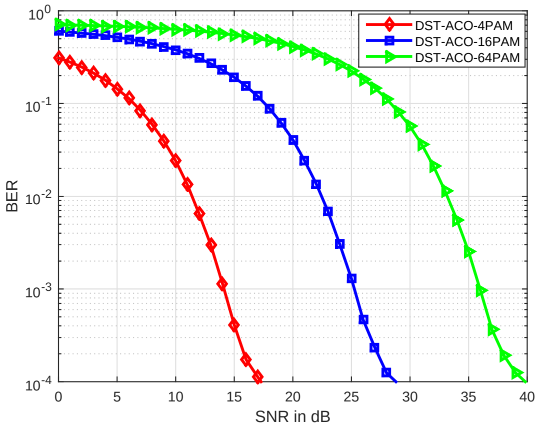

Figure 3.28: Performance analysis of DST-based ACO-OFDM considering NLOS Channel environment

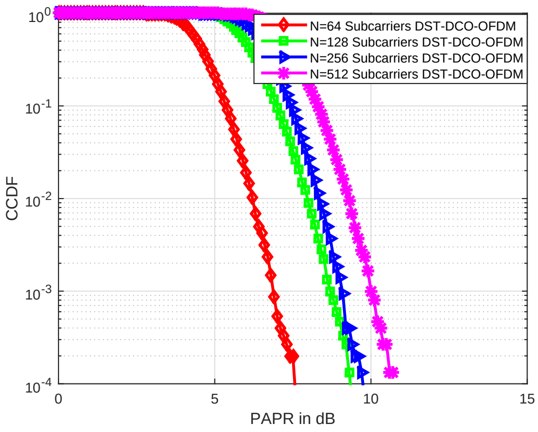

Figure 3.29: PAPR performance of DST-DCO-OFDM with varying subcarriers

from the figure, the amount of SNR required to attain a certain probability of error is less when compared with DST-DCO-OFDM system. This is because, DST-ACO-OFDM system doesn't require DC bias to attain a positive signal. However, for higher orders of PAM like 256-PAM, the clipping noise dominates and hence, it becomes difficult to attain the reduced error floor. It is interesting to note that, DST being a simple real transformation technique employs simple real mapping schemes like BPSK and M-PAM. Upon comparison with Hermitian Symmetry imposed FFT in OOFDM, to achieve the same amount of performance, Hermitian Symmetry imposed FFT-based DCO-OFDM and ACO-OFDM system requires $4, 16, 64, 256$ and 1024 QAM in contrast to $2, 4, 8, 16$ and 32 PAM as required in DST-DCO-OFDM/DST-ACO-OFDM system. Therefore, this confirms that DST supports double the constellation symbols to achieve the same amount of performance upon comparison with Hermitian Symmetry imposed FFT. This is confirmed through the simulated result as shown in Fig. 3.27. Upon comparison with Fig. 3.25, it can be inferred that, to achieve the error floor of 3.383×10^{-4}, at a SNR of 16 dB, 2-PAM is sufficient for DST-DCO-OFDM while 4-QAM is required in DFT-DCO-OFDM to achieve the same probability of error at the same SNR. Similarly, to achieve error probability of 1.307×10^{-4} and 1.769×10^{-4} at 27 dB and 36 dB of SNR, DST-DCO-OFDM uses 4-PAM and 16-PAM in contrast to 16-QAM and 256-QAM as used in DFT-DCO-OFDM. Therefore, this confirms that DST-based DCO-OFDM/ACO-OFDM are spectrally efficient when compared with DFT-based DCO-OFDM/ACO-OFDM.

Fig. 3.28, shows the BER vs SNR performance of DST-ACO-OFDM system over NLOS channel environment. The simulated result evidences that, due to the presence of reflections in the room environment, there is a slight deterioration in the BER performance at lower SNRs, because for lower SNRs, the probability of error is high. In order to reach the desired level of error floor, high SNRs are required. In particular, for 16-PAM at SNR of 19 dB, the obtained probability of error is 0.06177, while it requires 28 dB of SNR to achieve a reduced probability of error of 1.242×10^{-4}.

The CCDF curves for the variation of the number of subcarriers in DST-DCO-OFDM system is shown in Fig. 3.29. It is evident that, upon increasing the number of subcarriers from $N = 64, 128, 256$ and 512, the PAPR significantly increases.

Fig. 3.30 emphasizes the prominence of imposing DST spreading to DST-based DCO-OFDM using M-PAM modulation. This simulated result clearly signifies that, upon

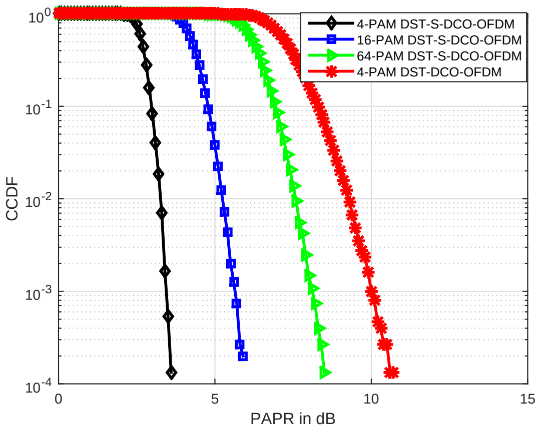

Figure 3.30: CCDF curves for DST-S-DCO-OFDM using M-PAM

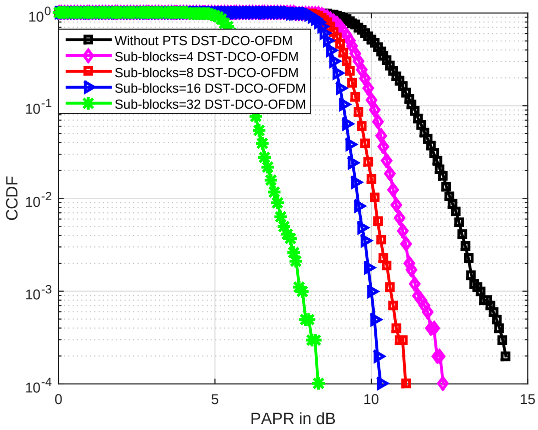

Figure 3.31: CCDF vs PAPR for PAPR reduction using Partial Transmit Sequence (PTS) in DST-DCO-OFDM system

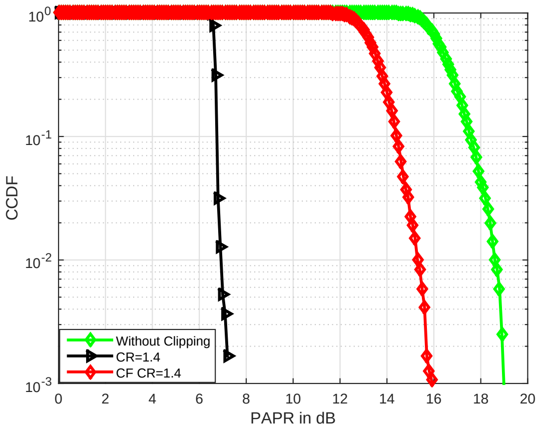

Figure 3.32: CCDF vs PAPR for PAPR reduction using Clipping and Filtering in DST-DCO-OFDM system

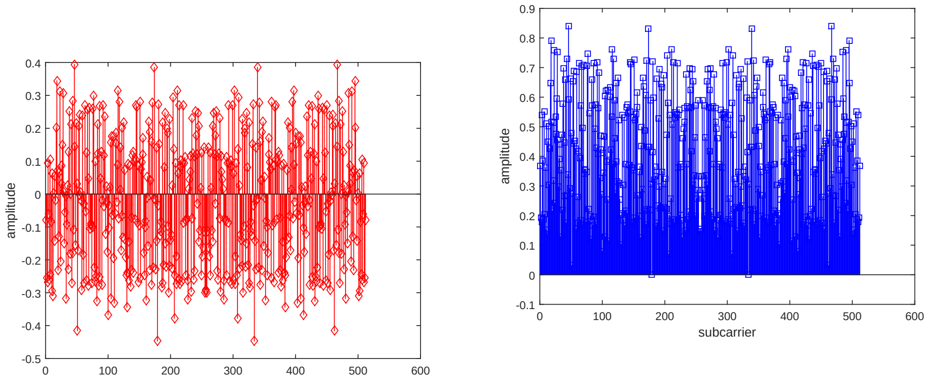

(a) Magnitude-Plot of DST-OIFDMA using 4-PAM modulation

(b) Magnitude-Plot of DST-OIFDMA using 4-PAM modulation after addition of DC bias

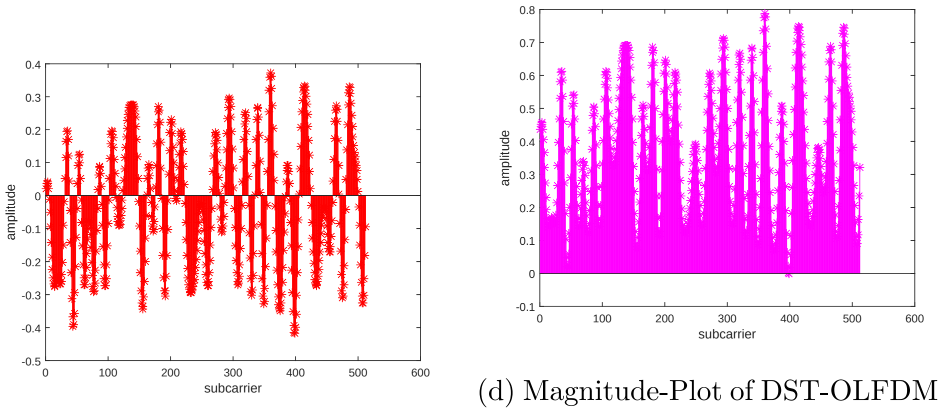

(c) Magnitude-Plot of DST-OLFDMA using 4-PAM modulation

(d) Magnitude-Plot of DST-OLFDMA using 4-PAM modulation after addition of DC bias

Figure 3.33: Comparison of time-domain signal of DST-OIFDMA/OLFDMA with and without the addition of DC bias

increasing the order of modulation, the PAPR performance deteriorates. It can be deduced that DST-S-DCO-OFDM utilizing 4-PAM modulation, at a probability of approximately 10^{-4} attains a PAPR of 3.6 dB, while a conventional DST-based DCO-OFDM system achieves a PAPR of 10.7 dB for the same order of modulation i.e., 4-PAM. Therefore, a gain of around 7.1 dB is achieved by enforcing spreading technique. Whereas, at a CCDF of 10^{-4} when employing 16-PAM and 64-PAM mapping in DST-S-DCO-OFDM system, the obtained PAPR is 5.9 and 8.5 dB respectively.

The simulation results illustrating the CCDF vs PAPR performance upon imposing PTS and clipping and filtering techniques in DST-DCO-OFDM system is shown in Fig. 3.31 and 3.32. The superiority upon imposing PTS technique for PAPR reduction can be evidenced in Fig. 3.31. As the number of sub-blocks increase from $4, 8, 16$ and 32 the reduction in PAPR is significant. At a probability of approximately 10^{-4}, PTS technique achieves a gain of around of 6 dB upon comparison with conventional DST-DCO-OFDM system. It can be inferred from Fig. 3.32 that clipping and filtering reduces the amount of PAPR in DST-DCO-OFDM system. However, the reduction in PAPR is not significant when compared with spreading technique. At a CCDF of 10^{-3}, for a clipping ratio of 1.4, clipping technique achieves a PAPR of 7 dB while clipping and filtering together attains a PAPR of 16 dB.

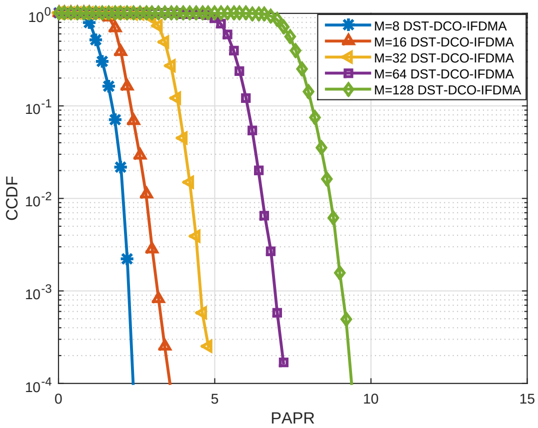

Figure 3.34: PAPR Performance of DST-OIFDMA

Fig. 3.33a, 3.33b, 3.33c and 3.33d depicts the time-domain signals with and without the addition of DC bias for DST-based OIFDMA and OLFDMA. Upon dynamic addition of DC bias, clipping noise can be reduced, this is clearly depicted in Fig. 3.33b and 3.33d.

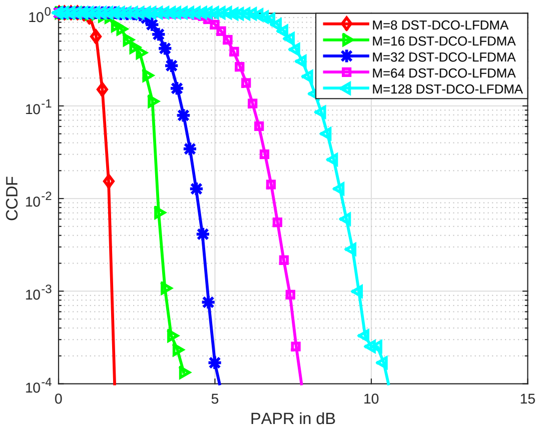

Figure 3.35: PAPR Performance of DST-OLFDMA

The PAPR performance analysis of the multiple access schemes which are compatible with IM/DD systems for VLC is delineated in Fig. 3.34, 3.35 and 3.36. Fig. 3.34 indicates the CCDF curves for DST-OIFDMA. The figure clearly depicts that upon increasing the value of M i.e., upon increasing the input blocks from $M = 8, 16, 32, 64$ and 128, the PAPR increases significantly. At a CCDF of 10^{-4}, the attained PAPR for the aforementioned input block sizes is 2.2 dB, 3.4 dB, 4.8 dB, 7.2 dB and 9 dB respectively. In a similar manner, the increase in PAPR with the increase in M for DST-OLFDMA can be evidenced in Fig. 3.35. It can be inferred that, for $M = 8, 16, 32, 64$ and 128, at a CCDF of 10^{-4}, the achievable PAPR is 2, 4, 5, 7.6 and 10.4 dB respectively. It can be surmised that, the increase in PAPR for DST-OLFDMA is more when compared with DST-OIFDMA and this is confirmed through the analytical expression of the time-domain signal which is shown by equations (3.76) and (3.80). Because this specifies that the time-domain signal is multiplied with additional weights.

In order to highlight the superiority of DST-based OIFDMA and DST-based OLFDMA, the PAPR performance is analysed for DST-based OOFDMA. This is elucidated in Fig. 3.36. At a CCDF of 10^{-4}, the attained PAPR for different values of M is 4.4, 6, 7.6, 9.4 and 11.2 dB. For $M = 128$, at a probability of 10^{-4}, the PAPR in DST-OIFDMA is lower by 1.4 dB and 2.2 dB than that of DST-OLFDMA and DST-OOFDMA. This confirms the dominance of DST-OIFDMA in terms of PAPR reduction than other multiple access schemes. The computational complexity analysis of DFT and DST transform techniques is clearly elucidated in Fig. 3.37. As stated earlier in subsection 3.7, due to the availabil-

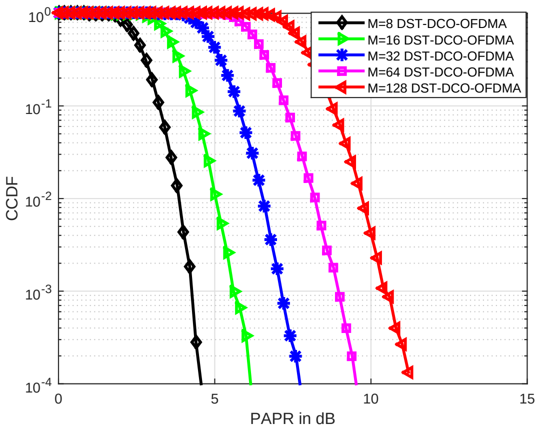

Figure 3.36: PAPR Performance of DST-OOFDMA

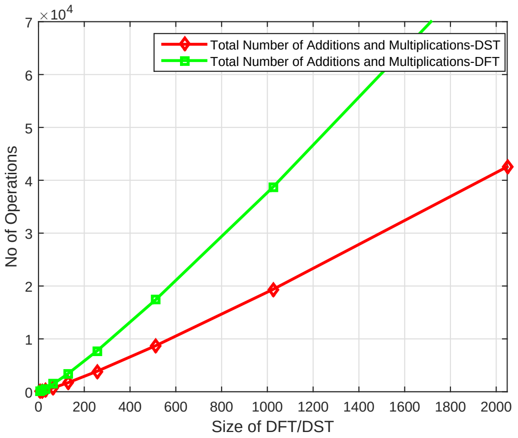

Figure 3.37: Interpretation of Computational Complexity analysis behind DFT and DST transform techniques

ity of sophisticated fast algorithms, the operation count which is also referred to as flop count (i.e., the total number of additions and multiplications together) of DFT algorithm and DST algorithm is drastically reduced and this is verified through mathematical expressions as enumerated by (3.108) and (3.109). This figure confirms the fact that DST requires less flop count when compared with that of the DFT transform technique.

3.10 Conclusion

This work analyzes the performance of FOOFDM system and proposes a DST based multicarrier modulation scheme which stems out to be as the simplified and alternative multicarrier modulation technique fulfilling the requirements of IM/DD systems for VLC. Additionally, this work evaluates the performance of DST-DCO-OFDM and DST-ACO-OFDM systems over VLC channel environment. It can be inferred from the simulated results that both DCT and DST-based optical OFDM system supports double the constellation symbols for the transmission of the same bit rate upon comparison with DFT-based optical OFDM system. Moreover, from the result analysis it can be evidenced that DCT/DST-DCO-OFDM system is power inefficient when compared with DST-ACO-OFDM system. However, the clipping noise in DST-ACO-OFDM system is dominant for higher orders of modulation.

DCT/DST-DCO-OFDM system in spite of being superior in terms of enhanced throughput when compared with DCT/DST-ACO-OFDM system, but the addition of DC bias enables it to evolve as a power-inefficient scheme. Consequently, this aspect emerges out to be more pronounced in IM/DD systems, this is due to the fact that the limited dynamic range of LEDs leads to clipping of the discretized time-domain signal which doesn't fit within its linear range thereby leading to the occurrence of deleterious non-linear distortion like clipping distortion.

Therefore, to significantly reduce the amount of PAPR in DCT/DST-DCO-OFDM system, this work proposes a DCT/DST-based spreading technique as a PAPR reduction scheme and furthermore compares with other PAPR reduction techniques like PTS, clipping and filtering for the same developed system models (i.e., DCT/DST-based optical OFDM systems). The simulation results emphasizes that the reduction in PAPR upon imposing DCT/DST-based spreading technique in DCT/DST-based optical OFDM system is significant when compared with conventional DCT/DST-based optical OFDM system where a gain of around 7.1 dB is observed for the same order of modulation. Upon imposing the other PAPR reduction schemes like PTS and clipping and filtering to DCT/DST-DCO-OFDM system, PAPR reduces by an appreciable amount. However, DCT/DST-based spreading technique dominates PTS and clipping and filtering techniques in terms of PAPR reduction.

In particular, due to the constraint of real and positive signal transmission, PAPR reduction schemes as used in RF based wireless communications cannot be enforced in a straightforward manner. Therefore, this work accomplishes a thorough mathematical analysis of the time-domain signal formats which are compatible with IM/DD systems for VLC. Additionally, in order to reduce the amount of PAPR incurred in a multicarrier system, this work expedites SC-FDMA and derives the mathematical expressions for the time-domain signal formats pertaining to different subcarrier mapping strategies like DCT/DST-OIFDMA and DCT/DST-OLFDMA as well as derives the analytical expressions for transmitted signal formats for DFT-OIFDMA and DFT-OLFDMA. The simulated results evidences that among the subcarrier mapping strategies, DCT/DST-OIFDMA is superior in terms of PAPR reduction than that of DCT/DST-OLFDMA. However, both the schemes achieves a better reduction in PAPR when compared with DCT/DST-OOFDMA. It's ease of simplicity as well as enhancement in the throughput will definitely enable DCT/DST-based multicarrier and multiple access system to be envisaged as attractive techniques for the cost-effective realization of IM/DD systems for VLC.

Chapter 4

Synchronization in DCO-OFDM and DCO-OFDMA-based IM/DD systems for VLC

4.1 Introduction and Motivation

Transmission of data by exploiting optical wireless communication as a medium stems out to be as one of the most potential technique in several critical areas, such as hospitals and aircraft cabins where RF-based transmission systems are strongly prohibited in order to avoid interference with the existing and most critical systems. Earlier studies in the literature reveal that transmission of data signal utilizing OOK turns out to be as an inflexible technique while dealing with serving multiple users/subscribers with variable data rate requirements. Therefore, this problem can be significantly addressed by employing OFDM to intensity modulate the LED.

Predominantly, an OWC system which is based on OFDM facilitates for the effective allocation of the bandwidth among the competing users. Furthermore, it provides the flexibility for adaptive selection of modulation as well as coding schemes in order to accomplish the data rates in accordant with the traffic demands. Conventionally, the transmission of data signal using OFDM relies on the fact that the subcarrier frequency components must be orthogonal to each other. The orthogonality among the subcarriers can be lost because of the occurrence of frequency and timing offsets. Timing synchronization/frame detection plays a significant role in optical OFDM systems for VLC. Imperfect timing synchronization enables the receiver to capture a mixture of interfering signals at its sampling instant. As a result, these interfering signals lead to the emergence of ISI in the transmitted data streams. Hence, this phenomena results in the increase of error rate thereby degrading the overall performance of the system. So, this entails to address the aspects of synchronization problems which includes analyzing the performance analysis of the overall system in the presence of offsets and estimation of different offsets for reducing the probability of error.

Previous studies in the literature as stated in [181–185] illustrate the effect of synchronization error on the modulating signal constellation in optical communication system. [181], gives the theoretical analysis of the effects of synchronization error in OOK and PPM-based optical communication systems. The authors in [182] proposes an inverse PPM (IPPM) modulation method to encapsulate communication data in the time domain without adversely affecting the illumination property. The research work in [183] illustrate that the authors have proposed coding framework to address the synchronization aspects of pulse position modulation formats. Further, the authors investigated the effects of clock time shift and jitter on the BER performance of the system. The works in [184,185] depicts the impact of synchronization error on optical OFDM system and also presents techniques to correct it. Much recent literature pertaining to the investigations of the effects of frequency and timing offsets can be delineated in [186] where the authors proposed a low-complexity maximum likelihood-based timing synchronization method for DCO-OFDM systems.

The indispensable virtue of this growing technology like VLC is to provide an ample opportunity to facilitate a flexible setup for the provision of assurance of multiple access support in both indoor and outdoor scenarios. However, a reliable networking solution can be offered by an appropriate choice of multiple access scheme to bestow efficient services to the users by allowing them to share the communication resources without any communal cross talk. In the perspective of networking, OFDM provides a straightforward implementation of a multiple access scheme i.e., OFDMA, a renowned multiple access approach widely exploited in $4G$ Long Term Evolution (LTE) cellular standards. The same access scheme can be incorporated in VLC provided, the signal transmission complies with the requirements of IM/DD systems.

In the recent times, VLC is interfaced with almost every infrastructural unit present in the smart city like street lighting, transportation sector, etc. Therefore, this ignited the attraction of ITS to exploit VLC for enhancing the road safety. The main motive is to enable the drivers travelling on road to communicate regarding the highly traffic prone areas, congestion, distance between moving vehicles, etc. In this way, road accidents can be controlled significantly. Hence, it is obvious that VLC will be the best complementary to RF persuading services to a multitude of customers rendering both illumination and communication. In spite of being endowed with considerable amount of prevalence when compared with RF, there are still several challenging issues which needs to be elucidated in VLC.

Ensuring adequate synchronization between the transmitter and receiver is very vital especially for VLC. Moreover, the frequency discrepancies often referred to as FO and timing disparities ably called as STO emanating between the transmitter and receiver in an uplink environment leads to several detrimental aspects like ICI and MUI which in turn leads to degradation of the performance of the system as there is a loss in orthogonality. Further, in case of V2V communication, Doppler Shift prevails between the moving vehicles [187]. Subsequently, due to this, FO occurs especially in case of real-time applications.

The next approach of this chapter is to clearly emphasize the Signal to Interference Noise Ratio (SINR) deterioration in a multiple access system compatible with IM/DD systems for VLC as well as to emphasize certain MUI cancellation strategies to ensure the perfect recovery of data signal in relevant to the corresponding subscriber. Much relevant work pertaining to the multiple access system for VLC can be reported in the following literature: the authors in [188] have demonstrated an indoor VLC positioning system based on OFDMA imparting both illumination and communication. Earlier work in [189], depicts the downlink analysis in DCO-OFDM-based optical network, where SINR analysis was carried considering only LOS environment. In [190], spectral efficient schemes were proposed for the aforementioned network. However, in all the aforesaid works, perfect synchronization was assumed and time-domain signal analysis in the presence of FO and STO was not considered.

Fig. 4.1a clearly depicts an uplink scenario in a typical indoor room environment. The omnipresence of LEDs allows their rapid installation in several room environments like multi-national companies, conference halls, auditoriums, etc. Therefore, in such scenarios, each LED acts as an OAP or as a base station meeting the demands of several

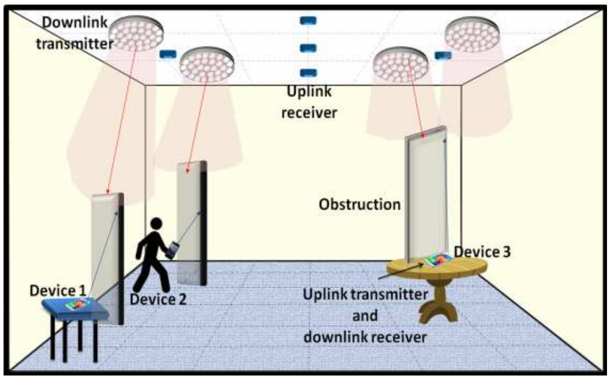

(a) Illustration of uplink scenario in an indoor room environment [191]

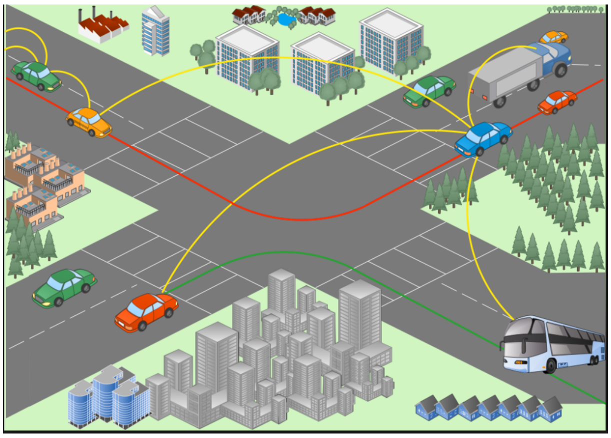

(b) Typical Schematic of vehicular communication exploiting VLC [187]

Figure 4.1: Exploitation of VLC in both indoor and outdoor environments

customers/subscribers which are within the vicinity of lighting fixtures. It is evident from the figure that, in order for the signal from a transmitter LED to reach the receiver terminal, there are several obstacles present. Therefore, due to this multipath propagation, the signal undergoes reflections, refractions due to the presence of walls, floor, ceiling, furniture and people. Therefore, Doppler Shift is inherently present in such kind of environments. As delineated in Fig. 4.1b, there are diverse number of vehicles travelling on road and exchanging data by utilizing the LED-based VLC technology. Therefore, in such kind of scenarios i.e., pertaining to outdoor communication, especially V2V communication, Doppler Shift occurs due to moving vehicles. Accordingly, this necessitates to analyse the deterioration of the received signal in the presence of different offsets. Therefore, this work focuses on the characterization of different sorts of interference which occur due to the existence of offsets.

Hence, it necessitates to investigate the effects of FO and STO on the received signal and to recommend sophisticated synchronization algorithms for estimating them. Accordingly, this chapter encapsulates the detrimental aspects of the aforementioned offsets in both multicarrier and multiple access systems like DCO-OFDM and DCO-OFDMA. Additionally, mathematical expressions are derived highlighting the deterioration of the received signal in the presence of these offsets for both the developed system models. The prominence of imposing different synchronization algorithms to the developed system models are confirmed through simulation results. Besides, CRLB is derived for the estimation of these offsets and is verified through simulation results.

4.2 Synchronization in DCO-OFDM system for VLC

4.2.1 System Model

Fig. 4.2, delineates DCO-OFDM system model which is developed with the inclusion of FO ϵ and STO δ. Elaborate mathematical analysis is done showing the affects of FO and STO. Here, at the transmitter side, the incoming bit stream is first mapped with the help of modulation formats such as M-PSK, M-QAM and M-PAM respectively, and then this serialized data stream is parallelized which is denoted as $X(k)$. Since, modified version of OFDM is prerequisite of optical transmission systems hence, DMT is incorporated,

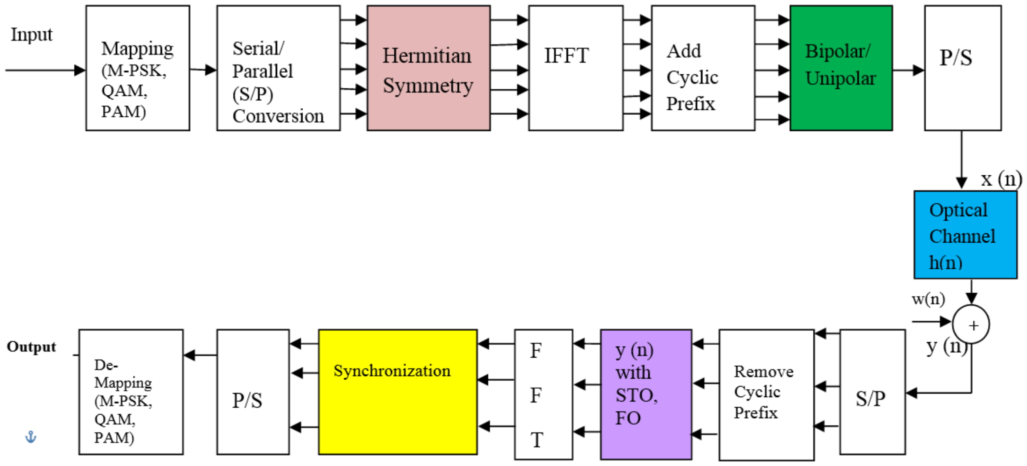

Figure 4.2: Synchronization in optical OFDM for Visible Light Communication

which allows us to work with real valued signal in spite of the usage of IFFT. So, here this parallelized signal is constrained to satisfy Hermitian Symmetry condition. i.e., if there are N number of subcarriers then according to Hermitian Symmetry constraint only $\frac{N}{2}$ are utilized for transmission of data

$$X\left[N-k\right]=X^{*}\left[k\right], \quad k=1,2,\cdots\frac{N}{2} \tag{4.1}$$

The first and the middle subcarrier are assigned zero to avoid the imaginary component in the time-domain signal

$$X\left[0\right]=X\left[\frac{N}{2}\right]=0 \tag{4.2}$$

Here, the signal which is to fed to the IFFT block can be treated as a vector with the following representation

$$X=\left[0,X_{1},X_{2}\cdots X_{\frac{N}{2}-1},0,X_{\frac{N}{2}-1}^{*},\cdots,X_{2}^{*},X_{1}^{*}\right] \tag{4.3}$$

4.2.2 Mathematical Illustration of the effects of FO

This section illustrates the effects of FO on the received signal. In particular, in case of mobile environment, FO arises because of the prevalence of Doppler Shift in both indoor as well as outdoor room environments. Thus, the advantages of OFDM can no longer be warranted by any means because of the loss of orthogonality among the subcarrier frequency components. Consequently, this results in a huge amount of degradation in the BER performance of the overall system. Then, under the effect of FO ϵ, the received signal is derived as follows:

Apparently, it is widely known fact that,

$$y_{l}\left[n\right]=IFFT\left[Y_{l}\left[q\right]\right] \tag{4.4}$$

Where $Y_{l}\left[q\right]=X_{l}\left[q\right]H_{l}\left[q\right]+W_{l}\left[q\right]$, upon substitution of the aforementioned condition in (4.4), the time domain signal when affected with FO of ϵ can be obtained as

$$y_{l}\left[n\right]=\frac{1}{N}\sum_{q=0}^{N-1}X_{l}\left[q\right]H_{l}\left[q\right]e^{\frac{j2\pi(q+\epsilon)n}{N}}+w_{l}\left[n\right] \tag{4.5}$$

$w_{l}\left[n\right]$ in (4.5) represents the AWGN which is given as $w_{l}\left[n\right]=\frac{1}{N}\sum_{q=0}^{N-1}W_{l}\left[q\right]e^{\frac{j2\pi qn}{N}}$.

It is to be noted that for the purpose of attaining a real-valued signal, the frequency domain symbols as represented by $X_l\left[q\right]$ is constrained to satisfy Hermitian Symmetry criteria. Accordingly, the time domain signal as represented in (4.5) when affected with FO is derived as follows: We need to incorporate equations (4.1) and (4.2) for accomplishing the criteria of IM/DD systems.

$$\begin{aligned} y_l\left[n\right] = \frac{1}{N}\Big[& X_l\left[0\right] H\left[0\right] e^{\frac{j2\pi\epsilon n}{N}} + \sum_{q=1}^{\frac{N}{2}-1} X_l\left[q\right] H\left[q\right] e^{\frac{j2\pi(q+\epsilon)n}{N}} \\ & + X_l\left[\frac{N}{2}\right] H\left[\frac{N}{2}\right] e^{\frac{j2\pi\left(\epsilon+\frac{N}{2}\right)n}{N}} + \sum_{q=\frac{N}{2}+1}^{N-1} X_l\left[q\right] H\left[q\right] e^{\frac{j2\pi(q+\epsilon)n}{N}} \Big] + w_l\left[n\right] \quad (4.6) \end{aligned}$$

In (4.6), 1^{st} and the 3^{rd} term are set to zero as $X\left(0\right) = X\left(\frac{N}{2}\right) = 0$. Hence, (4.6) reduces to

$$y_l\left[n\right] = \frac{1}{N}\left[\sum_{q=1}^{\frac{N}{2}-1} X_l\left[q\right] H\left[q\right] e^{\frac{j2\pi(q+\epsilon)n}{N}} + \sum_{q=\frac{N}{2}+1}^{N-1} X_l\left[q\right] H\left[q\right] e^{\frac{j2\pi(q+\epsilon)n}{N}}\right] + w_l\left[n\right] \qquad (4.7)$$

By, performing change in variable i.e., letting $N - q^{'} = q$ and accordingly the limits in the second term in the summation changes as

$$\begin{aligned} y_l\left[n\right] = \frac{1}{N}\Big[& \sum_{q=1}^{\frac{N}{2}-1} X_l\left[q\right] H\left[q\right] e^{\frac{j2\pi(q+\epsilon)n}{N}} + \\ & \sum_{q^{'}=\frac{N}{2}-1}^{1} X_l\left[N-q^{'}\right] H\left[N-q^{'}\right] e^{\frac{j2\pi\left(N-q^{'}+\epsilon\right)n}{N}} \Big] + w_l\left[n\right] \quad (4.8) \end{aligned}$$

After changing the order of limits, (4.8) can be reduced to

$$\begin{aligned} y_l\left[n\right] = \frac{1}{N}\Big[& \sum_{q=1}^{\frac{N}{2}-1} X_l\left[q\right] H\left[q\right] e^{\frac{j2\pi(q+\epsilon)n}{N}} + \\ & \sum_{q^{'}=1}^{\frac{N}{2}-1} X_l\left[N-q^{'}\right] H\left[N-q^{'}\right] e^{\frac{-j2\pi\left(N-q^{'}+\epsilon\right)n}{N}} \Big] + w_l\left[n\right] \quad (4.9) \end{aligned}$$

Since from (4.1), $X\left(N-q\right) = X^{*}\left(q\right),\ q = 1, 2, \cdots \frac{N}{2}$. After substitution and rearranging, (4.9) can be modified as

$$y_l\left[n\right] \ = \ \frac{1}{N}\Big[\sum_{q=1}^{\frac{N}{2}-1} X_l\left(q\right) H\left(q\right) e^{\frac{j2\pi(q+\epsilon)n}{N}} \ + \ \sum_{q=1}^{\frac{N}{2}-1} X_l^{*}\left(q\right) H\left(q\right) e^{\frac{-j2\pi(q+\epsilon)n}{N}}\Big] \ + \ w_l\left[n\right] \quad (4.10)$$

By making use of Euler's Inequalities that $e^{j\theta} = cos\theta + jsin\theta$ and by making use of signal processing identities like $\underset{RC}{x}[n] = \frac{x[n]+x^*[n]}{2}$ and $\underset{IC}{x}[n] = \frac{x[n]-x^*[n]}{2j}$, (4.10) can be solved as

$$y_l[n] = \frac{2}{N}\left[\sum_{q=1}^{\frac{N}{2}-1}\left(\underset{RC}{X_l}[q]cos\left(\frac{2\pi(q+\epsilon)n}{N}\right) - \underset{IC}{X_l}[q]sin\left(\frac{2\pi(q+\epsilon)n}{N}\right)\right)H(q)\right] + w_l[n] \tag{4.11}$$

Clearly, (4.11) illustrates that a real valued signal is attained satisfying the requirements of IM/DD systems. Now, the frequency domain representation of this received signal as represented in (4.11) can be expressed as

$$Y_l[k] = FFT[y_l[n]] \tag{4.12}$$

Therefore,

$$Y_l[k] = \sum_{n=0}^{N-1} y_l[n]\, e^{\frac{-j2\pi nk}{N}} \tag{4.13}$$

Further, upon substituting (4.11) into (4.13), the resultant expression is attained as follows

$$\begin{aligned} Y_l[k] = {} & \frac{2}{N}\sum_{n=0}^{N-1}\left(\sum_{q=1}^{\frac{N}{2}-1}\underset{RC}{X_l}[q]H[q]\,cos\left(\frac{2\pi(q+\epsilon)n}{N}\right)\right)e^{\frac{-j2\pi nk}{N}} - \\ & \frac{2}{N}\sum_{n=0}^{N-1}\left(\sum_{q=1}^{\frac{N}{2}-1}\underset{IC}{X_l}[q]H[q]\,sin\left(\frac{2\pi(q+\epsilon)n}{N}\right)\right)e^{\frac{-j2\pi nk}{N}} + W_l[k] \end{aligned} \tag{4.14}$$

Using the notation that $cos\theta = \frac{e^{j\theta}+e^{-j\theta}}{2}$ and $sin\theta = \frac{e^{j\theta}-e^{-j\theta}}{2j}$ in (4.14) and after substitution and rearranging,

$$\begin{aligned} Y_l[k] = {} & \frac{1}{N}\sum_{q=1}^{\frac{N}{2}-1}\underset{RC}{X_l}[q]H[q]\left\{\sum_{n=0}^{N-1}e^{\frac{j2\pi(q-k+\epsilon)n}{N}}\right\} + \frac{1}{N}\sum_{q=1}^{\frac{N}{2}-1}\underset{RC}{X_l}[q]H[q]\left\{\sum_{n=0}^{N-1}e^{\frac{-j2\pi(q+k+\epsilon)n}{N}}\right\} + \\ & \frac{j}{N}\sum_{q=1}^{\frac{N}{2}-1}\underset{IC}{X_l}[q]H[q]\left\{\sum_{n=0}^{N-1}e^{\frac{j2\pi(q-k+\epsilon)n}{N}}\right\} - \frac{j}{N}\sum_{q=1}^{\frac{N}{2}-1}\underset{IC}{X_l}[q]H[q]\left\{\sum_{n=0}^{N-1}e^{\frac{-j2\pi(q+k+\epsilon)n}{N}}\right\} + \\ & + W_l(k) \end{aligned} \tag{4.15}$$

In order to view the detrimental aspects of FO, we proceed further to yield the below representation:

Taking into consideration two scenarios when $q = k$ and $q \neq k$, the following frequency domain representation is obtained

$$\begin{aligned}Y_l\left[k\right] = &\left(\underset{RC}{X_l\left[k\right]} + j\underset{IC}{X_l\left[k\right]}\right) H\left[k\right]\left[\frac{1}{N}\sum_{n=0}^{N-1} e^{\frac{j2\pi\epsilon n}{N}}\right] + \\ &\left(\underset{RC}{X_l\left[k\right]} - j\underset{IC}{X_l\left[k\right]}\right) H\left[k\right]\left[\frac{1}{N}\sum_{n=0}^{N-1} e^{\frac{-j2\pi(2k+\epsilon)n}{N}}\right] + \\ &\sum_{\substack{q=1\\ q\neq k}}^{\frac{N}{2}-1}\left(\underset{RC}{X_l\left[q\right]} + j\underset{IC}{X_l\left[q\right]}\right) H\left[q\right]\left[\frac{1}{N}\sum_{n=0}^{N-1} e^{\frac{j2\pi(q+\epsilon-k)n}{N}}\right] + \\ &\sum_{\substack{q=1\\ q\neq k}}^{\frac{N}{2}-1}\left(\underset{RC}{X_l\left[q\right]} - j\underset{IC}{X_l\left[q\right]}\right) H\left[q\right]\left[\frac{1}{N}\sum_{n=0}^{N-1} e^{\frac{-j2\pi(q+k+\epsilon)n}{N}}\right] + W_l\left(k\right)\end{aligned} \tag{4.16}$$

Now, together with the noise there are totally 5 terms associated with (4.16) and solving each summation by making use of $\sum_{n=0}^{N-1} r^n = \frac{1-r^N}{1-r}$ yields

$$\begin{aligned}Y_l\left[k\right] = &\left(\underset{RC}{X_l\left[k\right]} + j\underset{IC}{X_l\left[k\right]}\right) H\left[k\right]\left[\frac{sin\pi\epsilon}{Nsin\left(\frac{\pi\epsilon}{N}\right)}\right] e^{\frac{j\pi\epsilon(N-1)}{N}} + \\ &\left(\underset{RC}{X_l\left[k\right]} - j\underset{IC}{X_l\left[k\right]}\right) H\left[k\right]\left[\frac{sin\pi\left(\epsilon+2k\right)}{Nsin\pi\left(\frac{\epsilon+2k}{N}\right)}\right] e^{\frac{-j\pi(2k+\epsilon)(N-1)}{N}} + \\ &\sum_{\substack{q=1\\ q\neq k}}^{\frac{N}{2}-1}\left(\underset{RC}{X_l\left[q\right]} + j\underset{IC}{X_l\left[q\right]}\right) H\left[q\right]\left[\frac{sin\pi\left(q-k+\epsilon\right)}{Nsin\pi\left(\frac{q-k+\epsilon}{N}\right)}\right] e^{\frac{j\pi(q-k+\epsilon)(N-1)}{N}} + \\ &\sum_{\substack{q=1\\ q\neq k}}^{\frac{N}{2}-1}\left(\underset{RC}{X_l\left[q\right]} - j\underset{IC}{X_l\left[q\right]}\right) H\left[q\right]\left[\frac{sin\pi\left(q+k+\epsilon\right)}{Nsin\pi\left(\frac{q+k+\epsilon}{N}\right)}\right] e^{\frac{-j\pi(q+k+\epsilon)(N-1)}{N}} + W_l\left[k\right]\end{aligned} \tag{4.17}$$

As seen here in (4.17), the 3^{rd} and 4^{th} terms in the summation represent ICI from other subcarriers and is denoted by $I_l\left[k\right]$ which can be expressed as

$$\begin{aligned}I_l\left[k\right] = &\sum_{\substack{q=1\\ q\neq k}}^{\frac{N}{2}-1}\left(\underset{RC}{X_l\left[q\right]} + j\underset{IC}{X_l\left[q\right]}\right) H\left[q\right]\left[\frac{sin\pi\left(q-k+\epsilon\right)}{Nsin\pi\left(\frac{q-k+\epsilon}{N}\right)}\right] e^{\frac{j\pi(q-k+\epsilon)(N-1)}{N}} + \\ &\sum_{\substack{q=1\\ q\neq k}}^{\frac{N}{2}-1}\left(\underset{RC}{X_l\left[q\right]} - j\underset{IC}{X_l\left[q\right]}\right) H\left[q\right]\left[\frac{sin\pi\left(q+k+\epsilon\right)}{Nsin\pi\left(\frac{q+k+\epsilon}{N}\right)}\right] e^{\frac{-j\pi(q+k+\epsilon)(N-1)}{N}}\end{aligned} \tag{4.18}$$

Finally, upon rearranging equation (4.17), the final expression of the frequency domain signal can be obtained as

$$\begin{gathered}Y_l\left[k\right] = \left(\underset{RC}{X_l\left[k\right]} + j\underset{IC}{X_l\left[k\right]}\right) H\left[k\right] \left[\frac{sin\pi\epsilon}{Nsin\left(\frac{\pi\epsilon}{N}\right)}\right] e^{\frac{j\pi\epsilon(N-1)}{N}} + \\ \left(\underset{RC}{X_l\left[k\right]} - j\underset{IC}{X_l\left[k\right]}\right) H\left[k\right] \left[\frac{sin\pi\left(\epsilon+2k\right)}{Nsin\pi\left(\frac{\epsilon+2k}{N}\right)}\right] e^{\frac{-j\pi(2k+\epsilon)(N-1)}{N}} + I_l\left[k\right] + W_l\left[k\right]\end{gathered} \tag{4.19}$$

It is clearly evident from equation (4.19) that ICI is occurring from neighbouring subcarriers into the k^{th} sub carrier, which further implies that the orthogonality among the sub carriers is destroyed.

4.2.3 Mathematical Illustration of the effects of STO

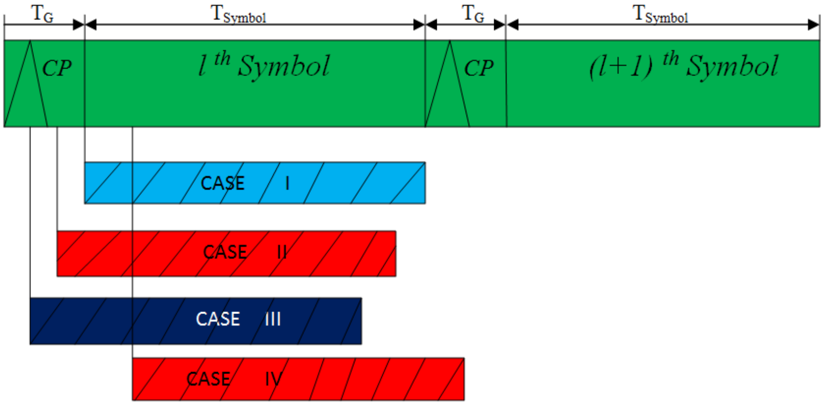

Figure 4.3: Illustration of STO on the received signal

Perfect timing synchronization is prerequisite to ensure a reliable communication. In this regard, it is essential to know the effect of STO on the received signal. Fig. 4.3, shows the pictorial representation which helps to elaborately view the effects of STO on the received signal. From the figure, it is clearly evident that there are four scenarios of timing offset where in the first case, the estimated starting point perfectly matches with the exact timing instance, for the second scenario it is a little earlier, whereas, in the third scenario it is too early, while in the last case, it is little later than the exact timing instance [177].

- **CASE I:** In this scenario, there is a perfect timing synchronization because there is a perfect coincidence between the estimated starting point of the optical OFDM symbol and the timing interval, thereby preserving the orthogonality among the subcarriers. Hence, in this scenario there is perfect recovery of the symbol without getting affected by any type of interference.

- **CASE II:** Here, the estimated point is earlier than the timing instant. It is apparent that, FFT and IFFT play a vital role at both the transmitting and receiving end of an optical or conventional OFDM system. The essential prerequisite for performing the N-point FFT operation at the receiving end is to ensure that the exact samples of the transmitted signal are obtained within the symbol duration. Let, $x\left[n\right]$ represent the time-domain signal which is the output from the IFFT block.

$$IFFT\left[X_l\left(u\right)\right] = x_l\left[n\right] \tag{4.20}$$

$$x_l[n] = \frac{1}{N}\sum_{u=0}^{N-1} X_l\left[u\right] e^{\frac{j2\pi nu}{N}} \tag{4.21}$$

Similarly, the time domain samples when affected with STO of δ can be expressed as

$$x_l[n+\delta] = \frac{1}{N}\sum_{u=0}^{N-1} X_l\left[u\right] e^{\frac{j2\pi(n+\delta)u}{N}} \tag{4.22}$$

Therefore, the signal which is received under the effect of STO can be put up as

$$Y_l\left[k\right] = \frac{1}{N}\sum_{n=0}^{N-1} x_l\left[n+\delta\right] e^{\frac{-j2\pi nk}{N}} \tag{4.23}$$

Since the input $X_l\left[u\right]$ needs to satisfy Hermitian Symmetry hence, there is a modification which has to be taken into account as follows

$$Y_l\left[k\right] = \frac{1}{N}\sum_{n=0}^{N-1}\left[\sum_{u=0}^{N-1} X_l\left[u\right] e^{\frac{j2\pi(n+\delta)u}{N}}\right] e^{\frac{-j2\pi nk}{N}} \tag{4.24}$$

$$Y_l\left[k\right] = \frac{1}{N}\sum_{n=0}^{N-1}\left[\sum_{u=1}^{\frac{N}{2}-1} X_l\left[u\right] e^{\frac{j2\pi(n+\delta)u}{N}} + \sum_{u=\frac{N}{2}+1}^{N-1} X_l\left[u\right] e^{\frac{j2\pi(n+\delta)u}{N}}\right] e^{\frac{-j2\pi nk}{N}} + W_l\left[k\right] \tag{4.25}$$

After applying change in variable and solving, finally the received signal in DCO-OFDM system under the effect of STO is represented as

$$Y_l\left[k\right] = \frac{2}{N}\sum_{n=0}^{N-1}\left[\sum_{u=1}^{\frac{N}{2}-1}\left(\underset{RC}{X_l\left[u\right]}cos\left(\frac{2\pi\left(n+\delta\right)u}{N}\right) - \underset{IC}{X_l\left[u\right]}sin\left(\frac{2\pi\left(n+\delta\right)u}{N}\right)\right)\right] e^{\frac{-j2\pi nk}{N}} + W_l\left[k\right] \tag{4.26}$$

On observing equation (4.26), it clearly represents a real signal satisfying the requirement of IM/DD system as light intensity cannot be a complex signal. Now, for this received signal, derivation is done to show the effect of STO in the received signal. By employing Euler's inequalities, the frequency domain representation of the received signal can be solved to attain

$$
\begin{aligned}
Y_l\,[k] = {} & \frac{1}{N}\sum_{u=1}^{\frac{N}{2}-1} \underset{RC}{X_l\,[u]} e^{\frac{j2\pi\delta u}{N}} \left[\sum_{n=0}^{N-1} e^{\frac{j2\pi(u-k)n}{N}}\right] + \\
& \frac{1}{N}\sum_{u=1}^{\frac{N}{2}-1} \underset{RC}{X_l\,[u]} e^{-\frac{j2\pi\delta u}{N}} \left[\sum_{n=0}^{N-1} e^{-\frac{j2\pi(u+k)n}{N}}\right] + \\
& \frac{j}{N}\sum_{u=1}^{\frac{N}{2}-1} \underset{IC}{X_l\,[u]} e^{\frac{j2\pi\delta u}{N}} \left[\sum_{n=0}^{N-1} e^{\frac{j2\pi(u-k)n}{N}}\right] - \\
& \frac{j}{N}\sum_{u=1}^{\frac{N}{2}-1} \underset{IC}{X_l\,[u]} e^{-\frac{j2\pi\delta u}{N}} \left[\sum_{n=0}^{N-1} e^{-\frac{j2\pi(u+k)n}{N}}\right] + W_l\,[k]
\end{aligned}
\tag{4.27}
$$

Solving for the two scenarios: i.e., when $u = k$ and $u \neq k$, the frequency domain representation can be derived as

$$
\begin{aligned}
Y_l\,(k) = {} & \left(\underset{RC}{X_l\,[K]} + \underset{IC}{X_l\,[k]}\right) e^{\frac{j2\pi k\delta}{N}} + \\
& \frac{1}{N}\sum_{\substack{u=1\\u\neq k}}^{\frac{N}{2}-1} \left(\underset{RC}{X_l\,[u]} + j\underset{IC}{X_l\,[k]}\right) e^{\frac{j2\pi u\delta}{N}} \left[\frac{sin\left(\pi\left(u-k\right)\right)}{N sin\left(\frac{\pi(u-k)}{N}\right)}\right] e^{\frac{j\pi(u-k)(N-1)}{N}} + \\
& \frac{1}{N}\sum_{\substack{u=1\\u\neq k}}^{\frac{N}{2}-1} \left(\underset{RC}{X_l\,[u]} - j\underset{IC}{X_l\,[u]}\right) e^{\frac{-j2\pi u\delta}{N}} \left[\frac{sin\left(\pi\left(u+k\right)\right)}{N sin\left(\frac{\pi(u+k)}{N}\right)}\right] e^{\frac{-j\pi(u+k)(N+1)}{N}} + W_l\,(k)
\end{aligned}
\tag{4.28}
$$

On carefully examining (4.28) the received signal is not only affected by amplitude and phase distortion but also due to ICI from other subcarriers. Hence, the above equation emphasizes that the orthogonality is no longer warranted.

- **CASE III:** In this scenario, as depicted from the figure, the present symbol overlaps with the previous symbol. This signifies that this scenario is prone to ISI leading to the disruption in the orthogonality among the sub-carrier components and besides, ICI can also occur.

- **CASE IV:** This scenario evidences a timing mismatch i.e., there is no perfect timing synchronization as the signal within the timing instant consists of a part of the current optical OFDM symbol $x_l\left[n\right]$ and some portion of the next symbol i.e., $x_{l+1}\left[n\right]$. Therefore, the signal received under such scenario can be represented as [177]

$$y_l\left[n\right] = \begin{cases} x_l\left[n+\delta\right] & for \quad 0 \leq n \leq N-1-\delta \\ x_{l+1}\left[n+2\delta-N_g\right] & for \quad N-\delta \leq n \leq N-1 \end{cases} \tag{4.29}$$

Thus, by making use of time-domain signal as represented in (4.29), the frequency domain representation of the signal can be expressed as

$$Y_l\left[k\right] = \sum_{n=0}^{N-1-\delta} x_l\left[n+\delta\right] e^{\frac{-j2\pi nk}{N}} + \sum_{n=N-\delta}^{N-1} x_{l+1}\left[n+2\delta-N_g\right] e^{\frac{-j2\pi nk}{N}} + W_l\left(k\right) \tag{4.30}$$

Where, $x_l\left[n\right]$ in (4.30) denotes the IFFT output and N_g depicts the length of the guard interval. Here, the input to the IFFT i.e., $X_l\left[u\right]$ must satisfy Hermitian Symmetry in order to yield a real valued signal. However, in order to make the signal unipolar, certain amount of DC bias is added. Hence, similarly

$$\begin{aligned} Y_l\left[k\right] = &\sum_{n=0}^{N-1-\delta} \left[\frac{1}{N}\sum_{u=0}^{N-1} X_l\left[u\right] e^{\frac{j2\pi(n+\delta)u}{N}}\right] e^{\frac{-j2\pi nk}{N}} \\ &+ \sum_{n=N-\delta}^{N-1} \left[\frac{1}{N}\sum_{u=0}^{N-1} X_{l+1}\left[u\right] e^{\frac{j2\pi\left(n+2\delta-N_g\right)u}{N}}\right] e^{\frac{-j2\pi nk}{N}} + W_l\left[k\right] \end{aligned} \tag{4.31}$$

By incorporating the necessary pre-requisites of IM/DD systems, (4.31) can be modified as

$$\begin{aligned} Y_l\left[k\right] = &\sum_{n=0}^{N-1-\delta} \Big[\frac{2}{N}\sum_{u=1}^{\frac{N}{2}-1} \Big(\underset{RC}{X_l}[u] cos\left(\frac{2\pi\left(n+\delta\right)u}{N}\right) - \\ &\qquad \underset{IC}{X_l}[u] sin\left(\frac{2\pi\left(n+\delta\right)u}{N}\right)\Big)\Big] e^{\frac{-j2\pi nk}{N}} + \\ &\sum_{n=N-\delta}^{N-1} \Big[\frac{2}{N}\sum_{u=1}^{\frac{N}{2}-1} \Big(\underset{RC}{X_{l+1}}[u] cos\left(\frac{2\pi\left(n+2\delta-N_g\right)u}{N}\right) - \\ &\qquad \underset{IC}{X_{l+1}}[u] sin\left(\frac{2\pi\left(n+2\delta-N_g\right)u}{N}\right)\Big)\Big] e^{\frac{-j2\pi nk}{N}} + W_l\left[k\right] \end{aligned} \tag{4.32}$$

(4.32) denotes that the signal is severely affected due to the existence of timing mismatch which is nothing but the presence of STO. In order to see the effect of

STO in DCO-OFDM we need to proceed further to obtain

$$\begin{aligned}
Y_l\left[k\right] = & \left(\frac{N-\delta}{N}\right)\left(X_{\underset{RC}{l}}\left[k\right] + jX_{\underset{IC}{l}}\left[k\right]\right)e^{\frac{j2\pi\delta k}{N}} + \\
& \left(X_{\underset{RC}{l}}\left[k\right] - jX_{\underset{IC}{l}}\left[k\right]\right)\left[\frac{sin\left(\frac{2\pi(N-\delta)k}{N}\right)}{Nsin\left(\frac{2\pi k}{N}\right)}\right]e^{\frac{-j2\pi(N-1)k}{N}} + \\
& \sum_{\substack{u=1\\u\neq k}}^{\frac{N}{2}-1}\left(X_{\underset{RC}{l}}\left[u\right] + jX_{\underset{IC}{l}}\left[u\right]\right)e^{\frac{j2\pi\delta u}{N}}\left[\frac{sin\left(\frac{\pi(u-k)(N-\delta)}{N}\right)}{Nsin\left(\frac{\pi(u-k)}{N}\right)}\right]e^{\frac{j\pi(u-k)(N-\delta-1)}{N}} + \\
& \sum_{\substack{u=1\\u\neq k}}^{\frac{N}{2}-1}\left(X_{\underset{RC}{l}}\left[u\right] - jX_{\underset{IC}{l}}\left[u\right]\right)e^{-\frac{j2\pi\delta u}{N}}\left[\frac{sin\left(\frac{\pi(u+k)(N-\delta)}{N}\right)}{Nsin\left(\frac{\pi(u+k)}{N}\right)}\right]e^{-\frac{j\pi(u+k)(N-\delta-1)}{N}} + \\
& \sum_{n=N-\delta}^{N-1}\left[\frac{2}{N}\sum_{u=1}^{\frac{N}{2}-1}\left(X_{\underset{RC}{l+1}}[u]cos\left(\frac{2\pi\left(n+2\delta-N_g\right)u}{N}\right) - \right.\right. \\
& \left.\left. X_{\underset{IC}{l+1}}[u]sin\left(\frac{2\pi\left(n+2\delta-N_g\right)u}{N}\right)\right)\right]e^{\frac{-j2\pi nk}{N}} + W_l\left[k\right] \qquad (4.33)
\end{aligned}$$

(4.33) emphasizes that the signal has been severely affected due to presence of STO. The first two terms of (4.33) represent that the signal has been affected due to amplitude and phase distortions. While, the 3^{rd} and 4^{th} term illustrate the ICI from the neighbouring sub-carrier components and the 5^{th} term represent the ISI due to the presence of next optical OFDM symbol $X_{\underset{RC}{l+1}}\left[u\right]$.

4.3 Synchronization Algorithms

Mathematical analysis has been carried out in the previous sections showing that the existence of FO and STO critically degrades the performance of the system. This is evident from the derived equations which clearly emphasizes that the orthogonality among the sub-carrier frequency components is no longer assured. Hence, at the receiver side, for successful reception of the transmitted signal, estimation of these offsets and compensation of them is essential. This can be achieved by employing synchronization algorithms. Here, this section revisits the synchronization algorithms such as Moose, Classen and Training symbol aided sequences. However, the synchronization algorithms as used in traditional RF-based optical OFDM cannot be directly enforced in a straightforward manner pertaining to optical OFDM i.e., DCO-OFDM system because of the constraint of real and positive signal transmission.

Training Symbol Based

Here, by incorporation of reduction in the distance between two blocks of samples for correlation, the range of FO estimation can be increased. This can be achieved by making use of the training symbols that are repetitive with some shorter period. The ratio of the optical OFDM symbol length to the length of a repetitive pattern is denoted by D which is an integer. If the transmitter transmits the training symbols with D repetitive patterns in the time domain, then these can be generated in the frequency domain by employing the IFFT of a comb-type signal and is given as

$$X_l\left[k\right] = \begin{cases} A_m, \quad if\ k = D.i,\ i = 0, 1, \cdots \left(\frac{N}{D} - 1\right) \\ 0\ \ , \quad if\ otherwise \end{cases} \tag{4.34}$$

Therefore, the receiver can make FO estimation as follows

$$\hat{\epsilon} = \frac{D}{2\pi} arg \left\{ \sum_{n=0}^{\frac{N}{D}-1} y_l^*\left[n\right] y_l \left[n + \frac{N}{D}\right] \right\} \tag{4.35}$$

Moose

Here, the idea proposed by Moose is incorporated, but it is applied with a slight modification to DCO-OFDM under optical channel environment. The basic idea behind Moose algorithm is to repeat the OFDM transmission symbol. In precise, if the OFDM transmission symbol is repeated, then the received signal in the absence of noise would be received as a $2N$ point sequence, this is familiar with respect to conventional RF communication. But, the case with optical OFDM is slightly different. In order to achieve a real signal, Hermitian Symmetry constraint is imposed and due to this, out of N subcarriers only $\frac{N}{2}$ are used for carrying data and rest are flipped complex conjugates of the previous ones. Hence, if the optical OFDM transmission symbol is repeated then one receives in the presence of FO and optical channel effect

$$r_n = \frac{2}{N} \left[\sum_{k=1}^{N-1} \underset{RC}{X\left[k\right]} H\left[k\right] cos \left(\frac{2\pi \left(k + \epsilon\right) n}{N} \right) \right] \tag{4.36}$$

in (4.36), sin component is ignored by considering the assumption that sin multiples of π is 0. The N point FFT of the first N points is

$$R_1\left[k\right] = \sum_{n=0}^{N-1} r_n e^{\frac{-j2\pi nk}{N}} \tag{4.37}$$

The second half of the sequence is represented as:

$$R_2\left[k\right] = \sum_{n=N}^{2N-1} r_n e^{\frac{-j2\pi nk}{N}} \tag{4.38}$$

Applying some change in variable transformation then (4.38) reduces to

$$R_2\left[k\right] = \sum_{n=0}^{N-1} r_{n+N} e^{\frac{-j2\pi nk}{N}} \tag{4.39}$$

Solving (4.36), the following representation can be attained

$$r_{n+N} = r_n cos\left(2\pi\epsilon\right) \tag{4.40}$$

The relationship between the first and the second sequence can be put up as follows

$$Y_1\left[k\right] = R_1\left[k\right] + W_1\left[k\right] \tag{4.41}$$

$$Y_2\left[k\right] = R_1\left[k\right] cos\left(2\pi\epsilon\right) + W_2\left[k\right] \tag{4.42}$$

The FO estimation error is given by Moose in [192].

Classen

Here, the pilot tones are inserted into the frequency domain based on a specific pilot arrangement called as comb type pilot arrangement. The received time domain signals $y_l\left[n\right]$ and $y_{l+D}\left[n\right]$ are stored in the memory. Recall that the received signal $y_l\left[n\right]$ is represented as

$$y_l\left[n\right] = x_l\left[n\right] * h\left[n\right] + w\left[n\right] \tag{4.43}$$

Where, the impulse response of the optical channel environment is denoted by $h\left[n\right]$ and $w\left[n\right]$ is the ambient and shot noise which is modelled as AWGN of 0 $Mean$ and σ^2 $variance$. $x_l\left[n\right]$ is the time domain signal which is obtained from the output of IFFT.

Taking into the consideration of IM/DD systems where, the input of the IFFT is forced to have Hermitian Symmetry condition. Therefore, the resultant time-domain signal is

$$x_l\left[n\right] = \frac{2}{N}\left[\sum_{k=1}^{\frac{N}{2}-1}\left(\underset{RC}{X_l}\left[k\right]cos\left(\frac{2\pi nk}{N}\right) - \underset{IC}{X_l}\left[k\right]sin\left(\frac{2\pi nk}{N}\right)\right)\right] \tag{4.44}$$

From (4.44), it can be emphasized that a real value time-domain signal is attained. But, we can't assure for its unipolarity, hence in order to transform it to real and unipolar a certain amount of DC bias B_{DC} is added. So, (4.44) can be modified as

$$\underset{Unipolar}{x_l\left[n\right]} = x_l\left[n\right] + B_{DC} \tag{4.45}$$

Where, DC bias is defined in the literature as

$$B_{DC} = 10log_{10}\left(k^2+1\right)dB \tag{4.46}$$

In (4.46), k represents the clipping factor. Using (4.43), the received signal can be solved to obtain

$$y_l\left[n\right] = \sum_{l=0}^{L-1} h\left[l\right]\underset{Unipolar}{x_l\left[n-l\right]} + z\left[n\right] \tag{4.47}$$

L represent the number of paths denoting a multipath channel model. And, at the receiver, the signals $y_l\left[n\right]$ and $y_{l+D}\left[n\right]$ are transformed back into the frequency domain by employing the FFT operation to obtain $Y_l\left[k\right]$ and $Y_{l+D}\left[k\right]$. Pilot tones are then extracted after performing the FFT operation. Hence, after estimation of FO from the pilot symbols in the frequency domain, the signal is compensated in the time domain with the estimated FO. In this regard, two different modes of estimation for FO such as Acquisition and Tracking mode are implemented. The range of FO estimated is large for the acquisition mode, whereas, fine FO is estimated for tracking mode. The FO which is estimated in the former is having the following representation [177]

$$\begin{aligned}\underset{acqui}{\hat{\epsilon}} = \frac{1}{2\pi T_{sub}}\underset{\epsilon}{max}\Bigg\{\Bigg|\sum_{u=0}^{N_p-1} & Y_{l+D}\left[p\left[u\right],\epsilon\right]Y_l^*\left[p\left[u\right],\epsilon\right] \\ & X_{l+D}^*\left[p\left[u\right]\right]X_l\left[p\left[u\right]\right]\Bigg|\Bigg\}\end{aligned} \tag{4.48}$$

Where,

- N_p represents the number of pilot tones which are inserted.
- $p\left[u\right]$ denotes the location of the u^{th} pilot tone.

- $X_l\left[p\left[u\right]\right]$ is the pilot tone which is located at $p\left[u\right]^{th}$ position in the frequency domain corresponding to the l^{th} symbol period.

Meanwhile, fine FO can be estimated as

$$\hat{\epsilon_f} = \frac{1}{2\pi T_{sub}D} arg\Big\{\Big| \sum_{u=0}^{N_p-1} Y_{l+D}\left[p\left[u\right], \underset{acqui}{\hat{\epsilon}}\right] Y_l^*\left[p\left[u\right], \underset{acqui}{\hat{\epsilon}}\right] X_{l+D}^*\left[p\left[u\right]\right] X_l\left[p\left[u\right]\right]\Big|\Big\} \tag{4.49}$$

Here, the FO is compensated by their sum.

4.4 CRLB for the estimators

This section derives the CRLB for FO and STO estimators by incorporating the joint parameter estimation by taking into consideration the AWGN channel environment. In general, the signal which is received under the combined effects of both STO and FO can be represented as

$$y\left[n\right] = IFFT\left[Y\left[k\right]\right] \tag{4.50}$$

$Y\left[k\right]$ in (4.50) can be expressed as

$$Y\left[k\right] = X\left[k\right] + W\left[k\right] \tag{4.51}$$

Upon substituting (4.51) into (4.50) results into

$$y\left[n\right] = IFFT\left[X\left[k\right]\right] + w\left[n\right] \tag{4.52}$$

$w\left[n\right]$ in (4.52) signifies the noise component which is a Gaussian random variable. Particularly, every Gaussian random variable is characterized by mean and variance. Consequently, $w\left[n\right]$ can be described as a Gaussian random variable with mean 0 and variance σ^2. Typically, this can be manifested as: $w\left[n\right] \sim N\left(0, \sigma^2\right)$. On further solving (4.52) by incorporating all the constraints that are necessary for IM/DD systems yields the resultant equation

$$y\left[n\right] = \frac{2}{N}\sum_{k=1}^{\frac{N}{2}-1}\left[\underset{RC}{X}\left[k\right] cos\left(\frac{2\pi\left(n+\alpha\right)\left(k+\beta\right)}{N}\right) - \underset{IC}{X}\left[k\right] sin\left(\frac{2\pi\left(n+\alpha\right)\left(k+\beta\right)}{N}\right)\right] + w\left[n\right] \tag{4.53}$$

From (4.53), it is clearly evident that, the parameters α and β to be estimated are hidden. So we make certain assumptions before we proceed further to attain the CRLB for STO and FO respectively. Let, $\frac{2\pi(n+\alpha)(k+\beta)}{N} = \mu$ and the parameters to be estimated be represented in a matrix format as $\Theta = [\alpha\ \beta]^T$. Therefore, we need to make joint parameter estimation. The Fisher Information Matrix can be formulated as [154]

$$[I(\Theta)]_{ij} = \frac{1}{\sigma^2}\sum_{n=0}^{N-1}\frac{\partial}{\partial\Theta_i}S[n,\Theta]\frac{\partial}{\partial\Theta_j}S[n,\Theta] \tag{4.54}$$

Where

$$S[n,\Theta] = \frac{2}{N}\sum_{k=1}^{\frac{N}{2}-1}\left[\underset{RC}{X}[k]cos\mu - \underset{IC}{X}[k]sin\mu\right] \tag{4.55}$$

We are interested in computing the Fisher Information pertaining to the estimates of the offsets α and β. The Fisher Information matrix pertaining to the estimation of timing offset of α can be formulated as

$$[I(\Theta)]_{11} = [I(\alpha)]_{11} = \frac{1}{\sigma^2}\sum_{n=0}^{N-1}\left[\frac{\partial}{\partial\alpha}S(n,\alpha)\right]^2 \tag{4.56}$$

It is to be noted that μ in (4.55) is a function of α. Hence, $\frac{\partial}{\partial\alpha}(cos\mu) = -(sin\mu)\left(\frac{2\pi(k+\beta)}{N}\right)$. Therefore, the Fisher Information Matrix as stated in (4.56) can be solved to attain

$$[I[\alpha]]_{11} = \frac{16\pi^2}{\sigma^2 N^4}\sum_{n=0}^{N-1}\left[\sum_{k=1}^{\frac{N}{2}-1}\left(-(k+\beta)\underset{RC}{X}[k]sin\mu - (k+\beta)\underset{IC}{X}[k]cos\mu\right)\right]^2 \tag{4.57}$$

(4.57) can be further solved to attain

$$[I[\alpha]]_{11} = \frac{16\pi^2}{\sigma^2 N^4}\sum_{n=0}^{N-1}\left(\sum_{k=1}^{\frac{N}{2}-1}(k+\beta)\underset{RC}{X}[k]sin\mu\right)^2 + \frac{16\pi^2}{\sigma^2 N^4}\sum_{n=0}^{N-1}\sum_{k=1}^{\frac{N}{2}-1}(k+\beta)^2\underset{RC}{X}[k]\underset{IC}{X}[k]sin(2\mu) + \frac{16\pi^2}{\sigma^2 N^4}\sum_{n=0}^{N-1}\left(\sum_{k=1}^{\frac{N}{2}-1}(k+\beta)\underset{IC}{X}[k]cos\mu\right)^2 \tag{4.58}$$

The second term in (4.58) can be set to zero with an assumption that for large values of N, $\sum_{n=0}^{N-1} sin(2\mu) = 0$. Then (4.58) can be reduced to

$$[I[\alpha]]_{11} = \frac{16\pi^2}{\sigma^2 N^4}\sum_{n=0}^{N-1}\left(\sum_{k=1}^{\frac{N}{2}-1}(k+\beta)\underset{RC}{X}[k]sin\mu\right)^2 + \frac{16\pi^2}{\sigma^2 N^4}\sum_{n=0}^{N-1}\left(\sum_{k=1}^{\frac{N}{2}-1}(k+\beta)\underset{IC}{X}[k]cos\mu\right)^2 \tag{4.59}$$

Here, in order to obtain a closed form estimate we employ certain assumptions that for higher values of μ, $sin\mu \simeq \mu$ and $cos\mu = 0$ in (4.59) to obtain

$$[I\left[\alpha\right]]_{11} = \frac{64\pi^4}{\sigma^2 N^6} \sum_{n=0}^{N-1} \left(n+\alpha\right)^2 \left(\sum_{k=1}^{\frac{N}{2}-1} \left(k+\beta\right)^2 \underset{RC}{X}[k] \right)^2 \tag{4.60}$$

Further (4.60) can be solved to attain

$$[I\left[\alpha\right]]_{11} = \frac{64\pi^4}{\sigma^2 N^6} \sum_{n=0}^{N-1} \left(n^2+2n\alpha+\alpha^2\right) \left(\sum_{k=1}^{\frac{N}{2}-1} \left(k+\beta\right)^2 \underset{RC}{X}[k] \right)^2 \tag{4.61}$$

The first summation in (4.61) can be solved by using the power series concept where the summation terms are given as $\sum_{n=0}^{n-1} = \frac{n(n+1)}{2}$, $\sum_{n=0}^{n-1} n^2 = \frac{n(n+1)(2n+1)}{6}$. Hence, upon solving (4.61), the Fisher Information Matrix regarding the estimation of timing offset STO of α is given as evaluated in equation (4.62).

$$[I\left[\alpha\right]]_{11} = \frac{32\pi^4}{\sigma^2 N^5} \left[\frac{2N^2+3N\left(1+2\alpha\right)+6\alpha\left(1+\alpha\right)+1}{3} \right] \left[\sum_{k=1}^{\frac{N}{2}-1} \left(k+\beta\right)^2 \underset{RC}{X}[k] \right]^2 \tag{4.62}$$

Accordingly, the variance of the estimate α which is denoted as $V\left(\hat{\alpha}\right)$ is given as

$$V\left[\hat{\alpha}\right] \geq \left[I\left(\alpha\right)\right]_{11}^{-1} \tag{4.63}$$

$$V\left(\hat{\alpha}\right) \geq \frac{3\sigma^2 N^5}{32\pi^4} \times \frac{1}{\left[2N^2+3N\left(1+2\alpha\right)+6\alpha\left(1+\alpha\right)+1\right] \left[\sum_{k=1}^{\frac{N}{2}-1} \left(k+\beta\right)^2 \underset{RC}{X}[k] \right]^2} \tag{4.64}$$

Secondly, the Fisher Information Matrix pertaining to FO β can be formulated as

$$\left[I\left(\Theta\right)\right]_{22} = \frac{1}{\sigma^2} \sum_{n=0}^{N-1} \left[\frac{\partial}{\partial\beta} S\left(n,\beta\right) \right]^2 \tag{4.65}$$

The differentiation operator as stated in (4.65) is a function of unknown parameter β which is to be estimated. Thereupon, the Fisher Information Matrix can be solved as

$$\left[I\left(\Theta\right)\right]_{22} = \left[I\left(\beta\right)\right]_{22} =$$

$$\frac{1}{\sigma^2} \sum_{n=0}^{N-1} \left\{ \frac{2}{N} \sum_{k=1}^{\frac{N}{2}-1} \left[-\underset{RC}{X}[k] sin\mu \left(\frac{2\pi\left(n+\alpha\right)}{N} \right) - \underset{IC}{X}[k] cos\mu \left(\frac{2\pi\left(n+\alpha\right)}{N} \right) \right] \right\}^2 \tag{4.66}$$

In the similar manner, upon incorporating the aforementioned assumptions, the Fisher Information Matrix for the estimation of FO as shown in (4.66) can be re-arranged to attain

$$[I\left[\beta\right]]_{22} = \frac{16\pi^2}{\sigma^2 N^4} \sum_{n=0}^{N-1} \left(n+\alpha\right)^2 \left[\left(\sum_{k=1}^{\frac{N}{2}-1} \underset{RC}{X}[k]\mu \right)^2 \right] \tag{4.67}$$

Upon substituting the value of μ in (4.67) yields,

$$[I[\beta]]_{22} = \frac{64\pi^4}{\sigma^2 N^6} \sum_{n=0}^{N-1} (n+\alpha)^4 \left(\sum_{k=1}^{\frac{N}{2}-1} (k+\beta) \underset{RC}{X[k]} \right)^2 \tag{4.68}$$

Further (4.68) can be solved as

$$[I[\beta]]_{22} = \frac{64\pi^4}{\sigma^2 N^6} \sum_{n=0}^{N-1} \left(n^4 + 4n^3\alpha + 6n^2\alpha^2 + 4n\alpha^3 + \alpha^4\right) \left(\sum_{k=1}^{\frac{N}{2}-1} (k+\beta) \underset{RC}{X[k]} \right)^2 \tag{4.69}$$

In (4.68), solving for the summation using $\sum_{n=0}^{N-1} n^4 = \frac{N(N+1)(2N+1)\left(3N^2+3N-1\right)}{30}$, $\sum_{n=0}^{N-1} n^3 = \frac{N^2(N+1)^2}{4}$ yields the Fisher Information Matrix for the estimation of FO as represented in equation (4.70).

$$[I(\beta)]_{22} = \frac{32\pi^4}{\sigma^2 N^5} \Big[6N^4 + 15N^3(1+2\alpha) + 10N^2(1+6\alpha(1+\alpha)) + \\ 30\alpha N\left(1+3\alpha+2\alpha^2\right) + \left(30\alpha_2(1+\alpha)^2 - 1\right) \Big] \left[\sum_{k=1}^{\frac{N}{2}-1} (k+\beta) \underset{RC}{X[k]} \right]^2 \tag{4.70}$$

$$V\left[\hat{\beta}\right] \geq [I(\beta)]_{22}^{-1} \tag{4.71}$$

Finally, substituting (4.70) into (4.71) yields the estimate of β as follows

$$V\left[\hat{\beta}\right] \geq \frac{\sigma^2 N^5}{32\pi^4} \times \Big[6N^4 + 15N^3(1+2\alpha) + 10N^2(1+6\alpha(1+\alpha)) + \\ 30\alpha N\left(1+3\alpha+2\alpha^2\right) + \left(30\alpha_2(1+\alpha)^2 - 1\right) \Big]^{-1} \left[\sum_{k=1}^{\frac{N}{2}-1} (k+\beta) \underset{RC}{X[k]} \right]^{-2} \tag{4.72}$$

4.5 Synchronization aspects in DCO-OFDMA-based IM/DD systems for VLC

4.5.1 System Model

The primary goal associated in the design of any communication system is to render high data rate transmission. Accordingly, this work analyzes the performance of a spectral-efficient DCO-OFDMA system as a candidate system. The pictorial representation of a basic cellular mobile communication scenario is delineated in Fig. 4.4a and 4.4b.

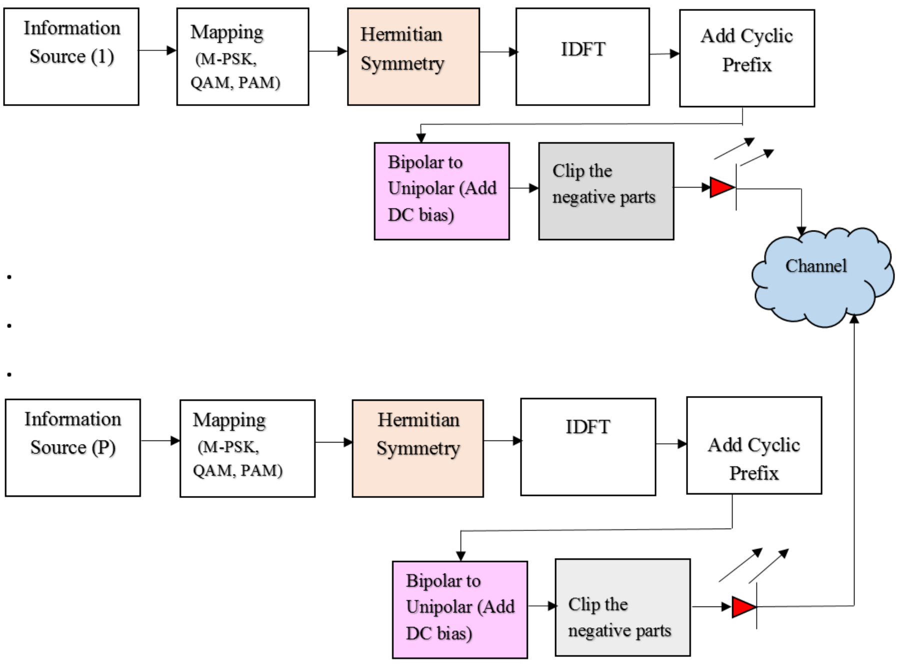

(a) Schematic representation of Transmitter illustrating the scenario of P Subscribers communicating to the Base Station (BS)

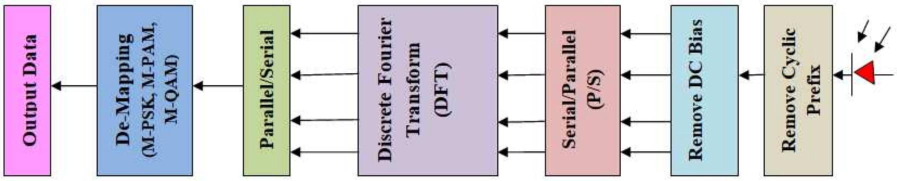

(b) Typical Schematic representation of Base Station

Figure 4.4: Depiction of Uplink scenario in multiple-access system for VLC

The transmitter and receiver blocks are designed in a manner such that they satisfy the requirements of IM/DD systems for VLC. As evident from the figures, there are several users/subscribers in specific, P number of users who are carrying on their transactions with multiple optical base stations. In general, we confine our discussion on transmitter and receiver design pertaining to a single/desired subscriber r. At the transmitter end, the incoming huge data stream is first split into a large number of low speed data sets by utilizing a S/P. Thereupon, these sets of data are encoded into M-QAM symbols. By using inverse Fourier signal processing, these complex symbols are transformed into a time-domain signal. It is to be noted that the desired subscriber of interest is denoted as r and the total number of subcarriers of each OFDM symbol is represented as N. Particularly, each subscriber is allocated with a fixed set of subcarriers to enable communication. Z_r specifies the total number of subcarriers appropriated to the rth subscriber and $\cup_{r=1}^{P} Z_r = \{0, 1, 2, \cdots N-1\}$. Consequently, the complex-mapped data corresponding to the rth subscriber on the kth subcarrier can be depicted as $X_k^{(r)}$. Now, this signal is necessitated to satisfy Hermitian Symmetry constraint before getting applied to the IFFT transformation block. We can treat $X_k^{(r)}$ as a vector with the following representation

$$\boldsymbol{X_k^{(r)}} = \left[0, X_1^{(r)}, X_2^{(r)}, \cdots X_{\frac{N}{2}-1}^{(r)}, 0, X_{\frac{N}{2}-1}^{*(r)}, \cdots, X_1^{*(r)}\right] \tag{4.73}$$

In addition, for the sake of avoiding any imaginary component at the output of the transmitter the first and the middle subcarrier are set to zero. i.e.,

$$\boldsymbol{X_0^{(r)}} = \boldsymbol{X_{\frac{N}{2}}^{(r)}} = 0 \tag{4.74}$$

And

$$X_{(N-k)}^{(r)} = X_{(k)}^{*(r)}, \; k = 1, 2, 3, \cdots \frac{N}{2} \tag{4.75}$$

Therefore, the corresponding time domain signal of the rth user can be obtained as

$$x_n^{(r)} = \frac{1}{N} \sum_{\substack{k=1 \\ k \in Z_r}}^{N-1} X_k^{(r)} e^{\frac{j2\pi nk}{N}} \tag{4.76}$$

Upon substituting the above said constraints (4.73), (4.74) and (4.75) in (4.76), then

$$x_n^{(r)} = \frac{1}{N} \left[\sum_{\substack{k=1 \\ k \in Z_r}}^{\frac{N}{2}-1} X_k^{(r)} e^{\frac{j2\pi nk}{N}} + \sum_{\substack{k=\frac{N}{2}+1 \\ k \in Z_r}}^{N-1} X_k^{(r)} e^{\frac{j2\pi nk}{N}} \right] \tag{4.77}$$

On further processing and applying change in variable we attain the time-domain signal as

$$x_n^{(r)} = \frac{2}{N} \left[\sum_{\substack{k=1 \\ k \in Z_r}}^{\frac{N}{2}-1} \left(X_{\substack{k \\ RC}}^{(r)} cos\left(\frac{2\pi nk}{N}\right) - X_{\substack{k \\ IC}}^{(r)} sin\left(\frac{2\pi nk}{N}\right) \right) \right] \tag{4.78}$$

Where $X_{\substack{k \\ RC}}^{(n)}$ and $X_{\substack{k \\ IC}}^{(n)}$ are the real and imaginary components of $X_k^{(r)}$. Further, to this real-valued signal as shown in (4.78), a suitable amount of cyclic prefix is added to eliminate ISI.

$$x_n^{(r)} = \frac{2}{N} \left[\sum_{\substack{k=1 \\ k \in Z_r}}^{\frac{N}{2}-1} \left(X_{\substack{k \\ RC}}^{(r)} cos\left(\frac{2\pi nk}{N}\right) - X_{\substack{k \\ IC}}^{(r)} sin\left(\frac{2\pi nk}{N}\right) \right) \right], -N_{cp} \le n \le N-1 \tag{4.79}$$

In addition, for assuring the positivity of $x_n^{(r)}$, a certain amount of DC bias value is added. For the purpose of converting a bipolar signal into unipolar, a fixed amount of DC bias which equals the absolute value of the maximum negative amplitude of the bipolar optical OFDM signal is added [193]. However, in case of OFDM, the high peaks which occur due to superimposition of huge number of subcarriers results in the increase in the addition of high amount of DC bias for the sake of assuring non-negativity signal transmission. For large values of the subcarriers employed, the amplitude of the optical time-domain signal can be approximated as a Gaussian distribution. Therefore, in order to prevent the addition of excess DC bias, one appropriate way is to add the DC bias which is proportional to the square root of the electrical power which is given as

$$B_{DC} = k\sqrt{E\left\{\left(x_n^{(r)}\right)^2\right\}} \tag{4.80}$$

Where k represents the clipping factor. In the literature, the amount of DC bias is given as:

$$\beta_{DC} = 10log_{10}\left(k^2+1\right) \tag{4.81}$$

While adding DC bias to the bipolar signal a point to be taken into consideration is that, too much amount of addition of DC bias leads to clipping of the peaks of the time-domain signal which is not within the linear range of LEDs. Hence, clipping induced distortion emanates. Therefore, it is much more flexible to add the amount of DC bias per symbol basis.

$$\beta_{DC} = |min\{x_n^{(r)}, n = 0, 1, 2, 3, \cdots N-1\}| + V_{TOV} \tag{4.82}$$

The LED turn on voltage is specified as V_{TOV}. In practical, the LED requires a certain amount of voltage to enter into conduction and this is referred to as turn on voltage of LED. The current-voltage characteristics of LED is shown in Fig. 4.5. Accordingly, the unipolar signal can be formulated as

$$\underset{DC}{x_n^{(r)}} = \frac{2}{N}\left[\sum_{\substack{k=1\\k\in Z_r}}^{\frac{N}{2}-1}\left(\underset{RC}{X_k^{(r)}}cos\left(\frac{2\pi nk}{N}\right) - \underset{IC}{X_k^{(r)}}sin\left(\frac{2\pi nk}{N}\right)\right)\right] + \beta_{DC} \tag{4.83}$$

Subsequently, the unipolar signal which is designated as $\underset{DC}{x_n^{(r)}}$ pertaining to the rth subscriber is passed through the channel comprising of impulse response $h_n^{(r)}$. Therefore, the received signal can be expressed as

$$y_n^{(r)} = \underset{DC}{x_n^{(r)}} * h_n^{(r)} + w_n^{(r)} \tag{4.84}$$

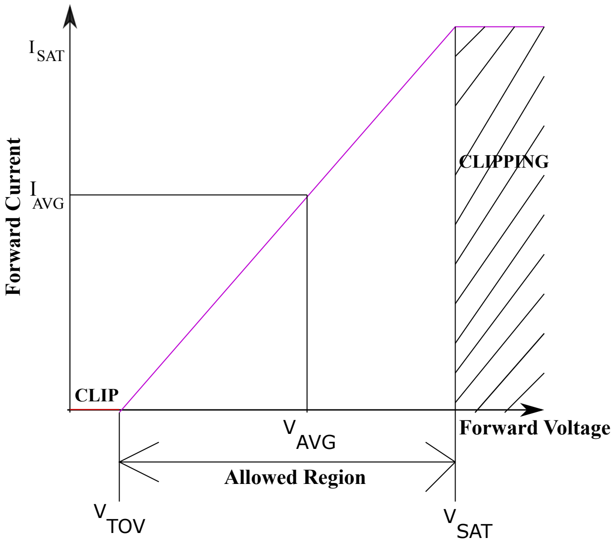

Figure 4.5: V-I Characteristics of LED

$w_n^{(r)}$ corresponds to the Additive White Gaussian Noise (AWGN) with mean 0 and variance σ^2 and the rth subscriber's channel impulse response $h_n^{(r)}$ is said to be non-zero only for the values of $n = 0, 1, 2, 3, \cdots L-1$. Therefore, the frequency response corresponding to the rth subscriber is given as

$$H_k^{(r)} = \sum_{l=0}^{L-1} h_n^{(r)} e^{\frac{-j2\pi nk}{N}} \tag{4.85}$$

Moreover, it is assumed that the channels belonging to all the subscribers are statistically independent.

Furthermore, due to slight movement of people within an indoor or outdoor environments, FO of β arises due to the Doppler Shift. The effect of it on the received signal is very detrimental because it leads to loss of orthogonality among the subcarrier components. This issue is more pronounced in a multi-user scenario, where ICI as well as multi user interference/multiple access interference (MUI)/(MAI) occur. The resultant time domain signal is further processed into frequency domain by applying N-Point DFT. Therefore, to highlight this impact of interferences we proceed further to attain the frequency domain signal after removal of the bias value and the cyclic prefix at the receiver end. Therefore, the frequency domain representation of $y_n^{(r)}$ is denoted by $Y_k^{(r)}$ which is given as

$$Y_k^{(r)} = \frac{1}{N} \sum_{n=0}^{N-1} y_n^{(r)} e^{\frac{-j2\pi nk}{N}} \tag{4.86}$$

From, (4.86), in order to look into the effects of FO we assume that a FO of β exists between the transmitter and receiver. Therefore, the time-domain signal $y_n^{(r)}$ can be expressed as

$$y_n^{(r)} = \frac{1}{N}\sum_{\substack{k=1\\k\in Z_r}}^{N-1} X_k^{(r)} H_k^{(r)} e^{\frac{j2\pi n(k+\beta_r)}{N}} + w_n^{(r)} \tag{4.87}$$

Upon substitution of (4.87) into (4.86), the frequency domain representation of the signal concerning the desired subscriber r can be derived to obtain as follows:

Taking into consideration the Hermitian Symmetry criterion, (4.87) can be re-arranged by employing (4.73) and (4.74) to yield

$$\begin{aligned} y_n^{(r)} = \frac{1}{N}\Big[X_0^{(r)} H_0^{(r)} e^{\frac{j2\pi\beta n}{N}} + \sum_{\substack{k=1\\k\in Z_r}}^{\frac{N}{2}-1} X_k^{(r)} H_k^{(r)} e^{\frac{j2\pi(k+\beta_r)n}{N}} + \\ X_{\frac{N}{2}}^{(r)} H_{\frac{N}{2}}^{(r)} e^{\frac{j2\pi\left(\frac{N}{2}+\beta_r\right)n}{N}} + \sum_{\substack{k=\frac{N}{2}+1\\k\in Z_r}}^{N-1} X_k^{(r)} H_k^{(r)} e^{\frac{j2\pi(k+\beta_r)n}{N}}\Big] + w_n^{(r)} \end{aligned} \tag{4.88}$$

In (4.88), following Hermitian Symmetry criteria, the first and the middle subcarriers are set to zero in order to avoid the presence of any imaginary component (i.e., the first and third terms are set as zeros) and upon incorporating change in variable to the 4th term by letting $N - k^{'} = k$ then (4.88) can be reduced as

$$y_n^{(r)} = \frac{1}{N}\left[\sum_{\substack{k=1\\k\in Z_r}}^{\frac{N}{2}-1} X_k^{(r)} H_k^{(r)} e^{\frac{j2\pi n(k+\beta_r)}{N}} + \sum_{\substack{k^{'}=\frac{N}{2}-1\\k^{'}\in Z_r}}^{1} X_{\left(N-k^{'}\right)}^{(r)} H_{\left(N-k^{'}\right)}^{(r)} e^{\frac{j2\pi n\left(N-k^{'}+\beta_r\right)}{N}}\right] \tag{4.89}$$

Further by making use of (4.75) as well as rearranging, (4.89) can be solved as

$$y_n^{(r)} = \frac{1}{N}\left[\sum_{\substack{k=1\\k\in Z_r}}^{\frac{N}{2}-1} X_k^{(r)} H_k^{(r)} e^{\frac{j2\pi(k+\beta_r)n}{N}} + \sum_{\substack{k=1\\k\in Z_r}}^{\frac{N}{2}-1} X_k^{*(r)} H_k^{(r)} e^{-\frac{j2\pi(k+\beta_r)n}{N}}\right] + w_n^{(r)} \tag{4.90}$$

Using Euler inequalities, $e^{j\theta} = cos\theta + jsin\theta$, $e^{-j\theta} = cos\theta - jsin\theta$ as well as using signal processing techniques like

$\underset{RC}{x\left[n\right]} = \frac{x[n]+x^{*}[n]}{2}$ and $\underset{IC}{x\left[n\right]} = \frac{x[n]-x^{*}[n]}{2j}$. Thereupon solving (4.90), we obtain

$$y_n^{(r)} = \frac{2}{N}\sum_{\substack{k=1\\k\in Z_r}}^{\frac{N}{2}-1}\left(\underset{RC}{X_k^{(r)}} cos\left(\frac{2\pi n\left(k+\beta_r\right)}{N}\right) - \underset{IC}{X_k^{(r)}} sin\left(\frac{2\pi n\left(k+\beta_r\right)}{N}\right)\right) H_k^{(r)} + w_n^{(r)} \tag{4.91}$$

Therefore, on substitution of (4.91) back into (4.86) and then rearranging, $Y_k^{(r)}$ is attained as

$$\begin{split} Y_k^{(r)} = \sum_{n=0}^{N-1} \frac{2}{N} \Big[\sum_{\substack{k=1\\k\in Z_r}}^{\frac{N}{2}-1} \Big(X_{\substack{k\\RC}}^{(r)} cos\left(\frac{2\pi n\left(k+\beta_r\right)}{N}\right) - \\ X_{\substack{k\\IC}}^{(r)} sin\left(\frac{2\pi n\left(k+\beta_r\right)}{N}\right)\Big)\Big] e^{\frac{-j2\pi nk}{N}} \sum_{l=0}^{L-1} h_l^{(r)} e^{\frac{-j2\pi lk}{N}} + \sum_{n=0}^{N-1} w_n^{(r)} e^{\frac{-j2\pi nk}{N}} \end{split} \tag{4.92}$$

Upon using the trigonometric identities $cos\left(\theta\right) = \frac{e^{j\theta}+e^{-j\theta}}{2}$ and $sin\left(\theta\right) = \frac{e^{j\theta}-e^{-j\theta}}{2j}$ in (4.92) and further solving attains

$$\begin{split} Y_k^{(r)} = \frac{1}{N} \sum_{n=0}^{N-1} \sum_{\substack{k=1\\k\in Z_r}}^{\frac{N}{2}-1} \left(X_{\substack{k\\RC}}^{(r)} + jX_{\substack{k\\IC}}^{(r)} \right) e^{\frac{j2\pi(k+\beta_r-k)n}{N}} \sum_{l=0}^{L-1} h_l^{(r)} e^{-\frac{j2\pi lk}{N}} + \\ \frac{1}{N} \sum_{n=0}^{N-1} \sum_{\substack{k=1\\k\in Z_r}}^{\frac{N}{2}-1} \left(X_{\substack{k\\RC}}^{(r)} - jX_{\substack{k\\IC}}^{(r)} \right) e^{-\frac{j2\pi(k+\beta_r+k)n}{N}} \sum_{l=0}^{L-1} h_l^{(r)} e^{-\frac{j2\pi lk}{N}} + \sum_{n=0}^{N-1} w_n^{(r)} e^{-\frac{j2\pi nk}{N}} \end{split} \tag{4.93}$$

Consequently, upon solving (4.93), the expression of the received signal pertaining to desired subscriber r as well as different interferences upon the desired subscriber are illustrated as follows:

$$\begin{split} Y_k^{(r)} = \underbrace{\left(X_{\substack{k\\RC}}^{(r)} + jX_{\substack{k\\IC}}^{(r)} \right) \sum_{l=0}^{L-1} h_l^{(r)} e^{\frac{-j2\pi lk}{N}} \gamma_{kk}^{(r)} + \left(X_{\substack{k\\RC}}^{(r)} - jX_{\substack{k\\IC}}^{(r)} \right) \sum_{l=0}^{L-1} h_l^{(r)} e^{\frac{-j2\pi lk}{N}} \gamma_{kk}^{'(r)}}_{Desired\ Signal\ corresponding\ to\ subscriber\ r} + \\ \underbrace{\sum_{\substack{p=1\\p\neq k\\p\in Z_r}}^{\frac{N}{2}-1} \left(X_{\substack{p\\RC}}^{(r)} + jX_{\substack{p\\IC}}^{(r)} \right) \sum_{l=0}^{L-1} h_l^{(r)} e^{\frac{-j2\pi lp}{N}} \gamma_{pk}^{(r)} + \sum_{\substack{p=1\\p\neq k\\p\in Z_r}}^{\frac{N}{2}-1} \left(X_{\substack{p\\RC}}^{(r)} - jX_{\substack{p\\IC}}^{(r)} \right) \sum_{l=0}^{L-1} h_l^{(r)} e^{\frac{-j2\pi lp}{N}} \gamma_{pk}^{'(r)} +}_{ICI} \\ \underbrace{\sum_{\substack{p=1\\s\neq r\\p\in Z_s}}^{\frac{N}{2}-1} \left(X_{\substack{p\\RC}}^{(s)} + jX_{\substack{p\\IC}}^{(s)} \right) \sum_{l=0}^{L-1} h_l^{(s)} e^{\frac{-j2\pi lp}{N}} \gamma_{pk}^{(s)} + \sum_{\substack{p=1\\s\neq r\\p\in Z_s}}^{\frac{N}{2}-1} \left(X_{\substack{p\\RC}}^{(s)} - jX_{\substack{p\\IC}}^{(s)} \right) \sum_{l=0}^{L-1} h_l^{(s)} e^{\frac{-j2\pi lp}{N}} \gamma_{pk}^{'(s)}}_{MUI/MAI} + W_k^{(r)} \end{split} \tag{4.94}$$

From (4.94), the 1st term underneath the under-brace represents the signal corresponding to the desired subscriber r while, 2nd term denotes the ICI i.e., the self interference among the subcarriers of the subscriber r. Finally, 3rd term represents the MAI or MUI which arises with the other subscriber s. In (4.94), $\gamma_{kk}^{(r)}$, $\gamma_{kk}^{'(r)}$, $\gamma_{pk}^{(r)}$, $\gamma_{pk}^{'(r)}$, $\gamma_{pk}^{(s)}$ and $\gamma_{pk}^{'(s)}$ can be further solved to attain

$$\gamma_{kk}^{(r)} = \frac{sin\left(\pi\beta_r\right)}{N sin\left(\frac{\pi\beta_r}{N}\right)} e^{j\pi\beta_r\,\left(N-{}^{1}\!/_{N}\right)} \tag{4.95}$$

$$\gamma_{kk}^{'(r)} = \frac{sin\pi\left(2k+\beta_r\right)}{N sin\pi\left(\frac{2k+\beta_r}{N}\right)} e^{-j\pi(2k+\beta_r)\,\left(N-{}^{1}\!/_{N}\right)} \tag{4.96}$$

$$\gamma_{pk}^{(r)} = \frac{sin\pi\left(p+\beta_r-k\right)}{N sin\pi\left(\frac{p+\beta_r-k}{N}\right)} e^{j\pi(p+\beta_r-k)\,\left(N-{}^{1}\!/_{N}\right)} \tag{4.97}$$

$$\gamma_{pk}^{'(r)} = \frac{sin\pi\left(p+\beta_r+k\right)}{N sin\pi\left(\frac{p+\beta_r+k}{N}\right)} e^{-j\pi(p+\beta_r+k)\,\left(N-{}^{1}\!/_{N}\right)} \tag{4.98}$$

$$\gamma_{pk}^{(s)} = \frac{sin\pi\left(p+\beta_s-k\right)}{N sin\pi\left(\frac{p+\beta_s-k}{N}\right)} e^{j\pi(p+\beta_s-k)\,\left(N-{}^{1}\!/_{N}\right)} \tag{4.99}$$

$$\gamma_{pk}^{'(s)} = \frac{sin\pi\left(p+\beta_s+k\right)}{N sin\pi\left(\frac{p+\beta_s-k}{N}\right)} e^{-j\pi(p+\beta_s+k)\,\left(N-{}^{1}\!/_{N}\right)} \tag{4.100}$$

Clearly, (4.94) specifies that the received DCO-OFDMA signal in the presence of FO is seriously distorted because it is affected with several amplitude and phase distortions. In addition, it can be claimed that there is a loss in orthogonality because of the prevalence of ICI which is also referred to as self interference among the subcarriers which are dedicated to a subscriber as well as MUI/MAI with other subscribers.

In the similar manner if the signal is affected with STO of α, then the time-domain signal can be formulated as

$$IFFT\left[X_k^{(r)}\right] = x_n^{(r)} \tag{4.101}$$

$$x_n^{(r)} = \frac{1}{N}\sum_{k=0}^{N-1} X_k^{(r)} e^{\frac{j2\pi nk}{N}} \tag{4.102}$$

So, the time domain samples when affected with STO of α can be expressed as

$$x_{n+\alpha_r}^{(r)} = \frac{1}{N}\sum_{k=0}^{N-1} X_k^{(r)} e^{\frac{j2\pi(n+\alpha_r)k}{N}} \tag{4.103}$$

Therefore, following the similar analysis i.e., upon imposing Hermitian Symmetry, the time-domain signal pertaining to the desired subscriber r under the effect of STO can be put up as follows

$$x_{n+\alpha_r}^{(r)} = \frac{2}{N}\sum_{\substack{k=1\\k\in Z_r}}^{\frac{N}{2}-1}\left(X_{\substack{k\\RC}}^{(r)} cos\left(\frac{2\pi\left(n+\alpha_r\right)k}{N}\right) - X_{\substack{k\\IC}}^{(r)} sin\left(\frac{2\pi\left(n+\alpha_r\right)k}{N}\right)\right) \tag{4.104}$$

4.6 Mathematical Illustration of deterioration of received signal due to occurrence of STO

The different possible timing misalignment intervals were adopted from [194], where analysis has been carried out for RF domain. Taking into consideration the above said aspects, we proceed further to interpret the deterioration of SINR in DCO-OFDMA in the presence of both STO α and FO β. It is to be noted that, $\alpha_u, u = \{1, 2, 3, 4, \cdots P\}$ denotes the uth subscriber's STO and $\beta_u, u = \{1, 2, 3, 4, \cdots P\}$ denotes the uth subscriber's FO normalized by the subcarrier spacing. It is probable that the timing errors to be both negative as well as positive. The different possible scenarios are illustrated in Fig. 4.6

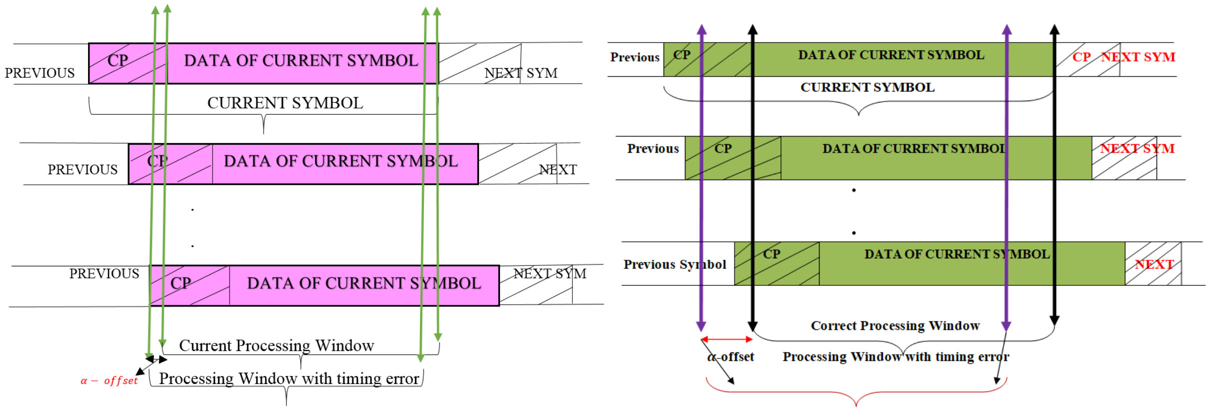

(a) Negative Timing Error (b) Overlap with Previous Frame

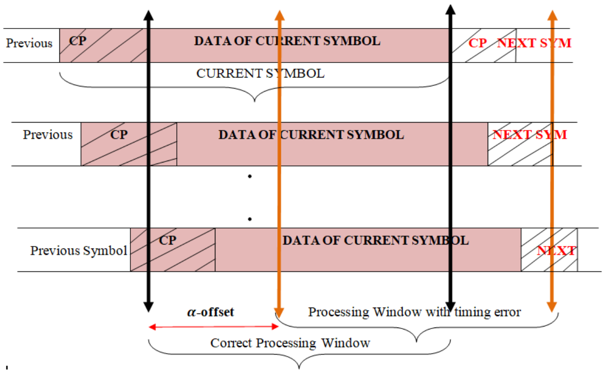

(c) Overlap with next Frame

Figure 4.6: Timing discrepancies in OPTICAL OFDMA

- **Scenario 1:**

  In this case, STO is negative i.e., $\alpha_u < 0$, and let us consider the interval where the value of the offset lies: $0 \leq -\alpha_u \leq N_{cp} - L + 1$ [194]. The output of the DFT transformation block of the subscribers $u = \{1, 2, 3, 4, \cdots P\}$ on the kth subcarrier can be formulated as:

$$Y_k^{(u)} = \sum_{n=0}^{N-1} y_n^{(u)} e^{\frac{-j2\pi nk}{N}} \tag{4.105}$$

Where, $y_n^{(u)}$ represents the convolution of the input signal corresponding to the uth subscriber with its channel. This can be put up as

$$Y_K^{(u)} = \sum_{n=0}^{N-1} \left(x_n^{(u)} * h_n^{(u)} + w_n^{(u)} \right) e^{\frac{-j2\pi nk}{N}} \tag{4.106}$$

Further, it is apparent that $y_n = IFFT\,(Y_k) = IFFT\,(X_k H_k + W_k)$, so on substituting in (4.105), the DFT of the received signal can be expressed as

$$\begin{aligned} Y_k^{(u)} = \sum_{n=0}^{N-1} \frac{2}{N} \Big[\sum_{\substack{k=1 \\ k \in Z_u}}^{\frac{N}{2}-1} \Big(X^{(u)}_{\substack{k \\ RC}} cos\left(\frac{2\pi\,(n+\alpha_u)\,(k+\beta_u)}{N} \right) - \\ X^{(u)}_{\substack{k \\ IC}} sin\left(\frac{2\pi\,(n+\alpha_u)\,(k+\beta_u)}{N} \right) \Big) \Big] e^{\frac{-j2\pi nk}{N}} \sum_{l=0}^{L-1} h_l^{(u)} e^{\frac{-j2\pi lk}{N}} + \\ \sum_{n=0}^{N-1} w_n^{(u)} e^{\frac{-j2\pi nk}{N}} \end{aligned} \tag{4.107}$$

(4.107) represents a generic case where, $Y_k^{(u)}$ symbolizes the DFT of uth user/subscriber on the kth subcarrier. Therefore, the DFT of the corresponding subscriber r on the kth subcarrier, in the presence of the signals invading from all the other subscribers over all the paths can be improvised as

$$\begin{aligned} Y_k^{(r)} = \underbrace{\left(X^{(r)}_{\substack{k \\ RC}} + jX^{(r)}_{\substack{k \\ IC}} \right) e^{\frac{j2\pi\alpha_r(k+\beta_r)}{N}} \sum_{l=0}^{L-1} h_l^{(r)} e^{\frac{-j2\pi lk}{N}} \Upsilon_{kk}^{(r)} + \\ \left(X^{(r)}_{\substack{k \\ RC}} - jX^{(r)}_{\substack{k \\ IC}} \right) e^{\frac{-2j\pi\alpha_r(k+\beta_r)}{N}} \sum_{l=0}^{L-1} h_l^{(r)} e^{\frac{-j2\pi lk}{N}} \Upsilon_{kk}^{\prime(r)}}_{Desired\ Signal\ of\ Subscriber\ r} + ICI + MUI + W_k^{(r)} \end{aligned} \tag{4.108}$$

From (4.108), it can be inferred that, the first two components in the summation represents the signal pertaining to the desired subscriber r. Furthermore, the chances of self interference which is termed as ICI i.e., the interference which arises among the subcarrier components that are dedicated to the subscriber r as well as the MUI that arises due to the presence of other subscribers can be formulated as:

$$ICI = \sum_{\substack{p=1\\ p\in Z_r\\ p\neq k}}^{\frac{N}{2}-1} \left(\underset{RC}{X_p^{(r)}} + j\underset{IC}{X_p^{(r)}}\right) e^{\frac{j2\pi\alpha_r(p+\beta_r)}{N}} \sum_{l=0}^{L-1} h_l^{(r)} e^{\frac{-j2\pi lp}{N}} \Upsilon_{pk}^{(r)} +$$

$$\sum_{\substack{p=1\\ p\in Z_r\\ p\neq k}}^{\frac{N}{2}-1} \left(\underset{RC}{X_p^{(r)}} - j\underset{IC}{X_p^{(r)}}\right) e^{\frac{-j2\pi\alpha_r(p+\beta_r)}{N}} \sum_{l=0}^{L-1} h_l^{(r)} e^{\frac{-2j\pi lp}{N}} \Upsilon'^{(r)}_{pk} \qquad (4.109)$$

From (4.109), it is evident that self interference arises among the subcarrier components p and k that are allocated to corresponding subscriber r.

$$MUI = \sum_{\substack{p=1\\ p\in Z_s\\ p\neq k}}^{\frac{N}{2}-1} \left(\underset{RC}{X_p^{(s)}} + j\underset{IC}{X_p^{(s)}}\right) e^{\frac{j2\pi\alpha_s(p+\beta_s)}{N}} \sum_{l=0}^{L-1} h_l^{(s)} e^{\frac{-j2\pi lp}{N}} \Upsilon_{pk}^{(s)} +$$

$$\sum_{\substack{p=1\\ p\in Z_s\\ p\neq k}}^{\frac{N}{2}-1} \left(\underset{RC}{X_p^{(s)}} - j\underset{IC}{X_p^{(s)}}\right) e^{\frac{-j2\pi\alpha_s(p+\beta_s)}{N}} \sum_{l=0}^{L-1} h_l^{(s)} e^{\frac{-2\pi lp}{N}} \Upsilon'^{(s)}_{pk} \qquad (4.110)$$

(4.110) confirms the fact that in the presence of multiple users, there is a chance for the occurrence of MUI. Here, it is shown as the interference arising from subscriber s to subscriber r. The Υ function can be generalized as

$$\Upsilon_{pk}^{(u)} = \frac{1}{N}\sum_{n=0}^{N-1} e^{\frac{j2\pi n(p+\beta_u-k)}{N}} = \frac{sin\pi\left(p+\beta_u-k\right)}{Nsin\pi\left(\frac{p+\beta_u-k}{N}\right)} e^{j\pi(p+\beta_u-k)}\left({}^{(N-1)}/_{N}\right) \qquad (4.111)$$

$$\Upsilon'^{u}_{pk} = \frac{1}{N}\sum_{n=0}^{N-1} e^{\frac{j2\pi n(p+\beta_u+k)}{N}} = \frac{sin\pi\left(p+\beta_u+k\right)}{Nsin\pi\left(\frac{p+\beta_u+k}{N}\right)} e^{-j\pi(p+\beta_u+k)}\left({}^{(N-1)}/_{N}\right) \qquad (4.112)$$

This scenario specifies that there are chances for ICI and MUI/MAI interference to occur. It can be evidenced from (4.108), that there is no interference from the previous symbol or next symbol.

- **Scenario 2:**

  This is also the case where we assume that the timing error is negative i.e, $\alpha < 0$ and lies in the interval of $N_{cp} - L + 1 < \alpha \leq N_{cp}$. In this situation, only some of the paths experience interference from the previous paths. This scenario emphasizes the phenomena of declination in the received signal when the previous frame's symbol interferes with the prevailing symbol. This is further fuelled with the existence of both STO and FO. (4.114), emphasizes that the received signal is seriously deteriorated due to mutual interference among the subcarrier components which are allotted to a specific subscriber r as well as MUI/MAI occurs from other users. Here, due to overlap with the previous symbols, a loss in orthogonality can be depicted from the below analysis. The received signal under the effects of both timing and frequency offset can be expressed as:

$$
\begin{aligned}
Y_k^{(u)} = & \sum_{n=0}^{-\alpha_u-N_{cp}+l-1} \frac{2}{N}\Bigg[\sum_{\substack{k=1\\ k\in Z_u}}^{\frac{N}{2}-1}\Bigg(X^{(u)}_{\underset{RC}{k}} cos\left(\frac{2\pi\left(n+N_{cp}+\alpha_u\right)\left(k+\beta_u\right)}{N}\right) - \\
& X^{(u)}_{\underset{IC}{k}} sin\left(\frac{2\pi\left(n+N_{cp}+\alpha_u\right)\left(k+\beta_u\right)}{N}\right)\Bigg)\Bigg] e^{\frac{-j2\pi nk}{N}} \sum_{l=N_{cp}+\alpha_u+1}^{L-1} h_l^{(u)} e^{\frac{-j2\pi lk}{N}} \\
& + \sum_{n=-\alpha_u-N_{cp}+l}^{N-1} \frac{2}{N}\Bigg[\sum_{\substack{k=1\\ k\in Z_u}}^{\frac{N}{2}-1}\Bigg(X^{(u)}_{\underset{RC}{k}} cos\left(\frac{2\pi\left(n+\alpha_u\right)\left(k+\beta_u\right)}{N}\right) - \\
& X^{(u)}_{\underset{IC}{k}} sin\left(\frac{2\pi\left(n+\alpha_u\right)\left(k+\beta_u\right)}{N}\right)\Bigg)\Bigg] e^{\frac{-j2\pi nk}{N}} \sum_{l=0}^{L-1} h_l^{(u)} e^{\frac{-j2\pi lk}{N}} + \sum_{n=0}^{N-1} w_n^{(u)} e^{\frac{-j2\pi nk}{N}}
\end{aligned}
\tag{4.113}
$$

(4.113), specifies that the current symbol is overlapped with the previous symbol and hence, the signal is split into two parts, one specifying the previous interval and the current interval. Therefore, the frequency domain signal at the DFT output pertaining to the rth subscriber on the kth subcarrier which is denoted as $Y_k^{(r)}$ can be derived as

$$
\begin{aligned}
Y_k^{(r)} = & \left(X^{(r)}_{\underset{RC}{k}} + jX^{(r)}_{\underset{IC}{k}}\right) e^{\frac{j2\pi\alpha_r(k+\beta_r)}{N}} \sum_{l=0}^{L-1} h_l^{(r)} e^{\frac{-j2\pi lk}{N}} \xi_{kk}^{(r)(l)} + \\
& \underbrace{\left(X^{(r)}_{\underset{RC}{k}} - jX^{(r)}_{\underset{IC}{k}}\right) e^{\frac{-j2\pi\alpha_r(k+\beta_r)}{N}} \sum_{l=0}^{L-1} h_l^{(r)} e^{\frac{-j2\pi lk}{N}} \xi'^{(r)(l)}_{kk}}_{Desired\ Signal\ of\ Subscriber\ r} + \\
& \underset{Current\ Frame}{ICI} + \underset{Current\ Frame}{MUI} + \underset{Previous\ Frame}{ICI} + \underset{Previous\ Frame}{MUI} + W_k^{(r)}
\end{aligned}
\tag{4.114}
$$

From (4.114), the calculation of different sorts of interferences like self interference, MUI which arises in the current frame as well as the interference coefficients like ICI and MUI which are associated due to the overlap with the previous frame are derived as follows.

$$\underset{Current\ Frame}{ICI} = \sum_{\substack{p=1\\p\neq k\\p\in Z_r}}^{\frac{N}{2}-1}\left(X^{(r)}_{\underset{RC}{p}} + jX^{(r)}_{\underset{IC}{p}}\right)e^{\frac{j2\pi\alpha_r(p+\beta_r)}{N}}\sum_{l=0}^{L-1}h_l^{(r)}e^{\frac{-j2\pi lp}{N}}\xi_{pk}^{(r)(l)}+$$
$$\sum_{\substack{p=1\\p\neq k\\p\in Z_r}}^{\frac{N}{2}-1}\left(X^{(r)}_{\underset{RC}{p}} - jX^{(r)}_{\underset{IC}{p}}\right)e^{\frac{-j2\pi\alpha_r(p+\beta_r)}{N}}\sum_{l=0}^{L-1}h_l^{(r)}e^{\frac{-j2\pi lp}{N}}\xi_{pk}^{\prime(r)(l)} \quad (4.115)$$

$$\underset{Current\ Frame}{MUI} = \sum_{\substack{p=1\\p\neq k\\p\in Z_s}}^{\frac{N}{2}-1}\left(X^{(s)}_{\underset{RC}{p}} + jX^{(s)}_{\underset{IC}{p}}\right)e^{\frac{j2\pi\alpha_s(p+\beta_s)}{N}}\sum_{l=0}^{L-1}h_l^{(s)}e^{\frac{-j2\pi lp}{N}}\xi_{pk}^{(s)(l)}+$$
$$\sum_{\substack{p=1\\p\neq k\\p\in Z_s}}^{\frac{N}{2}-1}\left(X^{(s)}_{\underset{RC}{p}} - jX^{(s)}_{\underset{IC}{p}}\right)e^{\frac{-j2\pi\alpha_s(p+\beta_s)}{N}}\sum_{l=0}^{L-1}h_l^{(s)}e^{\frac{-j2\pi lp}{N}}\xi_{pk}^{\prime(s)(l)} \quad (4.116)$$

$$\underset{Previous\ Frame}{ICI} =$$
$$\sum_{\substack{p=1\\p\neq k\\p\in Z_r}}^{\frac{N}{2}-1}\left(\underset{RC}{X_p}^{(r)(pr)} + j\underset{IC}{X_p}^{(r)(pr)}\right)e^{\frac{j2\pi(\alpha_r+N_{cp})(p+\beta_r)}{N}}\sum_{l=N_{cp}+\alpha_r+1}^{L-1}h_l^{(r)}e^{\frac{-j2\pi lp}{N}}\wp_{pk}^{(r)(l)}+$$
$$\sum_{\substack{p=1\\p\neq k\\p\in Z_r}}^{\frac{N}{2}-1}\left(\underset{RC}{X_p}^{(r)(pr)} - j\underset{IC}{X_p}^{(r)(pr)}\right)e^{\frac{-j2\pi(\alpha_r+N_{cp})(p+\beta_r)}{N}}\sum_{l=N_{cp}+\alpha_r+1}^{L-1}h_l^{(r)}e^{\frac{-j2\pi lp}{N}}\wp_{pk}^{\prime(r)(l)} \quad (4.117)$$

$$\underset{Previous\ Frame}{MUI} =$$
$$\sum_{\substack{p=1\\p\neq k\\p\in Z_s}}^{\frac{N}{2}-1}\left(\underset{RC}{X_p}^{(s)(pr)} + j\underset{IC}{X_p}^{(s)(pr)}\right)e^{\frac{j2\pi(\alpha_s+N_{cp})(p+\beta_s)}{N}}\sum_{l=N_{cp}+\alpha_s+1}^{L-1}h_l^{(s)}e^{\frac{-j2\pi lp}{N}}\wp_{pk}^{(s)(l)}+$$
$$\sum_{\substack{p=1\\p\neq k\\p\in Z_s}}^{\frac{N}{2}-1}\left(\underset{RC}{X_p}^{(s)(pr)} - j\underset{IC}{X_p}^{(s)(pr)}\right)e^{\frac{-j2\pi(\alpha_s+N_{cp})(p+\beta_s)}{N}}\sum_{l=N_{cp}+\alpha_s+1}^{L-1}h_l^{(s)}e^{\frac{-j2\pi lp}{N}}\wp_{pk}^{\prime(s)(l)} \quad (4.118)$$

Where, $\xi_{pk}^{(u)(l)}$, $\xi_{pk}^{'(u)(l)}$, $\wp_{pk}^{(u)(l)}$ and $\wp_{pk}^{'(u)(l)}$ in (4.114), (4.115), (4.116), (4.117) and (4.118) are given by

$$\xi_{pk}^{(u)(l)} = \frac{1}{N} \sum_{n=-\alpha_u - N_{cp}+l}^{N-1} e^{\frac{j2\pi(p+\beta_u-k)n}{N}} \tag{4.119}$$

$$\xi_{pk}^{'(u)(l)} = \frac{1}{N} \sum_{n=-\alpha_u - N_{cp}+l}^{N-1} e^{\frac{-j2\pi(p+\beta_u+k)n}{N}} \tag{4.120}$$

$$\wp_{pk}^{(u)(l)} = \frac{1}{N} \sum_{n=0}^{-\alpha_u - N_{cp}+l-1} e^{\frac{j2\pi(p+\beta_u-k)n}{N}} \tag{4.121}$$

$$\wp_{pk}^{'(u)(l)} = \frac{1}{N} \sum_{n=0}^{-\alpha_u - N_{cp}+l-1} e^{\frac{-j2\pi(p+\beta_u+k)n}{N}} \tag{4.122}$$

It is to be noted that, the notation $X_p^{(s)(pr)}$ signifies the sth user's data symbol on the pth subcarrier of the previous frame. The indication of interference from previous frame is denoted as (pr).

- **Scenario 3:** This is the situation which depicts that all the paths experience interference from the previous frame. This scenario also depicts when $\alpha < 0$ and $-\alpha > N_{cp}$. In this regard there is a chance for some of the symbols belonging to the present symbol to lose in the processing window, as well interference emanates from previous symbol. In addition, MUI/MAI also exists. Therefore, the DFT of the desired/corresponding subscriber r showing the effects of interference occurring from the previous frame's symbol can be formulated as

$$\begin{aligned} Y_k^{(u)} = & \sum_{n=0}^{-\alpha_u - N_{cp}+l-1} \frac{2}{N} \Big[\sum_{\substack{k=1 \\ k \in Z_u}}^{\frac{N}{2}-1} \Big(X_{\substack{k \\ RC}}^{(u)} cos\left(\frac{2\pi\left(n+\alpha_u\right)\left(k+\beta_u\right)}{N} \right) - \\ & X_{\substack{k \\ IC}}^{(u)} sin\left(\frac{2\pi\left(n+\alpha_u\right)\left(k+\beta_u\right)}{N} \right) \Big) \Big] e^{\frac{-j2\pi nk}{N}} \sum_{l=0}^{L-1} h_l^{(u)} e^{\frac{-j2\pi lk}{N}} + \\ & \sum_{n=-\alpha_u - N_{cp}+l}^{N-1} \frac{2}{N} \Big[\sum_{\substack{k=1 \\ k \in Z_u}}^{\frac{N}{2}-1} \Big(X_{\substack{k \\ RC}}^{(u)} cos\left(\frac{2\pi\left(n+N_{cp}+\alpha_u\right)\left(k+\beta_u\right)}{N} \right) - \\ & X_{\substack{k \\ IC}}^{(u)} sin\left(\frac{2\pi\left(n+N_{cp}+\alpha_u\right)\left(k+\beta_u\right)}{N} \right) \Big) \Big] e^{\frac{-j2\pi nk}{N}} \sum_{l=0}^{L-1} h_l^{(u)} e^{\frac{-j2\pi lk}{N}} + \\ & \sum_{n=0}^{N-1} w_n^{(u)} e^{\frac{-j2\pi nk}{N}} \end{aligned} \tag{4.123}$$

Further, (4.123) can be solved to attain

$$\begin{aligned}Y_k^{(r)} = {} & \left(\underset{RC}{X_k^{(r)}} + j\underset{IC}{X_k^{(r)}}\right) e^{\frac{j2\pi\alpha_r(k+\beta_r)}{N}} \sum_{l=0}^{L-1} h_l^{(r)} e^{\frac{-j2\pi lk}{N}} \xi_{kk}^{(r)(l)} + \\ & \underbrace{\left(\underset{RC}{X_k^{(r)}} - j\underset{IC}{X_k^{(r)}}\right) e^{\frac{-j2\pi\alpha_r(k+\beta_r)}{N}} \sum_{l=0}^{L-1} h_l^{(r)} e^{\frac{-j2\pi lk}{N}} \xi_{kk}^{\prime(r)(l)} +}_{Desired\ Signal\ of\ Subscriber\ r} \\ & \underset{Current\ Frame}{(ICI + MUI)} + \underset{Previous\ Frame}{(ICI + MUI)} + W_k^{(r)}\end{aligned} \tag{4.124}$$

In (4.124), the calculation of different types of interferences like ICI and MUI in the current frame as well as MUI which is arising from the next frame are detailed as below. Unlike Scenario 2, this scenario experiences interference from all paths emanating from the previous frame. Hence, this necessitates to categorize the different sorts of interferences. Firstly, the self interference i.e, the ICI which arises among the subcarrier components allocated to the corresponding subscriber is represented as $\underset{Current\ Frame}{ICI}$ and is given as

$$\begin{aligned}\underset{Current\ Frame}{ICI} = {} & \sum_{\substack{p=1\\p\neq k\\p\in Z_r}}^{\frac{N}{2}-1} \left(\underset{RC}{X_p^{(r)}} + j\underset{IC}{X_p^{(r)}}\right) e^{\frac{j2\pi\alpha_r(p+\beta_r)}{N}} \sum_{l=0}^{L-1} h_l^{(r)} e^{\frac{-j2\pi lp}{N}} \xi_{pk}^{(r)(l)} + \\ & \sum_{\substack{p=1\\p\neq k\\p\in Z_r}}^{\frac{N}{2}-1} \left(\underset{RC}{X_p^{(r)}} - j\underset{IC}{X_p^{(r)}}\right) e^{\frac{-j2\pi\alpha_r(p+\beta_r)}{N}} \sum_{l=0}^{L-1} h_l^{(r)} e^{\frac{-j2\pi lp}{N}} \xi_{pk}^{\prime(r)(l)}\end{aligned} \tag{4.125}$$

Secondly, the MUI which arises from the other subscribers on the desired subscriber i.e., the interference from subscriber s to desired user r in the current frame is denoted as $\underset{Current\ Frame}{MUI}$ which is given by the following expression

$$\begin{aligned}\underset{Current\ Frame}{MUI} = {} & \sum_{\substack{p=1\\p\neq k\\p\in Z_s}}^{\frac{N}{2}-1} \left(\underset{RC}{X_p^{(s)}} + j\underset{IC}{X_p^{(s)}}\right) e^{\frac{j2\pi\alpha_s(p+\beta_s)}{N}} \sum_{l=0}^{L-1} h_l^{(s)} e^{\frac{-j2\pi lp}{N}} \xi_{pk}^{(s)(l)} + \\ & \sum_{\substack{p=1\\p\neq k\\p\in Z_s}}^{\frac{N}{2}-1} \left(\underset{RC}{X_p^{(s)}} - j\underset{IC}{X_p^{(s)}}\right) e^{\frac{-j2\pi\alpha_s(p+\beta_s)}{N}} \sum_{l=0}^{L-1} h_l^{(s)} e^{\frac{-j2\pi lp}{N}} \xi_{pk}^{\prime(s)(l)}\end{aligned} \tag{4.126}$$

Thirdly, due to the overlap of the current frame with the previous frame, there is interference arising from the previous frame and here in this situation it is shown as the interference arisng from the previous frame subcarriers which is given as

$$\underset{Previous\ Frame}{ICI} = \\ \sum_{\substack{p=1\\ p\neq k\\ p\in Z_r}}^{\frac{N}{2}-1} \left(\underset{RC}{X_p}^{(r)(pr)} + j\underset{IC}{X_p}^{(r)(pr)}\right) e^{\frac{j2\pi(\alpha_r+N_{cp})(p+\beta_r)}{N}} \sum_{l=0}^{L-1} h_l^{(r)} e^{\frac{-j2\pi lp}{N}} \wp_{pk}^{(r)(l)} + \\ \sum_{\substack{p=1\\ p\neq k\\ p\in Z_r}}^{\frac{N}{2}-1} \left(\underset{RC}{X_p}^{(r)(pr)} - j\underset{IC}{X_p}^{(r)(pr)}\right) e^{\frac{-j2\pi(\alpha_r+N_{cp})(p+\beta_r)}{N}} \sum_{l=0}^{L-1} h_l^{(r)} e^{\frac{-j2\pi lp}{N}} \wp_{pk}^{'(r)(l)} \tag{4.127}$$

Finally, MUI also stems out from the previous frame and is predetermined as

$$\underset{Previous\ Frame}{MUI} = \\ \sum_{\substack{p=1\\ p\neq k\\ p\in Z_s}}^{\frac{N}{2}-1} \left(\underset{RC}{X_p}^{(s)(pr)} + j\underset{IC}{X_p}^{(s)(pr)}\right) e^{\frac{j2\pi(\alpha_s+N_{cp})(p+\beta_s)}{N}} \sum_{l=0}^{L-1} h_l^{(s)} e^{\frac{-j2\pi lp}{N}} \wp_{pk}^{(s)(l)} + \\ \sum_{\substack{p=1\\ p\neq k\\ p\in Z_s}}^{\frac{N}{2}-1} \left(\underset{RC}{X_p}^{(s)(pr)} - j\underset{IC}{X_p}^{(s)(pr)}\right) e^{\frac{-j2\pi(\alpha_s+N_{cp})(p+\beta_s)}{N}} \sum_{l=0}^{L-1} h_l^{(s)} e^{\frac{-j2\pi lp}{N}} \wp_{pk}^{'(s)(l)} \tag{4.128}$$

From (4.124), (4.125), (4.126), (4.127) and (4.128) the values of $\xi_{pk}^{(u)(l)}$, $\xi_{pk}^{'(u)(l)}$, $\wp_{pk}^{(u)(l)}$ and $\wp_{pk}^{'(u)(l)}$ are similar to the obtained values of Scenario 2 and are represented by (4.119), (4.120), (4.121) and (4.122) respectively.

- **Scenario 4:** This scenario is similar to that of Scenario 2, unlike Scenario 2, where interference is experienced form the previous frame's symbol, in this event the present/current symbol of the prevailing frame experience interference from the next frame's symbol. In precise, here the timing induced error is positive i.e., $\alpha > 0$ and lies in the interval $0 < \alpha < L$. So, mathematical effects elucidating the types of interferences like self interference which is occurring due to subcarriers allocated to a corresponding subscriber, as well as the effects of MUI is depicted in (4.130).

The DFT of the corresponding subscriber u can be expressed as

$$\begin{aligned} Y_k^{(u)} = & \sum_{n=0}^{N-\alpha_u+l-1} \frac{2}{N}\Big[\sum_{\substack{k=1\\k\in Z_u}}^{\frac{N}{2}-1}\Big(X^{(u)}_{\underset{RC}{k}} cos\left(\frac{2\pi\left(n+\alpha_u\right)\left(k+\beta_u\right)}{N}\right) - \\ & X^{(u)}_{\underset{IC}{k}} sin\left(\frac{2\pi\left(n+\alpha_u\right)\left(k+\beta_u\right)}{N}\right)\Big)\Big] e^{\frac{-j2\pi nk}{N}} \sum_{l=0}^{L-1} h_l^{(u)} e^{\frac{-j2\pi lk}{N}} + \\ & \sum_{n=N-\alpha_u+l}^{N-1} \frac{2}{N}\Big[\sum_{\substack{k=1\\k\in Z_u}}^{\frac{N}{2}-1}\Big(X^{(u)}_{\underset{RC}{k}} cos\left(\frac{2\pi\left(n+N_{cp}-\alpha_u\right)\left(k+\beta_u\right)}{N}\right) - \\ & X^{(u)}_{\underset{IC}{k}} sin\left(\frac{2\pi\left(n+N_{cp}-\alpha_u\right)\left(k+\beta_u\right)}{N}\right)\Big)\Big] e^{\frac{-j2\pi nk}{N}} \sum_{l=0}^{L-1} h_l^{(u)} e^{\frac{-j2\pi lk}{N}} \\ & + \sum_{n=0}^{N-1} w_n^{(u)} e^{\frac{-j2\pi nk}{N}} \end{aligned} \tag{4.129}$$

(4.129) can be further derived to yield the DFT of the dedicated subscriber r

$$\begin{aligned} Y_k^{(r)} = & \underbrace{\left(X^{(r)}_{\underset{RC}{k}} + jX^{(r)}_{\underset{IC}{k}}\right) e^{\frac{j2\pi\alpha_r(k+\beta_r)}{N}} \sum_{l=0}^{L-1} h_l^{(r)} e^{\frac{-j2\pi lk}{N}} \varrho_{kk}^{(r)(l)} + \left(X^{(r)}_{\underset{RC}{k}} - jX^{(r)}_{\underset{IC}{k}}\right) e^{\frac{-j2\pi\alpha_r(k+\beta_r)}{N}} \sum_{l=0}^{L-1} h_l^{(r)} e^{\frac{-j2\pi lk}{N}} \varrho_{kk}^{\prime(r)(l)}}_{Signal\ corresponding\ to\ dedicated\ subscriber\ r} + \\ & \underset{Current\ Frame}{\left(ICI+MUI\right)} + \underset{Next\ Frame}{\left(ICI+MUI\right)} + W_k^{(r)} \end{aligned} \tag{4.130}$$

$$\begin{aligned} \underset{Current\ Frame}{ICI} = & \sum_{\substack{p=1\\p\neq k\\p\in Z_r}}^{\frac{N}{2}-1} \left(X^{(r)}_{\underset{RC}{p}} + jX^{(r)}_{\underset{IC}{p}}\right) e^{\frac{j2\pi\alpha_r(p+\beta_r)}{N}} \sum_{l=0}^{L-1} h_l^{(r)} e^{\frac{-j2\pi lp}{N}} \varrho_{pk}^{(r)(l)} + \\ & \sum_{\substack{p=1\\p\neq k\\p\in Z_r}}^{\frac{N}{2}-1} \left(X^{(r)}_{\underset{RC}{p}} - jX^{(r)}_{\underset{IC}{p}}\right) e^{\frac{-j2\pi\alpha_r(p+\beta_r)}{N}} \sum_{l=0}^{L-1} h_l^{(r)} e^{\frac{-j2\pi lp}{N}} \varrho_{pk}^{\prime(r)(l)} \end{aligned} \tag{4.131}$$

$$\begin{aligned} \underset{Current\ Frame}{MUI} = & \sum_{\substack{p=1\\p\neq k\\p\in Z_s}}^{\frac{N}{2}-1} \left(X^{(s)}_{\underset{RC}{p}} + jX^{(s)}_{\underset{IC}{p}}\right) e^{\frac{j2\pi\alpha_s(p+\beta_s)}{N}} \sum_{l=0}^{L-1} h_l^{(s)} e^{\frac{-j2\pi lp}{N}} \varrho_{pk}^{(s)(l)} + \\ & \sum_{\substack{p=1\\p\neq k\\p\in Z_s}}^{\frac{N}{2}-1} \left(X^{(s)}_{\underset{RC}{p}} - jX^{(s)}_{\underset{IC}{p}}\right) e^{\frac{-j2\pi\alpha_s(p+\beta_s)}{N}} \sum_{l=0}^{L-1} h_l^{(s)} e^{\frac{-j2\pi lp}{N}} \varrho_{pk}^{\prime(s)(l)} \end{aligned} \tag{4.132}$$

$$\underset{Next\ Frame}{ICI} = \sum_{\substack{p=1\\p\neq k\\p\in Z_r}}^{\frac{N}{2}-1}\left(\underset{RC}{X_p}^{(r)(NS)} + j\underset{IC}{X_p}^{(r)(NS)}\right)e^{\frac{-j2\pi\left(N_{cp}-\alpha_r\right)(p+\beta_r)}{N}}\sum_{l=0}^{L-1}h_l^{(r)}e^{\frac{-j2\pi lp}{N}}\chi_{pk}^{(r)(l)}+$$

$$\sum_{\substack{p=1\\p\neq k\\p\in Z_r}}^{\frac{N}{2}-1}\left(\underset{RC}{X_p}^{(r)(NS)} - j\underset{IC}{X_p}^{(r)(NS)}\right)e^{\frac{-j2\pi\left(N_{cp}-\alpha_r\right)(p+\beta_r)}{N}}\sum_{l=0}^{L-1}h_l^{(r)}e^{\frac{-j2\pi lp}{N}}\chi_{pk}^{'(r)(l)} \tag{4.133}$$

$$\sum_{\substack{p=1\\p\neq k\\p\in Z_s}}^{\frac{N}{2}-1}\left(\underset{RC}{X_p}^{(s)(NS)} + j\underset{IC}{X_p}^{(s)(NS)}\right)e^{\frac{j2\pi\left(N_{cp}-\alpha_s\right)(p+\beta_s)}{N}}\sum_{l=0}^{L-1}h_l^{(s)}e^{\frac{-j2\pi lp}{N}}\chi_{pk}^{(s)(l)}$$

$$+\sum_{\substack{p=1\\p\neq k\\p\in Z_s}}^{\frac{N}{2}-1}\left(\underset{RC}{X_p}^{(s)(NS)} - j\underset{IC}{X_p}^{(s)(NS)}\right)e^{\frac{-j2\pi\left(N_{cp}-\alpha_s\right)(p+\beta_s)}{N}}\sum_{l=0}^{L-1}h_l^{(s)}e^{\frac{-j2\pi lp}{N}}\chi_{pk}^{'(s)(l)} \tag{4.134}$$

Where $X_p^{(s)(NS)}$ denotes the next frame's data symbol of the sth subscriber on the pth subcarrier.

From (4.130), the values of $\varrho_{pk}^{(u)(l)}$, $\varrho_{pk}^{'(u)(l)}$, $\chi_{pk}^{(u)(l)}$ and $\chi_{pk}^{'(u)(l)}$ are given as:

$$\varrho_{pk}^{(u)(l)} = \frac{1}{N}\sum_{n=0}^{N-\alpha_u+l-1} e^{\frac{j2\pi(p+\beta_u-k)n}{N}} \tag{4.135}$$

$$\varrho_{pk}^{'(u)(l)} = \frac{1}{N}\sum_{n=0}^{N-\alpha_u+l-1} e^{\frac{-j2\pi(p+\beta_u+k)n}{N}} \tag{4.136}$$

$$\chi_{pk}^{(u)(l)} = \frac{1}{N}\sum_{n=N-\alpha_u+l}^{N-1} e^{\frac{j2\pi(p+\beta_u-k)n}{N}} \tag{4.137}$$

$$\chi_{pk}^{'(u)(l)} = \frac{1}{N}\sum_{n=N-\alpha_u+l}^{N-1} e^{\frac{-j2\pi(p+\beta_u+k)n}{N}} \tag{4.138}$$

4.7 Analysis of Signal to Interference Noise Ratio (SINR)

This section derives the SINR for the aforementioned scenarios for DCO-OFDMA signal corresponding to the desired subscriber r. It is apparent that, the SINR is defined as

$$SINR = \frac{Signal\ Power}{Interference\ Power + Noise\ Power} \tag{4.139}$$

From (4.139), the total interference power includes the ICI and MUI from the current, previous and next symbol. The obtained equations (4.108), (4.114), (4.124) and (4.130), are the DFT outputs which depicts the possible cases of timing misalignment. Scenario 3 is similar to that of Scenario 2, hence, SINR analysis corresponding to it is not mentioned below.

Therefore, the average SINR of the corresponding subscriber r on the kth subcarrier considering all the possible misalignment scenarios can be derived by considering that if the number of subcarriers are large enough, then according to Central Limit Theorem (CLT), the transmitted signal $X_k\left(r\right)$ can be assumed to be Gaussian whose real and imaginary components $\underset{RC}{X^{(r)}}$ and $\underset{IC}{X^{(r)}}$ can be approximated to be independent.

Therefore, $E\left[\left|\underset{RC}{X^{(r)}}\right|^2\right]$ and $E\left[\left|\underset{IC}{X^{(r)}}\right|^2\right] = \frac{1}{2}$. Where the value $E\left[.\right]$ represents the expectation operator.

The value of $E\left[\left|H\right|^2\right]$ is denoted by σ_H^2 and the noise variance is represented as σ_n^2.

Finally, the SINR for each scenario can be calculated as follows:

$$SINR = \frac{E\left[\left|X_S\right|^2\right]}{E\left[\left|X_{ICI}\right|^2\right] + E\left[\left|X_{MUI}\right|^2\right] + \sigma^2} \tag{4.140}$$

Where the terms in numerator and denominator in (4.140) are:

- $E\left[\left|X_S\right|^2\right]$ denotes the signal power,
- $E\left[\left|X_{ICI}\right|^2\right]$ depicts the ICI power and
- $E\left[\left|X_{MUI}\right|^2\right]$ represent MUI power.

$$\underset{Scenario\ 1}{SINR} = \frac{\sigma_H^2\left(\left|\Upsilon_{kk}^{(r)}\right| + \left|\Upsilon_{kk}^{\prime(r)}\right|\right)^2}{\sum\limits_{\substack{p=1\\ p\in Z_r\\ p\neq k}}^{\frac{N}{2}-1}\sigma_H^2\left(\left|\Upsilon_{pk}^{(r)}\right| + \left|\Upsilon_{pk}^{\prime(r)}\right|\right)^2 + \sum\limits_{\substack{p=1\\ p\in Z_s\\ p\neq k}}^{\frac{N}{2}-1}\sigma_{H'}^2\left(\left|\Upsilon_{pk}^{(s)}\right| + \left|\Upsilon_{pk}^{\prime(s)}\right|\right)^2 + \sigma_n^2} \tag{4.141}$$

Similarly, SINR for Scenario 2 and 4 is given as

$$\underset{Scenario\ 2}{SINR} = \frac{\sigma_H^2\left(\left|\xi_{kk}^{(r)(l)}\right| + \left|\xi_{kk}^{'(r)(l)}\right|\right)^2}{\begin{array}{l}\sum_{\substack{p=1\\p\in Z_r\\p\neq k}}^{\frac{N}{2}-1}\sigma_H^2\left(\left|\xi_{pk}^{(r)(l)}\right| + \left|\xi_{pk}^{'(r)(l)}\right|\right)^2 + \sum_{\substack{p=1\\p\in Z_s\\p\neq k}}^{\frac{N}{2}-1}\sigma_{H'}^2\left(\left|\xi_{pk}^{(s)(l)}\right| + \left|\xi_{pk}^{'(s)(l)}\right|\right)^2\\ \quad + \sum_{\substack{p=1\\p\in Z_r\\p\neq k}}^{\frac{N}{2}-1}\sigma_H^2\left(\left|\wp_{pk}^{'(r)(l)}\right| + \left|\wp_{pk}^{'(r)(l)}\right|\right)^2 + \sum_{\substack{p=1\\p\in Z_s\\p\neq k}}^{\frac{N}{2}-1}\sigma_{H'}^2\left(\left|\wp_{pk}^{'(s)(l)}\right| + \left|\wp_{pk}^{'(s)(l)}\right|\right)^2 + \sigma_n^2\end{array}} \tag{4.142}$$

$$\underset{Scenario\ 4}{SINR} = \frac{\sigma_H^2\left(\left|\varrho_{kk}^{'(r)(l)}\right| + \left|\varrho_{kk}^{'(r)(l)}\right|\right)^2}{\begin{array}{l}\sum_{\substack{p=1\\p\in Z_r\\p\neq k}}^{\frac{N}{2}-1}\sigma_H^2\left(\left|\varrho_{pk}^{'(r)(l)}\right| + \left|\varrho_{pk}^{'(r)(l)}\right|\right)^2 + \sum_{\substack{p=1\\p\in Z_s\\p\neq k}}^{\frac{N}{2}-1}\sigma_{H'}^2\left(\left|\varrho_{pk}^{'(s)(l)}\right| + \left|\varrho_{pk}^{'(s)(l)}\right|\right)^2\\ \quad + \sum_{\substack{p=1\\p\in Z_r\\p\neq k}}^{\frac{N}{2}-1}\sigma_H^2\left(\left|\chi_{pk}^{'(r)(l)}\right| + \left|\chi_{pk}^{'(r)(l)}\right|\right)^2 + \sum_{\substack{p=1\\p\in Z_s\\p\neq k}}^{\frac{N}{2}-1}\sigma_{H'}^2\left(\left|\chi_{pk}^{'(s)(l)}\right| + \left|\chi_{pk}^{'(s)(l)}\right|\right)^2 + \sigma_n^2\end{array}} \tag{4.143}$$

4.8 Single User Detector (SUD) for VLC

In order to recover the signal corresponding to the desired subscriber, the single user detection scheme in RF consists of multiplying with a time-domain signal prior to DFT processing [195]. However, this strategy as employed in RF cannot be directly implemented in case of optical domain i.e, (VLC). The modified SUD schematic is illustrated in Fig. 4.7. The purpose of choosing this strategy is to reduce the effects of FO which arises due to the prevalence of Doppler Shift in case of outdoor scenarios especially the vehicular communication. From the figure, it is evident that the necessary signal processing operations are performed prior to DFT operation. The received signal under the effects of optical channel environment can be expressed as

$$y = r_m^{(u)} * h + B_{DC} + w \tag{4.144}$$

Since the main motive is to recover the signal corresponding to the desired subscriber and to cancel out ICI and MUI emanating from other subscribers, we emphasize only on the received signal r_m. As seen in the previous section, the received signal r_m with the effects of FO can be represented as

$$r_m^{(u)} = \frac{2}{N} \sum_{\substack{k=1 \\ k \in Z_u}}^{\frac{N}{2}-1} \left(X_{\substack{k \\ RC}}^{(u)} cos\left(\frac{2\pi m\left(k+\beta_u\right)}{N}\right) - X_{\substack{k \\ IC}}^{(u)} sin\left(\frac{2\pi m\left(k+\beta_u\right)}{N}\right)\right) \tag{4.145}$$

Now, this signal can be expressed as a sum of two components r_{m1} and r_{m2}

$$r_m^{(u)} = r_{m1}^{(u)} + r_{m2}^{(u)} \tag{4.146}$$

From (4.146), r_{m1} and r_{m2} are obtained by enforcing trigonometric identities into (4.145),

$$r_{m1}^{(u)} = \frac{1}{N} \sum_{\substack{k=1 \\ k \in Z_u}}^{\frac{N}{2}-1} \left(X_{\substack{k \\ RC}}^{(u)} + jX_{\substack{k \\ IC}}^{(u)} \right) e^{\frac{j2\pi mk}{N}} e^{\frac{j2\pi m\beta_u}{N}} \tag{4.147}$$

And

$$r_{m2}^{(u)} = \frac{1}{N} \sum_{\substack{k=1 \\ k \in Z_u}}^{\frac{N}{2}-1} \left(X_{\substack{k \\ RC}}^{(u)} - jX_{\substack{k \\ IC}}^{(u)} \right) e^{\frac{-j2\pi mk}{N}} e^{\frac{-j2\pi m\beta_u}{N}} \tag{4.148}$$

These individual signal components are multiplied with time-domain sequences $e^{\frac{-j2\pi\beta_r m}{N}}$ and $e^{\frac{j2\pi\beta_r m}{N}}$ respectively as shown in Fig. (4.7). Therefore, the resultant signal $r_m^{'(r)}$ obtained after the summation block is computed as

$$\begin{aligned} r_m^{'(r)} = & \underbrace{\frac{1}{N} \sum_{\substack{k=1 \\ k \in Z_u}}^{\frac{N}{2}-1} \left(X_{\substack{k \\ RC}}^{(r)} + jX_{\substack{k \\ IC}}^{(r)} \right) e^{\frac{j2\pi mk}{N}} + \frac{1}{N} \sum_{\substack{k=1 \\ k \in Z_u}}^{\frac{N}{2}-1} \left(X_{\substack{k \\ RC}}^{(r)} - jX_{\substack{k \\ IC}}^{(r)} \right) e^{\frac{-j2\pi mk}{N}} +}_{if\ r=u} \\ & \underbrace{\frac{1}{N} \sum_{\substack{k=1 \\ k \in Z_u}}^{\frac{N}{2}-1} \left(X_{\substack{k \\ RC}}^{(u)} + jX_{\substack{k \\ IC}}^{(u)} \right) e^{\frac{j2\pi mk}{N}} e^{\frac{j2\pi(\beta_u-\beta_r)m}{N}} +}_{r\neq u\ MUI} \\ & \underbrace{\frac{1}{N} \sum_{\substack{k=1 \\ k \in Z_u}}^{\frac{N}{2}-1} \left(X_{\substack{k \\ RC}}^{(u)} - jX_{\substack{k \\ IC}}^{(u)} \right) e^{\frac{-j2\pi mk}{N}} e^{\frac{-j2\pi(\beta_u-\beta_r)m}{N}}}_{r\neq u\ MUI} + B_{DC} + w_n^{(r)} \end{aligned} \tag{4.149}$$

Finally, upon solving (4.149), the SUD extracts the information of the corresponding or desired subscriber r.

$$r_m^{\prime(r)} = \underbrace{\frac{2}{N}\sum_{\substack{k=1\\k\in Z_u}}^{\frac{N}{2}-1}\left(X^{(r)}_{k_{RC}} cos\left(\frac{2\pi mk}{N}\right) - X^{(r)}_{k_{IC}} sin\left(\frac{2\pi mk}{N}\right)\right)}_{if\ r=u\ Denotes\ Corresponding\ Subscriber\ r} +$$
$$\underbrace{\frac{1}{N}\sum_{\substack{k=1\\k\in Z_u}}^{\frac{N}{2}-1}\left(X^{(u)}_{k_{RC}} + jX^{(u)}_{k_{IC}}\right) e^{\frac{j2\pi mk}{N}} e^{\frac{j2\pi(\beta_u-\beta_r)m}{N}}}_{r\neq u\ MUI} +$$
$$\underbrace{\frac{1}{N}\sum_{\substack{k=1\\k\in Z_u}}^{\frac{N}{2}-1}\left(X^{(u)}_{k_{RC}} - jX^{(u)}_{k_{IC}}\right) e^{\frac{-j2\pi mk}{N}} e^{\frac{-j2\pi(\beta_u-\beta_r)m}{N}}}_{r\neq u\ MUI} + B_{DC} + w_n^{(r)} \quad (4.150)$$

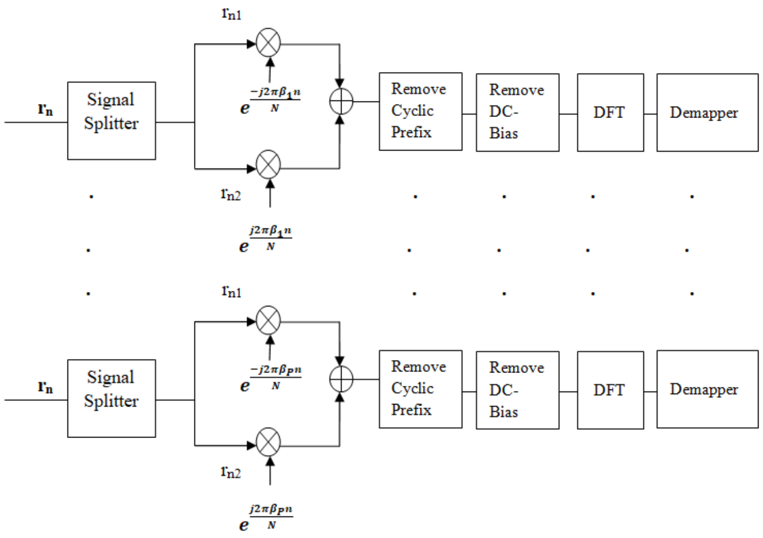

Figure 4.7: Single User Detector Compatible with Intensity Modulated (IM)/Direct Detection (DD) system for VLC

4.9 Synchronization algorithms for the estimation of STO

In the perspective of real-time applications, it is vital to have an effective estimate of the starting position of the frame. Generally, the starting position of the frame is exploited at the receiving end to determine the alignment of the FFT-window with the useful portion of the optical OFDM symbol. However, a false estimate of the frame start position disrupts the orthogonality of the system thereby leading to the occurrence of ISI. Furthermore, from the aforementioned mathematical analysis as elucidated in Section 4.6, it is seen that the received signal deteriorates due to frame misalignments. As a result, the system is prone to severe ICI, ISI, MUI/MAI. Therefore, this necessitates to estimate the frame start position in order to ensure perfect reliability of services in multi-user scenarios. Periodic structures within a signal can be exploited for estimation of the frame-start position. Particularly, in OFDM, cyclic prefix represents the last portion of the OFDM symbol which is appended to the front of the symbol. As evidenced form Fig. 4.8, periodic properties of the OFDM symbol are exploited to ensure effective frame synchronization. The cyclic prefix and the last portion of the OFDM data samples are included in two windows namely window A and window $A^{'}$. In particular, the length of these samples are taken as $\delta_{N_{cp}}$. The aforementioned windows can be slided to ensure the detection of identical nature of these samples which are contained within those two windows. In precise, the similarity index between the samples which are contained in windows A and $A^{'}$ is maximized when the difference between these sets of samples is minimized. Therefore, by taking into consideration the FO which emerges due to slight movement of people or vehicles, one appropriate way of estimation of STO is to effectively minimize the squared difference of the samples seized in window A and the conjugate of the data samples contained in window $A^{'}$.

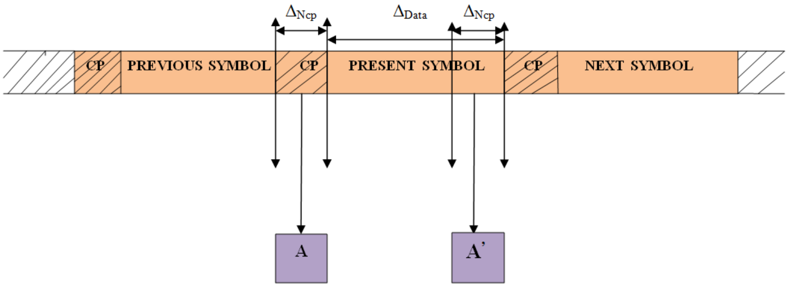

Figure 4.8: Cyclic Prefix (CP) based STO estimation

The estimate of STO pertaining to the corresponding subscriber r on the kth subcarrier for the qth symbol can be given as [177]

$$\hat{\alpha} = arg\,\underset{\alpha}{min} \left\{ \sum_{j=\alpha}^{N_{cp}-1+\alpha} \left(\left|y_q^{(r)}(n+j)\right| - \left|y_q^{*(r)}(n+N+j)\right| \right)^2 \right\} \tag{4.151}$$

Table 4.1: Parameters employed for Simulation

Parameter	Value
Size of IFFT/FFT	512
Total Number of Pilot Carriers	64
Cyclic Prefix Length	128
Orders of Modulation	BPSK, 4, 16-QAM
Range of FO	$[0, 0.05, 0.10, 0.15, 0.20]$
Type of optical OFDM methodology employed	DCO-OFDM
No of OFDM symbols	100
FO estimation algorithms	Classen, Moose, Training symbol assisted
Range of STO	[-3, 3]
STO estimation algorithms	Maximum Correlation, Minimum Difference

The second approach is to exploit the correlation between the data samples seized in the two windows A and $A^{'}$. Eventually, maximum likelihood way of estimation can be employed to obtain the STO estimate and is given as [177], [196]

$$\hat{\alpha} = \underset{\alpha}{arg\ max} \left\{ \sum_{j=\alpha}^{N_{cp}-1+\alpha} \left| y_q^{(r)}\left(n+j\right) y_q^{*(r)}\left(n+N+j\right) \right| \right\} \tag{4.152}$$

4.9.1 Results and Discussions

The above system models were developed using 512 subcarriers, where the pilot arrangement considered is comb type pilot arrangement and the pilot insertion frequency N_f is 8. Generally, the cyclic prefix's length is chosen as $\frac{1}{4}^{th}$ of the subcarrier's size. Mathematical analysis is carried out to clearly illustrate the effects of frequency and timing offsets on the received signal. Thus, synchronization algorithms such as Classen, Moose and Training symbol assisted algorithms are exploited in order to estimate these offsets. The simulation set-up is illustrated in Table. 4.1.

Fig. 4.9 and Fig. 4.10 depicts the constellation diagrams with and with out the effect of FO. From Fig. 4.10, it can be viewed that the constellation is distorted as it has a circular shape. Fig. 4.11, shows the MSE vs SNR performance of various synchroniza-

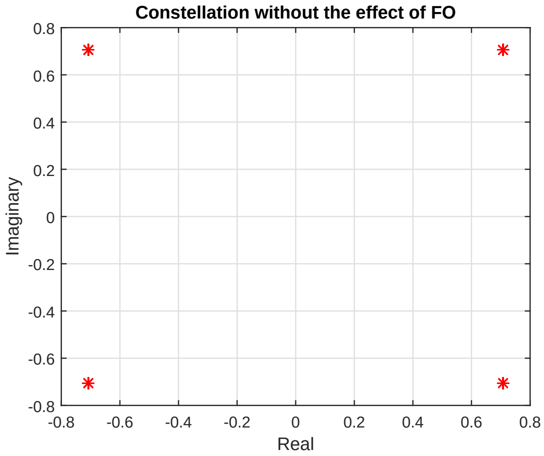

Figure 4.9: Constellation without the effect of FO

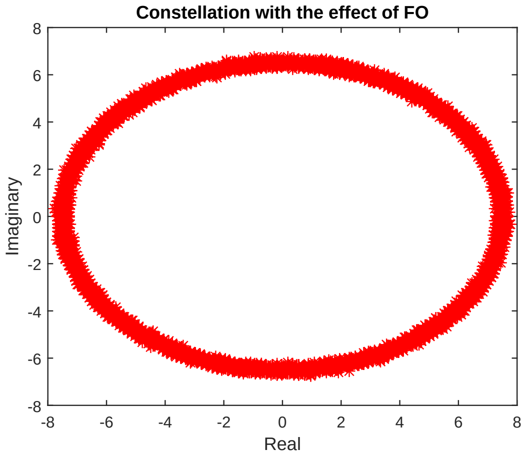

Figure 4.10: Constellation with the effect of FO

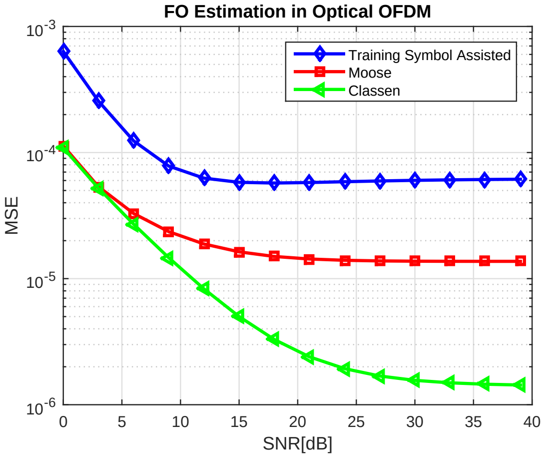

Figure 4.11: MSE vs SNR performance of different FO-Estimation algorithms in DCO-OFDM system without channel effect

tion algorithms such as Classen, Training Symbol assisted and Moose. Here, the optical channel environment is completely neglected. The results show that Classen gives better performance compared with the other two algorithms in terms of MSE. At SNR of 39 dB the MSE for Training based, Moose and classen are 0.7854×10^{-4}, 0.3273×10^{-4} and 3.197×10^{-6} respectively. While Fig. 4.12 represents the performance analysis of different

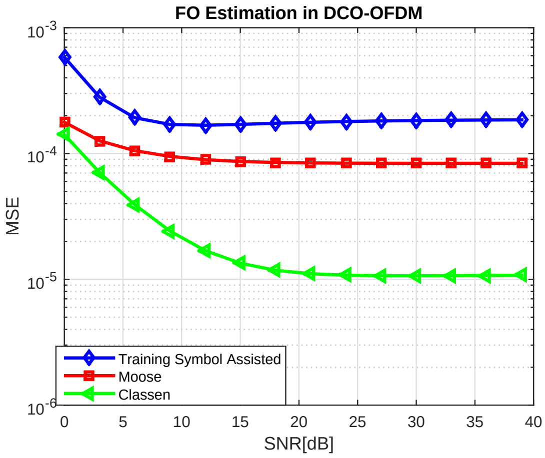

Figure 4.12: MSE vs SNR performance of different FO-Estimation algorithms in DCO-OFDM system under the effect of optical channel

channel estimation algorithms in DCO-OFDM under the effect of optical channel environment. Here, it is evident that due to the presence of channel effect the performance of the system is slightly degraded. At SNR of 39 dB, the MSE for the three algorithms namely, Training symbol assisted, Moose and Classen is 1.852×10^{-4}, 0.8365×10^{-4} and 1.077×10^{-5} respectively. The results obtained from Fig. 4.12 when compared with those obtained from Fig. 4.11 clearly emphasizes that the system performance is slightly degraded due to the presence of multipath optical channel effect.

The simulated results for DCO-OFDMA system for an uplink scenario is illustrated in the subsequent figures. For the aforementioned mathematical analysis described, the performance of the system is analysed by employing 1024 subcarriers and cyclic prefix is inserted at $\frac{1}{4}$th the subcarriers size. Generally, the amount of DC bias added is equal to the absolute value of the maximum negative amplitude of the time-domain signal and is added per symbol basis. This addition of DC bias is choosen in order to minimize the clipping of the negative peaks of the optical time-domain signal. In this work. we consider that FO arises due to Doppler Shift, be it with the moving vehicles on road or people moving in an indoor or outdoor room environment. The deterioration of the performance

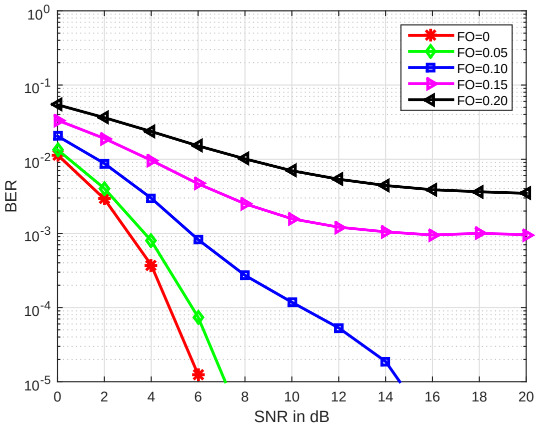

Figure 4.13: Performance analysis of DCO-OFDMA system using BPSK modulation in the presence of FO

of DCO-OFDMA system under the presence of different range of offsets is shown in Fig. 4.13. From the figure it is evident that, as the range of FO increases, the BER performance degrades. Furthermore, as the value of FO increases from 0.15 to 0.20, ..., (higher values of FO are omitted for simulation), there is an irreducible error floor. At SNR of 6 dB, the BER attained is 1.25×10^{-6} without any FO. While, as the value of FO increases from 0.05, 0.10, 0.15 and 0.20, for the same SNR of 6 dB, the obtained BER is 7.422×10^{-5}, 8.25×10^{-4}, 0.4659×10^{-2} and 0.1512×10^{-1} respectively. Fig. 4.14, clearly depicts the

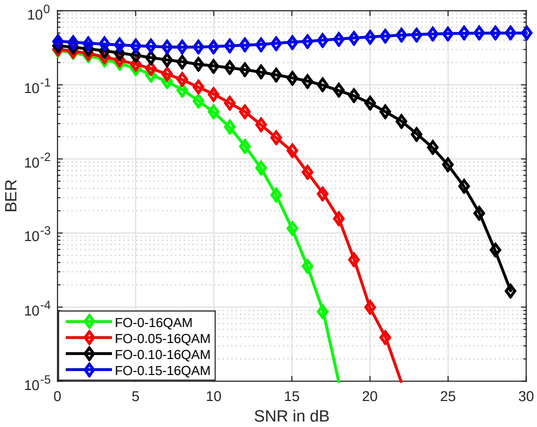

Figure 4.14: Performance of DCO-OFDMA using 4-QAM Modulation in the presence of FO

performance analysis of DCO-OFDMA using 4-QAM modulation for different values of FO. The same conclusion can be drawn as that of the previous case.

The simulation results emphasizing the variation of BER with respect to FO for DCO-

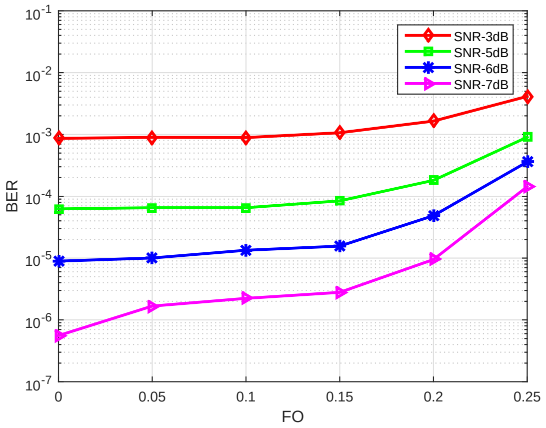

Figure 4.15: BER vs FO for different values of SNR in DCO-OFDMA system

OFDMA system by considering different values of SNR is depicted in Fig. 4.15. From the figure, it can be inferred that, the performance of the system deteriorates as the range of FO values increase from $0, 0.05, 0.1, 0.15, 0.2$. It is interesting to note that upon increasing the SNR values from $3, 5, 6$ and 7 dB a better BER is evidenced. This can be more precisely described as, at SNR of 3 dB, the achievable values of BER in the presence of different values of FO i.e., $0, 0.05, 0.1, 0.15, 0.2, 0.25$ are 8.823×10^{-4}, 8.811×10^{-4}, 9.196×10^{-4}, 1.069×10^{-3}, 1.658×10^{-3} and 0.4103×10^{-2}. While, employing 7 dB of SNR, the evidenced value of BER for increasing values of FO from 0 to 0.25 are 5.58×10^{-7}, 5.58×10^{-7}, 1.16×10^{-6}, 1.674×10^{-6}, 1.228×10^{-5} and 0.1473×10^{-3} respectively. Therefore, this confirms that a certain higher amount of SNR is required to achieve a reduced probability of error in the presence of FO for DCO-OFDMA system. The same inference can be drawn with multi user scenario which is elucidated in Fig. 4.16, indicating that the presence of different values of FO degrades the performance of system thereby hindering the detection capability of multiple users. This can be evidenced in Fig. 4.16, because with the increase in number of subscribers, the BER performance deteriorates for higher values of FO. The most detrimental aspect of this scenario is that, as the value of FO increases from 0.15, it is very difficult to achieve reduced error floor. Moreover, this existence of FO leads to the most deleterious issue which is none other than MUI. So, it necessitates to impose certain MUI cancellation strategies like SUD as dealt in Section 4.8.

SUD strategy is imposed for the developed system which is affected with FO as shown in Fig. 4.13 and 4.14. For the mathematical analysis carried forward in the aforementioned

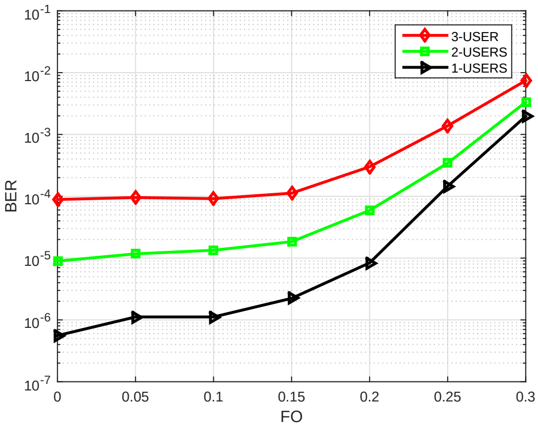

Figure 4.16: BER vs FO for multi-users in DCO-OFDMA system

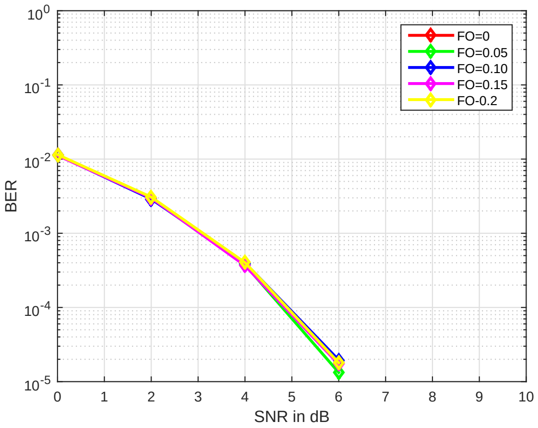

Figure 4.17: Singe User Detector (SUD) combating the MUI in DCO-OFDMA employing BPSK modulation

section, simulation result is delineated in Fig. 4.17 and 4.18. From the figures it can be emphasized that, FO can be effectively combated and the desired subscriber signal can be extracted. However, the complexity is increased because of the received signal format, where additional hardware like signal splitter is required at each stage. Upon comparison with RF domain, there is a necessity of incorporation of signal splitter. Therefore, this confirms the fact that, the existing RF domain MUI cancellation strategies cannot be directly applied while working with VLC due to the constraints of real and positive signal transmission.

For the purpose of estimating the possibilities of different timing discrepancies, i.e, the received signal with the existence of STO, two synchronization algorithms like Classen/minimum difference and Maximum Likelihood estimate/maximum correlation

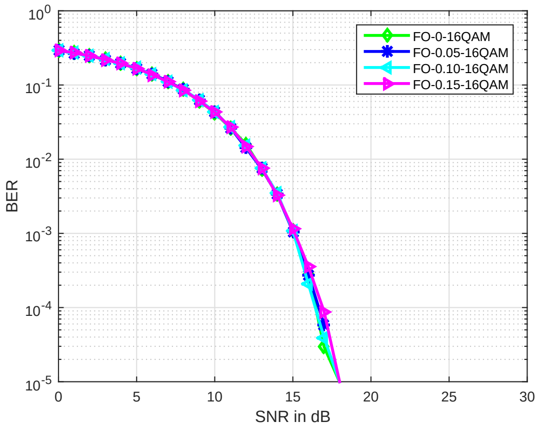

Figure 4.18: Singe User Detector (SUD) combating the MUI in DCO-OFDMA employing 4-QAM modulation

methods are revisited. These algorithms are imposed to the developed system model i.e., DCO-OFDMA system and the different scenarios are elucidated in Fig. 4.19a, 4.19b and 4.19c. Fig. 4.19a, illustrates the positive timing error, i.e, when the actual sample arrives a little early than required. In general, this scenario highlights the case of the prevalence of ICI among the subcarrier components of the current symbol, as well as MUI exists. Hence, synchronization algorithms are vital to be enforced to estimate the STO for DCO-OFDMA system. So, in this scenario an STO of 3 is considered, the simulations are carried without the existence of FO. From the figure, it can be inferred that, the actual and the estimated values of the minimum difference method and the maximum correlation method are in a good agreement. This is evident from the figure, where the maximum peak and the minimum value are located at $sample = 3$.

The timing discrepancies when the actual sample arrives a little late and too early than that is required are illustrated in Fig. 4.19b and 4.19c respectively. These are the most detrimental scenarios which depicts the overlap between the current symbol with the previous and next symbols, thereby leading to the emanation of ICI and MUI. In order to show the effects of FO, the simulations are carried with and without the existence of FO. Without the FO, the result analysis depicts the possibility of estimating the timing error, while in the presence of FO, it becomes difficult to estimate STO, this is clearly shown in Fig. 4.19c, where the estimated and the actual value of STO are not in an agreement. Fig. 4.20 and 4.21 illustrates the CRLB for both the estimations namely FO and STO. The figures represent that the derived minimum variance is plotted against

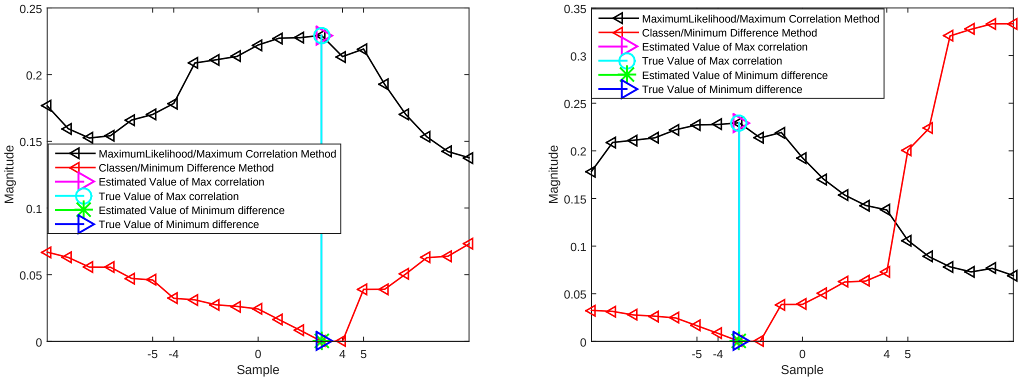

(a) Positive Timing Error (STO) estimation without the existence of FO

(b) Negative Timing Error (STO) estimation without the existence of FO

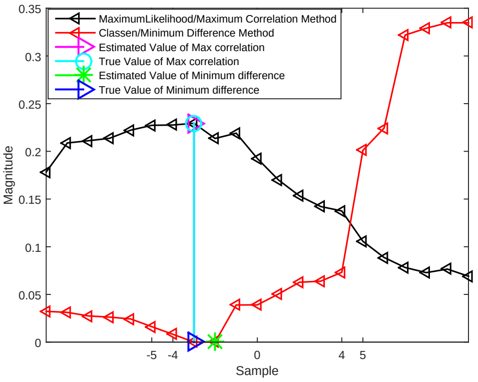

(c) Negative Timing Error (STO) estimation with the existence of FO

Figure 4.19: Exploiting Cyclic Prefix (CP) Based methods for the estimation of Different Timing Errors

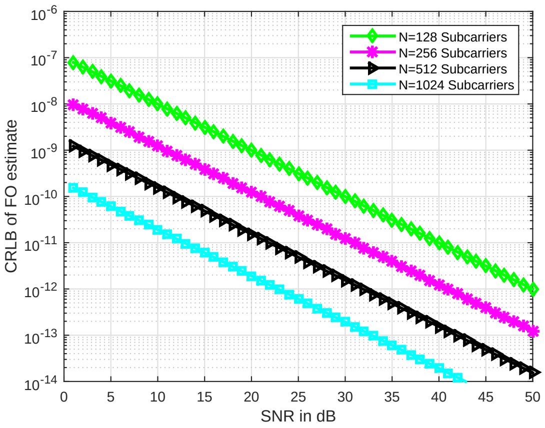

Figure 4.20: CRLB for the estimation of FO by varying the number of subcarriers

different ranges of SNR for different subcarriers ranging from $N = 128, 256, 512$ and 1024. Upon increasing the SNR, there is a significant improvement in the attained error floor. For the scenario of FO estimation, mean square error of 9.929×10^{-11} is observed at SNR of 30 dB, while a drastic improvement in error floor is attained for higher ranges of SNR i.e., at SNR of 50 dB, the achieved error is 9.29×10^{-13}. Whereas, pertaining to STO estimation, at SNR of 30 dB, in the case of 128 subcarriers, the obtained mean square error is 1.301×10^{-9}, while it requires 50 dB of SNR to reach a reduced error floor of 1.321×10^{-11}.

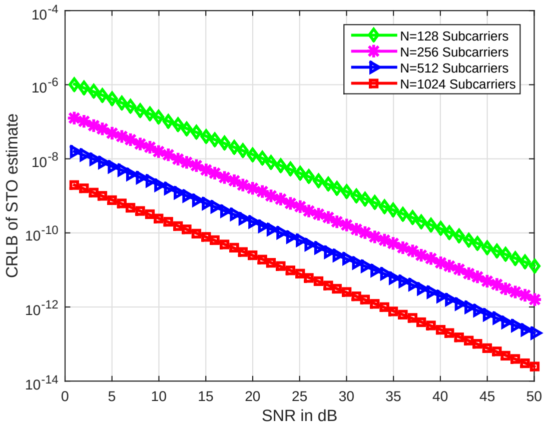

Figure 4.21: CRLB for the estimation of STO by varying the number of subcarriers

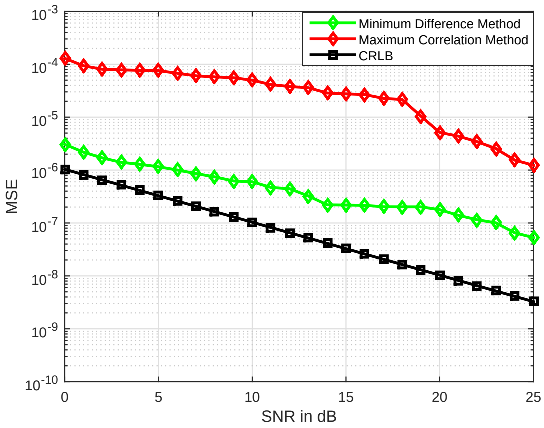

Figure 4.22: Performance analysis of MSE vs SNR for different STO estimation algorithms

Fig. 4.22 gives the mean square error vs SNR performance for the two STO estimation techniques. Furthermore, the performance of the two estimation techniques is compared with the derived CRLB for STO estimation. From the simulated result, it can be deduced that CRLB attains the minimum variance upon comparison with the other two estimation algorithms like Maximum Correlation method and Minimum difference method. At SNR of 25 dB, CRLB gives the minimum mean square error of 3.269×10^{-9}, while, Maximum Correlation method and Minimum difference method gives mean square error of 1.234×10^{-6} and 5.301×10^{-8}. Minimum difference method gives a better mean square error performance when compared with Maximum Correlation method for the estimation of STO in DCO-OFDMA system for VLC.

4.10 Conclusion

This chapter firstly focuses on the derivation of mathematical analysis for the purpose of depicting the effects of STO and FO on the received signal in a multicarrier system like DCO-OFDM system over VLC channel. Synchronization algorithms such as Training Symbol assisted sequences, Moose and Classen are revisited and the performance of these algorithms is analyzed for DCO-OFDM over optical channel environment. Further, CRLB is derived for different estimation errors like FO and STO and is verified through simulation results. The results show that Classen algorithm gave better performance without optical channel environment as well as in the presence of optical channel. Additionally, the simulation results emphasize that, CRLB attains the minimum variance when compared with other FO estimation algorithms. Illustration of the mathematical analysis provides a scope for further research, which enables to develop more sophisticated algorithms for the estimation of different offsets in order to improve the performance of the system.

Furthermore, this chapter derives the SINR analysis for DCO-OFDMA system and analyses the performance of the system in the presence of frequency and timing induced offsets. Moreover, an elaborate mathematical analysis is accomplished by taking into consideration the most detrimental aspects such as FO and STO. Handling, these issues is critical because, this growing technology called VLC can be easily interfaced with the lighting infrastructure in the smart city, so it necessitates to impart a reliable high data rate transmission. This work emphasizes on the characterization of the time-domain signal in accordant with IM/DD systems.

Besides, mathematical analysis is carried out illustrating the deterioration of frequency domain DCO-OFDMA signal in the presence of different offsets and categorized the different interferences like ICI and MUI emanating in multi user scenario especially in the optical domain. The maximum possibilities of timing discrepancies are considered along with the existence of FO for the aforementioned system in an uplink environment. The existing MUI cancellation methodologies in RF are revisited and a modified version of SUD for ensuring perfect detection of the signal corresponding to the desired subscriber is proposed in this work. In addition, with the intent of assuring adequate synchronization, different probable sets of timing errors (STO) are estimated using Classen and Maximum Likelihood techniques for DCO-OFDMA system. Further, CRLB for the FO and STO estimators is derived and is verified through simulation results.

From the result analysis it can be inferred that with the increase in the sensitivity of these offsets, there is drastic deterioration in the system performance. The proposed SUD strategy plays a vital role in reducing the probability of error and ensuring perfect detection of the signal corresponding to the desired user, but, at the expense of increase in the requirement of additional digital signal processing circuitry. The mathematical derivations illustrate the necessity of enforcing several synchronization algorithms in order to overcome the deleterious effects of the offsets. CRLB gives the minimum variance of the STO estimation when compared with Maximum Correlation and Minimum Difference methods.

Chapter 5

Effects of timing and frequency offsets in DCT-based DCO-OFDMA (DCO-FOFDMA) System

5.1 Synchronization aspects in DCT-based DCO-OFDMA (DCO-FOFDMA) system

5.1.1 Introduction and Motivation

In the previous chapter, Hermitian Symmetry imposed IFFT is used for implementing an uplink scenario in a multiple access system. However, it is possible to exploit other sinusoidal trigonometric transform like DCT for the realization of a multiple access system which is reconciling with IM/DD systems. The benefits of utilization of DCT in IM/DD systems is clearly underlined in chapter 3 and the advantages of it when compared with IFFT are also summarized. Principally, the most remarkable feature of DCT lies in its excellent spectral energy compaction property, which results most of the transmitted samples close to zero thereby surpassing the effects of ISI. Similar to DFT-based multiple access system, DCT-based multiple access system which is referred to as DCO-FOFDMA also suffer from frequency and timing offsets. Consequently, there is a necessity to characterize the performance of DCO-FOFDMA system in the presence of these offsets. Therefore, this chapter highlights through mathematical expressions the deterioration of the received signal in a DCO-FOFDMA system in the presence of FO and STO.

5.1.2 System Model

The simple schematic of uplink scenario in DCO-FOFDMA system in which the mobile and the base stations are designed in accordant with IM/DD systems for VLC is delineated in Fig. 5.1, where P subscribers/users are carrying on their transactions with the base stations through their relevant independent multipath optical channels. Looking into the details of transmitter and receiver blocks, at the transmitting terminal, huge sets of incoming BPSK, M-PAM mapped data streams are transmitted in parallel with the help of S/P converter.

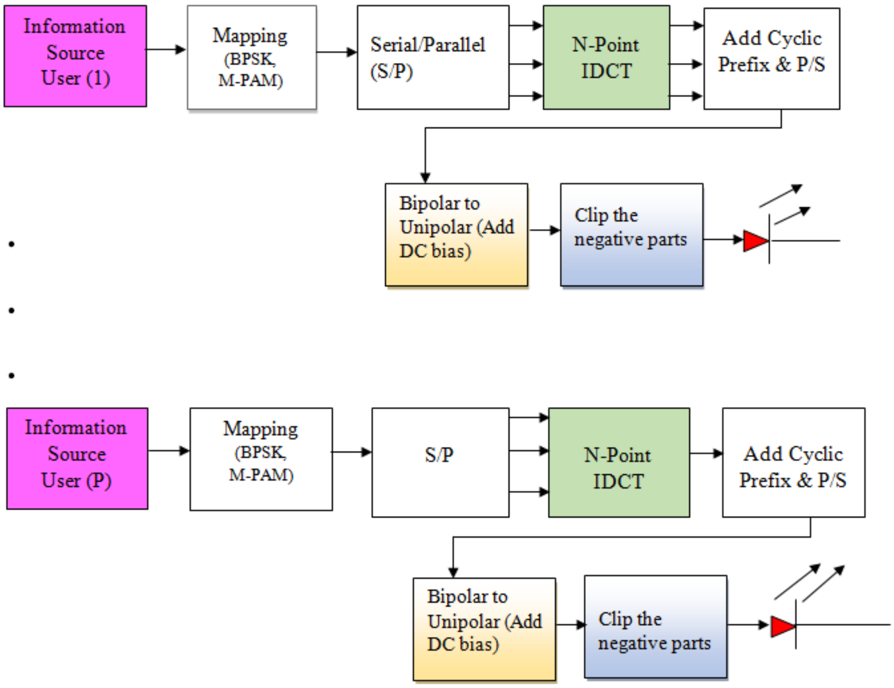

(a) Uplink Transmission Scenario in DCO-FOFDMA for VLC

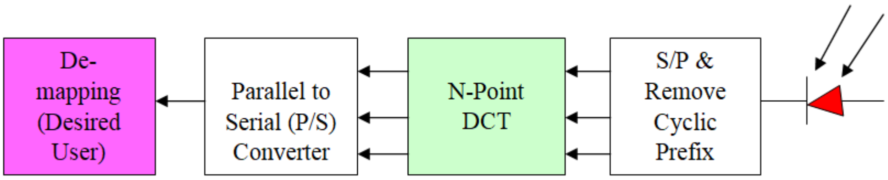

(b) DCO-FOFDMA Receiver

Figure 5.1: Illustration of Uplink transmitter and receiver in DCO-FOFDMA in accordant with IM/DD systems for VLC

In order to emphasize the detrimental aspects of FO and STO on the desired subscriber r, we surmise that the total number of subcarriers present in one OFDM symbol are N. Therefore, the mapped data corresponding to the rth subscriber on the kth subcarrier be represented as $X_k^{(r)}$, $k \in Z_r$, where Z_r is the set of subcarriers appropriated to the rth subscriber and $\cup_{r=1}^{P} Z_r = \{0, 1, 2, \cdots N-1\}$. Unlike, FFT-based optical OFDM, FOFDMA does not require Hermitian Symmetry criteria. Hence, $X_k^{(r)}$ is loaded into the N-Point IDCT block to yield the corresponding time-domain signal $x_n^{(r)}$ as follows [171]

$$x_n^{(r)} = \sqrt{\frac{2}{N}} \sum_{\substack{k=0 \\ k \in Z_r}}^{N-1} C_k X_k^{(r)} cos\left(\frac{\pi\,(2n+1)\,k}{2N}\right), \quad 0 \leq k \leq N-1 \tag{5.1}$$

From (3.66), C_k denotes

$$C_k = \begin{cases} \frac{1}{\sqrt{2}}, & k = 0 \\ 1, & k = 1, 2, 3, \cdots N-1 \end{cases} \tag{5.2}$$

The equation (5.1), clearly depicts the ease and simplicity of incorporation of DCT. In addition, there is an enhancement in the spectral efficiency as all of the subcarriers are utilized for data transmission. Generally, in an indoor room environment, ISI emanates due to the multipath dispersion as well as sudden blockage of signal due to presence of several obstacles like furniture, etc. Consequently, in order to prohibit ISI, a suitable amount of cyclic prefix or guard interval of length N_{cp} is added to $x_n^{(r)}$. The amount of cyclic prefix to be added is chosen as $\frac{1}{4}$th of the subcarriers' size and must be larger than the channel delay spread L. Therefore, the cyclic prefix added signal can be represented as

$$\begin{aligned} x_n^{(r)} = \sqrt{\frac{2}{N}} \sum_{\substack{k=0 \\ k \in Z_r}}^{N-1} C_k X_k^{(r)} cos\left(\frac{\pi\,(2n+1)\,k}{2N}\right), \quad & 0 \leq k \leq N-1 \\ & -N_{cp} < n \leq N-1 \end{aligned} \tag{5.3}$$

Equation (5.3), clearly emphasizes a real valued signal, further this can be transformed into a positive signal by adding a suitable amount of DC bias. Generally, the amount of DC bias to be added is equal to the absolute value of the maximum negative amplitude of the signal. In addition, the amount of DC bias to be added also has a direct relation with the constellation size of the modulation schemes. Too much amount of DC bias leads to power inefficiency, but however this is desired for illumination requirement in VLC. Minimal addition of DC bias leads to clipping of the peak values, thereby leading to the occurrence of clipping noise. Hence, an optimal choice of DC bias is desired to transform the negative real valued signal to positive signal.

In the literature, it is specified that, the amount of DC bias to be added is given as

$$\beta_{DC} = k\sqrt{E\{x^2\left[n\right]\}} \tag{5.4}$$

From (5.4), the factor k specifies the clipping factor. A fixed amount of bias which is to be added is given by $10log_{10}\left(k^2+1\right)\ dB$. Therefore, the DC bias added signal is given by

$$\underset{DC}{x_n^{(r)}} = \sqrt{\frac{2}{N}}\sum_{\substack{k=0\\k\in Z_r}}^{N-1} C_k X_k^{(r)} cos\left(\frac{\pi\left(2n+1\right)k}{2N}\right) + \beta_{DC} \tag{5.5}$$

And now, this signal corresponding to the rth subscriber i.e., $\underset{DC}{x_n^{(r)}}$ is subsequently passed through the channel with an impulse response $h_n^{(r)}$. Hence, the signal invading the receiver can be put up as

$$y_n^{(r)} = \underset{DC}{x_n^{(r)}} * h_n^{(r)} + w_n^{(r)} \tag{5.6}$$

It is to be noted that, the channel response corresponding to the rth subscriber is non-zero only for the values $l = 0, 1, 2, 3, \cdots L-1$. Hence, the frequency response of the channel corresponding to the rth subscriber is given as

$$H_k^{(r)} = \sqrt{\frac{2}{N}} C_k \sum_{l=0}^{L-1} h_l^{(r)} cos\left(\frac{\pi\left(2l+1\right)k}{2N}\right) \tag{5.7}$$

In addition, it is deduced that, the channels belonging to all the subscribers are statistically independent.

In order to elucidate the deleterious aspects of FO, we assume that, the received signal is affected with FO of β. As stated earlier in the previous chapter 4, the presence of FO leads to loss of orthogonality among the subcarriers and results in ICI. Besides, MUI or MAI emanates due to frequency discrepancies occurring among the uplink subscribers and even there are chances for dissimilarities to emerge between the uplink users and the base station. At the receiver terminal, reverse operations are incorporated like removal of cyclic prefix and DC bias. In order to highlight, the various interferences, we proceed further by stressing on the frequency domain signal. Accordingly, the frequency domain representation of $y_n^{(r)}$ is given as

$$Y_k^{(r)} = \sqrt{\frac{2}{N}} C_k \sum_{n=0}^{N-1} y_n^{(r)} cos\left(\frac{\pi\left(2n+1\right)k}{2N}\right) \tag{5.8}$$

It is well known that, $y_n^{(r)} = IDCT\left[Y_k^{(r)}\right]$ and using the fundamental signal processing operation that convolution in time domain is multiplication in frequency domain i.e., $Y_k^{(r)} = X_k^{(r)} H_k^{(r)}$.

Hence, it is apt to express $y_n^{(r)} = IDCT\left[Y_k^{(r)}\right] = IDCT\left[X_k^{(r)} H_k^{(r)}\right]$. Consequently, upon incorporating in (5.8), the following frequency domain signal is attained

$$Y_k^{(r)} = \sqrt{\frac{2}{N}} C_k \sum_{n=0}^{N-1} \left[\sqrt{\frac{2}{N}} \sum_{\substack{k=0\\ k\in Z_r}}^{N-1} C_k X_k^{(r)} cos\left(\frac{\pi\left(2n+1\right)\left(k+\beta_r\right)}{2N}\right) \right] \times cos\left(\frac{\pi\left(2n+1\right)k}{2N}\right) H_k^{(r)} + W_k^{(r)} \tag{5.9}$$

(5.9), can be further solved to attain

$$\begin{aligned} Y_k^{(r)} = & \underbrace{C_k^2 X_k^{(r)} \left[\sqrt{\frac{2}{N}} C_k \sum_{l=0}^{L-1} h_l^{(r)} cos\left(\frac{\pi\left(2l+1\right)k}{2N}\right) \right] \Gamma_{kk}^{(r)}}_{Desired\ Signal\ of\ Corresponding\ User\ r} + \\ & \underbrace{C_k \sum_{\substack{p=0\\ \boldsymbol{p\in Z_r}\\ \boldsymbol{p\neq k}}}^{N-1} C_p X_p^{(r)} \left[\sqrt{\frac{2}{N}} C_p \sum_{l=0}^{L-1} h_l^{(r)} cos\left(\frac{\pi\left(2l+1\right)p}{2N}\right) \right] \Gamma_{pk}^{(r)}}_{ICI\ emanating\ due\ to\ subcarrier\ components\ allocated\ to\ r} + \\ & \underbrace{C_k \sum_{\substack{p=0\\ \boldsymbol{p\in Z_s}\\ \boldsymbol{p\neq k}}}^{N-1} C_p X_p^{(s)} \left[\sqrt{\frac{2}{N}} C_p \sum_{l=0}^{L-1} h_l^{(s)} cos\left(\frac{\pi\left(2l+1\right)p}{2N}\right) \right] \Gamma_{pk}^{(s)}}_{MUI/MAI} + W_k^{(r)} \end{aligned} \tag{5.10}$$

From (5.10), $\Gamma_{kk}^{(r)}$, $\Gamma_{pk}^{(r)}$ and $\Gamma_{pk}^{(s)}$ can be expressed as

$$\Gamma_{kk}^{(r)} = \frac{1}{N} \sum_{n=0}^{N-1} \left[cos\left(\frac{\pi\left(2n+1\right)\left(2k+\beta_r\right)}{2N}\right) + cos\left(\frac{\pi\left(2n+1\right)\beta_r}{2N}\right) \right] \tag{5.11}$$

$$\Gamma_{pk}^{(r)} = \frac{1}{N} \sum_{n=0}^{N-1} \left[cos\left(\frac{\pi\left(2n+1\right)\left(p+\beta_r+k\right)}{2N}\right) + cos\left(\frac{\pi\left(2n+1\right)\left(p+\beta_r-k\right)}{2N}\right) \right] \tag{5.12}$$

$$\Gamma_{pk}^{(s)} = \frac{1}{N} \sum_{n=0}^{N-1} \left[cos\left(\frac{\pi\left(2n+1\right)\left(p+\beta_s+k\right)}{2N}\right) + cos\left(\frac{\pi\left(2n+1\right)\left(p+\beta_s-k\right)}{2N}\right) \right] \tag{5.13}$$

Accordingly, the interference components in (5.11), (5.12) and (5.13) can be solved to attain

$$\Gamma_{kk}^{(r)} = \frac{sin\pi\left(2k+\beta_r\right)}{2N sin\pi\left(\frac{2K+\beta_r}{2N}\right)} + \frac{sin\pi\left(\beta_r\right)}{2N sin\pi\left(\frac{\beta_r}{2N}\right)} \tag{5.14}$$

$$\Gamma_{pk}^{(r)} = \frac{sin\pi\left(p+\beta_r+k\right)}{2Nsin\pi\left(\frac{p+\beta_r+k}{2N}\right)} + \frac{sin\pi\left(p+\beta_r-k\right)}{2Nsin\pi\left(\frac{p+\beta_r-k}{2N}\right)} \tag{5.15}$$

$$\Gamma_{pk}^{(s)} = \frac{sin\pi\left(p+\beta_s+k\right)}{2Nsin\pi\left(\frac{p+\beta_s+k}{2N}\right)} + \frac{sin\pi\left(p+\beta_s-k\right)}{2Nsin\pi\left(\frac{p+\beta_s-k}{2N}\right)} \tag{5.16}$$

The first term in (5.10) specifies the desired signal, while the second term represents the ICI originating from the subcarrier components which are allocated to the desired user r, for the ease of depiction we showed as the interference occurring between k and p subcarriers, and the third term signifies the MUI/MAI arising due to user s. The terms β_r and β_s corresponds to the offset associated with user r and s.

5.1.3 Mathematical Illustration of deterioration of received signal due to occurrence of STO

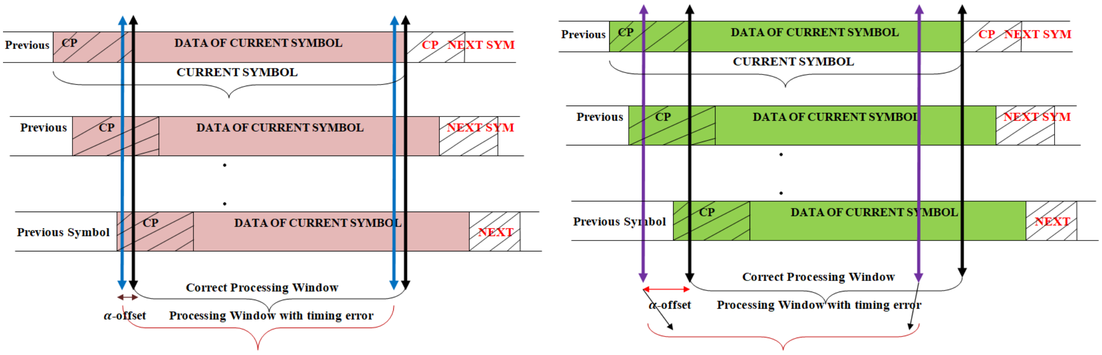

(a) Negative Timing Error (b) Overlap with previous Frame

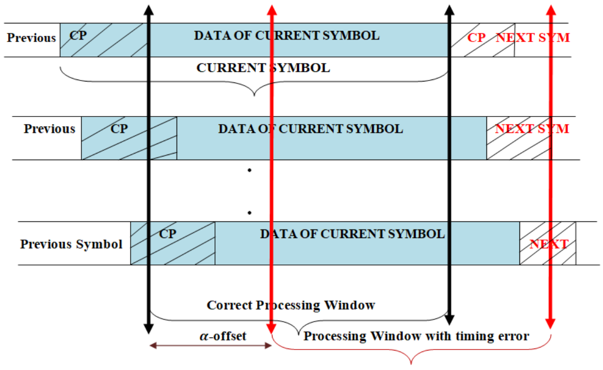

(c) Overlap with next Frame

Figure 5.2: Illustration of different timing discrepancies in DCO-FOFDMA in accordant with IM/DD systems for VLC

This section evaluates the different possibilities of timing discrepancies in a DCT-FOFDMA system. It is to be noted that, in the absence of other users, self interference i.e,

ICI arises among the subcarrier components which are allocated to the desired subscriber r. Whereas, in the presence of other users, MUI/MAI originates due to misalignments among the users, which manifests the previous frame or the next frame to overlap with the current frame. These different scenarios of timing errors are taken from [194] where analysis has been carried in the RF domain. In this work we have modeled fulfilling the prerequisite of IM/DD systems for VLC i.e, ensuring a real and positive signal transmission. The different scenarios of timing errors is summarized in Fig. 5.2.
Additionally, we assume that α_u and β_u, $u = \{1, 2, 3, \cdots P\}$ denotes the uth subscriber's FO and STO. It is likely that the timing errors to be both negative as well as positive.

- **Scenario 1:** This scenario is illustrated in Fig. 5.2a, which indicates negative timing error, i.e., $\alpha_u < 0$ and the interval where the offset lies is $0 \leq -\alpha_u \leq N_{cp} - L + 1$ [194]. Therefore, by using the aforesaid conditions, the frequency domain representation of the users $u = 1, 2, 3, \cdots P$ on the kth subcarrier can be formulated as

$$Y_k^{(u)} = \sqrt{\frac{2}{N}} C_k \sum_{n=0}^{N-1} \left[\sqrt{\frac{2}{N}} \sum_{\substack{k=0 \\ k \in Z_u}}^{N-1} C_k X_k^{(u)} cos \left(\frac{\pi \left(2 \left(n + \alpha_u\right) + 1\right) \left(k + \beta_u\right)}{2N} \right) \right]$$
$$\times \, cos \left(\frac{\pi \left(2n + 1\right) k}{2N} \right) H_k^{(u)} + W_k^{(u)} \quad (5.17)$$

  (5.17), signifies the DCT output of the uth user on the kth subcarrier. Inevitably, in order to illustrate the effects of mismatching timing interval, we confine our discussion with desired user as r. Hence, the frequency domain output of the dedicated user r on the kth subcarrier, in the presence of all the signals invading from all the paths belonging to different subscribers can be derived as stated in A.1 (please see Appendix A). Therefore, the scenario highlighted by (A.1) signifies that the received signal seriously suffers from ICI and MUI/MAI thereby, resulting in the degradation of the SINR. Furthermore, by making use of (A.1), the frequency domain output of the appropriate subscriber r is obtained as follows:

$$\begin{aligned} Y_k^{(r)} = & \underbrace{C_k^2 X_k^{(r)}\left[cos\left(\frac{\pi\alpha_r\left(k+\beta_r\right)}{N}\right)\Upsilon_{kk}^{(r)} - sin\left(\frac{\pi\alpha_r\left(k+\beta_r\right)}{N}\right)\Upsilon_{kk}^{'(r)}\right]H_k^{(r)}}_{Desired\ Signal\ of\ subscriber\ r} + \\ & \underbrace{C_k \sum_{\substack{p=0\\ \boldsymbol{p\in Z_r}\\ \boldsymbol{p\neq k}}}^{N-1} C_p X_p^{(r)}\left[cos\left(\frac{\pi\alpha_r\left(p+\beta_r\right)}{N}\right)\Upsilon_{pk}^{(r)} - sin\left(\frac{\pi\alpha_r\left(p+\beta_r\right)}{N}\right)\Upsilon_{pk}^{'(r)}\right]H_p^{(r)} +}_{ICI\ emanating\ among\ the\ subcarriers\ allocated\ to\ subscriber\ r} \\ & \underbrace{C_k \sum_{\substack{p=0\\ \boldsymbol{p\in Z_s}\\ \boldsymbol{p\neq k}}}^{N-1} C_p X_p^{(s)}\left[cos\left(\frac{\pi\alpha_s\left(p+\beta_s\right)}{N}\right)\Upsilon_{pk}^{(s)} - sin\left(\frac{\pi\alpha_s\left(p+\beta_s\right)}{N}\right)\Upsilon_{pk}^{'(s)}\right]H_p^{(s)}}_{MUI/MAI\ arising\ from\ subscriber\ s\ to\ r} + W_k^{(r)} \end{aligned} \tag{5.18}$$

From (5.18), the functions as denoted by $\Upsilon_{kk}^{(r)}$, $\Upsilon_{kk}^{'(r)}$, $\Upsilon_{pk}^{(r)}$, $\Upsilon_{pk}^{'(r)}$, $\Upsilon_{pk}^{(s)}$ and $\Upsilon_{pk}^{'(s)}$ are derived to attain the list of equations from (A.2) to (A.7). Further, the aforesaid list of equations from (A.2) to (A.7) are derived to yield the values of coefficients as follows:

$$\Upsilon_{kk}^{(r)} = \frac{sin\pi\left(2k+\beta_r\right)}{2Nsin\pi\left(\frac{2k+\beta_r}{2N}\right)} + \frac{sin\pi\beta_r}{2Nsin\pi\left(\frac{\beta_r}{2N}\right)} \tag{5.19}$$

$$\Upsilon_{kk}^{'(r)} = \frac{sin^2\pi\left(\frac{2k+\beta_r}{2}\right)}{2Nsin\pi\left(\frac{2k+\beta_r}{2N}\right)} + \frac{sin^2\pi\left(\frac{\beta_r}{2}\right)}{Nsin\pi\left(\frac{\beta_r}{2N}\right)} \tag{5.20}$$

$$\Upsilon_{pk}^{(r)} = \frac{sin\pi\left(p+\beta_r+k\right)}{2Nsin\pi\left(\frac{p+\beta_r+k}{2N}\right)} + \frac{sin\pi\left(p+\beta_r-k\right)}{2Nsin\pi\left(\frac{p+\beta_r-k}{2N}\right)} \tag{5.21}$$

$$\Upsilon_{pk}^{'(r)} = \frac{sin^2\pi\left(\frac{p+\beta_r+k}{2}\right)}{2Nsin\pi\left(\frac{p+\beta_r+k}{2N}\right)} + \frac{sin^2\pi\left(\frac{p+\beta_r-k}{2}\right)}{Nsin\pi\left(\frac{p+\beta_r-k}{2N}\right)} \tag{5.22}$$

$$\Upsilon_{pk}^{(s)} = \frac{sin\pi\left(p+\beta_s+k\right)}{2Nsin\pi\left(\frac{p+\beta_s+k}{2N}\right)} + \frac{sin\pi\left(p+\beta_s-k\right)}{2Nsin\pi\left(\frac{p+\beta_s-k}{2N}\right)} \tag{5.23}$$

$$\Upsilon_{pk}^{'(s)} = \frac{sin^2\pi\left(\frac{p+\beta_s+k}{2}\right)}{2Nsin\pi\left(\frac{p+\beta_s+k}{2N}\right)} + \frac{sin^2\pi\left(\frac{p+\beta_s-k}{2}\right)}{Nsin\pi\left(\frac{p+\beta_s-k}{2N}\right)} \tag{5.24}$$

The first term under the brace in (5.18), elucidates the signal of the corresponding subscriber r, while the second term specifies the amount of ICI generated among the subcarrier components k and p which are allocated to subscriber r. Whereas, the third term under the brace signifies MUI/MAI emanated from subscriber s to the dedicated subscriber r.

- **Scenario 2:** This is also the scenario which is depicting negative STO. Here, the STO α_u lies in the interval $N_{cp} - L + 1 < \alpha \leq N_{cp}$. This phenomena illustrates that only some of the paths experience interference from previous paths due to overlap with the previous frame. Thereupon, this clearly emphasizes the deterioration in the strength of the received signal, because the previous frame overlaps with the present frame thereby leading to loss of orthogonality which further leads to ICI and MUI/MAI exists. This scenario is clearly depicted in Fig. 5.2b, where some of the samples of the current frame are lost in the processing window due to overlap with the previous frame.

  The frequency domain signal at the output of N-Point DCT of the dedicated subscriber r on the kth subcarrier can be derived as follows:

$$
\begin{aligned}
&Y_k^{(u)} = \\
&\sqrt{\frac{2}{N}} C_k \sum_{n=0}^{-\alpha_u - N_{cp} + l - 1} \Bigg[\sqrt{\frac{2}{N}} \sum_{\substack{k=0 \\ k \in Z_u}}^{N-1} X_k^{(u)} C_k cos \left(\frac{\pi \left(k + \beta_u\right) \left(2 \left(n + \alpha_u + N_{cp}\right) + 1\right)}{2N} \right) \\
&\quad \times cos \left(\frac{\pi \left(2n+1\right) k}{2N} \right) \Bigg] \left[\sqrt{\frac{2}{N}} C_k \sum_{l=N_{cp}+\alpha_u-1}^{L-1} h_l^{(u)} cos \left(\frac{\pi \left(2l+1\right) k}{2N} \right) \right] + \\
&\sqrt{\frac{2}{N}} C_k \sum_{n=-\alpha_u - N_{cp} + l}^{N-1} \Bigg[\sqrt{\frac{2}{N}} \sum_{\substack{k=0 \\ k \in Z_u}}^{N-1} X_k^{(u)} C_k cos \left(\frac{\pi \left(k + \beta_u\right) \left(2 \left(n + \alpha_u\right) + 1\right)}{2N} \right) \\
&\quad \times cos \left(\frac{\pi \left(2n+1\right) k}{2N} \right) \Bigg] \left[\sqrt{\frac{2}{N}} C_k \sum_{l=0}^{L-1} h_l^{(u)} cos \left(\frac{\pi \left(2l+1\right) k}{2N} \right) \right] + W_k^{(u)} \qquad (5.25)
\end{aligned}
$$

  (5.25), specifies the general scenario, and now the DCT output of the desired user

r can be deduced as

$$\begin{aligned}
Y_k^{(r)} = {} & \underbrace{C_k^2 X_k^{(r)} \left[cos\left(\frac{\pi\left(k+\beta_r\right)\alpha_r}{N}\right)\Psi_{kk}^{(r)} - sin\left(\frac{\pi\left(k+\beta_r\right)\alpha_r}{N}\right)\Psi_{kk}^{\prime(r)}\right] H_k^{(r)}}_{Desired\ Signal\ corresponding\ to\ rth\ user} + \\
& \underbrace{C_k \sum_{\substack{p=0 \\ \boldsymbol{p\in Z_r} \\ \boldsymbol{p\neq k}}}^{N-1} C_p X_p^{(r)} \left[cos\left(\frac{\pi\left(p+\beta_r\right)\alpha_r}{N}\right)\Psi_{pk}^{(r)} - sin\left(\frac{\pi\left(p+\beta_r\right)\alpha_r}{N}\right)\Psi_{pk}^{\prime(r)}\right] H_p^{(r)} +}_{ICI} \\
& \underbrace{C_k \sum_{\substack{p=0 \\ \boldsymbol{p\in Z_s} \\ \boldsymbol{p\neq k}}}^{N-1} C_p X_p^{(s)} \left[cos\left(\frac{\pi\left(p+\beta_s\right)\alpha_s}{N}\right)\Psi_{pk}^{(s)} - sin\left(\frac{\pi\left(p+\beta_s\right)\alpha_s}{N}\right)\Psi_{pk}^{\prime(s)}\right] H_p^{(s)} +}_{MUI/MAI\ arising\ from\ subscriber\ s\ to\ r} \\
& C_k \sum_{\substack{p=0 \\ \boldsymbol{p\in Z_r} \\ \boldsymbol{p\neq k}}}^{N-1} C_p X_p^{(r)(Previous)} \left[cos\left(\frac{\pi\left(p+\beta_r\right)\left(N_{cp}+\alpha_r\right)}{N}\right)\chi_{pk}^{(r)} - \right. \\
& \underbrace{\left. sin\left(\frac{\pi\left(p+\beta_r\right)\left(N_{cp}+\alpha_r\right)}{N}\right)\chi_{pk}^{\prime(r)}\right] H_p^{\prime(r)} +}_{ICI\ emanating\ from\ previous\ frame\ symbol} \\
& C_k \sum_{\substack{p=0 \\ \boldsymbol{p\in Z_s} \\ \boldsymbol{p\neq k}}}^{N-1} C_p X_p^{(s)(Previous)} \left[cos\left(\frac{\pi\left(p+\beta_s\right)\left(N_{cp}+\alpha_s\right)}{N}\right)\chi_{pk}^{(s)} - \right. \\
& \underbrace{\left. sin\left(\frac{\pi\left(p+\beta_s\right)\left(N_{cp}+\alpha_s\right)}{N}\right)\chi_{pk}^{\prime(s)}\right] H_p^{\prime(s)}}_{MUI\ arising\ from\ subscriber\ s\ to\ r\ from\ previous\ symbol} + W_k^{(r)}
\end{aligned} \tag{5.26}$$

The mathematical expression as emphasized by (5.26) is obtained by making use of (A.10). The term $X_p^{(s)(Previous)}$ in (5.26), enumerates the sth subscriber's data symbol on the pth subcarrier of the previous frame. Further, from (5.26) it is evident that, the received signal of the desired user r is severely degraded due to the prevalence of ICI among the subcarrier components which are allocated to it and this is can be categorized as self-interference between subcarriers k and p. From (5.26), the frequency response of the channel when the signal is prone to interference with the previous symbol is given as

$$H_k^{(r)} = \left[\sum_{l=0}^{L-1} h_l^{(r)} cos\left(\frac{\pi\left(2l+1\right)k}{2N}\right)\right] \tag{5.27}$$

$$H_p^{(r)} = \left[\sum_{l=0}^{L-1} h_l^{(r)} cos\left(\frac{\pi\left(2l+1\right)p}{2N}\right)\right] \tag{5.28}$$

$$H_p^{(s)} = \left[\sum_{l=0}^{L-1} h_l^{(s)} cos\left(\frac{\pi\left(2l+1\right)p}{2N}\right)\right] \tag{5.29}$$

$$H_p^{'(r)} = \left[\sum_{l=N_{cp}+\alpha_r+1}^{L-1} h_l^{(r)} cos\left(\frac{\pi\left(2l+1\right)p}{2N}\right)\right] \tag{5.30}$$

$$H_p^{'(s)} = \left[\sum_{l=N_{cp}+\alpha_s+1}^{L-1} h_l^{(s)} cos\left(\frac{\pi\left(2l+1\right)p}{2N}\right)\right] \tag{5.31}$$

The function χ and Ψ in (5.26) can be derived as

$$\Psi_{kk}^{(r)} = \frac{1}{N}\sum_{n=-\alpha_r+N_{cp}+l}^{N-1}\left[cos\left(\frac{\pi\left(2k+\beta_r\right)\left(2n+1\right)}{2N}\right)+cos\left(\frac{\pi\beta_r\left(2n+1\right)}{2N}\right)\right] \tag{5.32}$$

$$\Psi_{kk}^{'(r)} = \frac{1}{N}\sum_{n=-\alpha_r+N_{cp}+l}^{N-1}\left[sin\left(\frac{\pi\left(2k+\beta_r\right)\left(2n+1\right)}{2N}\right)+sin\left(\frac{\pi\beta_r\left(2n+1\right)}{2N}\right)\right] \tag{5.33}$$

$$\Psi_{pk}^{(r)} = \frac{1}{N}\sum_{n=-\alpha_r+N_{cp}+l}^{N-1}\left[cos\left(\frac{\pi\left(p+\beta_r+k\right)\left(2n+1\right)}{2N}\right)+ cos\left(\frac{\pi\left(p+\beta_r-k\right)\left(2n+1\right)}{2N}\right)\right] \tag{5.34}$$

$$\Psi_{pk}^{'(r)} = \frac{1}{N}\sum_{n=-\alpha_r+N_{cp}+l}^{N-1}\left[sin\left(\frac{\pi\left(p+\beta_r+k\right)\left(2n+1\right)}{2N}\right)+ sin\left(\frac{\pi\left(p+\beta_r-k\right)\left(2n+1\right)}{2N}\right)\right] \tag{5.35}$$

$$\Psi_{pk}^{(s)} = \frac{1}{N}\sum_{n=-\alpha_s+N_{cp}+l}^{N-1}\left[cos\left(\frac{\pi\left(p+\beta_s+k\right)\left(2n+1\right)}{2N}\right)+ cos\left(\frac{\pi\left(p+\beta_s-k\right)\left(2n+1\right)}{2N}\right)\right] \tag{5.36}$$

$$\Psi_{pk}^{'(s)} = \frac{1}{N}\sum_{n=-\alpha_s+N_{cp}+l}^{N-1}\left[sin\left(\frac{\pi\left(p+\beta_s+k\right)\left(2n+1\right)}{2N}\right)+ sin\left(\frac{\pi\left(p+\beta_s-k\right)\left(2n+1\right)}{2N}\right)\right] \tag{5.37}$$

$$\begin{aligned}\chi_{pk}^{(r)(Previous)} = \frac{1}{N}\sum_{n=0}^{-\alpha_r+N_{cp}+l-1}\Bigg[cos\left(\frac{\pi\left(p+\beta_r+k\right)\left(2n+1\right)}{2N}\right)+\\ cos\left(\frac{\pi\left(p+\beta_r-k\right)\left(2n+1\right)}{2N}\right)\Bigg]\end{aligned} \tag{5.38}$$

$$\begin{aligned}\chi_{pk}^{'(r)(Previous)} = \frac{1}{N}\sum_{n=0}^{-\alpha_r+N_{cp}+l-1}\Bigg[sin\left(\frac{\pi\left(p+\beta_r+k\right)\left(2n+1\right)}{2N}\right)+\\ sin\left(\frac{\pi\left(p+\beta_r-k\right)\left(2n+1\right)}{2N}\right)\Bigg]\end{aligned} \tag{5.39}$$

$$\begin{aligned}\chi_{pk}^{(s)(Previous)} = \frac{1}{N}\sum_{n=0}^{-\alpha_s+N_{cp}+l-1}\Bigg[cos\left(\frac{\pi\left(p+\beta_s+k\right)\left(2n+1\right)}{2N}\right)+\\ cos\left(\frac{\pi\left(p+\beta_s-k\right)\left(2n+1\right)}{2N}\right)\Bigg]\end{aligned} \tag{5.40}$$

$$\begin{aligned}\chi_{pk}^{'(s)(Previous)} = \frac{1}{N}\sum_{n=0}^{-\alpha_s+N_{cp}+l-1}\Bigg[sin\left(\frac{\pi\left(p+\beta_s+k\right)\left(2n+1\right)}{2N}\right)+\\ sin\left(\frac{\pi\left(p+\beta_s-k\right)\left(2n+1\right)}{2N}\right)\Bigg]\end{aligned} \tag{5.41}$$

- **Scenario 3:** Similar to Scenario 2, this case also depicts the condition where the current symbol of the existing frame is overlapped with the next frame's symbol indicating that the present frame experiences interference from all the paths belonging to the next frame and this is detailed in Fig. 5.2c. Unlike, Scenario 1 and 2, the timing error α is positive in this case and lies in the interval $0 < \alpha < L$. Therefore, the DCT output in general (pertaining to any subscriber) can be represented as

$$\begin{aligned}Y_k^{(u)} = \sqrt{\frac{2}{N}}C_k\sum_{n=0}^{N-\alpha_u+l-1}\Bigg[\sqrt{\frac{2}{N}}\sum_{\substack{k=0\\k\in Z_u}}^{N-1}X_k^{(u)}C_k cos\left(\frac{\pi\left(k+\beta_u\right)\left(2\left(n+\alpha_u\right)+1\right)}{2N}\right)\\ \times\, cos\left(\frac{\pi\left(2n+1\right)k}{2N}\right)\Bigg]\left[\sqrt{\frac{2}{N}}C_k\sum_{l=0}^{L-1}h_l^{(u)}cos\left(\frac{\pi\left(2l+1\right)k}{2N}\right)\right]+\\ \sqrt{\frac{2}{N}}C_k\sum_{n=N-\alpha_u+l}^{N-1}\sqrt{\frac{2}{N}}\sum_{\substack{k=0\\k\in Z_u}}^{N-1}X_k^{(u)}C_k\\ \times\, cos\left(\frac{\pi\left(k+\beta_u\right)\left(2\left(n+N_{cp}-\alpha_u\right)+1\right)}{2N}\right)cos\left(\frac{\pi\left(2n+1\right)k}{2N}\right)\\ \left[\sqrt{\frac{2}{N}}C_k\sum_{l=0}^{L-1}h_l^{(u)}cos\left(\frac{\pi\left(2l+1\right)k}{2N}\right)\right]\end{aligned} \tag{5.42}$$

Thus, the DCT output of the dedicated user r on the kth subcarrier can be evaluated by making use of (A.11) where, it is further rearranged by segregating the desired signal as well as the interference components pertaining to the subscriber r. Finally, the expression for the DCT output for the desired subscriber r can be derived to yield:

$$
\begin{aligned}
Y_k^{(r)} = {} & \underbrace{C_k^2 X_k^{(r)}\left[cos\left(\frac{\pi\alpha_r\left(k+\beta_r\right)}{N}\right)\wp_{kk}^{(r)} - sin\left(\frac{\pi\alpha_r\left(k+\beta_r\right)}{N}\right)\wp_{kk}^{'(r)}\right]H_k^{(r)}}_{Desired\ user's\ Signal} + \\
& \underbrace{C_k \sum_{\substack{p=0\\ \boldsymbol{p\in Z_r}\\ \boldsymbol{p\neq k}}}^{N-1} C_p X_p^{(r)}\left[cos\left(\frac{\pi\alpha_r\left(p+\beta_r\right)}{N}\right)\wp_{pk}^{(r)} - sin\left(\frac{\pi\alpha_r\left(p+\beta_r\right)}{N}\right)\wp_{pk}^{'(r)}\right]H_p^{(r)}}_{ICI} + \\
& \underbrace{C_k \sum_{\substack{p=0\\ \boldsymbol{p\in Z_s}\\ \boldsymbol{p\neq k}}}^{N-1} C_p X_p^{(s)}\left[cos\left(\frac{\pi\alpha_s\left(p+\beta_s\right)}{N}\right)\wp_{pk}^{(s)} - sin\left(\frac{\pi\alpha_s\left(p+\beta_s\right)}{N}\right)\wp_{pk}^{'(s)}\right]H_p^{(s)}}_{MUI/MAI\ arising\ from\ subscriber\ s\ to\ r} + \\
& \underbrace{C_k \sum_{\substack{p=0\\ \boldsymbol{p\in Z_r}\\ \boldsymbol{p\neq k}}}^{N-1} C_p X_p^{(r)(Next)}\left[cos\left(\frac{\pi\left(N_{cp}-\alpha_r\right)\left(p+\beta_r\right)}{N}\right)\gamma_{pk}^{(r)} - sin\left(\frac{\pi\left(N_{cp}-\alpha_r\right)\left(p+\beta_r\right)}{N}\right)\gamma_{pk}^{'(r)}\right]H_p^{(r)}}_{ICI\ due\ to\ Next\ Frame} + \\
& \underbrace{C_k \sum_{\substack{p=0\\ \boldsymbol{p\in Z_s}\\ \boldsymbol{p\neq k}}}^{N-1} C_p X_p^{(s)(Next)}\left[cos\left(\frac{\pi\left(N_{cp}-\alpha_s\right)\left(p+\beta_s\right)}{N}\right)\gamma_{pk}^{(s)} - sin\left(\frac{\pi\left(N_{cp}-\alpha_s\right)\left(p+\beta_s\right)}{N}\right)\gamma_{pk}^{'(s)}\right]H_p^{(s)}}_{MUI/MAI\ arising\ from\ subscriber\ s\ to\ r\ due\ to\ Next\ Frame} + W_k^{(r)}
\end{aligned}
\tag{5.43}
$$

The interference components in (5.43) can be further solved to attain

$$
\wp_{kk}^{(r)} = \frac{1}{N}\sum_{n=0}^{N-\alpha_r+l-1}\left[cos\left(\frac{\pi\left(2k+\beta_r\right)\left(2n+1\right)}{2N}\right) + cos\left(\frac{\pi\beta_r\left(2n+1\right)}{2N}\right)\right] \tag{5.44}
$$

$$
\wp_{kk}^{'(r)} = \frac{1}{N}\sum_{n=0}^{N-\alpha_r+l-1}\left[sin\left(\frac{\pi\left(2k+\beta_r\right)\left(2n+1\right)}{2N}\right) + sin\left(\frac{\pi\beta_r\left(2n+1\right)}{2N}\right)\right] \tag{5.45}
$$

$$\wp_{pk}^{(r)} = \frac{1}{N} \sum_{n=0}^{N-\alpha_r+l-1} \left[cos \left(\frac{\pi \left(p + \beta_r + k\right)\left(2n+1\right)}{2N} \right) + cos \left(\frac{\pi \left(p + \beta_r - k\right)\left(2n+1\right)}{2N} \right) \right] \tag{5.46}$$

$$\wp_{pk}^{'(r)} = \frac{1}{N} \sum_{n=0}^{N-\alpha_r+l-1} \left[sin \left(\frac{\pi \left(p + \beta_r - k\right)\left(2n+1\right)}{2N} \right) + sin \left(\frac{\pi \left(p + \beta_r - k\right)\left(2n+1\right)}{2N} \right) \right] \tag{5.47}$$

$$\wp_{pk}^{(s)} = \frac{1}{N} \sum_{n=0}^{N-\alpha_s+l-1} \left[cos \left(\frac{\pi \left(p + \beta_s + k\right)\left(2n+1\right)}{2N} \right) + cos \left(\frac{\pi \left(p + \beta_s - k\right)\left(2n+1\right)}{2N} \right) \right] \tag{5.48}$$

$$\wp_{pk}^{'(s)} = \frac{1}{N} \sum_{n=0}^{N-\alpha_s+l-1} \left[sin \left(\frac{\pi \left(p + \beta_s + k\right)\left(2n+1\right)}{2N} \right) + sin \left(\frac{\pi \left(p + \beta_s - k\right)\left(2n+1\right)}{2N} \right) \right] \tag{5.49}$$

$$\gamma_{pk}^{(r)} = \frac{1}{N} \sum_{n=N-\alpha_r+l}^{N-1} \left[cos \left(\frac{\pi \left(p + \beta_r + k\right)\left(2n+1\right)}{2N} \right) + cos \left(\frac{\pi \left(p + \beta_r - k\right)\left(2n+1\right)}{2N} \right) \right] \tag{5.50}$$

$$\gamma_{pk}^{'(r)} = \frac{1}{N} \sum_{n=N-\alpha_r+l}^{N-1} \left[sin \left(\frac{\pi \left(p + \beta_r + k\right)\left(2n+1\right)}{2N} \right) + sin \left(\frac{\pi \left(p + \beta_r - k\right)\left(2n+1\right)}{2N} \right) \right] \tag{5.51}$$

$$\gamma_{pk}^{(s)} = \frac{1}{N} \sum_{n=N-\alpha_r+l}^{N-1} \left[cos \left(\frac{\pi \left(p + \beta_s + k\right)\left(2n+1\right)}{2N} \right) + cos \left(\frac{\pi \left(p + \beta_s - k\right)\left(2n+1\right)}{2N} \right) \right] \tag{5.52}$$

$$\gamma_{pk}^{'(s)} = \frac{1}{N} \sum_{n=N-\alpha_r+l}^{N-1} \left[sin \left(\frac{\pi \left(p + \beta_s + k\right)\left(2n+1\right)}{2N} \right) + sin \left(\frac{\pi \left(p + \beta_s - k\right)\left(2n+1\right)}{2N} \right) \right] \tag{5.53}$$

Therefore, the aforementioned mathematical analysis on the frequency-domain received signal emphasizes the need to compensate these offsets by incorporating suitable synchronization algorithms which are compatible with IM/DD systems for VLC. The simulation results are detailed in the next section.

5.1.4 Algorithms for the estimation of FO in DCO-FOFDMA system

Classen

This algorithm utilizes the pilot tones for the estimation of FO because, in the recent times, VLC can be even utilized in the outdoor environment to provide Internet hot spots using street lighting and mobile access. In such kind of dynamic environment, the communication link may experience shadowing or temporary blocking thereby degrading the quality of service [197]. In general, pilot tones are inserted along with the data based on a specific pilot arrangement called comb type pilot arrangement as shown in Fig. 5.3. Therefore, the transmitted signal comprises of both data as well as pilot tones. In general,

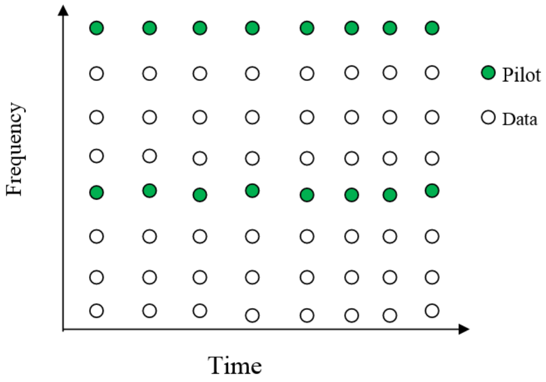

Figure 5.3: Comb type pilot arrangement

this algorithm as proposed by Classen comprises of two modes for the estimation of FO: acquisition and tracking, where the former deals with large range of FO while the latter involves only small frequency fluctuations. Let the time-domain signal corresponding to the desired subscriber be denoted as $y_n^{(r)}$ and the mathematical expression is given in (5.6) and let f denote the pilot insertion interval, therefore the pilot added time domain signal be represented as $y_{n+f}^{(r)}$. According to the principality of this algorithm, these two signals are saved in the memory and then they are transformed into frequency domain by computing the DCT operation. In general, the pilot tones are extracted and then the offset is estimated. This estimated offset is used for compensation in the time domain. Accordingly, the estimated FO of the desired subscriber r can be expressed as

$$\hat{\beta} = \frac{1}{2\pi T_{sub}} \underset{\beta}{max} \left\{ \left| \sum_{d=0}^{N_p-1} Y_{k+f}^{(r)} \left[q \left[d \right], \beta \right] Y_k^{*(r)} \left[q \left[d \right], \beta \right] X_{k+f}^{(r)} \left[q \left[d \right], \beta \right] X_k^{*(r)} \left[q \left[d \right], \beta \right] \right| \right\} \quad (5.54)$$

From (5.54), N_p denotes the total number of pilot tones, $q\left[d\right]$ specifies the location of the dth pilot tone and $X_k^{(r)}\left[q\left[d\right]\right]$ signifies the pilot tone in the frequency domain which corresponds to the kth symbol period of the desired user r.

5.1.5 CRLB for the estimation of offsets in DCO-FOFDMA system

CRLB for the estimation of FO

The aforementioned mathematical analysis as dealt in previous subsections clearly depicts the fact that the presence of FO leads to the emergence of ICI and MUI/MAI. Hence, it is necessary to estimate the FO. This section derives CRLB for the estimation of FO over AWGN channel. Therefore, the received signal pertaining to the rth subscriber can be put up as

$$y_n^{(r)} = IDCT\left[Y_k^{(r)}\right] \tag{5.55}$$

Where $Y_k^{(r)} = X_k^{(r)} + W_k^{(r)}$ and upon substitution in (5.55), the following expression is obtained

$$y_n^{(r)} = x_n^{(r)} + w_n^{(r)} \tag{5.56}$$

Furthermore, the received signal which is affected with FO of β_r can be expressed as

$$y_n^{(r)} = \sqrt{\frac{2}{N}} \sum_{\substack{k=0 \\ k\in Z_r}}^{N-1} C_k X_k^{(r)} cos\left(\frac{\pi\left(2n+1\right)\left(k+\beta_r\right)}{2N}\right) + w_n^{(r)} \tag{5.57}$$

The parameter β_r to be estimated is hidden in the argument of cosine term. This necessitates to assume $\frac{\pi(2n+1)(k+\beta r)}{2N}$ as μ.

$$y_n^{(r)} = \sqrt{\frac{2}{N}} \sum_{\substack{k=0 \\ k\in Z_r}}^{N-1} C_k X_k^{(r)} cos\mu + w_n^{(r)} \tag{5.58}$$

Therefore, the Fisher Information matrix pertaining to the estimation of any parameter Θ is given as

$$\left[I\left(\Theta\right)\right]_{ij} = \frac{1}{\sigma^2} \sum_{n=0}^{N-1} \frac{\partial}{\partial\Theta_i} S\left[n,\Theta\right] \frac{\partial}{\partial\Theta_j} S\left[n,\Theta\right] \tag{5.59}$$

Furthermore, (5.59) can be derived as shown in Appendix B to attain the expression as illustrated in (5.60).

$$\left[I\left(\Theta\right)_{11}\right] = \left[I\left(\beta_r\right)_{11}\right] = \frac{\pi^4}{8\sigma^2 N^4}\left\{\frac{\left(N+1\right)\left(48N^3+192N^2+248N+112\right)}{15}+1\right\} \times \left[\sum_{\substack{k=0 \\ k\in Z_r}}^{N-1} C_k X_k^{(r)}\left(k+\beta_r\right)\right]^2 \tag{5.60}$$

Therefore, the variance of the estimate β which is denoted as $V\left(\hat{\beta}\right)$ can be expressed as

$$V\left[\hat{\beta}\right] \geq \left[I\left(\beta\right)\right]_{11}^{-1} \tag{5.61}$$

Finally,

$$V\left[\hat{\beta}\right] \geq \frac{8\sigma^2 N^4}{\pi^4 \left\{\frac{(N+1)(48N^3+192N^2+248N+112)}{15} + 1\right\} \left[\sum_{\substack{k=0 \\ k\in Z_r}}^{N-1} C_k X_k^{(r)}\left(k+\beta_r\right)\right]^2} \tag{5.62}$$

CRLB for the estimation of STO

In the similar manner, when the received signal pertaining to the desired subscriber r is effected with a timing offset i.e., STO of α_r, then the expression can be formulated as

$$y_n^{(r)} = \sqrt{\frac{2}{N}} \sum_{\substack{k=0 \\ k\in Z_r}}^{N-1} C_k X_k^{(r)} cos\left(\frac{\pi\left(2\left(n+\alpha_r\right)+1\right)k}{2N}\right) + w_n^{(r)} \tag{5.63}$$

It is to be noted that the parameter α_r which is to be estimated is hidden in the argument of cosine term. Therefore, the argument term i.e., $\frac{\pi(2(n+\alpha_r)+1)k}{2N}$ can be assumed as μ. Therefore, (5.63) can be reduced as

$$y_n^{(r)} = \sqrt{\frac{2}{N}} \sum_{\substack{k=0 \\ k\in Z_r}}^{N-1} C_k X_k^{(r)} cos\mu + w_n^{(r)} \tag{5.64}$$

It is to be noted that μ is a function of α_r and making use of (5.59), the Fisher Information Matrix can be expressed as

$$\left[I\left(\alpha\right)\right]_{ij} = \frac{1}{\sigma^2} \sum_{n=0}^{N-1} \frac{\partial}{\partial \alpha_i} S\left[n, \alpha_i\right] \frac{\partial}{\partial \alpha_j} S\left[n, \alpha_j\right] \tag{5.65}$$

Finally, the Fisher Information Matrix can be derived as shown in Appendix C to yield the following expression

$$\left[I\left(\alpha\right)\right]_{11} = \frac{\pi^4}{6\sigma^2 N^4}\left[4\left(N+1\right)\left(N+3\alpha_r+2\right)+3\left(2\alpha_r+1\right)^2\right]\left[\sum_{\substack{k=0 \\ k\in Z_r}}^{N-1} k^2 C_k X_k^{(r)}\right]^2 \tag{5.66}$$

Therefore, the variance of the estimate α which is denoted as $V\left(\hat{\alpha}\right)$ can be expressed as

$$V\left[\hat{\alpha}\right] \geq \left[I\left(\alpha\right)\right]_{11}^{-1} \tag{5.67}$$

Finally,

$$V\left[\hat{\alpha}\right] \geq \frac{6\sigma^2 N^4}{\pi^4\left\{4\left(N+1\right)\left(N+3\alpha_r+2\right)+3\left(2\alpha_r+1\right)^2\right\}\left[\sum_{\substack{k=0\\k\in Z_r}}^{N-1} k^2 C_k X_k^{(r)}\right]^2} \tag{5.68}$$

5.2 Results and Discussion

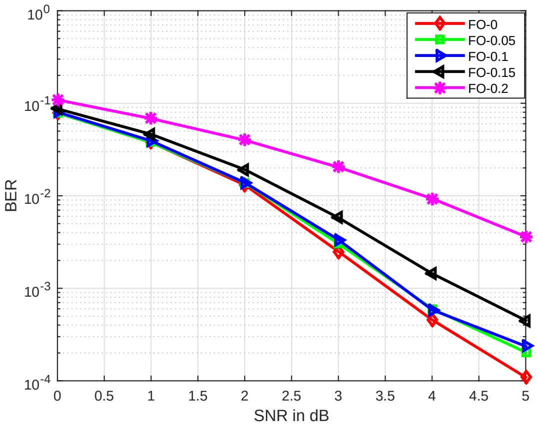

Figure 5.4: Performance Analysis of BER vs SNR in DCO-FOFDMA system employing BPSK modulation with the existence of FO for single user scenario

This section presents the simulated results for DCO-FOFDMA system employing 256 subcarriers. The length of cyclic prefix is taken as $\frac{1}{4}$th the subcarriers size. Following the literature, the amount of DC bias which is added to assure the positivity of signal is 7 dB. Since, DCT is employed, the system model emphasizes the dependency on real modulation schemes like M-PAM and BPSK, the same has been illustrated in the results. The simulation parameters employed are shown in Table. 5.1.

The performance analysis of DCO-FOFDMA using BPSK modulation is interpreted in Fig. 5.4. To emphasize the sensitivity of FO on the system performance, different range of FO values from $0.05, 0.1, 0.15, 0.2, 0.25, 3$ are taken into consideration. The simulated result as shown in Fig. 5.4, evidences that the increase in the range of FO worsens the system performance. At SNR of 4 dB, the attained error floor is 4.57×10^{-4} for BPSK modulation in DCO-FOFDMA system without the presence of FO. While, for FO values of $0.05, 0.01, 0.15$ and 0.2, the obtained probability of error floor is 5.82×10^{-4}, 0.0014 and 0.009348 respectively.

Table 5.1: Parameters employed for Simulation

Parameter	Value
Size of IDCT/DCT	256
Total Number of Pilot Carriers	32
Cyclic Prefix Length	64
Orders of Modulation	BPSK, 4, 16-PAM
Range of FO	$[0, 0.05, 0.10, 0.15, 0.20]$
Type of optical OFDM methodology employed	DCO-OFDM
No of OFDM symbols	100
FO estimation algorithms	Classen
Range of STO	[-5, -3, -2 2 3]
STO estimation algorithms	Maximum Correlation, Minimum Difference

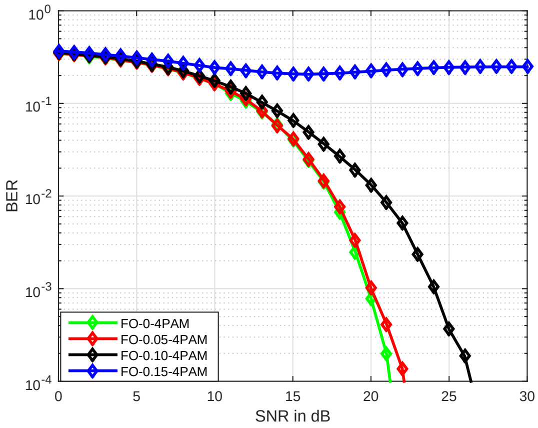

Figure 5.5: Illustration of BER vs SNR in DCO-FOFDMA system employing 4-PAM modulation in the presence of FO for single user scenario

For higher order of modulation like M-PAM, the performance of the system is more sensitive to FO and the same can be interpreted from Fig. 5.5. A similar inference can be drawn pertaining to the performance of the system as that of the aforementioned case. Here, it is evident that, for higher values of FO like 0.15, it is impossible to achieve a reduced error floor. Consequently, this hinders the detection capability in case of multi user scenario, thereby making MUI inevitable. Fig. 5.6, delineates the variation of BER

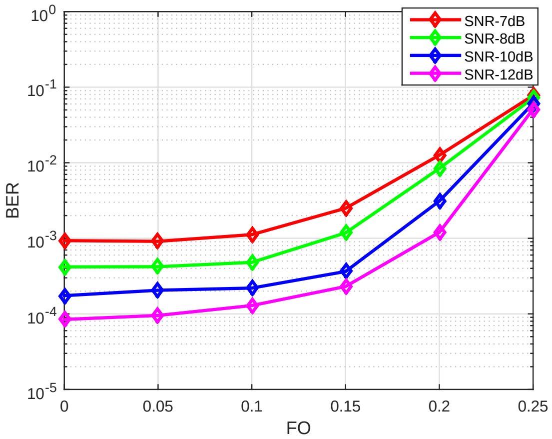

Figure 5.6: BER vs FO in DCO-FOFDMA system employing BPSK modulation

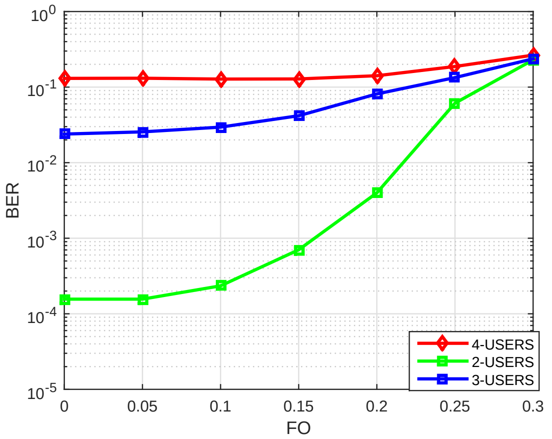

Figure 5.7: BER vs FO in DCO-FOFDMA system illustrating multi-user scenario

with respective to FO for different values of SNR. From the figure, it can be inferred that, the performance of the system deteriorates as the range of FO values increase from $0, 0.05, 0.1, 0.15, 0.2$. The same inference can be drawn with multi user scenario which is elucidated in Fig. 5.7, indicating the presence of different values of FO degrades the performance of system thereby hindering the detection capability of multiple users. This can be evidenced in Fig. 5.7, because with the increase in number of subscribers, the BER performance deteriorates for higher values of FO. It can be interpreted that when there is no FO i.e., for FO=0, the achievable BER is 7.813×10^{-5}, while, upon increasing the range of FO from $0.05, 0.1, 0.15, 0.2, 0.25, 0.3$ the obtained probability of error is $3.906 \times 10^{-4}, 5.469 \times 10^{-4}, 7.813 \times 10^{-4}, 3.828 \times 10^{-3}, 6.477 \times 10^{-2}$ and 2.291×10^{-1} respectively. The detrimental aspects of FO and STO on the received signal is clearly illustrated through mathematical analysis in the aforementioned sections. Moreover, different pos-

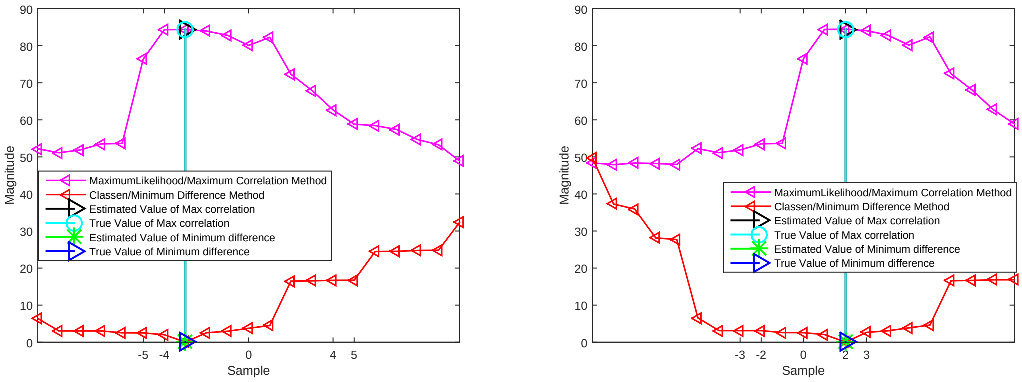

(a) Negative Timing Error (STO) estimation without the existence of FO

(b) Positive Timing Error (STO) estimation without the existence of FO

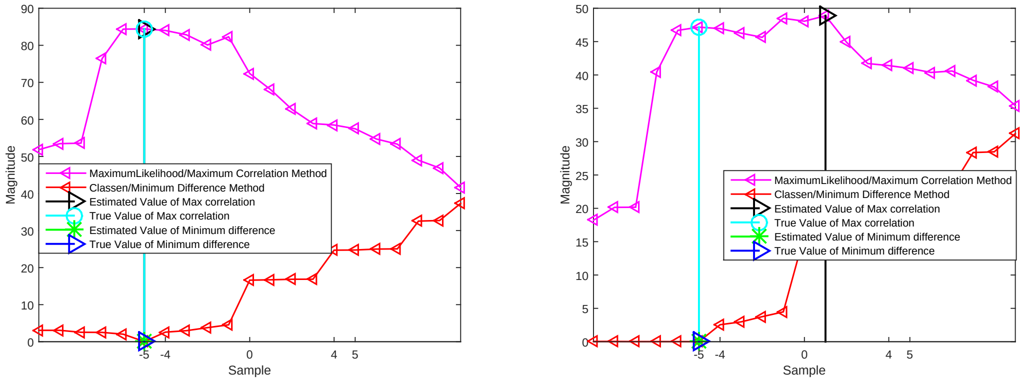

(c) Negative Timing Error (STO) estimation without the existence of FO

(d) Negative Timing Error (STO) estimation with the existence of FO

Figure 5.8: Different Timing Error estimations using Cyclic Prefix (CP) Based methods

sible scenarios of timing mismatch intervals are also illustrated to clearly highlight the impact of negative and positive time error. Therefore, in order to estimate these timing errors, it is vital to employ synchronization algorithms. Consequently, two synchronization algorithms such as Classen which is also known as minimum difference method and Maximum Likelihood estimate or maximum correlation method are exploited and these are imposed to the developed DCO-FOFDMA system model. The details of mathematical analysis pertaining to these STO estimation algorithms are given in previous chapter 4. The simulation results as shown in Fig. 5.8a and 5.8b clearly depicts the scenario of negative and positive timing error. It indicates the scenario where the actual sample value arrives too late and little early at the receiving end. However, these scenarios are considered without the existence of FO. It is interesting to note that, the actual and the estimated samples upon imposing the aforesaid algorithms are in a good agreement. Furthermore, the exact peak and the minimum value coincides with each other.

In order to further elucidate the detrimental aspects of FO on the received signal, Fig. 5.8c and 5.8d illustrates the scenario of estimation of the negative timing error with and without the existence of FO. As evident, the presence of FO hinders the estimation capability of the sample values upon using maximum correlation method while, the estimated and actual sample values coincides with each other upon enforcing minimum difference method.

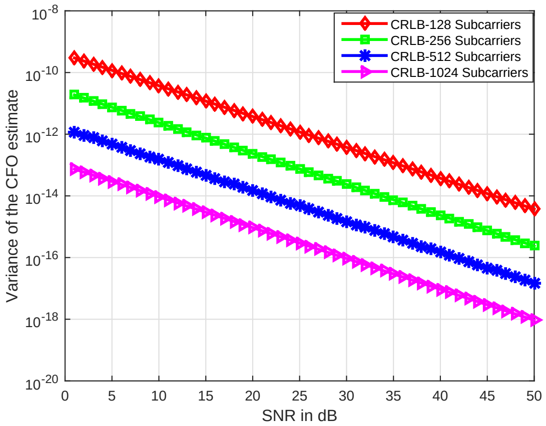

Figure 5.9: CRLB for FO estimation with varying number of subcarriers in DCO-FOFDMA system pertaining to desired subscriber

Fig. 5.9 depicts the bound vs SNR for the estimation of FO of the corresponding subscriber in DCO-FOFDMA system. As depicted in the Fig. 5.9, the error reduces upon

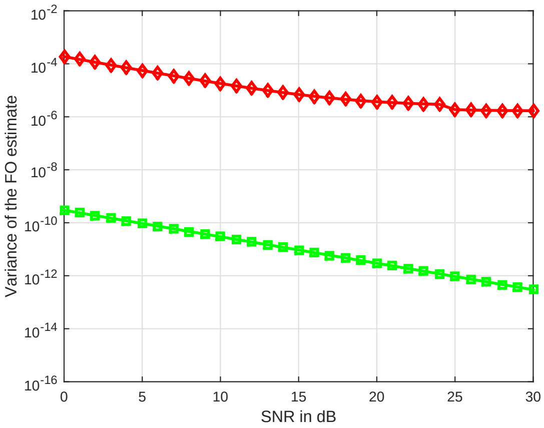

Figure 5.10: Mean Square Error (MSE) for Classen vs CRLB (Red–Classen, Green-CRLB)

increasing the SNR. For $N = 128$ subscribers, at SNR of 50 dB the error achieved was 10^{-14}. Fig. 5.10 depicts the performance comparison of Classen algorithm against CRLB where, the simulated result analysis emphasizes that Classen algorithm attains a better reduction in MSE for higher values of SNR. Even though, there is a significant improvement in the accuracy of the MSE curve of Classen algorithm, it is far from the CRLB and exhibits high error floor when compared with CRLB. The CRLB for the estimation

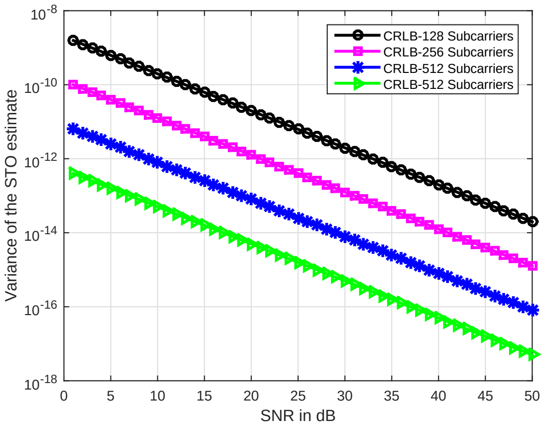

Figure 5.11: CRLB for STO estimation with varying number of subcarriers in DCO-FOFDMA system pertaining to desired subscriber

of STO pertaining to desired subscriber is delineated in the Fig. 5.11. It can be inferred that, higher amount of SNR is desired to attain a reduced variance of error. In particular, at SNR of 15 dB, the achieved error is 6.233×10^{-11} while at SNR of 50 db, the obtained error is 1.971×10^{-14}.

5.3 Conclusion

This chapter highlights the most detrimental aspect like interference which is encountered in mobile wireless communication environment. Unlike RF, handling these issues is not straight forward, due to real and positive nature of the signal transmission. Consequently, this work evaluates the effects of FO and different scenarios of timing induced disparities (i.e., STO) on the received signal in DCO-FOFDMA system. Furthermore, a thorough mathematical analysis is accomplished emphasizing the different forms of interference like ICI which emanates especially due to overlap of different subcarrier components allocated to the corresponding subscriber and MUI/MAI also occur in the presence of multiple users. The simulation results infer that the system performance is seriously deteriorated due to the presence of these offsets, thereby hindering the detection capability of multiple users in uplink scenario. Furthermore, it becomes difficult to achieve a reduced error floor when the sensitivity of these offsets increases.

In this work we have incorporated the real trigonometric transform like DCT in order to relieve the burden of Hermitian Symmetry criteria which is mandatory in FFT based optical OFDM. In doing so, there is an increase in spectral efficiency when compared with conventional optical OFDM system. Hence, the proposed multiple access system provides a flexibility to impart high data rate communication to the end-users without relying on RF counterparts. The analysis provided in this work emphasizes the necessity to estimate these offsets and then to compensate them by employing suitable synchronization algorithms which are compatible with IM/DD systems for VLC. Consequently, this work revisits the synchronization algorithms like Classen/Minimum difference method and Maximum Likelihood method/Maximum correlation method for the estimation of different scenarios of timing mismatches. Furthermore, the simulation results emphasizes that, the presence of FO hinders the estimation capability of Maximum correlation method to accurately estimate the STO. This work derives the CRLB for the estimation of FO and STO.

Chapter 6

Conclusions and Future Scope

6.1 Conclusions

The tremendous intensification in the demand for data services thrusts the wireless networks to bestow higher capacities and better spectrum efficiency. This issue is more pronounced with the rapid proliferation of a wave of novel wireless communication based applications which includes cloud-based services, online gaming, video streaming, virtual and augmented realities, etc. This continuous increase in the demand for wireless services strains the existing RF spectrum. Inevitably, the visible light portion of the electromagnetic spectrum garnered the attraction of several research communities to evolve it as an intriguing alternative to the existing RF spectrum because of its distinguished features like its vast, low cost and unlicensed spectrum which is free from electromagnetic interference. Among the candidate technologies, VLC emerges to be the most potential candidate to mitigate the immediate demand for spectrum. Consequently, the introduction of this thesis investigates the current state of art research aspects which are pertaining to VLC.

With the motive of improving the signal spectral efficiency for ensuring high speed VLC transmission, advanced multicarrier modulation formats like optical OFDM have been exploited. Accordingly, this work analyses the performance of optical OFDM over dispersive VLC channel environment. Owing to the drawbacks associated with Hermitian Symmetry imposed IFFT in optical OFDM, in a motive to reduce the amount of computational complexity, power consumption and to obtain an enhancement in spectral efficiency, different real transformation techniques like DHT, DCT, DST, HCM-FWHT and WPDM are exploited to accomplish the OFDM modulation and demodulation in the optical domain. Taking into consideration the dispersive nature of the wireless channel environment, it is vital to enforce channel estimation techniques in order to ensure perfect reception of the transmitted data. In our work, we have developed a comb-type pilot arrangement based ACO-OFDM system which is exploiting different transformation techniques like Hermitian Symmetry imposed IFFT and DHT. Furthermore, in order to estimate the channel, different channel estimation techniques like LS, MMSE and interpolation techniques like linear, spline and low-pass are enforced. Additionally, the BER performance of the developed systems are compared with multicarrier systems like HCM-FWHT and WPDM-based optical OFDM.

Secondly, the next approach of this thesis addresses the most vital aspect like PAPR which needs to be investigated in IM/DD systems for VLC. For the purpose of reducing the amount of PAPR in a multicarrier system to the level of a single carrier system, real trigonometric transform based spreading i.e., DCT/DST-Spread is proposed and superimposed to a DCT/DST based DCO/ACO-OFDM systems. Furthermore, the PAPR analysis of the aforesaid systems is compared with other PAPR reduction schemes like PTS and clipping with filtering. The simulated results infers that, upon imposing DCT/DST-based Spreading in DCT/DST based optical OFDM systems, the amount of PAPR is reduced significantly upon comparison with the traditional systems and a gain of around 7 dB is observed. Among the multiple access schemes, DCT/DST-based IFDMA results in less PAPR than that of the other multiple access techniques. Furthermore, the simulation results emphasize that upon comparison with traditional optical OFDM systems, in order to achieve the same amount of performance, Hermitian Symmetry imposed IFFT-based DCO and ACO-OFDM systems require $4, 16, 64, 256$ and 1024 QAM in contrast to $2, 4, 8, 16$ and 32 PAM as required by DHT/DCT/DST-based DCO and ACO-OFDM systems. This confirms the fact that the real trigonometric transform based optical OFDM systems supports double the constellation symbols to achieve the same amount of performance when compared with traditional optical OFDM systems.

Finally, the most indispensable issues like the deterioration of the performance of the system due to the presence of different timing and frequency induced offsets are evaluated through mathematical derivations in a multicarrier system like DCO-OFDM system. Additionally, this work addresses the most detrimental aspect like interference which is encountered in mobile wireless communication environment. Unlike RF, handling these issues is not straight forward, due to real and positive nature of the signal transmission. Consequently, this work evaluates the effects of different scenarios of timing induced disparities (i.e., STO) on the received signal in DCO-OFDMA system. Further, in order to take the advantages of real trigonometric transformation techniques, this work proposes a multiple access system which is based on DCT i.e., (DCO-FOFDMA) and evaluates the performance of the system in the presence of FO and STO. A thorough mathematical analysis is accomplished highlighting the different forms of interference like ICI which emanates especially due to overlap of different subcarrier components allocated to the corresponding subscriber and MUI/MAI also occur in the presence of multiple users. The simulation results infer that the system performance is seriously deteriorated due to the presence of these offsets, thereby hindering the detection capability of multiple users in uplink scenario. Besides, it becomes difficult to achieve a reduced error floor when the sensitivity of these offsets increase. The analytical analysis provided in this work emphasizes the necessity to estimate these offsets and then to compensate them by employing suitable synchronization algorithms which are compatible with IM/DD systems for VLC. Consequently, this work revisits the synchronization algorithms like Classen/Minimum difference method and Maximum Likelihood method/Maximum correlation method for the estimation of different scenarios of timing mismatches. CRLB for the estimators is derived and is verified through simulation results.

6.2 Future Scope

1. **Flickering and Dimming issues:** Flickering induces serious health hazards to humans when it is noticed. This is more pronounced in case of slow data rate communications because the changes become perceptible to the human eye. Therefore, design of sophisticated modulation formats to combat the detrimental aspects of flickering stems out to be a sensitive issue. On the other hand, it is desired to expeditiously dim a light source based on the needs of the application. Therefore, future research should be towards designing robust dimming control algorithms so that desired amount of illumination can be acquired in an appropriate manner. Consequently, it can be claimed that flicker mitigation and dimming support imposes as

two major challenges which needs to be handled in the indoor scenarios.

2. **Deployment of Organic LEDs (OLEDs):** Research is rapidly progressing to enable OLEDs to penetrate the solid state lighting (SSL) market. Several studies in the literature claim that OLEDs cannot be seen as direct replacement to inorganic based LEDs however, they can be termed as feasible substitutes where inorganic based devices fails to find their applicability in offering large area displays, flat panels, etc. Even though OLEDs offer large photoactive areas for illumination, the major drawback associated with them is their limited available bandwidth. Therefore, to render high data rate communication it is vital to stress on several equalization techniques as well as multicarrier modulation formats.

3. **Influence of Ambient Noise on the performance of VLC system:** When VLC is exploited for outdoor applications like vehicular communications, the noise emanating due to the presence of background solar radiation and the interference which is arising due to the other sources of artificial lighting units like street lights which are made of incandescent lamps, fluorescent lamps and fluorescent lamps which are geared by electronic ballasts perturbs the communication. Due to the presence of these perturbing elements, the SNR at the receiving end is drastically reduced in case of automotive applications. Hence, a conclusion can be drawn that outdoor VLC applications is strongly affected by the noise and hence combating its effect for the purpose of facilitating high data rate transfer for long distance communications turns out to be the most potential task. Therefore, it is vital to employ effective optical filters to eradicate the effects of noise prior to reception of the transmitted signal. Furthermore, in case of a VLC receiver, the receiver's FOV plays a major role to allow for the interception of the incident intensity modulated transmitted light signal. Thus, in addition to taking the desired signal, there might be chances for the receiver to accept the noise content also. Hence, if wider receiver FOV is allowed, then, not only desired signal is captured, but also large amount of noise content is also accepted. Therefore, one way to counteract the effects of noise is to narrow the receiver's FOV. Still, there is a need to emphasize several other techniques to mitigate the effects of noise in case of outdoor VLC applications.

4. **Exploiting novel physical waveforms:** Exploring novel $5G$ physical waveforms

like Generalized Frequency Division Multiplexing (GFDM) a non-orthogonal multicarrier technique can be one alternative to OFDM. GFDM exploits the block based structure and circular pulse shaped nature at the expense of computational complexity. The pulse shaping property relaxes the synchronization requirements and out-of band emission. Unlike OFDM, each GFDM block comprises of single cyclic prefix which yields higher spectral efficiency.

5. **Synchronization aspects:** Synchronization is one of the indispensable issue which needs to be addressed when the robust multicarrier modulation scheme like OFDM is employed for VLC. The slight deviations in the transmitter and receiver disrupts the orthogonality of the system and leads to the emanation of deleterious interferences like ICI. Additionally, frame synchronization is one of the crucial aspect which should be addressed. It is because, the improper timing alignments leads to the overlap of the present frame with the previous and next frames. This phenomena hinders the detection capability at the receiving end. Therefore, suggestion of appropriate and sophisticated synchronization algorithms compatible with IM/DD systems for VLC in order to compensate the signal with the estimated FO and STO stems out to be the major concern. Additionally, while analyzing the high speed communication systems, it is vital to take into consideration synchronization jitter. Because, proper clock function is of major prerequisite for the purpose of providing accurate synchronization as well as to achieve the desired BER.

Appendix A

Mathematical Illustration

Scenario 1: By making use of the mathematical expression as stated in (5.17), the frequency domain signal corresponding to the desired user r on the kth subcarrier can be derived as: In this derivation, it is assumed that the total number of subcarriers which are allocated to the desired/dedicated user r belongs to the set $\boldsymbol{Z_r} = \{0, 1, 2, 3, \cdots N-1\}$. (5.17), is derived in a such a manner to highlight the ICI which is originating among the subcarrier components which are allocated to the user r i.e., here it can be depicted as the ICI which is arising among the subcarrier components p and k which are belonging to the set $\boldsymbol{Z_r}$. Furthermore, MUI/MAI which is emerging out due to subscriber s is also delineated. Thus, (5.17) can be solved to attain

$$\begin{aligned}
Y_k^{(r)} = C_k^2 X_k^{(r)} \frac{1}{N} \sum_{n=0}^{N-1} \Bigg[cos \left(\frac{\pi \left(2k+\beta_r\right)\left(2n+1\right)}{2N} + \frac{\pi \alpha_r \left(k+\beta_r\right)}{N} \right) + \\
cos \left(\frac{\pi \beta_r \left(2n+1\right)}{2N} + \frac{\pi \alpha_r \left(k+\beta_r\right)}{N} \right) \Bigg] H_k^{(r)} + \\
C_k \sum_{\substack{p=0 \\ \boldsymbol{p\in Z_r} \\ \boldsymbol{p\neq k}}}^{N-1} C_p X_p^{(r)} \frac{1}{N} \sum_{n=0}^{N-1} \Bigg[cos \left(\frac{\pi \left(p+\beta_r+k\right)\left(2n+1\right)}{2N} + \frac{\pi \alpha_r \left(p+\beta_r\right)}{N} \right) + \\
cos \left(\frac{\pi \left(p+\beta_r-k\right)\left(2n+1\right)}{2N} + \frac{\pi \alpha_r \left(p+\beta_r\right)}{N} \right) \Bigg] H_p^{(r)} + \\
C_k \sum_{\substack{p=0 \\ \boldsymbol{p\in Z_s} \\ \boldsymbol{p\neq k}}}^{N-1} C_p X_p^{(s)} \frac{1}{N} \sum_{n=0}^{N-1} \Bigg[cos \left(\frac{\pi \left(p+\beta_s+k\right)\left(2n+1\right)}{2N} + \frac{\pi \alpha_s \left(p+\beta_s\right)}{N} \right) + \\
cos \left(\frac{\pi \left(p+\beta_s-k\right)\left(2n+1\right)}{2N} + \frac{\pi \alpha_s \left(p+\beta_s\right)}{N} \right) \Bigg] H_p^{(s)} + W_k^{(r)} \qquad \text{(A.1)}
\end{aligned}$$

It is to be noted that from (A.1), $\boldsymbol{Z_s}$ specifies the set of subcarriers which are appropriated to the user s.

From (5.18), the functions which are denoted by $\Upsilon^{(r)}_{kk}$, $\Upsilon'^{(r)}_{kk}$, $\Upsilon^{(r)}_{pk}$, $\Upsilon'^{(r)}_{pk}$, $\Upsilon^{(s)}_{pk}$ and $\Upsilon'^{(s)}_{pk}$ can be solved to attain

$$\Upsilon^{(r)}_{kk} = \frac{1}{N}\sum_{n=0}^{N-1}\left[cos\left(\frac{\pi\left(2k+\beta_r\right)\left(2n+1\right)}{2N}\right)+cos\left(\frac{\pi\beta_r\left(2n+1\right)}{2N}\right)\right] \tag{A.2}$$

$$\Upsilon'^{(r)}_{kk} = \frac{1}{N}\sum_{n=0}^{N-1}\left[sin\left(\frac{\pi\left(2k+\beta_r\right)\left(2n+1\right)}{2N}\right)+sin\left(\frac{\pi\beta_r\left(2n+1\right)}{2N}\right)\right] \tag{A.3}$$

$$\Upsilon^{(r)}_{pk} = \frac{1}{N}\sum_{n=0}^{N-1}\left[cos\left(\frac{\pi\left(p+\beta_r+k\right)\left(2n+1\right)}{2N}\right)+cos\left(\frac{\pi\left(p+\beta_r-k\right)\left(2n+1\right)}{2N}\right)\right] \tag{A.4}$$

$$\Upsilon'^{(r)}_{pk} = \frac{1}{N}\sum_{n=0}^{N-1}\left[sin\left(\frac{\pi\left(p+\beta_r+k\right)\left(2n+1\right)}{2N}\right)+sin\left(\frac{\pi\left(p+\beta_r-k\right)\left(2n+1\right)}{2N}\right)\right] \tag{A.5}$$

$$\Upsilon^{(s)}_{pk} = \frac{1}{N}\sum_{n=0}^{N-1}\left[cos\left(\frac{\pi\left(p+\beta_s+k\right)\left(2n+1\right)}{2N}\right)+cos\left(\frac{\pi\left(p+\beta_s-k\right)\left(2n+1\right)}{2N}\right)\right] \tag{A.6}$$

$$\Upsilon'^{(s)}_{pk} = \frac{1}{N}\sum_{n=0}^{N-1}\left[sin\left(\frac{\pi\left(p+\beta_s-k\right)\left(2n+1\right)}{2N}\right)+sin\left(\frac{\pi\left(p+\beta_s-k\right)\left(2n+1\right)}{2N}\right)\right] \tag{A.7}$$

Further, by making use of Euler's Inequality $cos\theta = \frac{e^{j\theta}+e^{-j\theta}}{2}$ and $sin\theta = \frac{e^{j\theta}-e^{-j\theta}}{2j}$, the aforementioned equations as listed above from (A.2) to (A.7) can be derived as follows: Beginning with (A.2), it can be further expressed as:

$$\Upsilon^{(r)}_{kk} = \frac{1}{N}\sum_{n=0}^{N-1}\left[\frac{e^{\frac{j\pi(2k+\beta_r)(2n+1)}{2N}}+e^{-\frac{j\pi(2k+\beta_r)(2n+1)}{2N}}}{2}+\frac{e^{\frac{j\pi\beta_r(2n+1)}{2N}}+e^{\frac{-j\pi\beta_r(2n+1)}{2N}}}{2}\right] \tag{A.8}$$

(A.8), can be further rearranged as:

$$\Upsilon^{(r)}_{kk} = \frac{1}{2N}\left[e^{\frac{j\pi(2k+\beta_r)}{2N}}\sum_{n=0}^{N-1}e^{\frac{j\pi(2k+\beta_r)n}{N}}+e^{\frac{-j\pi(2k+\beta_r)}{2N}}\sum_{n=0}^{N-1}e^{\frac{-j\pi(2k+\beta_r)n}{N}}+\right.$$
$$\left.e^{\frac{j\pi\beta_r}{2N}}\sum_{n=0}^{N-1}e^{\frac{j\pi\beta_r n}{N}}+e^{\frac{-j\pi\beta_r}{2N}}\sum_{n=0}^{N-1}e^{\frac{-j\pi\beta_r n}{N}}\right] \tag{A.9}$$

By making use of $\sum_{n=0}^{N-1} r^n = \frac{1-r^N}{1-r}$, the summation terms in the aforementioned equation (A.9) can be solved to obtain the mathematical expression as described in (5.19). In the similar manner, the rest of the aforementioned list of equations from (A.3) to (A.7) can be solved to yield the equations as represented by (5.20) to (5.24).

Scenario 2: As stated in Chapter 5, this scenario signifies the interference arising from the previous symbol. Upon employing the mathematical expression as depicted in (5.25), the frequency domain representation of the desired user r can be derived as:

$$
\begin{aligned}
Y_k^{(r)} = C_k^2 X_k^{(r)} \frac{1}{N} \sum_{n=-\alpha_r-N_{cp}+l}^{N-1} & \left[cos\left(\frac{\pi\left(2k+\beta_r\right)\left(2n+1\right)}{2N} + \frac{\pi\alpha_r\left(k+\beta_r\right)}{N} \right) + \right. \\
& \left. cos\left(\frac{\pi\beta_r\left(2n+1\right)}{2N} + \frac{\pi\alpha_r\left(k+\beta_r\right)}{N} \right) \right] H_k^{(r)} + \\
C_k \sum_{\substack{p=0\\ \boldsymbol{p\in Z_r}\\ \boldsymbol{p\neq k}}}^{N-1} C_p X_p^{(r)} \frac{1}{N} \sum_{n=-\alpha_r-N_{cp}+l}^{N-1} & \left[cos\left(\frac{\pi\left(p+\beta_r+k\right)\left(2n+1\right)}{2N} + \frac{\pi\alpha_r\left(p+\beta_r\right)}{N} \right) + \right. \\
& \left. cos\left(\frac{\pi\left(p+\beta_r-k\right)\left(2n+1\right)}{2N} + \frac{\pi\alpha_r\left(p+\beta_r\right)}{N} \right) \right] H_p^{(r)} + \\
C_k \sum_{\substack{p=0\\ \boldsymbol{p\in Z_s}\\ \boldsymbol{p\neq k}}}^{N-1} C_p X_p^{(s)} \frac{1}{N} \sum_{n=-\alpha_s-N_{cp}+l}^{N-1} & \left[cos\left(\frac{\pi\left(p+\beta_s+k\right)\left(2n+1\right)}{2N} + \frac{\pi\alpha_s\left(p+\beta_s\right)}{N} \right) + \right. \\
& \left. cos\left(\frac{\pi\left(p+\beta_s-k\right)\left(2n+1\right)}{2N} + \frac{\pi\alpha_s\left(p+\beta_s\right)}{N} \right) \right] H_p^{(s)} + \\
& C_k \sum_{\substack{p=0\\ \boldsymbol{p\in Z_r}\\ \boldsymbol{p\neq k}}}^{N-1} C_p X_p^{(r)(Previous)} \frac{1}{N} \sum_{n=0}^{-\alpha_r-N_{cp}+l-1} \\
& \times \left[cos\left(\frac{\pi\left(p+\beta_r+k\right)\left(2n+1\right)}{2N} + \frac{\pi\left(N_{cp}+\alpha_r\right)\left(p+\beta_r\right)}{N} \right) + \right. \\
& \left. cos\left(\frac{\pi\left(p+\beta_r-k\right)\left(2n+1\right)}{2N} + \frac{\pi\left(N_{cp}+\alpha_r\right)\left(p+\beta_r\right)}{N} \right) \right] H_p^{'(r)} + \\
& C_k \sum_{\substack{p=0\\ \boldsymbol{p\in Z_s}\\ \boldsymbol{p\neq k}}}^{N-1} C_p X_p^{(s)(Previous)} \frac{1}{N} \sum_{n=0}^{-\alpha_s-N_{cp}+l-1} \\
& \times \left[cos\left(\frac{\pi\left(p+\beta_s+k\right)\left(2n+1\right)}{2N} + \frac{\pi\left(N_{cp}+\alpha_s\right)\left(p+\beta_s\right)}{N} \right) + \right. \\
& \left. cos\left(\frac{\pi\left(p+\beta_s-k\right)\left(2n+1\right)}{2N} + \frac{\pi\left(N_{cp}+\alpha_s\right)\left(p+\beta_s\right)}{N} \right) \right] H_p^{'(s)} + W_k^{(r)} \qquad \text{(A.10)}
\end{aligned}
$$

Scenario 3: This is the scenario, which indicates the interference arising from the next symbol. By exploiting the mathematical expression as represented by (5.42), the frequency domain signal pertaining to the desired subscriber r can be solved as

$$
\begin{aligned}
Y_k^{(r)} = C_k^2 X_k^{(r)} \frac{1}{N} \sum_{n=0}^{N-\alpha_r+l-1} & \left[cos\left(\frac{\pi\left(2k+\beta_r\right)\left(2n+1\right)}{2N} + \frac{\pi\alpha_r\left(k+\beta_r\right)}{N}\right) + \right. \\
& \left. cos\left(\frac{\pi\beta_r\left(2n+1\right)}{2N} + \frac{\pi\alpha_r\left(k+\beta_r\right)}{N}\right)\right] \left[\sum_{l=0}^{L-1} h_l^{(r)} cos\left(\frac{\pi\left(2l+1\right)k}{2N}\right)\right] + \\
& C_k \sum_{\substack{p=0\\ \boldsymbol{p\in Z_r}\\ \boldsymbol{p\neq k}}}^{N-1} C_p X_p^{(r)} \frac{1}{N} \sum_{n=0}^{N-\alpha_r+l-1} \left[cos\left(\frac{\pi\left(p+\beta_r+k\right)\left(2n+1\right)}{2N} + \frac{\pi\alpha_r\left(p+\beta_r\right)}{N}\right) + \right. \\
& \left. cos\left(\frac{\pi\left(p+\beta_r-k\right)\left(2n+1\right)}{2N} + \frac{\pi\alpha_r\left(p+\beta_r\right)}{N}\right)\right] \left[\sum_{l=0}^{L-1} h_l^{(r)} cos\left(\frac{\pi\left(2l+1\right)p}{2N}\right)\right] + \\
& C_k \sum_{\substack{p=0\\ \boldsymbol{p\in Z_s}\\ \boldsymbol{p\neq k}}}^{N-1} C_p X_p^{(s)} \frac{1}{N} \sum_{n=0}^{N-\alpha_s+l-1} \left[cos\left(\frac{\pi\left(p+\beta_s+k\right)\left(2n+1\right)}{2N} + \frac{\pi\alpha_s\left(p+\beta_s\right)}{N}\right) + \right. \\
& \left. cos\left(\frac{\pi\left(p+\beta_s-k\right)\left(2n+1\right)}{2N} + \frac{\pi\alpha_s\left(p+\beta_s\right)}{N}\right)\right] \left[\sum_{l=0}^{L-1} h_l^{(s)} cos\left(\frac{\pi\left(2l+1\right)p}{2N}\right)\right] + \\
& C_k \sum_{\substack{p=0\\ \boldsymbol{p\in Z_r}\\ \boldsymbol{p\neq k}}}^{N-1} C_p X_p^{(r)(Next)} \frac{1}{N} \sum_{n=N-\alpha_r+l}^{N-1} \left[cos\left(\frac{\pi\left(p+\beta_r+k\right)\left(2n+1\right)}{2N} + \frac{\pi\left(N_{cp}-\alpha_r\right)\left(p+\beta_r\right)}{N}\right) + \right. \\
& \left. cos\left(\frac{\pi\left(p+\beta_r-k\right)\left(2n+1\right)}{2N} + \frac{\pi\left(N_{cp}-\alpha_r\right)\left(p+\beta_r\right)}{N}\right)\right] \left[\sum_{l=0}^{L-1} h_l^{(r)} cos\left(\frac{\pi\left(2l+1\right)p}{2N}\right)\right] + \\
& C_k \sum_{\substack{p=0\\ \boldsymbol{p\in Z_s}\\ \boldsymbol{p\neq k}}}^{N-1} C_p X_p^{(s)(Next)} \frac{1}{N} \sum_{n=0}^{N-1} \times \left[cos\left(\frac{\pi\left(p+\beta_s+k\right)\left(2n+1\right)}{2N} + \frac{\pi\left(N_{cp}-\alpha_s\right)\left(p+\beta_s\right)}{N}\right) + \right. \\
& \left. cos\left(\frac{\pi\left(p+\beta_s-k\right)\left(2n+1\right)}{2N} + \frac{\pi\left(N_{cp}-\alpha_s\right)\left(p+\beta_s\right)}{N}\right)\right] \left[\sum_{l=0}^{L-1} h_l^{(s)} cos\left(\frac{\pi\left(2l+1\right)p}{2N}\right)\right] \\
& + W_k^{(r)} \qquad \text{(A.11)}
\end{aligned}
$$

Appendix B

Derivation of Fisher Information Matrix of FO

The expression for $S\left[n,\Theta\right]$ in (5.59) can be represented as

$$S\left[n,\Theta\right]=\sqrt{\frac{2}{N}}\sum_{\substack{k=0\\k\in Z_r}}^{N-1}C_kX_k^{(r)}cos\mu \tag{B.1}$$

It is to be noted that the parameter Θ in (B.1) signifies the FO β_r, therefore, (B.1) can be expressed as

$$\left[I\left(\beta\right)\right]_{ij}=\frac{1}{\sigma^2}\sum_{n=0}^{N-1}\frac{\partial}{\partial\beta_i}S\left[n,\beta\right]\frac{\partial}{\partial\beta_j}S\left[n,\beta\right] \tag{B.2}$$

As stated earlier, μ is a function of β. Hence, $\frac{\partial}{\partial\beta}\left(cos\mu\right)=-\left(sin\mu\right)\left(\frac{\pi(2n+1)}{2N}\right)$. Therefore, the fisher information matrix can be solved to attain

$$\left[I\left(\Theta\right)_{11}\right]=\left[I\left(\beta_r\right)_{11}\right]=\frac{1}{\sigma^2}\sum_{n=0}^{N-1}\left[\sqrt{\frac{2}{N}}\sum_{\substack{k=0\\k\in Z_r}}^{N-1}C_kX_k^{(r)}sin\mu\left(\frac{\pi\left(2n+1\right)}{2N}\right)\right]^2 \tag{B.3}$$

(B.3) can be further solved to attain

$$\left[I\left(\Theta\right)_{11}\right]=\left[I\left(\beta_r\right)_{11}\right]=\frac{1}{\sigma^2}\sum_{n=0}^{N-1}\frac{2}{N}\frac{\pi^2\left(2n+1\right)^2}{4N^2}\left[\sum_{\substack{k=0\\k\in Z_r}}^{N-1}C_kX_k^{(r)}sin\mu\right]^2 \tag{B.4}$$

Using paraxial approximations where $sin\mu=\mu$, (B.4) can be reduced to obtain

$$\left[I\left(\Theta\right)_{11}\right]=\left[I\left(\beta_r\right)_{11}\right]=\frac{\pi^4}{8\sigma^2N^5}\sum_{n=0}^{N-1}\left(2n+1\right)^4\left[\sum_{\substack{k=0\\k\in Z_r}}^{N-1}C_kX_k^{(r)}\left(k+\beta_r\right)\right]^2 \tag{B.5}$$

Furthermore, upon solving the summation in (B.5), the Fisher Information matrix can be derived as shown by (5.60).

Appendix C

Derivation of Fisher Information Matrix of STO

In (5.65), $S\left[n,\alpha\right]$ can be illustrated as

$$S\left[n,\alpha\right]=\sqrt{\frac{2}{N}}\sum_{\substack{k=0\\k\in Z_r}}^{N-1}C_kX_k^{(r)}cos\mu \tag{C.1}$$

Therefore, upon differentiating (C.1) with respect to α_r, the following is obtained

$$\frac{\partial}{\partial\alpha}S\left[n,\alpha\right]=-\sqrt{\frac{2}{N}}\sum_{\substack{k=0\\k\in Z_r}}^{N-1}C_kX_k^{(r)}sin\mu\left(\frac{\pi k}{N}\right) \tag{C.2}$$

Upon substitution of (C.2) in (5.65), the following expression can be attained

$$\left[I\left(\alpha\right)\right]_{11}=\frac{1}{\sigma^2}\sum_{n=0}^{N-1}\left[-\sqrt{\frac{2}{N}}\sum_{\substack{k=0\\k\in Z_r}}^{N-1}C_kX_k^{(r)}sin\mu\left(\frac{\pi k}{N}\right)\right]^2 \tag{C.3}$$

Furthermore, by employing paraxial approximations where $sin\mu\simeq\mu$, the Fisher Information matrix corresponding to (C.3) can be reduced as

$$\left[I\left(\alpha\right)\right]_{11}=\frac{2\pi^2}{\sigma^2N^3}\sum_{n=0}^{N-1}\left[\sum_{\substack{k=0\\k\in Z_r}}^{N-1}kC_kX_k^{(r)}\left(\frac{\pi\left(2\left(n+\alpha_r\right)+1\right)k}{2N}\right)\right]^2 \tag{C.4}$$

(C.4) can be further solved as

$$\left[I\left(\alpha\right)\right]_{11}=\frac{\pi^4}{2\sigma^2N^5}\sum_{n=0}^{N-1}\left(2\left(n+\alpha_r\right)+1\right)^2\left[\sum_{\substack{k=0\\k\in Z_r}}^{N-1}k^2C_kX_k^{(r)}\right]^2 \tag{C.5}$$

(C.5) can be further solved to attain

$$[I(\alpha)]_{11} = \frac{\pi^4}{2\sigma^2 N^5} \sum_{n=0}^{N-1} \left(4n^2 + 4n(2\alpha_r + 1) + (2\alpha_r + 1)^2\right) \left[\sum_{\substack{k=0 \\ k\in Z_r}}^{N-1} k^2 C_k X_k^{(r)}\right]^2 \tag{C.6}$$

Upon solving the summation in (C.6),

$$[I(\alpha)]_{11} = \frac{\pi^4}{2\sigma^2 N^5} \sum_{n=0}^{N-1} \left(4n^2 + 4n(2\alpha_r + 1) + (2\alpha_r + 1)^2\right) \left[\sum_{\substack{k=0 \\ k\in Z_r}}^{N-1} k^2 C_k X_k^{(r)}\right]^2 \tag{C.7}$$

(C.7) can be further solved as

$$\begin{aligned}[I(\alpha)]_{11} = \frac{\pi^4}{2\sigma^2 N^5} &\left[\frac{4N(N+1)(2N+1)}{6} + \frac{4N(N+1)(2\alpha_r + 1)}{2} + N(2\alpha_r + 1)^2\right] \\ &\times \left[\sum_{\substack{k=0 \\ k\in Z_r}}^{N-1} k^2 C_k X_k^{(r)}\right]^2 \end{aligned} \tag{C.8}$$

Finally, (C.8) can be rearranged to obtain the Fisher Information Matrix as shown in (5.66).

Publications

List of International Journals:

---

1. Vappangi Suseela, and Venkata Mani Vakamulla. "Synchronization in visible light communication for smart cities." *IEEE Sensors Journal*, 18.5 (2018): 1877-1886. doi=10.1109/JSEN.2017.2777998. (**IEEE-SCI Journal**)
2. Vappangi Suseela, and Venkata Mani Vakamulla. "Channel estimation in ACO-OFDM employing different transforms for VLC." *AEU-International Journal of Electronics and Communications*, volume 84, pp- 111-122, 2018. https://doi.org/10.1016/j.aeue.2017.11.016. (**Elsevier-SCI Journal**)
3. Vappangi Suseela, and Venkata Mani Vakamulla. "A low PAPR multicarrier and multiple access schemes for VLC." *Optics Communications*, volume 425, pp- 121-132, 2018. https://doi.org/10.1016/j.optcom.2018.04.064. (**Elsevier-SCI Journal**)
4. Vappangi Suseela, and V. V. Mani. "Effects of frequency and timing offsets in DCT-based multiple access system for VLC." *Optics Communications*, volume 435, pp-297-310, 2019. https://doi.org/10.1016/j.optcom.2018.11.023. (**Elsevier-SCI Journal**)
5. Vappangi Suseela, and V. V. Mani. "Performance analysis of DST-based Intensity modulated/direct detection (IM/DD) systems for VLC." *IEEE Sensors Journal* (2018). doi=10.1109/JSEN.2018.2882378 (**IEEE-SCI Journal**).
6. Vappangi Suseela, and V. V. Mani. "Concurrent illumination and communication: A survey on Visible Light Communication." *Physical Communication*, volume 33,

pp- 90-114, 2019.
https://doi.org/10.1016/j.phycom.2018.12.017. (**Elsevier-SCI Journal**).

7. Vappangi Suseela, and V. V. Mani. "Interference Analysis and MUI-Cancellation in DCO-OFDMA-based IM/DD systems for VLC." *Optics Communications*, volume 448, pp-130-146 , 2019. (**Elsevier-SCI Journal**)

List of International Conferences:

---

1. Vappangi Suseela, and V. V. Mani. "Performance analysis of fast optical OFDM for VLC." *2017, 20th International Symposium on Wireless Personal Multimedia Communications (WPMC).* IEEE, 2017. doi=10.1109/WPMC.2017.8301809.

2. Vappangi Suseela, and V. V. Mani. "A Power efficient DST-based multicarrier and multiple access systems for VLC." *2018, IEEE International Conference on Advanced Networks and Telecommunications Systems, (ANTS).* IEEE, 2018. doi=10.1109/ANTS.2018.8710100.

3. Vappangi Suseela, and V. V. Mani. "Interference Analysis in DCT-Based Multiple Access System for VLC." *2018, 21st International Symposium on Wireless Personal Multimedia Communications (WPMC).* IEEE, 2018. doi=10.1109/WPMC.2018.8713031.

4. Vappangi Suseela, and V. V. Mani. "A Low PAPR DST-based optical OFDM (OOFDM) for Visible Light Communication." *2018, 21st International Symposium on Wireless Personal Multimedia Communications (WPMC).* IEEE, 2018. doi=10.1109/WPMC.2018.8713142.

Bibliography

[1] C. V. N. Index, "Global mobile data traffic forecast update, 2015–2020 white paper," *link: http://goo. gl/ylTuVx*, 2016.

[2] M. Z. Chowdhury, M. T. Hossan, A. Islam, and Y. M. Jang, "A comparative survey of optical wireless technologies: Architectures and applications," *IEEE Access*, vol. 6, pp. 9819–9840, 2018.

[3] L. I. Albraheem, L. H. Alhudaithy, A. A. Aljaser, M. R. Aldhafian, and G. M. Bahliwah, "Toward designing a li-fi-based hierarchical iot architecture," *IEEE Access*, vol. 6, pp. 40 811–40 825, 2018.

[4] M. Fchtenhans, E. H. Grosse, and C. H. Glock, "Use cases and potentials of smart lighting systems in industrial settings," *IEEE Engineering Management Review*, pp. 1–1, 2019.

[5] Y. Tanaka, S. Haruyama, and M. Nakagawa, "Wireless optical transmissions with white colored led for wireless home links," in *11th IEEE International Symposium on Personal Indoor and Mobile Radio Communications. PIMRC 2000. Proceedings (Cat. No.00TH8525)*, vol. 2, Sep. 2000, pp. 1325–1329 vol.2.

[6] "Visible light communications consortium (vlcc)," *link: http://www.vlcc.net.*

[7] E. S. I. Association *et al.*, "Japan electronics and information technology industries association," *Korea Semiconductor Industry Association, Taiwan Semiconductor Industry Association, and Semiconductor Industry Association:"International Technology Roadmap for Semiconductors: Yield Enhance*, p. 27, 2003.

[8] "Infrared data association (irda)," *link: http://www.irda.org.*

[9] K. D. Langer, J. Grubor, O. Bouchet, M. E. Tabach, J. W. Walewski, S. Randel, M. Franke, S. Nerreter, D. C. O'Brien, G. E. Faulkner, I. Neokosmidis, G. Ntogari, and M. Wolf, "Optical wireless communications for broadband access in home area networks," in *2008 10th Anniversary International Conference on Transparent Optical Networks*, vol. 4, June 2008, pp. 149–154.

[10] "Home gigabit access (omega)," *Project. [Online]. Available: http://www.ict-omega.eu/.*

[11] "Visible light communications association (vlca)," *[Online]. Available:http://vlca.net/.*

[12] Y. Jang, "Current status of ieee 802.15. 7r1 owc standardization," in *Proceedings of the International Conference and Exhibition on Visible Light Communications 2015*, 2015.

[13] "Ieee standard for local and metropolitan area networks–part 15.7: Short-range optical wireless communications," *IEEE Std 802.15.7-2018 (Revision of IEEE Std 802.15.7-2011)*, pp. 1–407, April 2019.

[14] L. E. M. Matheus, A. B. Vieira, L. F. M. Vieira, M. A. M. Vieira, and O. Gnawali, "Visible light communication: Concepts, applications and challenges," *IEEE Communications Surveys Tutorials*, pp. 1–1, 2019.

[15] R. Kraemer and M. Katz, *Short-range wireless communications: Emerging technologies and applications.* John Wiley & Sons, 2009.

[16] S. Randel, F. Breyer, S. C. J. Lee, and J. W. Walewski, "Advanced modulation schemes for short-range optical communications," *IEEE Journal of Selected Topics in Quantum Electronics*, vol. 16, no. 5, pp. 1280–1289, Sep. 2010.

[17] W. meteorological organization (Geneva)., *Guide to meterological instruments and methods of observation.* Secretariat of the World Meteorological Organization, 1996.

[18] M. Grabner and V. Kvicera, "On the relation between atmospheric visibility and optical wave attenuation," in *Mobile and Wireless Communications Summit, 2007. 16th IST.* IEEE, 2007, pp. 1–5.

[19] "Ieee standard for local and metropolitan area networks–part 15.7: Short-range wireless optical communication using visible light," *IEEE Std 802.15.7-2011*, pp. 1–309, Sept 2011.

[20] A. M. Cailean, B. Cagneau, L. Chassagne, M. Dimian, and V. Popa, "Miller code usage in visible light communications under the phy i layer of the ieee 802.15.7 standard," in *2014 10th International Conference on Communications (COMM)*, May 2014, pp. 1–4.

[21] C. Quintana, J. Rabadan, J. Rufo, F. Delgado, and R. Perez-Jimenez, "Time-hopping spread-spectrum system for wireless optical communications," *IEEE Transactions on Consumer Electronics*, vol. 55, no. 3, pp. 1083–1088, August 2009.

[22] J. Kim, D. Lee, K. D. Kim, and Y. Park, "Performance improvement in visible light communication by using spread spectrum coding," in *OECC 2010 Technical Digest*, July 2010, pp. 278–279.

[23] A. M. Cailean, B. Cagneau, L. Chassagne, V. Popa, and M. Dimian, "Evaluation of the noise effects on visible light communications using manchester and miller coding," in *2014 International Conference on Development and Application Systems (DAS)*, May 2014, pp. 85–89.

[24] H. Elgala and T. D. C. Little, "Reverse polarity optical-ofdm (rpo-ofdm): dimming compatible ofdm for gigabit vlc links," *Opt. Express*, vol. 21, no. 20, pp. 24 288–24 299, Oct 2013. [Online]. Available: `http://www.opticsexpress.org/abstract.cfm?URI=oe-21-20-24288`

[25] J. Grubor, S. C. J. Lee, K. D. Langer, T. Koonen, and J. W. Walewski, "Wireless high-speed data transmission with phosphorescent white-light leds," in *33rd European Conference and Exhibition of Optical Communication - Post-Deadline Papers (published 2008)*, Sept 2007, pp. 1–2.

[26] S. Park, D. Jung, H. Shin, D. Shin, Y. Hyun, K. Lee, and Y. Oh, "Information broadcasting system based on visible light signboard," *Proceedings of the Wireless and Optical Communications, Montreal, QC, Canada*, vol. 30, pp. 311–313, 2007.

[27] H. L. Minh, D. O'Brien, G. Faulkner, L. Zeng, K. Lee, D. Jung, and Y. Oh, "High-speed visible light communications using multiple-resonant equalization," *IEEE Photonics Technology Letters*, vol. 20, no. 14, pp. 1243–1245, July 2008.

[28] J. Vucic, C. Kottke, S. Nerreter, K. Habel, A. Buttner, K. D. Langer, and J. W. Walewski, "125 mbit/s over 5 m wireless distance by use of ook-modulated phosphorescent white leds," in *2009 35th European Conference on Optical Communication*, Sept 2009, pp. 1–2.

[29] J. Vui, C. Kottke, S. Nerreter, K. Habel, A. Bttner, K. Langer, and J. W. Walewski, "230 mbit/s via a wireless visible-light link based on ook modulation of phosphorescent white leds," in *2010 Conference on Optical Fiber Communication (OFC/NFOEC), collocated National Fiber Optic Engineers Conference*, March 2010, pp. 1–3.

[30] N. Fujimoto and H. Mochizuki, "477 mbit/s visible light transmission based on ook-nrz modulation using a single commercially available visible led and a practical led driver with a pre-emphasis circuit," in *2013 Optical Fiber Communication Conference and Exposition and the National Fiber Optic Engineers Conference (OFC/NFOEC)*, March 2013, pp. 1–3.

[31] H. Li, X. Chen, B. Huang, D. Tang, and H. Chen, "High bandwidth visible light communications based on a post-equalization circuit," *IEEE Photonics Technology Letters*, vol. 26, no. 2, pp. 119–122, Jan 2014.

[32] H. Li, X. Chen, J. Guo, and H. Chen, "A 550 mbit/s real-time visible light communication system based on phosphorescent white light led for practical high-speed low-complexity application," *Opt. Express*, vol. 22, no. 22, pp. 27 203–27 213, Nov 2014. [Online]. Available: `http://www.opticsexpress.org/abstract.cfm?URI=oe-22-22-27203`

[33] N. Fujimoto and H. Mochizuki, "614 mbit/s ook-based transmission by the duobinary technique using a single commercially available visible led for high-speed visible light communications," in *2012 38th European Conference and Exhibition on Optical Communications*, Sept 2012, pp. 1–3.

[34] P. A. Haigh, Z. Ghassemlooy, S. Rajbhandari, I. Papakonstantinou, and W. Popoola, “Visible light communications: 170 mb/s using an artificial neural network equalizer in a low bandwidth white light configuration,” *Journal of Lightwave Technology*, vol. 32, no. 9, pp. 1807–1813, May 2014.

[35] H. Sugiyama, S. Haruyama, and M. Nakagawa, “Brightness control methods for illumination and visible-light communication systems,” in *Wireless and Mobile Communications, 2007. ICWMC ’07. Third International Conference on*, March 2007, pp. 78–78.

[36] G. Ntogari, T. Kamalakis, J. Walewski, and T. Sphicopoulos, “Combining illumination dimming based on pulse-width modulation with visible-light communications based on discrete multitone,” *IEEE/OSA Journal of Optical Communications and Networking*, vol. 3, no. 1, pp. 56–65, January 2011.

[37] C. N. Georghiades, “Modulation and coding for throughput-efficient optical systems,” *IEEE Transactions on Information Theory*, vol. 40, no. 5, pp. 1313–1326, Sep 1994.

[38] D.-S. Shiu and J. M. Kahn, “Differential pulse-position modulation for power-efficient optical communication,” *IEEE Transactions on Communications*, vol. 47, no. 8, pp. 1201–1210, Aug 1999.

[39] S. Rajagopal, R. D. Roberts, and S. K. Lim, “Ieee 802.15.7 visible light communication: modulation schemes and dimming support,” *IEEE Communications Magazine*, vol. 50, no. 3, pp. 72–82, March 2012.

[40] J. H. Yoo, B. W. Kim, and S. Y. Jung, “Modelling and analysis of m-ary variable pulse position modulation for visible light communications,” *IET Optoelectronics*, vol. 9, no. 5, pp. 184–190, 2015.

[41] B. Bai, Z. Xu, and Y. Fan, “Joint led dimming and high capacity visible light communication by overlapping ppm,” in *The 19th Annual Wireless and Optical Communications Conference (WOCC 2010)*, May 2010, pp. 1–5.

[42] H. Sugiyama and K. Nosu, "Mppm: a method for improving the band-utilization efficiency in optical ppm," *Journal of Lightwave Technology*, vol. 7, no. 3, pp. 465–472, March 1989.

[43] T. Ohtsuki, I. Sasase, and S. Mori, "Overlapping multi-pulse pulse position modulation in optical direct detection channel," in *Communications, 1993. ICC '93 Geneva. Technical Program, Conference Record, IEEE International Conference on*, vol. 2, May 1993, pp. 1123–1127 vol.2.

[44] ——, "Performance analysis of overlapping multi-pulse pulse position modulation (omppm) in noisy photon counting channel," in *Proceedings of 1994 IEEE International Symposium on Information Theory*, June 1994, pp. 80–.

[45] ——, "Capacity and cutoff rate of overlapping multi-pulse pulse position modulation (omppm) in optical direct-detection channel: Quantum-limited case," *IEICE TRANSACTIONS on Fundamentals of Electronics, Communications and Computer Sciences*, vol. 77, no. 8, pp. 1298–1308, 1994.

[46] ——, "Trellis coded overlapping multi-pulse pulse position modulation in optical direct detection channel," in *Communications, 1994. ICC '94, SUPERCOMM/ICC '94, Conference Record, 'Serving Humanity Through Communications.' IEEE International Conference on*, May 1994, pp. 675–679 vol.2.

[47] ——, "Error performance of overlapping multi-pulse pulse position modulation (omppm) and trellis coded omppm in optical direct-detection channel," *IEICE transactions on communications*, vol. 77, no. 9, pp. 1133–1143, 1994.

[48] D. Zwillinger, "Differential ppm has a higher throughput than ppm for the band-limited and average-power-limited optical channel," *IEEE Transactions on Information Theory*, vol. 34, no. 5, pp. 1269–1273, Sep 1988.

[49] T. Ohtsuki, I. Sasase, and S. Mori, "Differential overlapping pulse position modulation in optical direct-detection channel," in *Communications, 1994. ICC '94, SUPERCOMM/ICC '94, Conference Record, 'Serving Humanity Through Communications.' IEEE International Conference on*, May 1994, pp. 680–684 vol.2.

[50] M. Noshad and M. Brandt-Pearce, “Expurgated ppm using symmetric balanced incomplete block designs,” *IEEE Communications Letters*, vol. 16, no. 7, pp. 968–971, July 2012.

[51] ——, “Multilevel pulse-position modulation based on balanced incomplete block designs,” in *2012 IEEE Global Communications Conference (GLOBECOM)*, Dec 2012, pp. 2930–2935.

[52] K. Lee and H. Park, “Modulations for visible light communications with dimming control,” *IEEE Photonics Technology Letters*, vol. 23, no. 16, pp. 1136–1138, Aug 2011.

[53] A. B. Siddique and M. Tahir, “Joint rate-brightness control using variable rate mppm for led based visible light communication systems,” *IEEE Transactions on Wireless Communications*, vol. 12, no. 9, pp. 4604–4611, September 2013.

[54] Z. Yang, M. Jiang, L. Zhang, and H. Z. Tan, “Enhanced multiple pulse position modulation aided reverse polarity optical ofdm system with extended dimming control,” *IEEE Photonics Journal*, vol. 10, no. 3, pp. 1–17, June 2018.

[55] X. Deng, S. Mardanikorani, G. Zhou, and J. M. G. Linnartz, “Dc-bias for optical ofdm in visible light communications,” *IEEE Access*, vol. 7, pp. 98 319–98 330, 2019.

[56] “Coded 64-cap adsl in an impulse-noise environment-modeling of impulse noise and first simulation results,” *IEEE Journal on Selected Areas in Communications*, vol. 13, no. 9, pp. 1611–1621, Dec 1995.

[57] K. O. Akande, P. A. Haigh, and W. O. Popoola, “On the implementation of carrierless amplitude and phase modulation in visible light communication,” *IEEE Access*, vol. 6, pp. 60 532–60 546, 2018.

[58] R. Rodes, M. Wieckowski, T. T. Pham, J. B. Jensen, and I. T. Monroy, “Vcsel-based dwdm pon with 4 bit/s/hz spectral efficiency using carrierless amplitude phase modulation,” in *2011 37th European Conference and Exhibition on Optical Communication*, Sept 2011, pp. 1–3.

[59] L. Tao, Y. Ji, J. Liu, A. P. T. Lau, N. Chi, and C. Lu, “Advanced modulation formats for short reach optical communication systems,” *IEEE Network*, vol. 27, no. 6, pp. 6–13, November 2013.

[60] G. Stepniak and J. Siuzdak, “Experimental investigation of pam, cap and dmt modulations efficiency over a double-step-index polymer optical fiber,” *Optical Fiber Technology*, vol. 20, no. 4, pp. 369–373, 2014.

[61] R. Kruglov, S. Loquai, C. A. Bunge, M. Schueppert, J. Vinogradov, and O. Ziemann, “Comparison of pam and cap modulation schemes for data transmission over si-pof,” *IEEE Photonics Technology Letters*, vol. 25, no. 23, pp. 2293–2296, Dec 2013.

[62] F. M. Wu, C. T. Lin, C. C. Wei, C. W. Chen, H. T. Huang, and C. H. Ho, “1.1-gb/s white-led-based visible light communication employing carrier-less amplitude and phase modulation,” *IEEE Photonics Technology Letters*, vol. 24, no. 19, pp. 1730–1732, Oct 2012.

[63] F. M. Wu, C. T. Lin, C. C. Wei, C. W. Chen, Z. Y. Chen, H. T. Huang, and S. Chi, “Performance comparison of ofdm signal and cap signal over high capacity rgb-led-based wdm visible light communication,” *IEEE Photonics Journal*, vol. 5, no. 4, pp. 7 901 507–7 901 507, Aug 2013.

[64] G. Stepniak, L. Maksymiuk, and J. Siuzdak, “Experimental comparison of pam, cap, and dmt modulations in phosphorescent white led transmission link,” *IEEE Photonics Journal*, vol. 7, no. 3, pp. 1–8, June 2015.

[65] S. Long, M. A. Khalighi, M. Wolf, Z. Ghassemlooy, and S. Bourennane, “Performance of carrier-less amplitude and phase modulation with frequency domain equalization for indoor visible light communications,” in *2015 4th International Workshop on Optical Wireless Communications (IWOW)*, Sept 2015, pp. 16–20.

[66] K. O. Akande and W. O. Popoola, “Spatial carrierless amplitude and phase modulation technique for visible light communication systems,” *IEEE Systems Journal*, vol. 13, no. 3, pp. 2344–2353, Sep. 2019.

[67] ——, “Impact of timing jitter on the performance of carrier amplitude and phase modulation,” in *2016 International Conference for Students on Applied Engineering (ICSAE)*, Oct 2016, pp. 259–263.

[68] M. Yasir, S. Ho, and B. N. Vellambi, “Indoor positioning system using visible light and accelerometer,” *Journal of Lightwave Technology*, vol. 32, no. 19, pp. 3306–3316, Oct 2014.

[69] Y. Hou, S. Xiao, H. Zheng, and W. Hu, “Multiple access scheme based on block encoding time division multiplexing in an indoor positioning system using visible light,” *IEEE/OSA Journal of Optical Communications and Networking*, vol. 7, no. 5, pp. 489–495, May 2015.

[70] A. A. Saed, S. Ho, and C. W. Sung, “Adaptive modulation for two users in vlc,” in *2015 IEEE Globecom Workshops (GC Wkshps)*, Dec 2015, pp. 1–6.

[71] H. Ma, L. Lampe, and S. Hranilovic, “Coordinated broadcasting for multiuser indoor visible light communication systems,” *IEEE Transactions on Communications*, vol. 63, no. 9, pp. 3313–3324, Sep. 2015.

[72] A. Mousa and H. Mahmoud, “Channels estimation in ofdm system over rician fading channel based on comb-type pilots arrangement,” *IET Signal Processing*, vol. 4, no. 5, pp. 598–602, Oct 2010.

[73] O. Şayli, H. Doğan, and E. Panayirci, “On channel estimation in dc biased optical ofdm systems over vlc channels,” in *Advanced Technologies for Communications (ATC), 2016 International Conference on.* IEEE, 2016, pp. 147–151.

[74] H. Dogan, O. ayl, and E. Panayirci, “Pilot assisted channel estimation for asymmetrically clipped optical ofdm over visible light channels,” in *2016 IEEE International Black Sea Conference on Communications and Networking (BlackSeaCom)*, June 2016, pp. 1–4.

[75] X. Chen and M. Jiang, “Enhanced bayesian mmse channel estimation for visible light communication,” in *2016 IEEE 27th Annual International Symposium on Personal, Indoor, and Mobile Radio Communications (PIMRC)*, Sep. 2016, pp. 1–6.

[76] ——, “Adaptive statistical bayesian mmse channel estimation for visible light communication,” *IEEE Transactions on Signal Processing*, vol. 65, no. 5, pp. 1287–1299, March 2017.

[77] L. Wu, J. Cheng, Z. Zhang, J. Dang, and H. Liu, “Channel estimation for optical-ofdm-based multiuser miso visible light communication,” *IEEE Photonics Technology Letters*, vol. 29, no. 20, pp. 1727–1730, Oct 2017.

[78] N. Lourenço, D. Terra, N. Kumar, L. N. Alves, and R. L. Aguiar, “Visible light communication system for outdoor applications,” in *2012 8th International Symposium on Communication Systems, Networks & Digital Signal Processing (CSNDSP).* IEEE, 2012, pp. 1–6.

[79] Y. Zhu, Z. Sun, J. Zhang, and Y. Zhang, “A fast blind detection algorithm for outdoor visible light communications,” *IEEE Photonics Journal*, vol. 7, no. 6, pp. 1–8, Dec 2015.

[80] B. Lin, X. Tang, Z. Ghassemlooy, S. Zhang, Y. Li, Y. Wu, and H. Li, “Efficient frequency-domain channel equalisation methods for ofdm visible light communications,” *IET Communications*, vol. 11, no. 1, pp. 25–29, 2017.

[81] H. Elgala, R. Mesleh, and H. Haas, “An led model for intensity-modulated optical communication systems,” *IEEE Photonics Technology Letters*, vol. 22, no. 11, pp. 835–837, June 2010.

[82] H. Elgala, R. Mesleh, and H. Haas, “Non-linearity effects and predistortion in optical ofdm wireless transmission using leds,” *International Journal of Ultra Wideband Communications and Systems*, vol. 1, no. 2, pp. 143–150, 2009.

[83] S. Dimitrov and H. Haas, “Information rate of ofdm-based optical wireless communication systems with nonlinear distortion,” *Journal of Lightwave Technology*, vol. 31, no. 6, pp. 918–929, March 2013.

[84] R. Ramirez-Iniguez, S. M. Idrus, and Z. Sun, *Optical wireless communications: IR for wireless connectivity.* Auerbach Publications, 2008.

[85] D. Wulich and L. Goldfeld, "Reduction of peak factor in orthogonal multicarrier modulation by amplitude limiting and coding," *IEEE Transactions on Communications*, vol. 47, no. 1, pp. 18–21, Jan 1999.

[86] C. Li, S. Wang, and C. Wang, "Novel low-complexity slm schemes for papr reduction in ofdm systems," *IEEE Transactions on Signal Processing*, vol. 58, no. 5, pp. 2916–2921, May 2010.

[87] S. Wang and C. Li, "A low-complexity papr reduction scheme for sfbc mimo-ofdm systems," *IEEE Signal Processing Letters*, vol. 16, no. 11, pp. 941–944, Nov 2009.

[88] C. Li, S. Wang, and K. Chan, "Low complexity transmitter architectures for sfbc mimo-ofdm systems," *IEEE Transactions on Communications*, vol. 60, no. 6, pp. 1712–1718, June 2012.

[89] S. H. Muller and J. B. Huber, "Ofdm with reduced peak-to-average power ratio by optimum combination of partial transmit sequences," *Electronics Letters*, vol. 33, no. 5, pp. 368–369, Feb 1997.

[90] R. Zakaria and D. Le Ruyet, "A novel filter-bank multicarrier scheme to mitigate the intrinsic interference: Application to mimo systems," *IEEE Transactions on Wireless Communications*, vol. 11, no. 3, pp. 1112–1123, March 2012.

[91] and, "Nonlinear companding transform for reducing peak-to-average power ratio of ofdm signals," *IEEE Transactions on Broadcasting*, vol. 50, no. 3, pp. 342–346, Sep. 2004.

[92] and and, "A complementary clipping transform technique for the reduction of peak-to-average power ratio of ofdm system," *IEEE Transactions on Consumer Electronics*, vol. 49, no. 4, pp. 922–926, Nov 2003.

[93] H. Zhang, Y. Yuan, and W. Xu, "Papr reduction for dco-ofdm visible light communications via semidefinite relaxation," *IEEE Photonics Technology Letters*, vol. 26, no. 17, pp. 1718–1721, Sep. 2014.

[94] Y. Hei, J. Liu, W. Li, X. Xu, and R. T. Chen, "Branch and bound methods based tone injection schemes for papr reduction of dco-ofdm visible light

communications," *Opt. Express*, vol. 25, no. 2, pp. 595–604, Jan 2017. [Online]. Available: `http://www.opticsexpress.org/abstract.cfm?URI=oe-25-2-595`

[95] J. G. Doblado, A. C. O. Oria, V. Baena-Lecuyer, P. Lopez, and D. Perez-Calderon, "Cubic metric reduction for dco-ofdm visible light communication systems," *Journal of Lightwave Technology*, vol. 33, no. 10, pp. 1971–1978, May 2015.

[96] J. Bai, Y. Li, Y. Yi, W. Cheng, and H. Du, "Papr reduction based on tone reservation scheme for dco-ofdm indoor visible light communications," *Opt. Express*, vol. 25, no. 20, pp. 24 630–24 638, Oct 2017. [Online]. Available: `http://www.opticsexpress.org/abstract.cfm?URI=oe-25-20-24630`

[97] Y. Hei, J. Liu, H. Gu, W. Li, X. Xu, and R. T. Chen, "Improved tkm-tr methods for papr reduction of dco-ofdm visible light communications," *Opt. Express*, vol. 25, no. 20, pp. 24 448–24 458, Oct 2017. [Online]. Available: `http://www.opticsexpress.org/abstract.cfm?URI=oe-25-20-24448`

[98] Z. Yu, R. J. Baxley, and G. T. Zhou, "Iterative clipping for papr reduction in visible light ofdm communications," in *2014 IEEE Military Communications Conference*, Oct 2014, pp. 1681–1686.

[99] K. Bandara, P. Niroopan, and Y. Chung, "Papr reduced ofdm visible light communication using exponential nonlinear companding," in *2013 IEEE International Conference on Microwaves, Communications, Antennas and Electronic Systems (COMCAS 2013)*, Oct 2013, pp. 1–5.

[100] W. O. Popoola, Z. Ghassemlooy, and B. G. Stewart, "Pilot-assisted papr reduction technique for optical ofdm communication systems," *Journal of Lightwave Technology*, vol. 32, no. 7, pp. 1374–1382, April 2014.

[101] F. B. Ogunkoya, W. O. Popoola, A. Shahrabi, and S. Sinanovi, "Performance evaluation of pilot-assisted papr reduction technique in optical ofdm systems," *IEEE Photonics Technology Letters*, vol. 27, no. 10, pp. 1088–1091, May 2015.

[102] F. B. Offiong, S. Sinanovi, and W. O. Popoola, "On papr reduction in pilot-assisted optical ofdm communication systems," *IEEE Access*, vol. 5, pp. 8916–8929, 2017.

[103] Y. Xiao, M. Chen, F. Li, J. Tang, Y. Liu, and L. Chen, "Papr reduction based on chaos combined with slm technique in optical ofdm im/dd system," *Optical Fiber Technology*, vol. 21, pp. 81 – 86, 2015. [Online]. Available: `http://www.sciencedirect.com/science/article/pii/S106852001400131X`

[104] M. Z. Farooqui, P. Saengudomlert, and S. Kaiser, "Average transmit power reduction in ofdm-based indoor wireless optical communications using slm," in *International Conference on Electrical Computer Engineering (ICECE 2010)*, Dec 2010, pp. 602–605.

[105] W. Hu and D. Lee, "Papr reduction for visible light communication systems without side information," *IEEE Photonics Journal*, vol. 9, no. 3, pp. 1–11, June 2017.

[106] W. Hu, "Papr reduction in dco-ofdm visible light communication systems using optimized odd and even sequences combination," *IEEE Photonics Journal*, vol. 11, no. 1, pp. 1–15, Feb 2019.

[107] J. Dang and Z. Zhang, "Comparison of optical ofdm-idma and optical ofdma for uplink visible light communications," in *2012 International Conference on Wireless Communications and Signal Processing (WCSP)*, Oct 2012, pp. 1–6.

[108] X. Li, Y. J. Kim, and N. Y. Park, "A low papr wled communication system using sc-fdma techniques," in *2011 IEEE 73rd Vehicular Technology Conference (VTC Spring)*, May 2011, pp. 1–5.

[109] Z. Li and C. Zhang, "An improved fd-dfe structure for downlink vlc systems based on sc-fdma," *IEEE Communications Letters*, vol. 22, no. 4, pp. 736–739, April 2018.

[110] T. T.Tjhung and B. Caron, "Ser performance evaluation and optimization of ofdm system with residual frequency and timing offsets from imperfect synchronization," *IEEE Transactions on Broadcasting*, vol. 49, no. 2, pp. 170–177, June 2003.

[111] P. H. Moose, "A technique for orthogonal frequency division multiplexing frequency offset correction," *IEEE Transactions on Communications*, vol. 42, no. 10, pp. 2908–2914, Oct 1994.

[112] J. J. van de Beek, M. Sandell, and P. O. Borjesson, “Ml estimation of time and frequency offset in ofdm systems,” *IEEE Transactions on Signal Processing*, vol. 45, no. 7, pp. 1800–1805, July 1997.

[113] and and, “Decision-directed maximum-likelihood estimation of ofdm frame synchronisation offset,” *Electronics Letters*, vol. 30, no. 25, pp. 2153–2154, Dec 1994.

[114] ——, “Frequency and timing period offset estimation technique for ofdm systems,” *Electronics Letters*, vol. 34, no. 6, pp. 520–521, March 1998.

[115] M. Luise and R. Reggiannini, “Carrier frequency acquisition and tracking for ofdm systems,” *IEEE Transactions on Communications*, vol. 44, no. 11, pp. 1590–1598, Nov 1996.

[116] L. He and F. Yang, “Robust timing and frequency synchronization for tds-ofdm over multipath fading channels,” in *2010 IEEE International Conference on Communication Systems*, Nov 2010, pp. 451–455.

[117] P. Papadimitratos, A. D. L. Fortelle, K. Evenssen, R. Brignolo, and S. Cosenza, “Vehicular communication systems: Enabling technologies, applications, and future outlook on intelligent transportation,” *IEEE Communications Magazine*, vol. 47, no. 11, pp. 84–95, November 2009.

[118] A. M. Cilean and M. Dimian, “Toward environmental-adaptive visible light communications receivers for automotive applications: A review,” *IEEE Sensors Journal*, vol. 16, no. 9, pp. 2803–2811, May 2016.

[119] X. Long, J. He, J. Zhou, L. Fang, X. Zhou, F. Ren, and T. Xu, “A review on light-emitting diode based automotive headlamps,” *Renewable and Sustainable Energy Reviews*, vol. 41, pp. 29 – 41, 2015. [Online]. Available: `http://www.sciencedirect.com/science/article/pii/S1364032114007047`

[120] S. Kitano, S. Haruyama, and M. Nakagawa, “Led road illumination communications system,” in *2003 IEEE 58th Vehicular Technology Conference. VTC 2003-Fall (IEEE Cat. No.03CH37484)*, vol. 5, Oct 2003, pp. 3346–3350 Vol.5.

[121] N. Kumar, “Smart and intelligent energy efficient public illumination system with ubiquitous communication for smart city,” in *Smart Structures and Systems (ICSSS), 2013 IEEE International Conference on*, March 2013, pp. 152–157.

[122] C. V. S. C. Consortium *et al.*, “Vehicle safety communications project task 3 final report, mar. 2005,” *Online: http://www. intellidriveusa. org/documents/vehicle-safety. pdf.*

[123] W. G. Najm, J. Koopmann, J. D. Smith, and J. Brewer, “Frequency of target crashes for intellidrive safety systems,” Tech. Rep., 2010.

[124] V. T. B. Tram and M. Yoo, “Vehicle-to-vehicle distance estimation using a low-resolution camera based on visible light communications,” *IEEE Access*, vol. 6, pp. 4521–4527, 2018.

[125] Y. Goto, I. Takai, T. Yamazato, H. Okada, T. Fujii, S. Kawahito, S. Arai, T. Yendo, and K. Kamakura, “A new automotive vlc system using optical communication image sensor,” *IEEE Photonics Journal*, vol. 8, no. 3, pp. 1–17, June 2016.

[126] Y. H. Kim, W. A. Cahyadi, and Y. H. Chung, “Experimental demonstration of vlc-based vehicle-to-vehicle communications under fog conditions,” *IEEE Photonics Journal*, vol. 7, no. 6, pp. 1–9, Dec 2015.

[127] D. R. Kim, S. H. Yang, H. S. Kim, Y. H. Son, and S. K. Han, “Outdoor visible light communication for inter- vehicle communication using controller area network,” in *2012 Fourth International Conference on Communications and Electronics (ICCE)*, Aug 2012, pp. 31–34.

[128] T. Nawaz, M. Seminara, S. Caputo, L. Mucchi, F. Cataliotti, and J. Catani, “Ieee 802.15.7-compliant ultra-low latency relaying vlc system for safety-critical its,” *IEEE Transactions on Vehicular Technology*, pp. 1–1, 2019.

[129] W. Boubakri, W. Abdallah, and N. Boudriga, “A light-based communication architecture for smart city applications,” in *2015 17th International Conference on Transparent Optical Networks (ICTON)*, July 2015, pp. 1–6.

[130] S. Ayub, S. Kariyawasam, M. Honary, and B. Honary, “A practical approach of vlc architecture for smart city,” in *2013 Loughborough Antennas Propagation Conference (LAPC)*, Nov 2013, pp. 106–111.

[131] M. Jani, P. Garg, and A. Gupta, “Performance analysis of a mixed cooperative plcvlc system for indoor communication systems,” *IEEE Systems Journal*, pp. 1–8, 2019.

[132] R. Perez-Jimenez, J. Rabadan, J. Rufo, E. Solana, and J. M. Luna-Rivera, “Visible light communications technologies for smart tourism destinations,” in *2015 IEEE First International Smart Cities Conference (ISC2)*, Oct 2015, pp. 1–5.

[133] J. Armstrong and B. J. C. Schmidt, “Comparison of asymmetrically clipped optical ofdm and dc-biased optical ofdm in awgn,” *IEEE Communications Letters*, vol. 12, no. 5, pp. 343–345, May 2008.

[134] B. Aly, “Performance analysis of adaptive channel estimation for u-ofdm indoor visible light communication,” in *2016 33rd National Radio Science Conference (NRSC)*, Feb 2016, pp. 217–222.

[135] M. S. Islim and H. Haas, “Modulation techniques for li-fi,” *ZTE communications*, vol. 14, no. 2, pp. 29–40, 2016.

[136] S. Coleri, M. Ergen, A. Puri, and A. Bahai, “Channel estimation techniques based on pilot arrangement in ofdm systems,” *IEEE Transactions on Broadcasting*, vol. 48, no. 3, pp. 223–229, Sep 2002.

[137] R. Bouziane, P. A. Milder, R. J. Koutsoyannis, Y. Benlachtar, J. C. Hoe, M. Glick, and R. I. Killey, “Dependence of optical ofdm transceiver asic complexity on fft size,” in *OFC/NFOEC*, March 2012, pp. 1–3.

[138] J. W. Cooley and J. W. Tukey, “An algorithm for the machine calculation of complex fourier series,” *Mathematics of computation*, vol. 19, no. 90, pp. 297–301, 1965.

[139] A. A. Raj and T. Latha, *VLSI design.* PHI Learning Pvt. Ltd., 2008.

[140] M. S. Moreolo, “Performance analysis of dht-based optical ofdm using large-size constellations in awgn,” *IEEE Communications Letters*, vol. 15, no. 5, pp. 572–574, May 2011.

[141] R. N. Bracewell, “The fast hartley transform,” *Proceedings of the IEEE*, vol. 72, no. 8, pp. 1010–1018, 1984.

[142] H. S. Hou, “The fast hartley transform algorithm,” *IEEE Transactions on Computers*, no. 2, pp. 147–156, 1987.

[143] H. Sorensen, D. Jones, C. Burrus, and M. Heideman, “On computing the discrete hartley transform,” *IEEE Transactions on Acoustics, Speech, and Signal Processing*, vol. 33, no. 5, pp. 1231–1238, 1985.

[144] P. Duhamel and M. Vetterli, “Cyclic convolution of real sequences: Hartley versus fourier and new schemes,” in *ICASSP’86. IEEE International Conference on Acoustics, Speech, and Signal Processing*, vol. 11. IEEE, 1986, pp. 229–232.

[145] ——, “Improved fourier and hartley transform algorithms: Application to cyclic convolution of real data,” *IEEE Transactions on Acoustics, Speech, and Signal Processing*, vol. 35, no. 6, pp. 818–824, 1987.

[146] M. Noshad and M. Brandt-Pearce, “Hadamard-coded modulation for visible light communications,” *IEEE Transactions on Communications*, vol. 64, no. 3, pp. 1167–1175, March 2016.

[147] M. S. Ahmed, S. Boussakta, B. S. Sharif, and C. C. Tsimenidis, “Ofdm based on low complexity transform to increase multipath resilience and reduce papr,” *IEEE Transactions on Signal Processing*, vol. 59, no. 12, pp. 5994–6007, Dec 2011.

[148] J. Xiao, J. Yu, X. Li, Q. Tang, H. Chen, F. Li, Z. Cao, and L. Chen, “Hadamard transform combined with companding transform technique for papr reduction in an optical direct-detection ofdm system,” *IEEE/OSA Journal of Optical Communications and Networking*, vol. 4, no. 10, pp. 709–714, Oct 2012.

[149] and, “Ber minimized ofdm systems with channel independent precoders,” *IEEE Transactions on Signal Processing*, vol. 51, no. 9, pp. 2369–2380, Sep. 2003.

[150] W. Huang, C. Gong, and Z. Xu, "System and waveform design for wavelet packet division multiplexing-based visible light communications," *Journal of Lightwave Technology*, vol. 33, no. 14, pp. 3041–3051, July 2015.

[151] T. Komine and M. Nakagawa, "Fundamental analysis for visible-light communication system using led lights," *IEEE Transactions on Consumer Electronics*, vol. 50, no. 1, pp. 100–107, Feb 2004.

[152] Z. Ghassemlooy, W. Popoola, and S. Rajbhandari, *Optical wireless communications: system and channel modelling with Matlab®*. CRC press, 2012.

[153] F. R. Gfeller and U. Bapst, "Wireless in-house data communication via diffuse infrared radiation," *Proceedings of the IEEE*, vol. 67, no. 11, pp. 1474–1486, Nov 1979.

[154] S. M. Kay, *Fundamentals of statistical signal processing.* Prentice Hall PTR, 1993.

[155] J. Proakis, *Digital Communications*, 4th ed. McGraw-Hill, 2000.

[156] J. Heiskala and J. Terry Ph D, *OFDM wireless LANs: A theoretical and practical guide.* Sams, 2001.

[157] J. Zhao and A. D. Ellis, "Discrete-fourier transform based implementation for optical fast ofdm," in *36th European Conference and Exhibition on Optical Communication.* IEEE, 2010, pp. 1–3.

[158] E. Giacoumidis, S. K. Ibrahim, J. Zhao, J. M. Tang, I. Tomkos, and A. D. Ellis, "Experimental demonstration of cost-effective intensity-modulation and direct-detection optical fast-ofdm over 40km smf transmission," in *OFC/NFOEC*, March 2012, pp. 1–3.

[159] E. Giacoumidis, A. Tsokanos, C. Mouchos, G. Zardas, C. Alves, J. L. Wei, J. M. Tang, C. Gosset, Y. Jaoun, and I. Tomkos, "Extensive comparisons of optical fast-ofdm and conventional optical ofdm for local and access networks," *IEEE/OSA Journal of Optical Communications and Networking*, vol. 4, no. 10, pp. 724–733, Oct 2012.

[160] J. Zhou, Y. Qiao, Z. Cai, and Y. Ji, “Asymmetrically clipped optical fast ofdm based on discrete cosine transform for im/dd systems,” *Journal of Lightwave Technology*, vol. 33, no. 9, pp. 1920–1927, May 2015.

[161] J. Zhao and A. D. Ellis, “A novel optical fast ofdm with reduced channel spacing equal to half of the symbol rate per carrier,” in *Optical Fiber Communication (OFC), collocated National Fiber Optic Engineers Conference, 2010 Conference on (OFC/NFOEC)*. IEEE, 2010, pp. 1–3.

[162] Z. Yang, S. Yu, L. Chen, J. Zhou, Y. Qiao, and W. Gu, “Qam accommodated double-side band fast ofdm based on idct,” *Optics Express*, vol. 21, no. 26, pp. 32 441–32 449, 2013.

[163] J. Zhao and A. Ellis, “Advantage of optical fast ofdm over ofdm in residual frequency offset compensation,” *IEEE Photonics Technology Letters*, vol. 24, no. 24, pp. 2284–2287, Dec 2012.

[164] J. Zhou, Y. Qiao, T. Zhang, E. Sun, M. Guo, Z. Zhang, X. Tang, and F. Xu, “Fofdm based on discrete cosine transform for intensity-modulated and direct-detected systems,” *Journal of Lightwave Technology*, vol. 34, no. 16, pp. 3717–3725, Aug 2016.

[165] K. R. Rao and P. C. Yip, *The transform and data compression handbook*. CRC press, 2000.

[166] S. A. Martucci, “Symmetric convolution and the discrete sine and cosine transforms,” *IEEE Transactions on Signal Processing*, vol. 42, no. 5, pp. 1038–1051, May 1994.

[167] Z. Wang and B. Hunt, “The discrete w transform,” *Applied Mathematics and Computation*, vol. 16, no. 1, pp. 19–48, 1985.

[168] S. A. Martucci, “Convolution-multiplication properties for the entire family of discrete sine and cosine transforms,” *Proc. 1992 CISS, Princeton, NJ*, 1992.

[169] V. Britanak, P. C. Yip, and K. R. Rao, *Discrete cosine and sine transforms: general properties, fast algorithms and integer approximations*. Elsevier, 2010.

[170] N. Ahmed, T. Natarajan, and K. R. Rao, "Discrete cosine transform," *IEEE transactions on Computers*, vol. 100, no. 1, pp. 90–93, 1974.

[171] E. Feig and S. Winograd, "Fast algorithms for the discrete cosine transform," *IEEE Transactions on Signal processing*, vol. 40, no. 9, pp. 2174–2193, 1992.

[172] J. S. Sheu, B. J. Li, and J. K. Lain, "Led non-linearity mitigation techniques for optical ofdm-based visible light communications," *IET Optoelectronics*, vol. 11, no. 6, pp. 259–264, 2017.

[173] G. Berardinelli, L. A. M. Ruiz de Temino, S. Frattasi, M. I. Rahman, and P. Mogensen, "Ofdma vs. sc-fdma: performance comparison in local area imt-a scenarios," *IEEE Wireless Communications*, vol. 15, no. 5, pp. 64–72, October 2008.

[174] S. P. Yadav and S. C. Bera, "Papr analysis of single carrier fdma system for uplink wireless transmission," in *2015 10th International Conference on Information, Communications and Signal Processing (ICICS)*, Dec 2015, pp. 1–5.

[175] J. Zhou and Y. Qiao, "Low-papr asymmetrically clipped optical ofdm for intensity-modulation/direct-detection systems," *IEEE Photonics Journal*, vol. 7, no. 3, pp. 1–8, 2015.

[176] M. Vetterli, H. J. Nussbaumer *et al.*, "Simple fft and dct algorithms with reduced number of operations," *Signal processing*, vol. 6, no. 4, pp. 267–278, 1984.

[177] Y. S. Cho, J. Kim, W. Y. Yang, and C. G. Kang, *MIMO-OFDM wireless communications with MATLAB*. John Wiley & Sons, 2010.

[178] X. Shao and S. G. Johnson, "Type-iv dct, dst, and mdct algorithms with reduced numbers of arithmetic operations," *Signal Processing*, vol. 88, no. 6, pp. 1313–1326, 2008.

[179] S. G. Johnson and M. Frigo, "A modified split-radix fft with fewer arithmetic operations," *IEEE Transactions on Signal Processing*, vol. 55, no. 1, pp. 111–119, 2007.

[180] R. Mesleh, H. Elgala, and H. Haas, "On the performance of different ofdm based optical wireless communication systems," *J. Opt. Commun. Netw.*, vol. 3, no. 8, pp. 620–628, Aug 2011. [Online]. Available: `http://jocn.osa.org/abstract.cfm?URI=jocn-3-8-620`

[181] R. M. Gagliardi and S. Karp, "Optical communications," *New York, Wiley-Interscience, 1976. 445 p.*, 1976.

[182] S. Arnon, "The effect of clock jitter in visible light communication applications," *journal of lightwave technology*, vol. 30, no. 21, pp. 3434–3439, 2012.

[183] Y. Fujiwara, "Self-synchronizing pulse position modulation with error tolerance," *IEEE Transactions on Information Theory*, vol. 59, no. 9, pp. 5352–5362, 2013.

[184] B. Ghimire, I. Stefan, H. Elgala, and H. Haas, "Time and frequency synchronisation in optical wireless ofdm networks," in *2011 IEEE 22nd International Symposium on Personal, Indoor and Mobile Radio Communications.* IEEE, 2011, pp. 819–823.

[185] M. F. G. Medina, O. González, S. Rodríguez, and I. R. Martín, "Timing synchronization for ofdm-based visible light communication system," in *2016 Wireless Telecommunications Symposium (WTS).* IEEE, 2016, pp. 1–4.

[186] Y. Jiang, Y. Wang, P. Cao, M. Safari, J. Thompson, and H. Haas, "Robust and low-complexity timing synchronization for dco-ofdm lifi systems," *IEEE Journal on Selected Areas in Communications*, vol. 36, no. 1, pp. 53–65, 2018.

[187] Y. Yi, P. Li, C. Li, and C. Azurdia, "An effective scheme for optical doppler shift alleviation in intelligent transportation system integrating visible light communication," in *13th International Conference on Advanced Communication Technology (ICACT2011)*, Feb 2011, pp. 1253–1258.

[188] B. Lin, X. Tang, Z. Ghassemlooy, C. Lin, and Y. Li, "Experimental demonstration of an indoor vlc positioning system based on ofdma," *IEEE Photonics Journal*, vol. 9, no. 2, pp. 1–9, April 2017.

[189] C. Chen, M. Ijaz, D. Tsonev, and H. Haas, "Analysis of downlink transmission in dco-ofdm-based optical attocell networks," in *2014 IEEE Global Communications Conference*, Dec 2014, pp. 2072–2077.

[190] H. Kazemi, M. Safari, and H. Haas, "Spectral efficient cooperative downlink transmission schemes for dco-ofdm-based optical attocell networks," in *2016 IEEE 84th Vehicular Technology Conference (VTC-Fall)*, Sept 2016, pp. 1–6.

[191] S. V. Tiwari, A. Sewaiwar, and Y. H. Chung, "Optical bidirectional beacon based visible light communications," *Optics express*, vol. 23, no. 20, pp. 26 551–26 564, 2015.

[192] P. H. Moose, "A technique for orthogonal frequency division multiplexing frequency offset correction," *IEEE Transactions on communications*, vol. 42, no. 10, pp. 2908–2914, 1994.

[193] H. Elgala, R. Mesleh, and H. Haas, "Practical considerations for indoor wireless optical system implementation using ofdm," in *2009 10th International Conference on Telecommunications*, June 2009, pp. 25–29.

[194] K. Raghunath and A. Chockalingam, "Sir analysis and interference cancellation in uplink ofdma with large carrier frequency/timing offsets," *IEEE Transactions on Wireless Communications*, vol. 8, no. 5, 2009.

[195] D. Huang and K. B. Letaief, "An interference-cancellation scheme for carrier frequency offsets correction in ofdma systems," *IEEE Transactions on Communications*, vol. 53, no. 7, pp. 1155–1165, July 2005.

[196] M. Speth, F. Classen, and H. Meyr, "Frame synchronization of ofdm systems in frequency selective fading channels," in *1997 IEEE 47th Vehicular Technology Conference. Technology in Motion*, vol. 3, May 1997, pp. 1807–1811 vol.3.

[197] P. Chvojka, S. Zvanovec, P. A. Haigh, and Z. Ghassemlooy, "Channel characteristics of visible light communications within dynamic indoor environment," *Journal of Lightwave Technology*, vol. 33, no. 9, pp. 1719–1725, May 2015.